2015

Light metal hydrides for reversible hydrogen storage applications

Guanglin Xia
University of Wollongong, gx168@uowmail.edu.au

Recommended Citation

LIGHT METAL HYDRIDES FOR REVERSIBLE HYDROGEN STORAGE APPLICATIONS

A thesis submitted in fulfilment of the requirements for the award of the degree

DOCTOR of PHILOSOPHY

From the

UNIVERSITY OF WOLLONGONG

By

GUANGLIN XIA, B. Sc., M. Eng.

INSITITUTE FOR SUPERCONDUCTING & ELECTRONIC MATERIALS, FACULTY OF ENGINEERING

2015

CERTIFICATION

I, Guanglin Xia, declare that this thesis, submitted in fulfilment of the requirements for the award of Doctor of Philosophy, in the Institute for Superconducting & Electronic Materials, Faculty of Engineering, University of Wollongong, is wholly my own work unless otherwise referenced or acknowledged. The document has not been submitted for qualifications at any other academic institution.

Guanglin Xia

2015.7.10

ABSTRACT

Although hydrogen as a fuel has been extensively regarded as one of the best alternatives, because the exhaust gases in hydrogen-powered vehicles mainly contain water, storage of hydrogen in an efficient, safe, and economical method remains an unsolved challenge for its widespread use. Nanoconfinement has been widely verified to be an effective and efficient tool to relieve the high kinetic barriers and thermodynamic stability of various complex hydrides which have high gravimetric and volumetric hydrogen capacities.The objective of this thesis is to improve the hydrogen storage performance of certain complex hydrides, such as sodium zinc borohydride, lithium borohydride, lithium nitride, and lithium amidoborane, by taking advantage of nanoconfinement. Based on the special physical and chemical properties of different materials, a series of synthetic methods were designed, and the synergistic effects of space-confinement, nanosize, and morphology towards enhancing hydrogen storage performance have been investigated in detail.

$NaZn(BH_4)_3$ with high purity was first synthesized by a wet-chemical method, which led to the formation of pure $NaZn(BH_4)_3$ solution in tetrahydrofuran, and nanoconfinement of $NaZn(BH_4)_3$ in mesoporous SBA-15 was successfully realized by typical solvent infiltration via capillary action. It was demonstrated that the nanoconfined $NaZn(BH_4)_3$ could desorb hydrogen at temperatures between 50 and 150 $^{\circ}C$ without the emission of diborane. Induced by the nanosize effect, the dehydrogenation kinetics was significantly improved, and the apparent activation energy of $NaZn(BH_4)_3$ was reduced by 5.3 kJ mol^{-1}.

A famous reactive metal hydride composite of $LiAlH_4$ and $LiBH_4$ was successfully nanoconfined in mesoporous carbon via a typical infusion through the capillary effect.

By virtue of the synergistic effect between thermodynamic destabilization and nanoconfinement, the nanostructured $2LiBH_4$-$LiAlH_4$ composite exhibited significantly improved hydrogen storage properties compared with its ball-milled counterpart, including the complete suppression of toxic diborane, a much lower hydrogen release temperature, and faster kinetics for dehydrogenation at a relatively lower temperature. More importantly, it was discovered that the thus-tailored thermodynamics and kinetics of the nanostructured composite laid the foundation for the extremely stable regeneration of Li_3AlH_6, which was realized for the first time without the addition of any catalysts. Overall, the capacity retention for the nanoconfined $2LiBH_4$-$LiAlH_4$ composite from the 2nd to the 7th desorption remained over 98%, while lower than 15% was observed for the ball-milled composite, even after only 5 cycles.

A simple one-pot method for the *in-situ* synthesis of three-dimensional (3D) porous carbon-coated Li_3N nanofibers was developed and has been reported, based on a single-nozzle electrospinning technique with poly(vinyl alcohol) and LiN_3 as the precursor. Due to the explosive release of N_2 from the transformation of LiN_3 into Li_3N, which leads to the volume expansion of poly(vinyl alcohol) during heating, and the good distribution of LiN_3 inside the as-electrospun nanofibers, 3D porous carbon-coated Li_3N nanofibers were synthesized, which were full of mesopores and macropores. The mesoporous and macroporous structure provides favorable pathways for H_2 delivery into and out of the of Li_3N nanoparticles. The thus-fabricated Li_3N nanofibers exhibit significantly improved thermodynamics and kinetics towards hydrogen storage performance compared with their bulk counterpart, which endows them with complete reversibility with a capacity close to the theoretical value at a temperature as low as 250 ^{o}C. This is the lowest temperature reported to date. More

importantly, it was found that the thus-tailored Li_3N nanostructure features extremely stable regeneration without any apparent degradation after 10 de-/re-hydrogenation cycles at a temperature as low as 250 $^{\circ}$C.

Well-dispersed lithium amidoborane (LiAB) nanoparticles inside carbon nanofibers were fabricated by using carbon-coated Li_3N nanofibers as the template. An abundance of micropores, mesopores, and macropores were generated during the formation of Li_3N, which produced Li_3N nanoparticles *in-situ* that were well-distributed and space-confined inside the separate pores, with sufficient space for the accommodation of ammonia borane to interact with Li_3N, so that they serve as "smart" nanoreactors. Each Li_3N nanoparticle is an active site separated by a porous carbon shell inside the porous carbon nanofibers and can initiate the formation of $LiNH_2BH_3$ via the reaction with AB with a molar ratio of 1:3 under the steric hindrance of the carbon coating, while simultaneously realizing the controllable synthesis of $LiNH_2BH_3$ with high loading, good dispersion, and robust stability. Taking advantage of the hierarchical porous architecture and the nanoscale size effects, the thus-formed $LiNH_2BH_3$ nanoparticles can release 10.6 wt.% hydrogen, approaching the theoretical value within only 15 min at a temperature as low as 100 $^{\circ}$C.

ACKNOWLEDGEMENTS

TABLE OF CONTENTS

LIST OF PUBLICATIONS

1. **Guanglin Xia**, Xiaowei Chen, Cuifeng Zhou, Chaofeng Zhang, Dan Li, Qinfen Gu, Zaiping Guo, Huakun Liu, Zongwen Liu, Xuebin Yu. Nano-confined multi-synthesis of a Li-Mg-N-H nanocomposite towards low-temperature hydrogen storage with stable reversibility. *J. Mater. Chem. A* 2015, 3, 12646.

2. Jie Chen, **Guanglin Xia**, Zaiping Guo, Zhenguo Huang, Huakun Liu, Xuebin Yu. Porous Ni nanofibers with enhanced catalytic effect on the hydrogen storage performance of MgH_2. *J. Mater. Chem. A* 2015, DOI: 10.1039/C5TA03721B. (co-first author).

3. **Guanglin Xia**, Yingbin Tan, Dan Li, Zaiping Guo, Huakun Liu, Zongwen Liu, Xuebin Yu. Hierarchical porous $Li_2Mg(NH)_2$@C nanowires with long cycle life towards stable hydrogen storage. *Sci. Rep.* 2014, 4, 6599.

4. **Guanglin Xia**, Jie Chen, Weiwei Sun, Yingbin Tan, Zaiping Guo, Huakun Liu, Xuebin Yu. Well-dispersed lithium amidoborane nanoparticles through nanoreactor engineering for improved hydrogen release. *Nanoscale* 2014, 6, 12333.

5. **Guanglin Xia**, Dan Li, Xiaowei Chen, Yingbin Tan, Ziwei Tang, Zaiping Guo, Huakun Liu, Zongwen Liu, Xuebin Yu. Carbon-coated Li_3N nanofibers for advanced hydrogen storage. *Adv. Mater.* 2013, 25, 6238.

6. **Guanglin Xia**, Yingbin Tan, Xiaowei Chen, Zaiping Guo, Huakun Liu, Xuebin Yu. Mixed-metal (Li, Al) amidoborane: Synthesis and enhanced hydrogen storage properties. *J. Mater. Chem. A* 2013, 1, 1810.

7. **Guanglin Xia**, Qing Meng, Zaiping Guo, Qinfen Gu, Huakun Liu, Zongwen Liu, Xuebin Yu. Nanoconfinement significantly improves the thermodynamics and kinetics of co-infiltrated $2LiBH_4$-$LiA1H_4$ composites: Stable reversibility of hydrogen absorption/resorption. *Acta Mater.* 2013, 61, 6882.

8. **Guanglin Xia**, Li Li, Zaiping Guo, Qinfen Gu, Yanhui Guo, Xuebin Yu, Huakun Liu, Zongwen Liu. Stabilization of NaZn(BH$_4$)$_3$ via nanoconfinement in SBA-15 towards enhanced hydrogen release. *J. Mater. Chem. A* 2013, 1, 250.

9. Yingbin Tan, Xiaowei Chen, **Guanglin Xia**, Xuebin Yu. Efficient chemical regeneration of LiBH$_4$ NH$_3$ spent fuel for hydrogen storage. *Int. J. Hydorgen Energy* 2015, 40, 146.

10. Yanhui Guo, Minghong Wang, **Guanglin Xia**, Xiaohua Ma, Fang Fang, Yonghui Deng. Advanced H$_2$-storage system fabricated through chemical layer deposition in a well-designed porous carbon scaffold. *J. Mater. Chem. A* 2014, 2, 15168.

11. Meng Li, **Guanglin Xia**, Yingbin Tan, Qinfen Gu, Xuebin Yu. Combination of two H-enriched B-N based hydrides towards improved dehydrogenation properties. *Int. J. Hydrogen Energy* 2014, 39, 11668.

LIST OF FIGURES

LIST OF TABLES

CHAPTER 1 INTRODUCTION

1. 1 Overview of hydrogen storage

Undoubtedly, the global demand for enhanced energy productionis one of the most important topics in the 21st century, along with the environment issues it raises. At least 10 terawatt of carbon-free power is required by the mid-century in order to satisfy the world's growing requirement for energy while keeping our planet safe.[1] With concerning current trends in serious pollution and continual consumption of fossil energy resources, clean and renewable energy sources, which could replace fossil fuels, are in high demanded to satisfy the sustainable development of the global economy.

Among various alternative strategies, the adoption of hydrogen, which is an environmental fuel and, at the same time, a primary energy carrier, is capable of ensuring a clean and secure energy future based on the following reasons: [2] (i) Hydrogen is the most abundant element on Earth. (ii) It undergoes a perfectly clean combustion reaction with oxygen to yield energy and water. (iii) It has the highest possible energy density of any hydrogen-based fuel. The chemical energy produced per unit mass of hydrogen is around 142 MJ kg^{-1}, which is at least three times larger than those of other chemical fuels (for instance, the equivalent value is 47 MJ kg^{-1} for liquid hydrocarbons).; (iv) Hydrogen can be easily adopted to run a fuel cell, which has significantly increased efficiency over internal combustion engines (~ 32% efficiency for diesel-electric; 90% potential efficiency for a fuel cell with thermal capture, 85% for an electric motor, 77% overall efficiency), while eliminating the formation of carbon particulates, sulfur, and/or nitrogen oxides. [3]

1. 2 Hydrogen economy
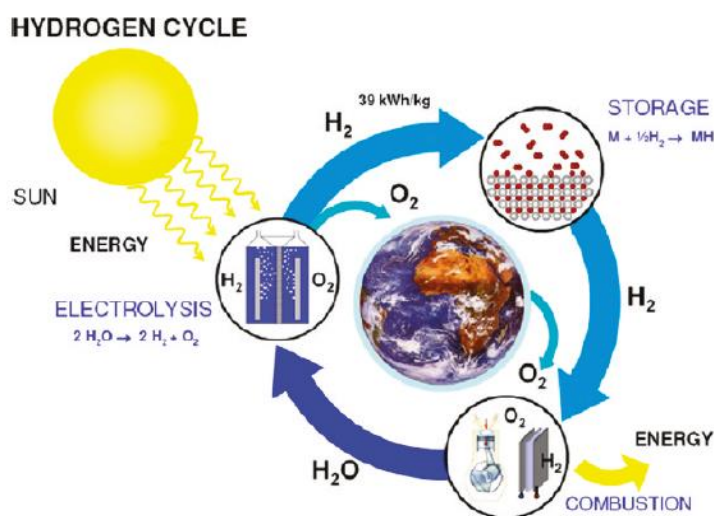
Figure 1. 1 Hydrogen cycle for application. [4]

Since hydrogen is the most abundant element in the universe, which has the highest energy density per unit mass and produces water, it is widely regarded as a solution for transport applications. Nonetheless, it should be noted that hydrogen, which is not freely avaible in nature, is not an energy source but rather an energy carrier. In an ideal hydrogen cycle (Figure 1.1), hydrogen is fabricated by splitting water via electrolysis with solar energy, storing it reversibly in a solid, and using it in a fuel cell to produce electrical energy and heat. This is the so-called "hydrogen economy", which could effectively address the major energy challenges of the 21st century.

Unfortunately, there are still many problems to achieve this dream in daily life: (i) the cost of safe and efficient production and transportation of hydrogen needs to be lowered to be competitive with gasoline without adverse environmental impact; (ii) on-board hydrogen storage systems should allow a driving range of greater than 300 miles while meeting vehicle cost, packaging, and performance requirements; (iii) an effective and efficient fuel cell system is needed. [5] Among them, hydrogen storage is the main bottleneck, particularly for mobile applications. [6] Because hydrogen is an extremely volatile gas, its volumetric energy density is much too low for pratical

applications. [7] Therefore, a means to store hydrogen efficiently and safely is required for the flexible use of hydrogen as a carrier of energy.

1. 3 Requirements for hydrogen storage

The U.S. Department of Energy (DOE) has established a set of technical trargets for on-board hydrogen storage systems, considering the economic and environmental parameters shown in Table 1.1. It should be noted that the targets relate to the properties of the entire storage system, which means the cost, volume, and mass of any components involved in the fabrication of the system should be taken into account. In principle, high storage capacities, high gravimetric and volumetric densities, fast kinetics for dehydrogenation and hydrogenation, long and stable cycling performance, effective thermal transfer during operation, safe operation, and reasonable risks under abnormal conditions are required for a practical hydrogen storage system. In addition, various requirements must be simultaneously fulfilled for particular applicatiosn. Moreover, the toxicity properties and the cost for the fabrication of the storage system should be carefully considered for the achievement of the set goals.

Table 1. 1 Summary of the "old" (2003) [5] and "new" (2009) [8] DOE hydrogen storage targets.

Storage parameter	Units	Old targets (2003)		New targets (2009)		
		2010	2015	2010	2015	Ultimate
System gravimetric capacity	kWh/kg	2	3	1.5	1.8	2.5
	wt% H_2	6	9	4.5	5.5	7.5
System volumetric capacity	kWh/L	1.5	2.7	0.9	1.3	2.3
	g H_2/L	45	81	28	40	70
H_2 delivery temp. (to FC)	°C	−40/85	−40/85	−40/85	−40/85	−40/95–105
Operating pressure (min./max.)	MPa	0.4/10	0.3/10	0.5/1.2	0.5/1.2	0.3/1.2
Kinetics	(g H_2/s)/kW	0.02	0.02	0.02	0.02	0.02
Cost	$/kWh net	4	2		To be determined	

1. 4 Hydrogen storage approachs

Hydrogen could be stored, in principle, in physical form (gas or liquid) or in a chemical form. Currently, a series of hydrogen storage approaches are being discussed or adopted to reversibly store hydrogen.

i) Compressed hydrogen gas: The most common storage system is high-pressure gas cylinders with a maximum pressure of 20 MPa. Carbon-fiber-reinforced composite tanks can reach a pressure of 80 MPa, and these are already being used in prototype hydrogen-powered vehicles. Nonetheless, the safety of the cylinders under high pressure, especially in highly populated areas, is an important issue of concern and, more importantly, the hydrogen gravimetric density is still low, which is a significant obstacle to its pratical applications. [9]

ii) Liquid hydrogen tanks: As the volumetric capacity of liquid hydrogen is 0.070 kg L^{-1}, which is much higher than that of pressurized hydrogen at 70 MPa (0.039 kg L^{-1}), more hydrogen in a given volume could be stored in liquid hydrogen tanks than in compressed gas tanks. The consumption of energy for hydrogen liquefaction, hydrogen boil-off, and the cost of the special tanks are major issues for the practical application of liquid hydrogen tanks. Although the loss of hydrogen due to boil-off could be eliminated to obtain the maximum driving force, the energy used to liquefy the hydrogen, over 30% of the lower heating value of hydrogen, remains a big drawback, which could also have an impact on the cost of fuel and degrade fuel cycle energy efficiency. [5]

iii) Physisorption of hydrogen on high surface area sorbents and carbon-based materials: The weak *van der Waals* interaction between hydrogen and most sorbents with high surface area, described as physisorptive attraction, leads to reversible storage of hydrogen on a wide range of candidates, such as carbon-based materials (nanotubes,

fullerenes, and graphene) [10,11], metal-organic frameworks (MOFs) [12], zeolites[13], and covalent-organic frameworks (COFs) [14,15]. MOF-177 in particular, which possesses a surface area of 5900 m^2 g^{-1}, was observed to have a hydrogen uptake of 7.5 wt.% at -196 $^{\circ}$C. [16] All sorbents, however, suffer from a common limitation, i.e., the weak interaction between molecular hydrogen and the sorbent, which means an operating temperature at or close to that of liquid nitrogen (-196 $^{\circ}$C).

iv) Solid-state chemical hydrides: By incorporation of hydrogen into the crystal structure of solid-state storage materials, it can be reversibly stored. In order to develop a suitable on-board hydrogen storage system for the transportation industry that is competitive with current vehicles in the market place, compact, light, safe, and affordable containment is required, which should cover a driving range of 400 km. Therefore 4 kg hydrogen is needed for an electric car with a fuel cell. A direct comparison of the volume for storing 4 kg of hydrogen in the above-mentioned ways (i.e., liquefied hydrogen tank, high-pressure hydrogen cylinder, and solid complex hydrides.) is presented in Figure 1.2. It is obvious that due to the large volumetric density of solid metal hydride, it is now regarded as a more effective way to use hydrogen than liquid hydrogen and compressed gas. A series of materials have been recently demonstrated to be suitable for chemical storage of hydrogen with high gravimetric and volumetric capacities. Unfortunately, none of the materials investigated to date is capable of fulfilling all the requirements for practical applications. Therefore the topic of this thesis is focused on the further improvement of solid-state chemical hydrides, which it will be discussed in detail in the following chapters.

Figure 1. 2 Volume of 4 kg of hydrogen compacted in different ways, with size relative to the size of the car. [2]

1. 5   Research aims and scope

Recently, a multitude of novel materials with fascinating properties, e.g., high gravimetric capacity and volumetric capacity, and/or reasonable thermodynamics, have been discovered. For example, high gravimetric and volumetric densities of 18.5 wt.% and 121 kg H_2 m^{-3}, respectively, have been discovered for $LiBH_4$[17], and the $Mg(NH_2)_2$-2LiH system exhibits favorable thermodynamics of 39 kJ mol^{-1} H_2, which equals an working temperature of 90 °C under 1 bar of equilibrium hydrogen pressure and could satify the practical tragets for proton exchange membrane fuel cells [18]. Despite substantial research efforts and improvements within solid-state hydrogen storage materials, a material that can fulfil all the set targets simultaneously and act as the successor for gasoline in on-board mobile application has not yet been realized, owing to thermodynamic or kinetic, and/or the simultaneous release of by-products during dehydrogenation. [19]

Fortunately, after intensive investigations on hydrogen storage materials, a series of methodologies to improve the thermodynamics and kinetics of the candidates have been well-established, e.g., doping with catalysts, thermodynamic destabilization, and nanostructuring.[20,21] One of the most outstanding approaches for improving the performance is to reduce the particle size of hydrogen storage materials down to nanometer size, as their physicochemical properties could change with the particle size decreased to the nanometer range. As hydrogen is incorporated into the crystal structure of solid-state chemical hydrides, a significant fraction of the atoms, including hydrogen, could be situated on the surface, with the interior atoms close to the surface, which could lead to rapid kinetics for hydrogen charge and discharge. More interestingly, the thermodynamics of hydrogen storage could also be be changed due to the tremendous contribution of the surface energy to the total stability of the nanoparticles. The change in equilibrium dehydrogenation temperatures under 1 bar of H_2 pressure relative to particle size for different metal-metal hydrides is theoretically predicted in Figure 1.3, which illustrates how large changes in equilibrium pressure could be expected when particle size is below 2-5 nm. As expected, significant enhancement has been verified in a myriad of solid-state chemical hydrides.[22,23]
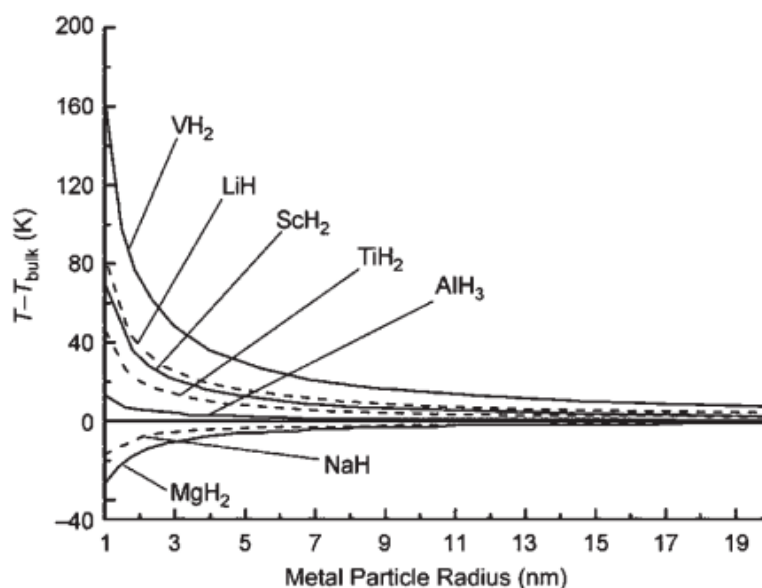
Figure 1. 3 Variation in the metal/metal hydride transition temperature relative to the particle size for bulk materials based on DFT calculations. [24]

Nanosized particles, however, are inherently unstable and easily grow into larger crystallites or aggregates during thermal treatment. Therefore, a method to stabilize the as-synthesized nanoparticles during repeated cycles of hydrogen charge and discharege is needed, which could effectively prevent particle growth during heating and improve the gas-solid interface during hydrogenation and dehydrogenation at elevated temperature. Nanoconfinement, which refers to the confinement of solid materials within the pores of a scaffold with porous structure, could lead to direct synthesis of nanostructured materials by physical nanoconfinement in nanosized pores, and, on the other hand, effectively maintain the three-dimensional sizes of composites. The significantly enhanced kinetics and cycling performance of various solid-state hydrogen storage materials after nanoconfinement in porous scaffolds have been intensively confirmed.

Inspired by the significant improvement that is possible based on nanoconfinement, the central goal of this study is to increase the feasibility of producing complex

hydrides for practical application via nanostructuring to promote the kinetics, tailor the thermodynamics, and enhance the cycling stability. Although some advances have been achieved recently that promote the hydrogen storage performance via nanotechnology, the nanostructuring of light metal hydrides with a great potential for application is still a big challenge due to their high reactivity. Therefore, the major purposes of this present work are: 1) to develop a reasonable method for nanostructuring various complex hydrides; 2) to investigate the effects of nanostructuring on both the hydrogenation and the dehydrogenation performance of these materials; 3) to examine the mechanisms of nanostructuring-induced improvement.

The following is a brief summary of the contentsof this thesis:

- Chapter 2 presents an extensive literature review of recently reported solid-state chemical hydrides, especially recent advances on complex hydrides via nanostructuring.

- Chapter 3 presents the experimental equipment that was generally used, the chemicals that were used, and the methods to test the hydrogen storage performance.

- Chapter 4 presents the synthesis of pure $NaZn(BH_4)_3$ and the stabilization of $NaZn(BH_4)_3$ via nanoconfinement in SBA-15 towards enhanced hydrogen release.

- Chapter 5 presents the nanoconfinement of co-infiltrated $2LiBH_4–LiAlH_4$ composites and an investigation of the thermodynamics, kinetics, and reversibility of hydrogen absorption/resorption.

- Chapter 6 presents the nanoconfined multi-step synthesis of a Li-Mg-N-H nanocomposite for low-temperature hydrogen storage with stable reversibility.

- Chapter 7 exhibits the synthesis of carbon-coated Li₃N nanofibers for advanced hydrogen storage.

- Chapter 8 presents the fabrication of well-dispersed lithium amidoborane nanoparticles through nanoreactor engineering for improved hydrogen release.

- Chapter 9 gives an overall summary of this doctoral work and discusses possible future research work related to these light metal hydrides and the outlook for hydrogen storage.

1. 6   References

[1]   Muradov, N. Z.; Veziroğlu, T. N. *International Journal of Hydrogen Energy* **2008**, *33*, 6804.

[2]   Schlapbach, L.; Zuttel, A. *Nature* **2001**, *414*, 353.

[3]   Boudghene Stambouli, A.; Traversa, E. *Renewable and Sustainable Energy Reviews* **2002**, *6*, 295.

[4]   Jena, P. *The Journal of Physical Chemistry Letters* **2011**, *2*, 206.

[5]   Satyapal, S.; Petrovic, J.; Read, C.; Thomas, G.; Ordaz, G. *Catalysis Today* **2007**, *120*, 246.

[6]   Grochala, W.; Edwards, P. P. *Chemical Reviews* **2004**, *104*, 1283.

[7]   Murray, L. J.; Dinca, M.; Long, J. R. *Chemical Society Reviews* **2009**, *38*, 1294.

[8]   *http://www1.eere.energy.gov/hydrogenandfuelcells/storage/pdfs/targets_on board_hydro_storage.pdf.* .

[9]   Züttel, A. *Naturwissenschaften* **2004**, *91*, 157.

[10]   Dillon, A. C.; Jones, K. M.; Bekkedahl, T. A.; Kiang, C. H.; Bethune, D. S.; Heben, M. J. *Nature* **1997**, *386*, 377.

[11]   Pumera, M. *Energy & Environmental Science* **2011**, *4*, 668.

[12]   Rowsell, J. L. C.; Yaghi, O. M. *Angewandte Chemie, International Edition* **2005**, *44*, 4670.

[13]   Li, Y.; Yang, R. T. *The Journal of Physical Chemistry B* **2006**, *110*, 17175.

[14]   Furukawa, H.; Yaghi, O. M. *Journal of the American Chemical Society* **2009**, *131*, 8875.

[15]   Han, S. S.; Furukawa, H.; Yaghi, O. M.; Goddard, W. A. *Journal of the American Chemical Society* **2008**, *130*, 11580.

[16]   Wong-Foy, A. G.; Matzger, A. J.; Yaghi, O. M. *Journal of the American Chemical Society* **2006**, *128*, 3494.

[17]   Züttel, A.; Rentsch, S.; Fischer, P.; Wenger, P.; Sudan, P.; Mauron, P.; Emmenegger, C. *Journal of Alloys and Compounds* **2003**, *356-357*, 515.

[18]   Xiong, Z. T.; Hu, J. J.; Wu, G. T.; Chen, P.; Luo, W. F.; Gross, K.; Wang, J. *Journal of Alloys and Compounds* **2005**, *398*, 235.

[19]   Ley, M. B.; Jepsen, L. H.; Lee, Y.-S.; Cho, Y. W.; Bellosta von Colbe, J. M.; Dornheim, M.; Rokni, M.; Jensen, J. O.; Sloth, M.; Filinchuk, Y.; Jørgensen, J. E.; Besenbacher, F.; Jensen, T. R. *Materials Today* **2014**, *17*, 122.

[20]   Rönnebro, E. C. E.; Majzoub, E. H. *MRS Bulletin* **2013**, *38*, 452.

[21]   Dalebrook, A. F.; Gan, W.; Grasemann, M.; Moret, S.; Laurenczy, G. *Chemical Communications* **2013**, *49*, 8735.

[22]   Wu, H. *ChemPhysChem* **2008**, *9*, 2157.

[23]   Fichtner, M. *Physical Chemistry Chemical Physics* **2011**, *13*, 21186.

[24]   Ki Chul, K.; Bing, D.; Johnson, J. K.; David, S. S. *Nanotechnology* **2009**, *20*, 204001.

2   CHAPTER 2 LITERATURE REVIEW

This chapter will briefly give the overall background on the methods for nanoconfinement and on solid-state chemical hydrides, such as complex hydrides, magnesium-based hydrogen storage materials, and chemical hydrides, as hydrogen storage materials. Nanoconfinement-induced improvement of their hydrogen storage performance will be also presented in brief.

2.1 Strategies for preparing nanoconfined hydrogen storage materials

The nanoconfinemt should fulfil a number of different functions, i.e., preserving nanoscale crystallites under harsh conditions and/or high temperature, while still providing access of hydrogen to the active phase. In addition, since the scaffolds adopted for nanoconfinement do not contribute directly to the hydrogen storage functionality, they will unavoidably decrease the gravimentric hydrogen density, thus reducing normalized performance. Thefore, the host should comply with several requirements: 1) chemical inertness is important, which could limit reaction with hydrogen storage materials during the synthesis and the following hydrogen storage process; 2) the melting point must be high in order to avoid collapse during thermal treatment for both dehydrogenation and hydrogenation; 3) the bulk density should be sufficiently low to achieve high weight specific performance; 4) the templates should ideally be highly elastic to accommodate the volume changes in the hydrogen storage materials during hydrogen charge and discharge; 5) low cost is an important consideration.[1,2]

2.1.1   Solvent mediated infiltration

Solvent mediated infiltration (also known as wet or solution infiltration) is based on a solvent which can dissolve the precursors or other ingredients to form a

homogeneous solution, in which the porous templates are submerged.[3] The solution must then effectively infiltrate the pores, and the hydrogen storage materials will solidify and/or be synthesized to form nanocrystalline and/or amorphous particles inside the porous structure upon elimination of the solvent during evaporation. It should be pointed out that the solvent that is adopted should be weakly coordinating to both the targeted materials and the templates, which could help in eliminating the solvent and therefore avoiding possible decomposition or contamination of the hydrogen storage materials during heating. One advantage of solution infiltration is that infiltration could be realized under milder circumstances compared with the following method of melt infiltration. Nonetheless, it can be a big challenge to discover an appropriate solvent to dissolve the materials without reacting with either the materials or the porous templates in some cases.

2.1.2 Melt infiltration

Melt infiltration is a method arising from the field of ceramic nanoparticles, which isbased on the encapsulation of active materials in porous scaffolds through the melting of any precursors or active phases.[4] It could be adopted as an impregation method if the melting point of the hydrogen storage materials is relatively lower than the decomposition temperature of the templates, depending on the minimization of the overall interfacial energy in the molten species and the host system. Melt infiltration is advantageous because no solvents or precursors are used, which avoids treatments after the nanoconfinement process and possible contamination of the solvent and/or other substrates. Nevertheless, due to the fact that most of the metals or relatively complex hydrides have high reactivity when molten, finding an inert template could be a big challenge. In addition, special strategies such as high hydrogen

pressure should be adopted to avoid the decomposition of the hydrogen storage materials during the infiltration process.

2.1.3   In-situ synthesis

The encapsulation of hydrogen storage materials could be achieved in-situ during the fabrication of the porous scaffolds, which is probably the most perfect way to nanoconfinement. It could avoid the work of searching for templates, the tedious infiltration process, and the blocking of pores during the process of encapsulation. Due to the high reactivity of most hydrogen storage materials, finding suitable proper precursors that could be utilized to simultaneously synthesize both templates and hydrogen storage materials is a big challenge for this method.

2.2 Complex hydrides

Complex hydrides refer to Groups I, II, and III salts of alanates, amides, borohydrides, and their derivatives. Due to their high gravimetric densities and commercial availability, these materials have been widely regarded as viable candidates for practical application.[5]

2.2.1   Alanates

2.2.1.1 Introduction

During the past decades, alanates, which can be found as hexahydroaluminates or tetrahydroaluminates, have received the most attention among the group of complex hydrides. Some of the most common alanates are listed in Table 2.1, among which, $LiAlH_4$ exhibits the highest storage capacity, i.e., 10.5 wt.%. Alkali metal alanates dehydrogenate at temperatures ranging from 200 ºC to 300 ºC, leading to the formation

of aluminium metal and the corresponding alkali metal hydrides based on the following two-step equation:

$$3NaAlH_4 \leftrightarrow Na_3AlH_6 + 2Al + 3H_2 \leftrightarrow 3NaH + 3Al + 9/2H_2 \quad (2.1)$$
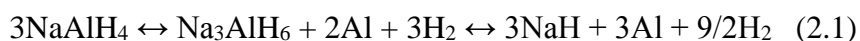
In contrast to the alkali metal alanates, $Mg(AlH_4)_2$ exhibits a dehydrogenation process according to Equation (2.1), but without the formation of hexahydroaluminates as an intermediate phase. Further dehydrogenation could be achieved by the decomposition of MgH_2 to form Mg, which will react with aluminium at ~400 ^{o}C to produce Al_3Mg. Unfortunately, the exothermic nature of the dehydrogenation reaction of $Mg(AlH_4)_2$ precludes its direct rehydrogenation.

$$Mg(AlH_4)_2 \rightarrow MgH_2 + 2Al + 3/2H_2 \quad (2.2)^{[6]}$$
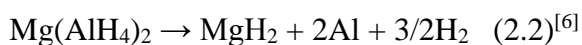
In terms of $NaAlH_4$, the first reaction is thermodynamically favourable at temperatures above 33 ^{o}C at 1 bar H_2 pressure.[7] The high kinetic barrier, however, leads to higher temperature and hydrogen pressure being required for hydrogen adsorption and desorption. Recently, it has been demonstrated that a reversible capacity of 4 wt.% at 160 ^{o}C could be achieved over 100 cycles in Ti-catalyzed $NaAlH_4$.[8]

Table 2.1 Commonly known complex aluminium hydrides. The mixed cation alanates are also listed.[9]

Complex hydride	Hydrogen capacity (wt%)	Desorption temperature (°C)		Desorption enthalpy (kJ/mol H$_2$)		Status of reversibility
		Step 1	Step 2	Step 1	Step 2	
LiAlH$_4$	10.5	150 (5.3 wt%)	180 (2.6 wt%)	−10	25	Not reversible
NaAlH$_4$	7.4	185 (3.7 wt%)	230 (1.85 wt%)	37	47	Reversible (5.5 wt%)
KAlH$_4$	5.7	290 (2.9 wt%)	350 (1.4 wt%)	55	70	Reversible (4.2 wt%)
Mg(AlH$_4$)$_2$	9.3	140 (6.9 wt%)	280 (3.6 wt%)	41	76	Not reversible
Ca(AlH$_4$)$_2$	7.8	127 (1.0 wt%)	250 (4.2 wt%)	−7	28	Not reversible
LiMg(AlH$_4$)$_3$	9.7	100 (4.8 wt%)	100 (2.8 wt%)	−15.1	-	Not reversible
Na$_2$LiAlH$_6$	6.98	245	-	53.5±1.2	-	Reversible (2.6 wt%)
K$_2$NaAlH$_6$	4.47	325	-	98	-	Reversible
K$_2$LiAlH$_6$	5	227	-	82	-	Reversible (2.5 wt%)
NaAlH$_4$+Mg(AlH$_4$)$_2$ mixture	7.5	140	-	-	-	-

2.2.1.2 Nanoconfinement of alanates

The first example of alanates nanoconfined in porous templates is NaAlH$_4$, reported by K. P. de Jong via solution infiltration into carbon nanofiber support.[10,11] They further fabricated carbon nanofiber-supported NaAlH$_4$ having different particle sizes of 1-10 μm, 19-30 nm, and 2-10 nm, and verified that the hydrogen release temperature decreased from 186 °C down to 70 °C, while the activation energies were reduced from 116 kJ mol^{-1} to 58 kJ mol^{-1}. Subsequently, Sun et al. reported the synthesis of space-confined NaAlH$_4$ in ordered mesoporous silica via wet infiltration, as illustrated in Figure 2.1.[12] As shown in Figure 2.2, the kinetics of dehydrogenation is greatly improved when NaAlH$_4$ is nanoconfined by mesopores of mesoporous silica, with a value of 3.0 wt.% hydrogen released at 180 °C in 60 min.
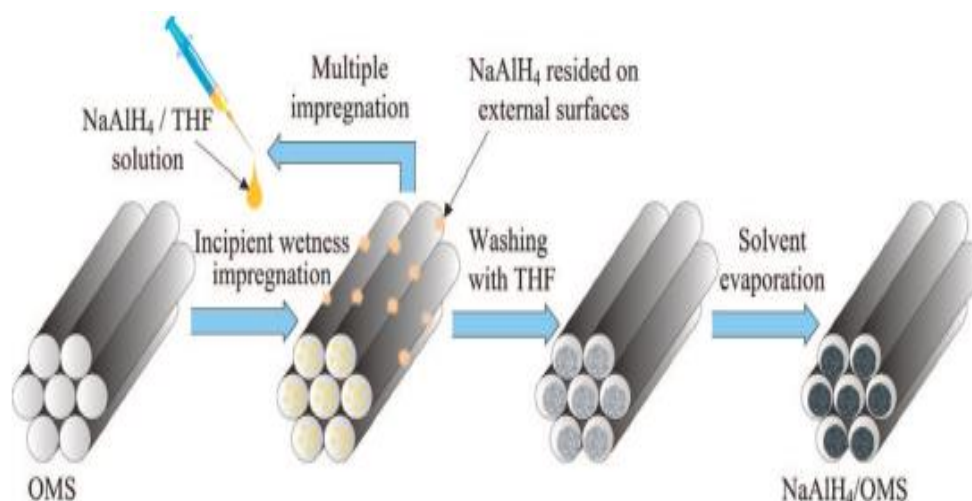
Figure 2.1 Preparation process for NaAlH₄ nanoparticles space-confined in ordered mesoporous silica (OMS).[12]
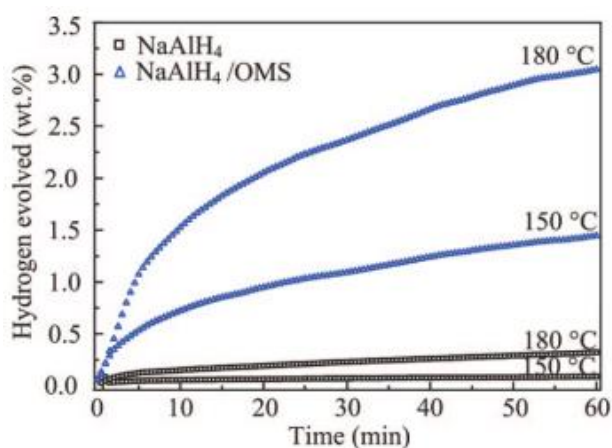
Figure 2.2 Dehydrogenation curves for pristine NaAlH₄ and NaAlH₄ nanoparticles space-confined in ordered mesoporous silica (NaAlH₄/OMS) at 150 ºC and 180 ºC.[12]

Since both nanoconfinement and the addition of $TiCl_3$ could lead to superior hydrogen storage performance in $NaAlH_4$, Jensen et al. adopted a $TiCl_3$-loaded carbon aerogel to nanoconfine $NaAlH_4$ and the resulting $NaAlH_4$ nanoparticle started to release hydrogen at around room temperature with a peak temperature of only 125 ºC, which was attributed to the synergetic effects between nanoconfinement and the

catalytic effects of TiCl$_3$.[13] More recently, NaAlH$_4$ was infiltrated into well tailored porous carbons with pore sizes of 200 nm, 60 nm, 30 nm, and 4 nm via melt infiltration (Figure 2.3).[14] It was found that NaAlH$_4$ started to release hydrogen at a temperature of ~ 100 ^{o}C with a peak of 172 ^{o}C when the pore size of the adopted templates was reduced to 30 nm, and the apparent activation energy for hydrogen discharge was determined to be 69.7 kJ mol^{-1} for NaAlH$_4$ confined in 4 nm porous carbons, reduced by 58 kJ mol^{-1} compared to the first step dehydrogenation of its bulk counterpart.
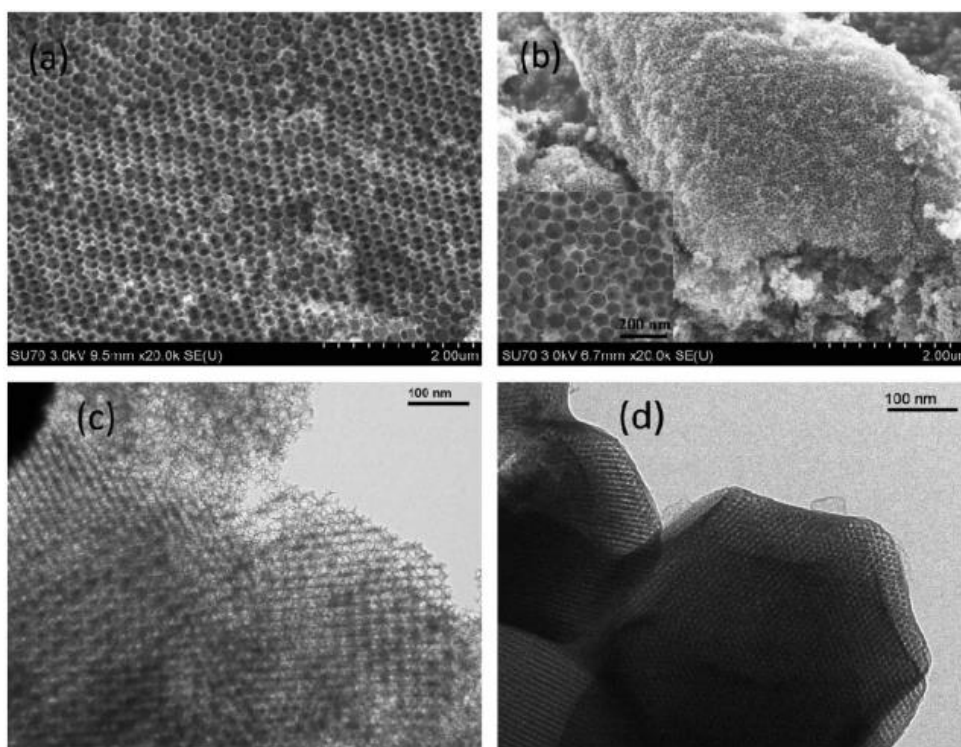
Figure 2.3 Uniform porous carbons with different pore sizes: (a) 200 nm; (b) 60 nm; (c) 30 nm; and (d) 4 nm.[14]

Another alanate which has been successfully nanoconfined is LiAlH$_4$, which was infiltrated into Ni-containing mesoporous carbon scaffold via solution infiltration.[15] It was demonstrated that LiAlH$_4$ confined in Ni-containing porous carbon starts to release hydrogen at 66 ^{o}C, which is 84 ^{o}C lower than for neat LiAlH$_4$. The effects of

nanoconfinement, the catalytic effect of Ni, and compartmentalization effects during the sintering of particles could have contributed to the decrease in the apparent activation energy (E_a = 39.67 kJ mol^{-1}) of LiAlH$_4$.

2.2.2   Borohydrides

2.2.2.1 Introduction

Borohydrides, also referred to as tetrahydroborate, are identified as a group of hydrides in which hydrogen is covalently bonded to the central atoms (B) in the [BH$_4$]$^-$ [1] complex anion. Due to their high gravimetric and volumetric hydrogen capacity (e.g., 18.6 wt.% hydrogen for LiBH$_4$), borohydrides have been regarded as highly promising hydrogen storage resources. One of the more popular borohydrides is LiBH$_4$, which decomposes at temperatures above 380 °C and forms LiH and B with a capacity of 13.5 wt.% based on the following reaction:

$$2LiBH_4 \rightarrow 2LiH + 2B + 3H_2 \qquad (2.3)$$
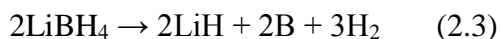
The dehydrogenated LiBH$_4$ could be partially rehydrogenated at 600-650 °C under 70-350 bar of hydrogen. Interestingly, a correlation between the experimental dehydrogenation temperature and the electronegativity of the metal in metal borohydrides was found, and these compounds, which have less ionic character than diborane, are expeceted to be unstable and release diborane during dehydrogenation. On the other hand, additional compounds have been extensively introduced into borohydrides with the aim of tailoring their respective thermodynamic stabilities. For instance, the reaction enthalpy could be lowered by 25 kJ mol^{-1} H$_2$ with the addition of MgH$_2$ into LiBH$_4$.[16,17]

Sodium borohydride (NaBH$_4$) was dehydrogenated at a temperature of 534 °C to its parent elements, based on Equation (2.4), owing to the lower stability of NaH

compared with LiH, which is formed in the dehydrogenation of $LiBH_4$.[18] A similar reaction to $NaBH_4$ was observed for the decomposition of KBH_4, which occurs at an even higher temperatures of ~585 $^{\circ}$C.[5]

$$NaBH_4 \rightarrow Na(l) + B + 2H_2 \qquad (2.4)$$
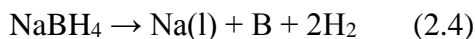
Magnesium borohydride ($Mg(BH_4)_2$) possess a high gravimetric hydrogen capacity of 14.9 wt.% H_2 and favourable thermodynamics of 39.3 kJ mol^{-1} H_2 at 1 bar of hydrogen pressure.[19,20] The dehydrogenation of $Mg(BH_4)_2$ takes place in more than two steps in the temperature range of 290-350 $^{\circ}$C, leading to the formation of $MgB_{12}H_{12}$, MgH_2, and MgB_2 according to the proposed reaction pathway (Equation 2.5).[21] The dehydrogenated $Mg(BH_4)_2$ could be rehydrogenated at 270 $^{\circ}$C under 400 bar after 48 h of treatment.

$$Mg(BH_4)_2 \rightarrow 1/6MgB_{12}H_{12} + 5/6MgH_2 + 13/6H_2$$

$$\rightarrow MgB_2 + 4H_2 \qquad (2.5)$$
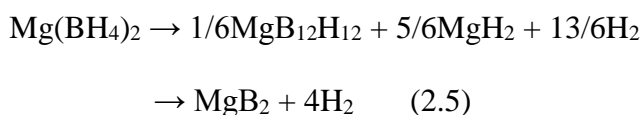
Transition metal borohydrides generally decompose at much lower temperatures than the alkali metal borohydrides. For example, decomposition of $Y(BH_4)_3$ could occur at temperatures ranging from room temperature to around 500 $^{\circ}$C, based on the following Equation (2.6),[22] and rehydrogenation could be achieved at 260 $^{\circ}$C under 35 bar of hydrogen.[23]

$$Y(BH_4)_3 \rightarrow YH_3 + 3B + 9/2H_2$$

$$\rightarrow YH_2 + 3B + 10/2H_2 \quad (2.6)$$
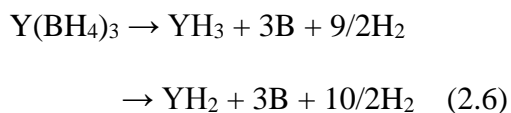
Furthermore, as shown in Figure 2.4, a nearly linear relationship was observed between the electronegativity of metals in the compounds, which have strong coordination to the borohydride groups, and the experimental temperature of decomposition.[24] For example, the dehydrogenation temperature for a bialkali metal

borohydride (LiK(BH$_4$)$_2$) is around the average of the dehydrogenation temperatures for their corresponding mono alkali borohydrides, i.e., LiBH$_4$ and KBH$_4$.[25]
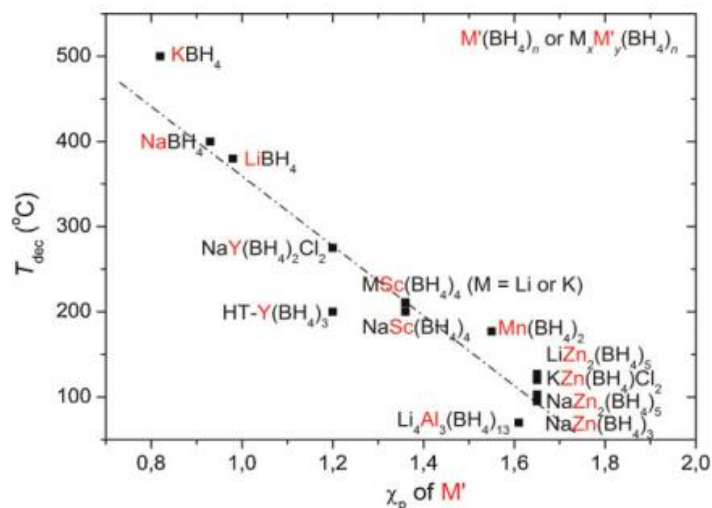
Figure 2.4 Decomposition temperature (T_{dec}) for metal borohydrides as a function of the electronegativity of the metal (M′).

2.2.2.2 Nanoconfinement of borohydrides

Various borohydrides, such as LiBH$_4$, NaBH$_4$, Ca(BH$_4$)$_2$, and Mg(BH$_4$)$_2$, have been successfully nanoconfined in porous templates, e.g., carbon-based scaffolds[26-28], metal oxides[29], metal-organic frameworks (MOFs)[30], SBA-15[31], and polymer matrix[32,33].

Nanoconfinement of LiBH$_4$ could be achieved by both solution infiltration and melt infiltration under the protection of hydrogen with high pressure. For example, LiBH$_4$ was firstly infiltrated into an activated carbon scaffold using solution infiltration, which shows an onset dehydrogenation temperature of just 220 °C, 150 °C lower than that of bulk LiBH$_4$.[26] Moreover, the temperature for hydrogenation was tremendously decreased via the nanoconfinement of LiBH$_4$ in activated carbon scaffold. It has been verified that the production of amorphous LiBH$_4$ is favoured when porous carbon with

pore sizes smaller than 2 nm is adopted as the scaffold, along with the method of solution infiltration, which leads to an onset dehydrogenation temperature that is further decreased down to 200 $^{\circ}$C. A hydrogen capacity of 4.0 wt.% was obtained at only 300 $^{\circ}$C.[34] By comparison, the hydrogen desorption from bulk LiBH$_4$ is negligible at the same temperature. Yu et al. found that Cu-MOFs is a viable template to load LiBH$_4$, and the nanoconfined LiBH$_4$ in Cu-MOFs could start to release hydrogen at around 60 $^{\circ}$C (Figure 2.5).[30] The release of diborane, however, is detected during the dehydrogenation of LiBH$_4$ nanoconfined in Cu-MOFs.
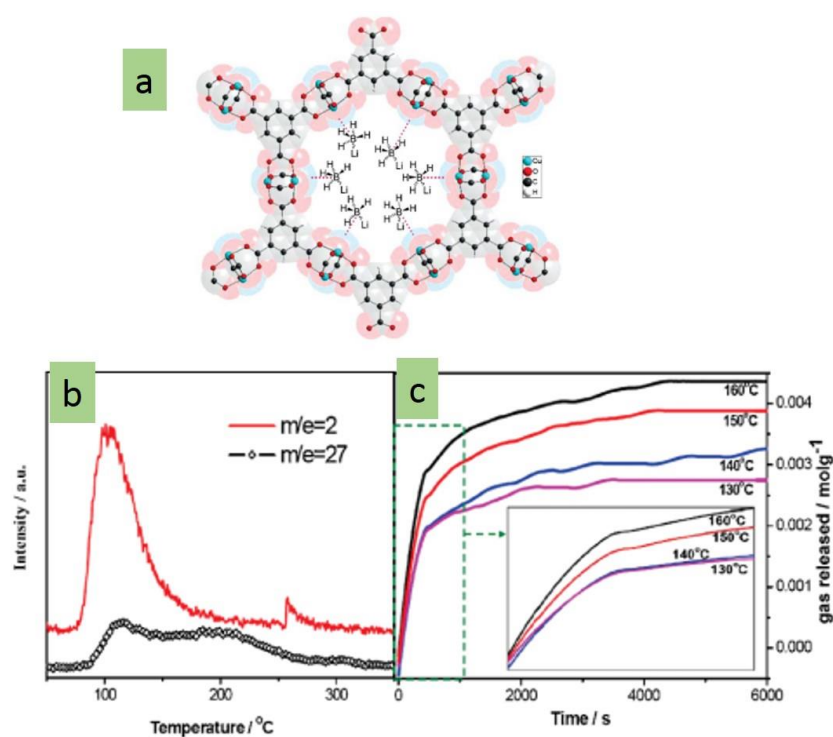
Figure 2.5 (a) Schematic diagram of LiBH$_4$ nanoconfined in Cu-MOFs; (b) Mass spectra of LiBH$_4$ nanoconfined in Cu-MOFs; (c) dehydrogenation plots of the 1st step hydrogen release from LiBH$_4$ nanoconfined in Cu-MOFs.[30]

In the meantime, Majzoub et al. investigated the wetting and decomposition behaviour of LiBH$_4$ during nanoconfinement in highly ordered nanoporous hard carbon templates in detail.[35] The nanoconfinement of LiBH$_4$ in a framework with

pore size of 2 nm resulted in the formation of an amorphous substrate and the significant reduction of the onset dehydrogenation temperature from 460 ºC to 220 ºC compared with bulk LiBH$_4$. More importantly, the release of diborane is obviously suppressed during the decomposition of amorphous LiBH$_4$ that is space-confined in porous templates. Following that, Yu et al. went on to comprehensively investigate the effects of a series of template pore sizes on the structural phase transition, dehydrogenation and hydrogenation, and the release of toxic diborane during the dehydrogenation of LiBH$_4$.[36] With the reduction of pore size, the dehydrogenation of LiBH$_4$ shows a systematic and monotonic reduction in desorption temperature and a gradual reduction of the desorption of diborane. In order to enhance the hydrogen storage density of nanoconfined LiBH$_4$, Chen et al. employed zeolite-templated carbon with high porosity and excellent mechanical stability to nanoconfine LiBH$_4$ (Figure 2.6).[37] With ultra-high pressure densification and a high loading amount of LiBH$_4$, the nanoconfined system could realize a volumetric capacity of 75.43 g L^{-1} and gravimetric capacity of 6.92 wt.%, and moreover, an onset dehydriding temperature of 194 ºC was observed.
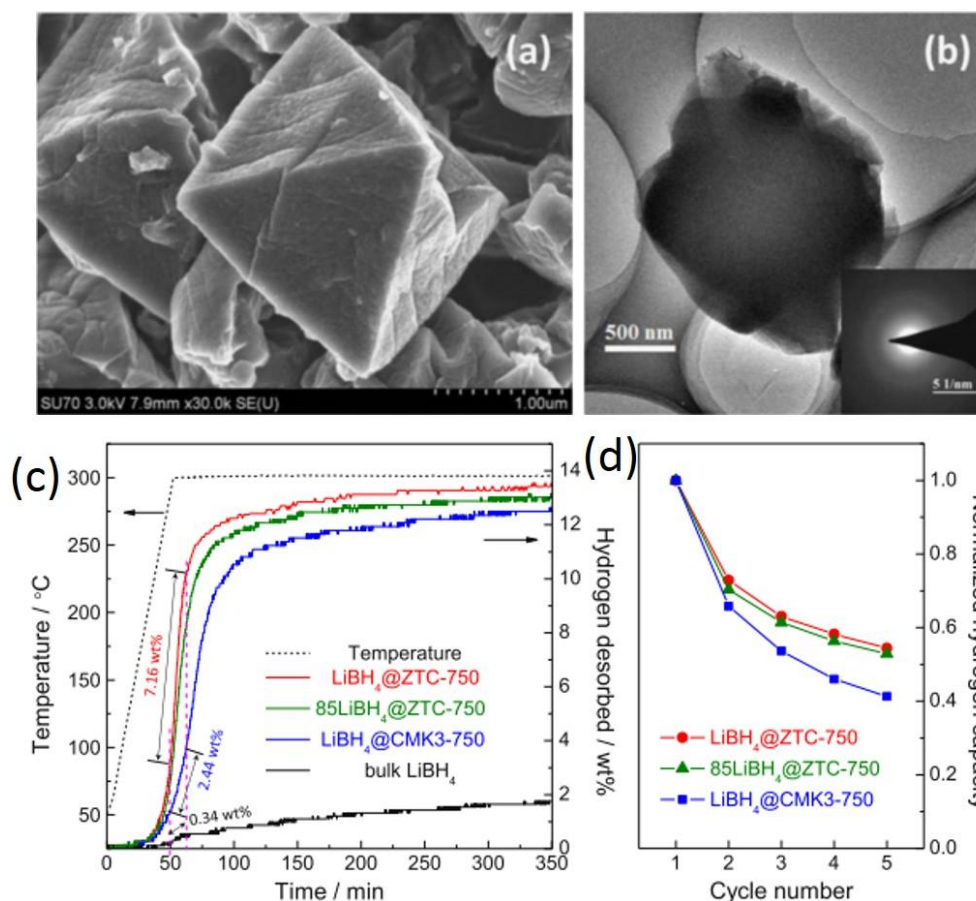
Figure 2.6 (a) Scanning electron microscope (SEM) and (b) transmission electron

microscope (TEM) image of nanoconfined LiBH$_4$ in zeolite-templated carbon

(LiBH$_4$@ZTC-750); (c) Dehydrogenation curves and (d) normalized cyclic hydrogen

storage capacities of nanoconfined LiBH$_4$ in ZTC-750 and CMK-3 at 300 °C under

0.02 bar H$_2$.[37]

Since LiBH$_4$ is highly reactive when exposed to air, especially on the nanometer scale,

Zhu et al. adopted poly(methylmethacrylate) (PMMA), which has better gas selectivity

towards H$_2$ and O$_2$, to modify LiBH$_4$ via themal destabilization and

nanoconfinement.[33] A diameter distribution of 19-73 nm was observed for LiBH$_4$ is

observed (Figure 2.7) after the process of nanoconfinement, and it was amorphous

from the selected-area electron diffraction pattern. Furthermore, LiBH$_4$@PMMA

starts to desorb hydrogen at only 53 °C, with the main peak first observed at 116 °C with a hydrogen capacity of 5.2 wt.% desorbed at 162 °C in 1 h.
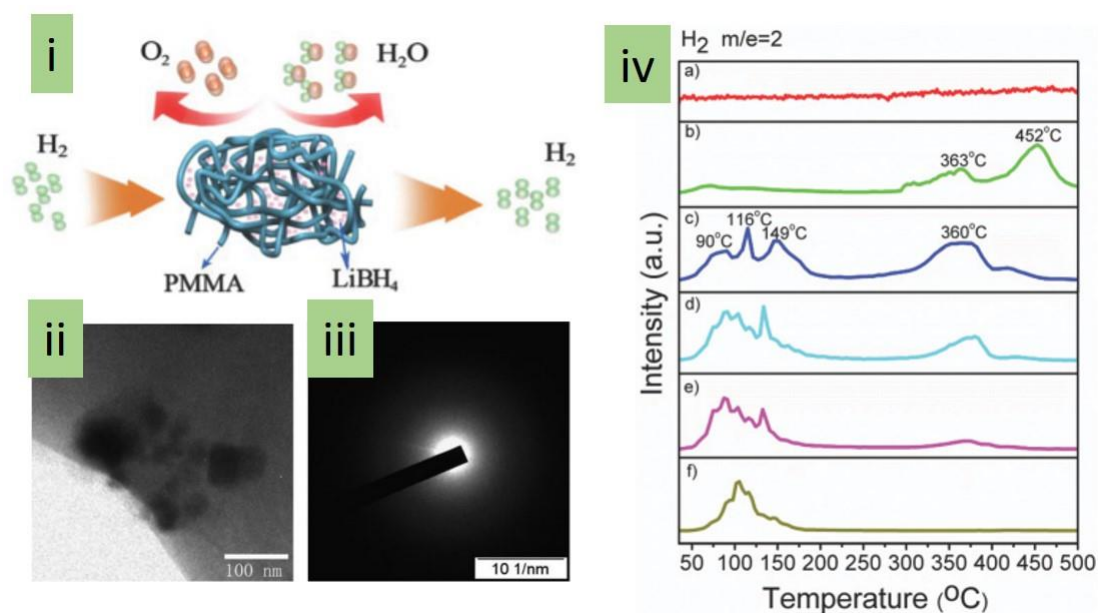
Figure 2.7 (i) Schematic illustration of LiBH$_4$ confined by PMMA to avoid contamination from oxygen and water; (ii) TEM image and (iii) selected area electron diffraction (SAED) pattern of LiBH$_4$@PMMA composite; (iv) mass spectra during dehydrogenation of (c) fresh LiBH$_4$@PMMA composite and after exposure of the LiBH$_4$@PMMA composite to air for 1 h (d), 4 h (e), 8 h (f), compared with pure PMMA (a) and LiBH$_4$ (b).[33]

In the case of NaBH$_4$, de Jongh et al. firstly reported its nanoconfinement via both solution and melt infiltration.[38] It was demonstrated that the dehydrogenation temperature could be significantly decreased by confining NaBH$_4$ in nanoporous carbon material, with most of hydrogen desorbed at around 350 °C in the nanocomposite in comparison with 560 °C for its bulk counterpart. Interestingly, Meganne L. Christian et al. prepared nanometer size (< 30nm) NaBH$_4$ particles by an antisolvent precipitation method and then added nickel chloride at these nanoparticles' surfaces to form NaBH$_4$@Ni core-shell nanostructures.[39] This unique structure could

confine the molten NaBH₄ and its dehydrogenation products in a limited space so as to realize rapid kinetics and stable reversibility owing to the short diffusion lengths of the active species, the decomposition of the as-formed nickel borohydride, and the catalytic effects on the dehydrogenation. Hence, the onset dehydrogenation temperature of this core-shell nanostructure was reduced to 50 $^{\circ}$C, and more importantly, NaBH₄ realized full reversibility for the first time with hydrogen desorption/absorption at 4 MPa and 350 $^{\circ}$C (Figure 2.8). Moreover, the hydrogen storage capacity of NaBH₄@Ni was 5 wt.%. Subsquently, the authors reported that other metals (e.g., Co, Cu, Fe, Ni, Sn) could aslo be loaded on NaBH₄ to fabricate a core-shell nanostructure with different morphologies by the same method.[40]
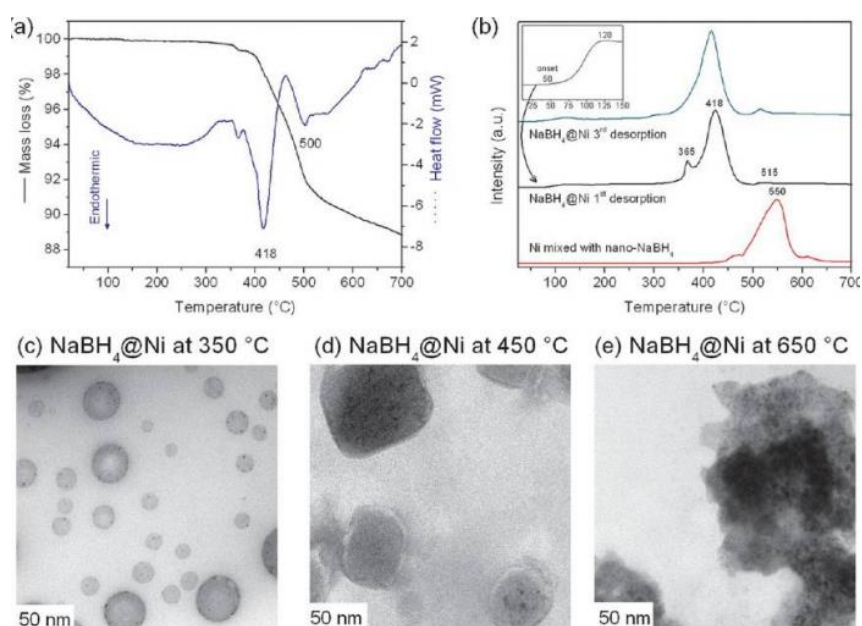
Figure 2.8 (a) Thermal decomposition as characterized by thermogravimetric analysis –differential scanning calorimetry (TGA/DSC) of as-synthesized NaBH₄@N. (b) Hydrogen evolution as characterized by mass spectroscopy (MS) for Ni physically mixed with nano-NaBH₄, as-synthesized NaBH₄@Ni, and NaBH₄@Ni after undergoing 2 cycles at 350 $^{\circ}$C. Insetis a magnification of the onset of hydrogen release. No other gases were detected by MS. TEM images of NaBH₄@Ni after

heating the material up to (c) 350 °C, (d) 450 °C, (e) and 650 °C. The observed

evolution in morphology was not reversible.[39]

Due to the solubility of $Mg(BH_4)_2$ in tetrahydrofuran, nanoconfined $Mg(BH_4)_2$ has

been fabricated via solution infiltration into nanoporous activated carbon.[41] $Ca(BH_4)_2$,

however, could not be nanoconfined by either melt infiltration or solution infiltration

due to lack of a melting point or a suitable solvent. It is interesting that a porous

$Ca(BH_4)_2$-based hydride, CaB_2H_7, with nanoporous TiO_2 introduced in-situ was

prepared by mixing $Ca(BH_4)_2$ with $Ti(OEt)_4$ followed by thermal treatment, as

illustrated in Figure 2.9.[42] The dehydrogenation peak temperature of the CaB_2H_7-

$0.1TiO_2$ system could be decreased by 50 °C, with a capacity of 5 wt.% achieved below

300 °C.
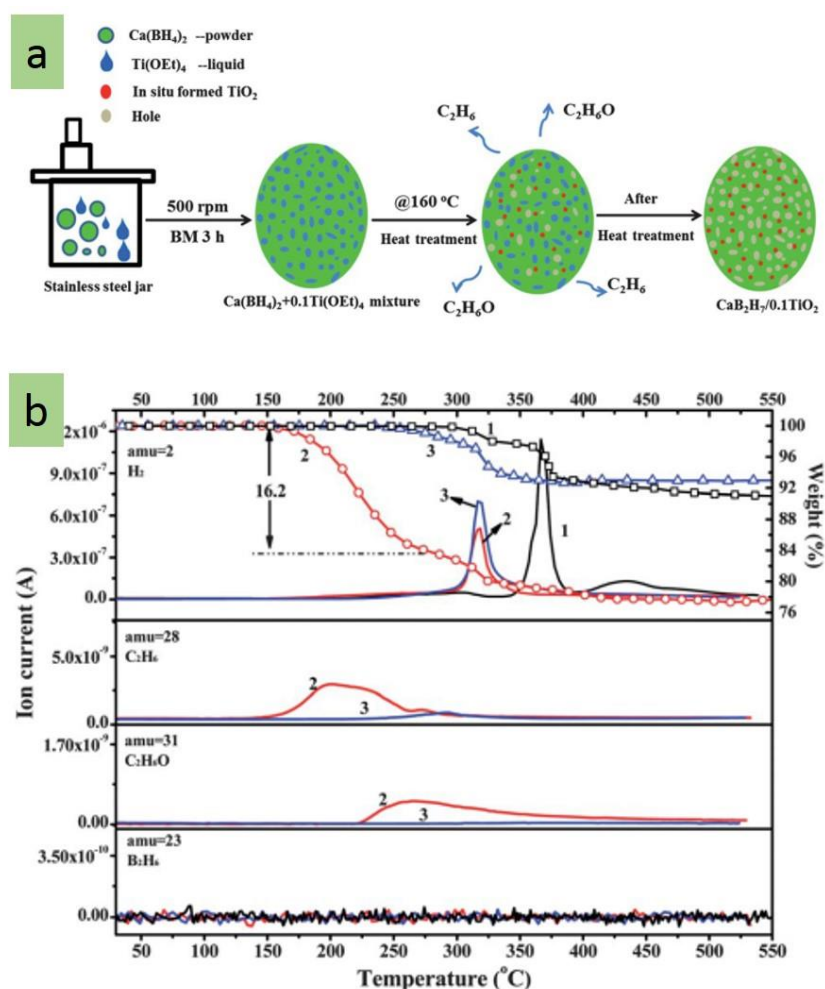
Figure 2.9 (a) Schematic illustration of the synthetic procedure to fabricate the

CaB$_2$H$_7$-0.1TiO$_2$ system; (b) TG –MS curves of the pure Ca(BH$_4$)$_2$ (1), the as-milled

Ca(BH$_4$)$_2$ + 0.1Ti(OEt)$_4$ mixture (2), and the porous CaB$_2$H$_7$-0.1TiO$_2$ system (3).[42]

2.2.3 Amides

2.2.3.1 Introduction

Metal-N-H compounds, consisting of Li-N-H, Li-B-N-H, Li-Mg-N-H, Li-Al-N-H, and the like, are among the best known attractive hydrogen storage resources owing to their outstandingly high gravimetric hydrogen density. The research work in this system has grown rapidly, since lithium nitride can store 11.5 wt.% hydrogen.[43] Generally, it is accepted that the hydrogenation and dehydrogenation of Li$_3$N could proceed by the following reversible pathways:

$$Li_3N + 2H_2 \rightarrow Li_2NH + LiH + H_2 \qquad (2.7)$$

$$Li_2NH + LiH + H_2 \rightarrow LiNH_2 + 2LiH \qquad (2.8)$$
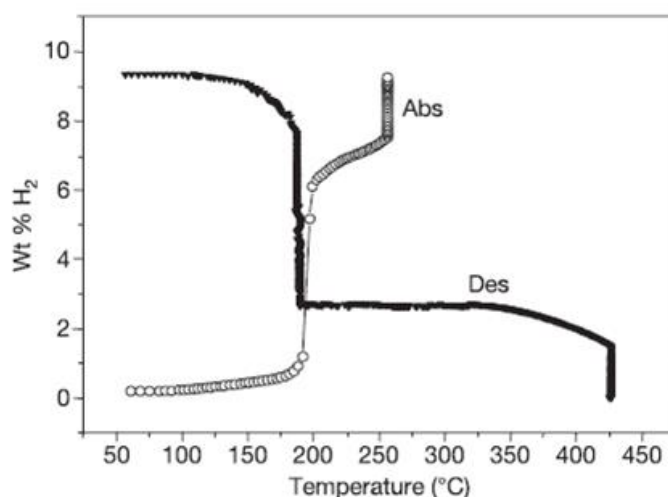
Figure 2.10 Weight variations of Li$_3$N sample during the hydrogenation and

dehydrogenation processes.[43]

There is a significant hydrogen uptake in Li_3N from 170-210 ^{o}C (Figure 2.10). With respect to the first reaction, the second step can absorb and desorb hydrogen at a much lower temperature due to the smaller enthalpy change. Nevertheless, the temperature of complete hydrogen desorption in the fully hydrogenated Li_3N is still above 250 ^{o}C. Therefore, it is not suitable for practical applications. In order to enhance the reaction kinetics and decrease the desorption temperature of the metal-N-H system, the mechanism behind the conversion of hydride and amide should be clearly understood. To date, there have been several mechanism models proposed. One is the multimolecule reaction mechanism, which can be described as a solid-solid reaction based on the strong affinity between positively charged H^+ in amide and negatively charged H^- in hydride.[44] Another group proposed an ion migration model, suggesting that the presence of Frenkel defect pairs is crucial in the desorption and hydrogenation processes, with the mobility of small ions promoting the kinetics of this process.[45] Ichikawa's group, however, considered a two-step ammonia mediated mechanism more reasonable:[46]

$$2LiNH_2 \rightarrow Li_2NH + NH_3 \qquad (2.9)$$

$$LiH + NH_3 \rightarrow LiNH_2 + H_2 \qquad (2.10)$$
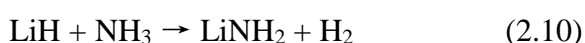
According to this, the combination of $LiNH_2$ and LiH, with proper treatment, such possible ball milling or the like, is necessary in order to better remove the ammonia and reduce the NH_3 contamination.

Among the other amides, Li-Mg-N-H is also a potential alternative as a promising hydrogen storage materials owing to its good reversibility, better thermodynamic properties, and comparatively high gravimetric density. The molar ratio between $Mg(NH_2)_2$ and LiH is 1:2, and 5.5 wt.% H_2 is adsorbed/desorbed following the equation below:[47-50]

$$Mg(NH_2)_2 + 2LiH \rightarrow Li_2Mg(NH)_2 + 2H_2 \qquad (2.11)$$

According to the calculations, this reaction can occur at 90 °C under 1 atm H_2 with desorption enthalpy of 39 kJ/mol^{-1}. A detectable H_2 desorption rate of the reaction was only obtained above 200 °C, however, indicating poor kinetic properties. In terms of kinetics and the solid state reaction pathways, Chen et al. proposed that the origin kinetic barrier was the ternary imide that was formed on the interface and the mass transport through the imide layer.[51] Thus, methods for decreasing the particle size and improving the mixing of reagents are beneficial for attaining better kinetic properties.

2.2.3.2 Nanoconfinement of amides

Pan et Al. successfully prepared nanosized $Li_2MgN_2H_2$ by sintering a mixture of $Mg(NH_2)_2$-2LiNH$_2$, then milling it for different times.[52] The sizes of samples obtained by hand milling, ball milling for 3 h, and ball milling for 36 h are 800 nm to 100 nm, respectively. The onset hydrogen absorption temperature of $Li_2MgN_2H_2$ with a particle size of 100-200 nm is only 80 °C, and absorption of 3 wt % hydrogen could be achieved at 180 °C. In addition, tremendously improved kinetics for hydrogenation and dehydrogenation could be expected when the particle size is reduced down to nanometer range. This suggests that decreasing the particle size is an efficient tool for improving the hydrogen storage performance of metal-N-H systems. Additionally, hollow $LiNH_2$ spheres were successfully synthesized by plasma metal reaction on the basis of the Kirkendall effect.[53] The sizes of the obtained $LiNH_2$ nanoparticles were in the range from 100-200 nm. The sample of hollow $LiNH_2$ could adsorb 6 wt.% hydrogen in 1 min at 200 °C, and there was also a decrease of 115 °C for hydrogen desorption compared to the bulk $LiNH_2$. As the nanosized particles easily grow larger and agglomerate, however, their favorable properties are gradually lost within several hydrogenation/dehydrogenation cycles.
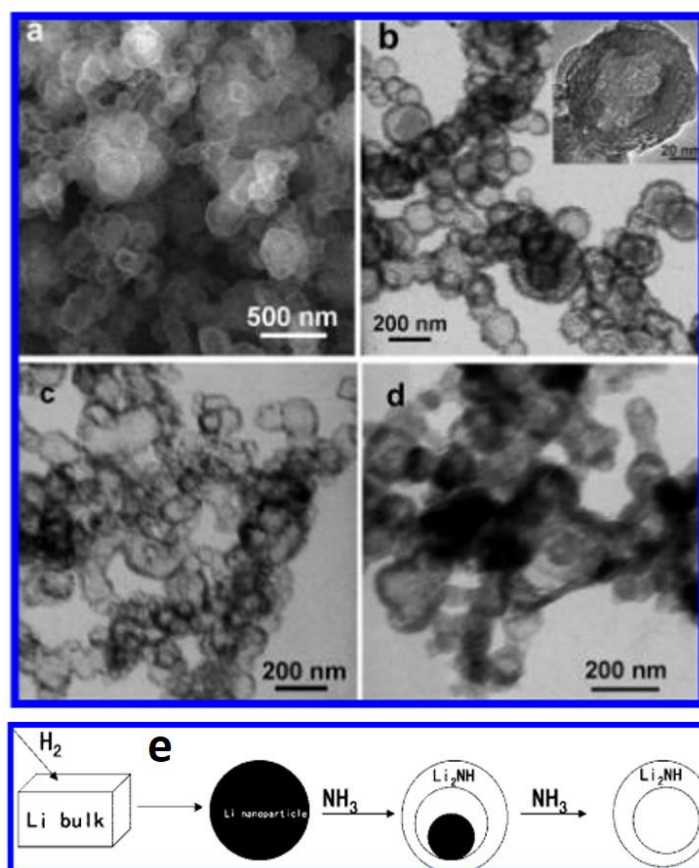
Figure 2.11 (a) SEM and (b) TEM images of the as-prepared Li_2NH hollow nanoparticles; (c) TEM image of the Li_2NH hollow nanospheres annealed at 300 ºC under vacuum for 1 h; (d) TEM image of the Li_2NH hollow nanospheres after hydrogenation at 300 ºC for 1 h under 35 bar of hydrogen; (e) mechanism for the formation of the Li_2NH hollow nanospheres.[53]

The first work on nanoconfining amides used LiN_3 as the precursor to produce confined Li_3N in mesoporous carbon, as reported by Janot et al. The nano β-Li_3N was well stabilized by the mesoporous carbon.[54] The resulting Li_3N@carbon composites showed a reversible hydrogen storage capacity of 1.8 wt.%, which is equal to around 9 wt.% per mass of Li_3N.

2.3 Chemical hydrides

2.3.1   Introduction

Representative chemical hydride materials include ammonia borane (NH_3BH_3, denoted as AB hereafter), metal amidoborane (denoted as MAB hereafter), and the related metal borohydride ammoniate (denoted as MBA hereafter).

Ammonia borane is a special molecular solid consisting of NH_3 and BH_3 buliding blocks held together by intermolecular dihydrogen bonds and dative B-N bonds.[55,56] It has a hydrogen capacity of 19.6 wt.% and could release all bonded hydrogen according to the Equation 2.12, yielding ~6.5 wt.% hydrogen below 100 °C.[57,58]

$$NH_3BH_3 \longrightarrow \text{"}NH_2BH_2\text{"} + H_2$$
$$\downarrow$$
$$\text{"}NHBH\text{"} + H_2$$
$$\downarrow$$
$$\text{"}BN\text{"} + H_2 \qquad (2.12)$$
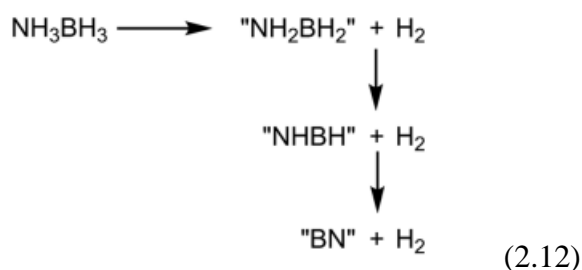
Although AB could quickly decompose when heated to 105 °C, the dehydrogenation kinetics at moderate temperature is slow and normally has a long induction period. Another major problem for using AB as a solid-state hydrogen storage alternative is the simultaneous release of diverse volatile by-products, e.g., aminoborane, diborane, borazine, and aminodiborane, during dehydrogenation.[59-61]

MAB is one of a series of derivatives of ammonia borane that is synthesized by replacing one of the hydrogen atoms bonded with N in AB with an alkali or alkaline earth element.[62-65] Due to the electron contribution from the metal to the N, B-H bonds are weakened in MABs, which leads to improved reactivity of the hydridic H. Therefore, MABs typically exhibit improved dehydrogenation kinetics with suppressed volatile by-products compared with the parent AB.[66-68] For example, $LiNH_2BH_3$ starts to desorb hydrogen at ~84 °C with a peak temperature of ~ 90 °C,

and 11 wt.% hydrogen could be released at a temperature of 91 $^{\circ}$C without detection of any by-products.[69-71] Nonetheless, metal amidoboranes are kinetically unstable, so that they may undergo spontaneous decomposition during storage and are a risk for transportation. In addition, the efficient regeneration of the spent fuel is a big challenge for MABs as practical hydrogen storage materials.
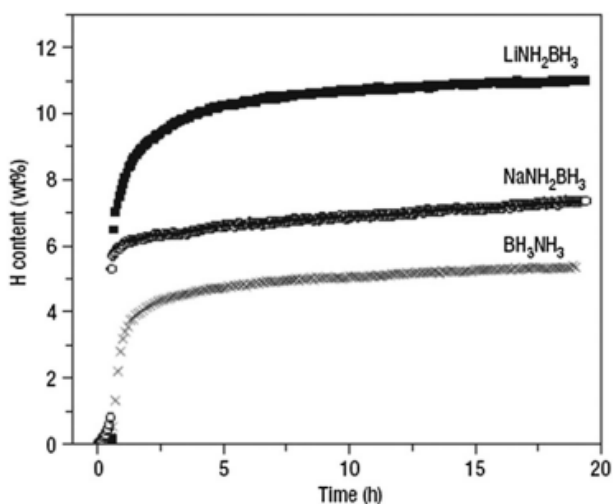
Figure 2.12 Dehydrogenation from alkali amidoboranes and post-milled AB at ~91 $^{\circ}$C.[69]

Recently, the investigation of metal borohydride ammoniates as potential hydrogen storage materials has attracted tremendous attention.[72-77] MBAs with high hydrogen capacities often exhibit much lower dehydrogenation temperatures compared with their parent metal borohydride due to the dihydrogen elimination of hydrogen. For instance, $LiBH_4$ $4/3NH_3$ with equivalent hydridic and protic hydrogen could release 17.8 wt.% hydrogen in a closed system between 135-250 $^{\circ}$C, while a temperature above 380 $^{\circ}$C is required for the dehydrogenation of $LiBH_4$. Furthermore, ammonia could be used to stabilize unstable metal borohydrides with high electronegativity, e.g., $Al(BH_4)_3$ nNH_3, which is induced by the direct coordination of ammonia with the metal.[73,76]

2.3.2   Nanoconfinement of chemical hydrides

Since AB can be easily dissolved in tetrahydrofuran, methanol, and diethyl ether, the main method for the nanoconfinement of ammonia borane is solvent infiltration. Autrey and co-workers demonstrated for the first time that AB could be encapsulated in mesoporous silica.[78] The resulting nanoparticles of ammonia borane present significant enhancements, such as enhanced dehydrogenation kinetics and thermodynamics. Interfacial catalytic effects of the terminal SiO-H groups in the silica templates were proposed as the major contribution to the enhancement of the dehydrogenation performance. This finding points the way to a suitable strategy for enhancing the hydrogen storage performance of chemical hydrides. Subsequently, ammonia borane was impregnated into a coherent carbon cryogel via the solution infiltration process.[79] As a result of the nanoconfinement effects of the carbon cryogel, a dehydrogenation temperature below 90 ^{o}C was observed, as well as the suppression of volatile borazine. Moreover, further investigation indicates that the adoption of catalysts, such as Li and Pt, could exert a synergistic effect towards enhancing the hydrogen storage performance of ammonia borane.[80,81] For instance, a hydrogen capacity of ~7wt.% could be released from ammonia borane nanoconfined in Li-doped CMK-3 at 60 ^{o}C. Following these works, various templates, such as carbon-based porous hosts[82,83], MOFs[84-88], metal oxides[89], and polymer[90,91] have been introduced to investigate the hydrogen storage properties of ammonia borane induced by the synergistic effects of nanoconfinement and the catalytic effects of the particular templates. As shown in Figure 2.13, 10.2 wt.% hydrogen could be released in only 10 min from AB inside JUC-32-Y at 95 ^{o}C, and it could desorb 8 wt.% hydrogen at 85 ^{o}C. By comparison, no hydrogen could be detached from neat AB at this temperature.[88]
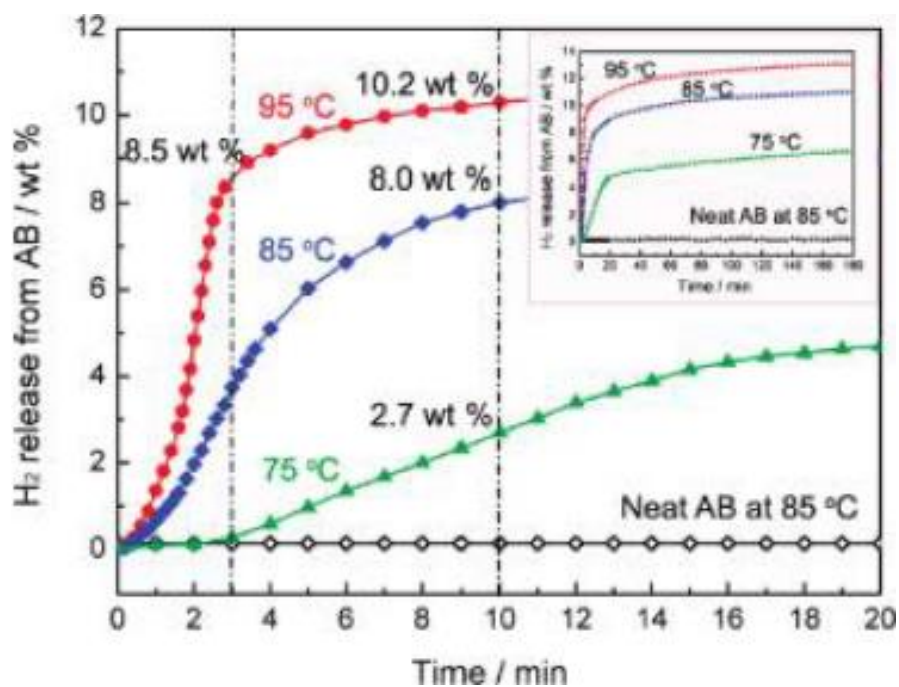
Figure 2. 13 Dehydriding kinetics of ammonia borane nanoconfined in JUC-32-Y.[88]

2.4 Mg-based hydrides

2.4.1 Introduction

Mg-based materials have been widely investigated as solid-state hydrogen storage materials. The large hydrogen capacities (e.g., 7.7 wt.% for MgH_2), great abundance of Mg in the Earth's crust, and the low cost of Mg constitutes the main advantages of Mg-based materials as hydrogen storage candidates. Unfortunately, the high activation energies of hydrogenation (100 kJ mol^{-1}) and dehydrogenation (160 kJ mol^{-1}) leads to the extremely slow formation of MgH_2 from Mg and H_2, and very slow reversible dehydrogenation from MgH_2.[92-94] Therefore, a temperature higher than 300 °C is required for common Mg to absorb hydrogen, and an even higher temperature is needed for the reversible dehydrogenation to proceed because of the thermodynamic stability. The sluggish kinetics is mainly attributed to the low hydrogen diffusion

coefficient (4×10^{-13} and 1.5×10^{-16} m^2 s^{-1} for bulk Mg and MgH_2, respectively), a sluggish dissociation rate of hydrogen on Mg (with 432 kJ mol^{-1} required to split molecules of hydrogen), and the possible synthesis of MgO.[95]

Compared with the bulk substrates, a large part of the atoms would be located on the surface when the particle size is made sufficiently small, and therefore, surface adsorption and desorption would dominate the processes of both hydrogenation and dehydrogenation. As a result, the features of both hydrogenation and dehydrogenation could be changed via nanostructuring of Mg-based hydrides. A significantly decreased energy for hydrogen absorption and desorption has been validated by different theoretical calculations when the crystal size of Mg-based hydrides is reduced down to a few nanometers.[96-101] For example, a desorption enthalpy of 37.55 kJ mol^{-1} H_2 was achieved for MgH_2 nanowires ~0.7 nm in diameter, which is half of the value for their bulk counterpart.[102] According to this result, the dehydriding temperature is calculated to be only 13.85 ℃ under an equilibrium pressure of 1 atm, which suggests that reversible hydrogen storage could be achieved in MgH_2 nanowires even at ambient temperature. The effects of nanostructuring towards improving the hydrogen storage properties of Mg-based hydrides have been experimentally verified. In 2007, Li et al. fabricated Mg nanowires with diameters ranging from 30–170 nm by the vapor-transport approach and clarified their size-controlled hydriding/dehydriding properties, as shown in Figure 2.15.[103] At 300 ℃, the Mg nanowires with the smallest diameter absorbed 7.60 wt.% and desorbed 6.77 wt.% hydrogen within 30 min and 15 min, respectively, while the nanowires with the largest diameter adsorbed 6.50 wt.% (Figure 2.16). In addition, Kondo-Franco and co-workers successfully prepared surfactant-stabilized magnesium nanoparticles with a diameter of 5 nm by electrochemical synthesis.[104] The as-prepared Mg nanoparticles could reversibly store ~7.6 wt.%

hydrogen at room temperature (1.34 wt.% taking the surfactant into account). At the temperature of 85 ℃, the colloidal MgH₂ starts to absorb hydrogen under a hydrogen pressure of 300 Pa and fully desorbed its hydrogen within 5.3 h. The reduced stability of the Mg nanoparticles could have been induced by the stabilizer and/or the high ratio of surface to volume atoms.
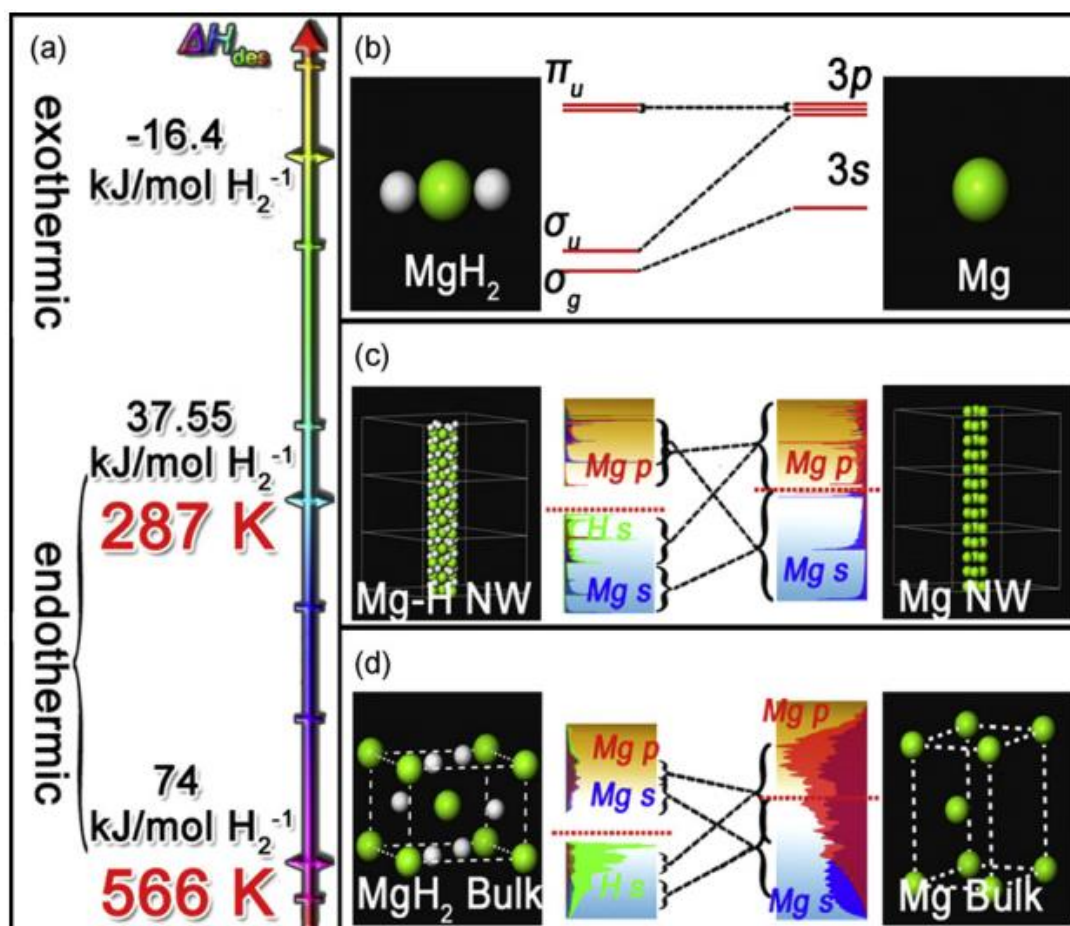
Figure 2.14 Significant differences in the thermodynamic features (a) and the electronic structures among molecules (b), nanowires (c) and bulk (d) of Mg/MgH₂.[102]
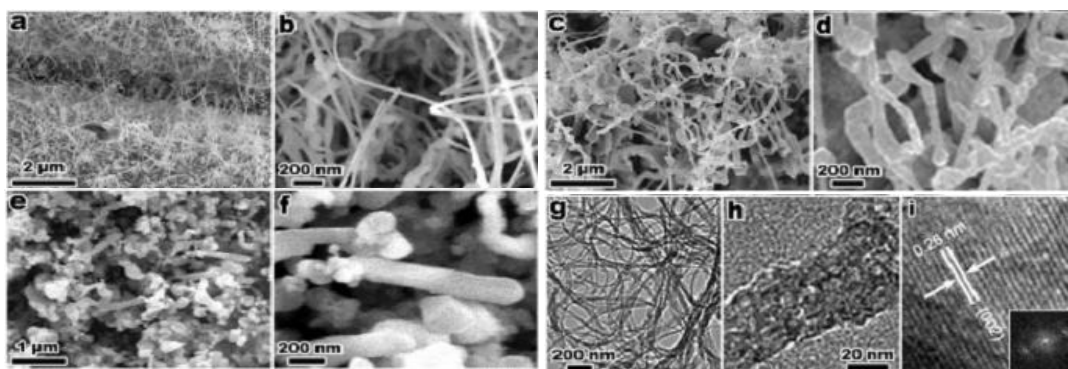
Figure 2.15 SEM images of the Mg nanowires with diameters of 30–50 nm (a, b), 80–100 nm (c, d), 150–170 nm (e, f); TEM (g, h), and HRTEM (i) images of wires (30–50 nm in diameter) with the corresponding fast Fourier transform (FFT) pattern (inset to (i)).[103]
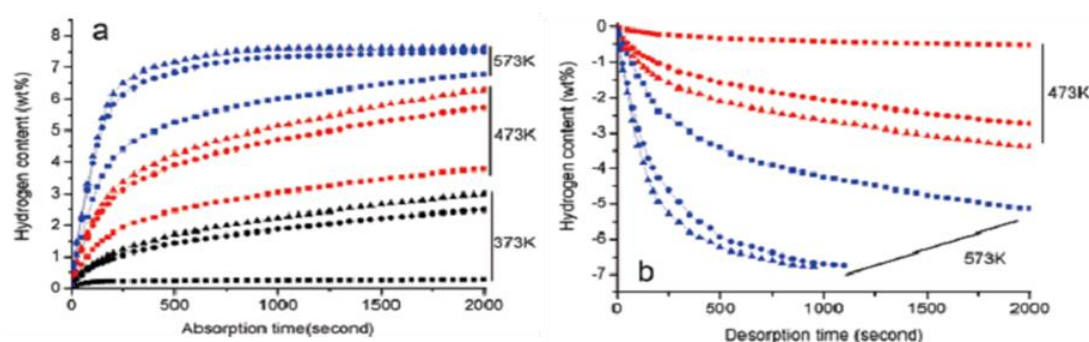
Figure 2.16 Hydrogen absorption (a) and desorption (b) of Mg nanowires (diameter of 30–50 nm, triangles; 80–100 nm, circles; 150–170 nm, squares) at different temperatures (373 K, black; 473 K, red; 573 K, blue). [103]

2.4.2   Nanoconfinemnt of Mg-based hydrides

The nanoconfinement of Mg-based hydrides was first achieved by melt infiltration, due to the fact that no suitable solvent is available to dissolve Mg/MgH$_2$ or its precursors. By means of melt infiltration of molten Mg, de Jongh et al. first reported the preparation of Mg nanoparticles nanoconfined in nanoporous carbon.[105] No bulk magnesium could be detected if the loading capacity was lower than 15 wt%. This indicates that molten infiltration is an effective way to nanoconfine Mg/MgH$_2$.

Subsequently, a suitable precursor to prepare MgH_2 was found, i.e., dibutyl magnesium ($Mg(C_4H_9)_2$), which could be dissolved in hexane and form MgH_2 according to the following Equation (2.13).[106,107] It provides a viable route to directly prepare MgH_2 nanoparticles via the solution infiltration process. For instance, Nielsen et al. embedded MgH_2 nanoparticles in porous scaffold materials (carbon aerogel monoliths) through dibutyl magnesium.[107] The pore size of the scaffold material plays a significantly important role in enhancing the hydrogen desorption kinetics of nanoconfined MgH_2. Further investigation proved that direct hydrogenation of dibutyl magnesium inside the pores of carbon templates could lead to the formation of MgH_2 nanoparticles with a size below 3 nm.[108] Due to the tremendous decrease in the particle size, the activation energy for the hydrogen desorption is reduced by 52 kJ mol^{-1} in comparison with its bulk counterpart (Figure 2.17). Recently, Konarova et al. investigated the formation of MgH_2 via wet infiltration in detail.[109] The TEM results for Mg confined in SBA-15 revealed MgO impurities on the surface, while no MgO phase was observed in MgH_2 nanoconfined into CMK-3 (Figure 2.18). The hydrogenation curves indicate that 3 wt.% hydrogen could be absorbed within 20 min at 250 ^{o}C under 2 MPa hydrogen pressure. By comparison, bulk MgH_2 and MgH_2 nanoconfined in SBA-15 exhibit extremely slow kinetics.

$$Mg(C_4H_9)_2 + 2H_2 \rightarrow MgH_2 + 2C_4H_{10} \quad (2.13)$$

.
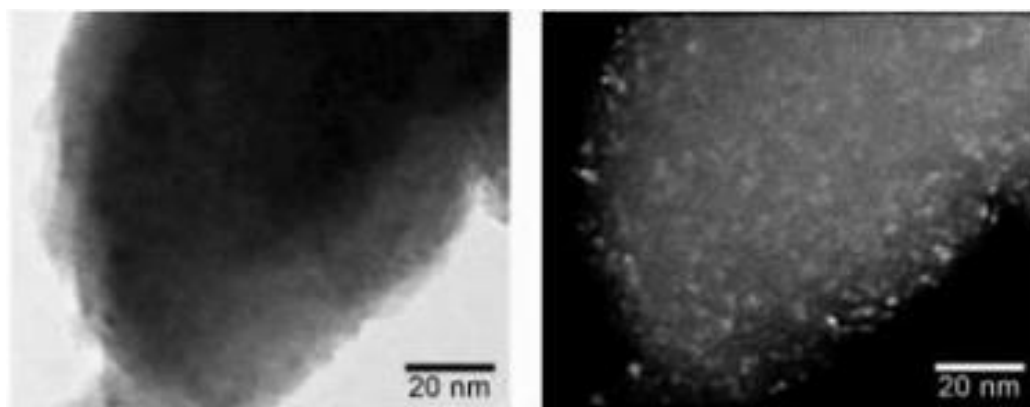
Figure 2.17 Bright-field and dark-field mode TEM images of Mg nanoconfined in

nanoporous carbon.[105]
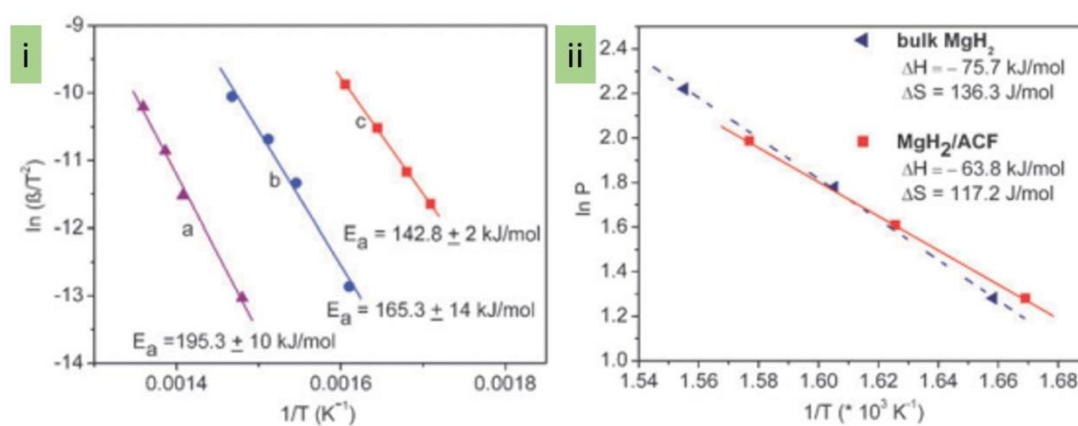
Figure 2.18 (i) Kissinger plots of the dehydrogenation of (a) commercial MgH_2, (b)

a ball-milled composite of MgH_2 and graphite, (c) nanoconfined MgH_2; (ii) van't

Hoff plots for the hydrogenation of the nanoconfined MgH_2 and the bulk MgH_2.[108]
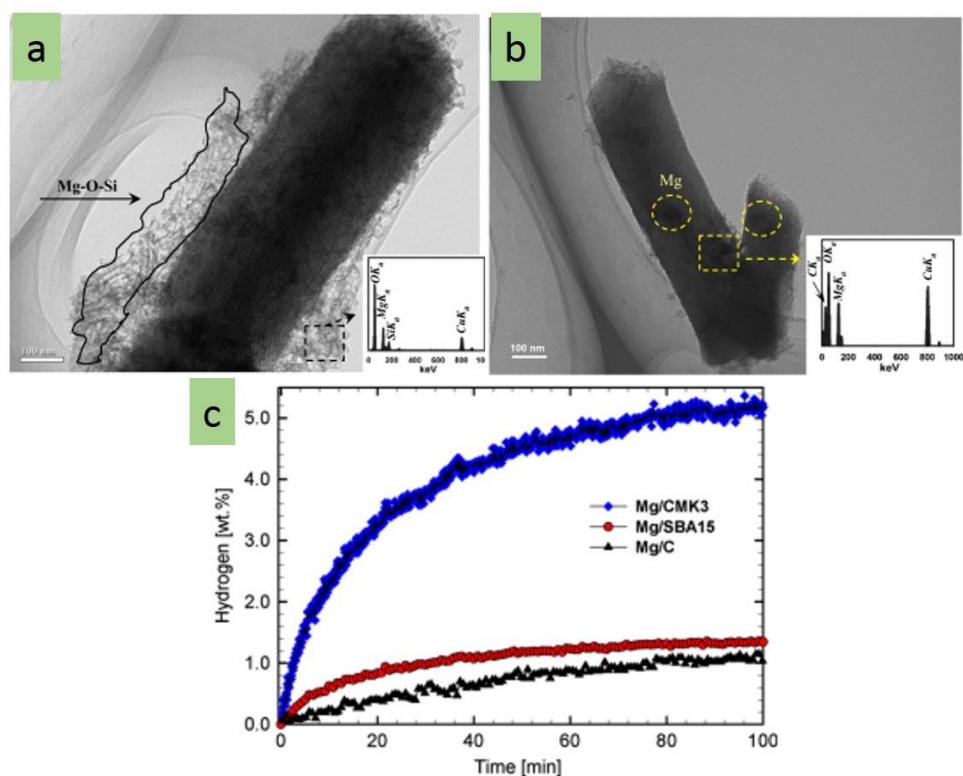
Figure 2.19 TEM images of MgH$_2$ nanoconfined in (a) SBA-15 and (b) CMK-3; (c) hydrogenation curves of nanoconfined MgH$_2$ under 2 MPa hydrogen at 250 °C.[109]

It is well known that MgH$_2$/Mg is highly reactive towards air, especially on the nanometer scale, which would lead to significant formation of MgO. Accordingly, Jeon et al. reported the synthesis of an air-stable composite that consisted of Mg nanocrystals (NCs) in a gas-barrier polymer, i.e., poly(methyl methacrylate) (PMMA), matrix , as shown in Figure 2.20.[110] PMMA could act as a suitable ligand for nanosized Mg, let hydrogen in while holding back oxygen and water, and provide a spatial structure for the volume expansion that metals undergo during absorption cycling. This original Mg nanocomposite has large hydrogen storage capacity (up to 6 wt.% of Mg, 4 wt.% for the composite) and rapid kinetics (loading in < 30 min at 200 °C) without using expensive heavy-metal catalysts. The synthesis method for this fascinating nanocomposites broke a new path towards preparing novel low-cost, high-capacity hydrogen storage media.
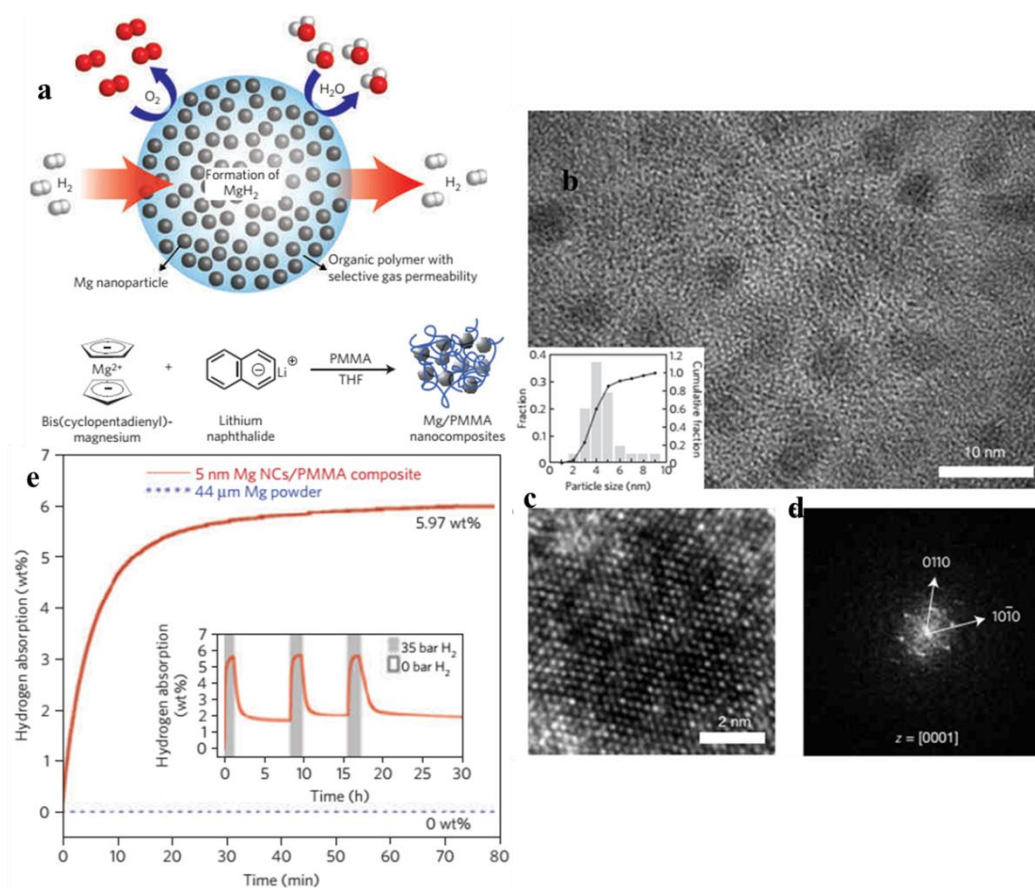
Figure 2. 20 (a) Mg NCs in a gas-barrier polymer matrix. Schematic illustration of composite material for hydrogen storage: high-capacity Mg NCs are encapsulated by a selectively gas-permeable polymer (top left), with synthetic approach to the formation of Mg NCs/PMMA nanocomposites (below). (b) High-resolution TEM micrograph of as-synthesized Mg NCs/PMMA composites. Inset: Histogram and cumulative distribution function of Mg particle size distribution, showing that the average Mg NC diameter is 4.9 ±2.1 nm. (c) Atomic-resolution image of a single Mg NC; (d) digital diffractogram of the Mg NC in (c), revealing the presence of lattice fringes with a separation of 2.789 Å, in agreement with the (002) interplanar *d*-spacing of hexagonal magnesium (JCPDS 04-0770, 2.7782 Å). Further analysis shows evidence of a slight trigonal distortion in some of the nanocrystals studied. (e) Enhancement in hydrogen absorption properties of Mg NCs/PMMA composite (absorption at 200 ∘C and 35 bar) in comparison to bulk Mg. The Mg NCs/PMMA

composite displays a calculated hydrogen absorption capacity value of 5.97 wt.% Mg
(~4 wt.% total). Inset: Hydrogen absorption/desorption cycling at 200 ∘C.[110]

2.5 References

[1]   Schüth, F., *Chemistry of Materials* 2013, **26**, 423.

[2]   de Jongh, P. E.; Allendorf, M.; Vajo, J. J.; Zlotea, C. *MRS Bulletin* **2013**, *38*, 488.

[3]   Nielsen, T. K.; Besenbacher, F.; Jensen, T. R. *Nanoscale* **2011**, *3*, 2086.

[4]   de Jongh, P. E.; Eggenhuisen, T. M. *Advanced Materials* **2013**, *25*, 6672.

[5]   Orimo, S.-i.; Nakamori, Y.; Eliseo, J. R.; Züttel, A.; Jensen, C. M. *Chemical Reviews* **2007**, *107*, 4111.

[6]   Fichtner, M.; Fuhr, O.; Kircher, O. *Journal of Alloys and Compounds* **2003**, *356–357*, 418.

[7]   Gross, K. J.; Thomas, G. J.; Jensen, C. M. *Journal of Alloys and Compounds* **2002**, *330–332*, 683.

[8]   Srinivasan, S. S.; Brinks, H. W.; Hauback, B. C.; Sun, D.; Jensen, C. M. *Journal of Alloys and Compounds* **2004**, *377*, 283.

[9]   Pukazhselvan, D.; Kumar, V.; Singh, S. K. *Nano Energy* **2012**, *1*, 566.

[10]   Baldé, C. P.; Hereijgers, B. P. C.; Bitter, J. H.; de Jong, K. P. *Angewandte Chemie, International Edition* **2006**, *45*, 3501.

[11]   Baldé, C. P.; Hereijgers, B. P. C.; Bitter, J. H.; Jong, K. P. d. *Journal of the American Chemical Society* **2008**, *130*, 6761.

[12]   Zheng, S.; Fang, F.; Zhou, G.; Chen, G.; Ouyang, L.; Zhu, M.; Sun, D. *Chemistry of Materials* **2008**, *20*, 3954.

[13]   Nielsen, T. K.; Polanski, M.; Zasada, D.; Javadian, P.; Besenbacher, F.; Bystrzycki, J.; Skibsted, J.; Jensen, T. R. *ACS Nano* **2011**, *5*, 4056.

[14] Fan, X.; Xiao, X.; Shao, J.; Zhang, L.; Li, S.; Ge, H.; Wang, Q.; Chen, L. *Nano Energy* **2013**, *2*, 995.

[15] Wahab, M. A.; Beltramini, J. N. *International Journal of Hydrogen Energy* **2014**, *39*, 18280.

[16] Bösenberg, U.; Doppiu, S.; Mosegaard, L.; Barkhordarian, G.; Eigen, N.; Borgschulte, A.; Jensen, T. R.; Cerenius, Y.; Gutfleisch, O.; Klassen, T.; Dornheim, M.; Bormann, R. *Acta Materialia* **2007**, *55*, 3951.

[17] Vajo, J. J.; Skeith, S. L.; Mertens, F. *The Journal of Physical Chemistry B* **2005**, *109*, 3719.

[18] Martelli, P.; Caputo, R.; Remhof, A.; Mauron, P.; Borgschulte, A.; Züttel, A. *The Journal of Physical Chemistry C* **2010**, *114*, 7173.

[19] Hanada, N.; Chlopek, K.; Frommen, C.; Lohstroh, W.; Fichtner, M. *Journal of Materials Chemistry* **2008**, *18*, 2611.

[20] Chlopek, K.; Frommen, C.; Leon, A.; Zabara, O.; Fichtner, M. *Journal of Materials Chemistry* **2007**, *17*, 3496.

[21] Hwang, S.-J.; Bowman, R. C.; Reiter, J. W.; Rijssenbeek; Soloveichik, G. L.; Zhao, J.-C.; Kabbour, H.; Ahn, C. C. *The Journal of Physical Chemistry C* **2008**, *112*, 3164.

[22] Ravnsbæk, D. B.; Filinchuk, Y.; Černý, R.; Ley, M. B.; Haase, D. r.; Jakobsen, H. J.; Skibsted, J. r.; Jensen, T. R. *Inorganic Chemistry* **2010**, *49*, 3801.

[23] Yan, Y.; Li, H.-W.; Sato, T.; Umeda, N.; Miwa, K.; Towata, S.-i.; Orimo, S.-i. *International Journal of Hydrogen Energy* **2009**, *34*, 5732.

[24] Rude, L. H.; Nielsen, T. K.; Ravnsbæk, D. B.; Bösenberg, U.; Ley, M. B.; Richter, B.; Arnbjerg, L. M.; Dornheim, M.; Filinchuk, Y.; Besenbacher, F.; Jensen, T. R. *Physica Status Solidi (a)* **2011**, *208*, 1754.

[25]   Nickels, E. A.; Jones, M. O.; David, W. I. F.; Johnson, S. R.; Lowton, R. L.; Sommariva, M.; Edwards, P. P. *Angewandte Chemie, International Edition* **2008**, *47*, 2817.

[26]   Fang, Z. Z.; Wang, P.; Rufford, T. E.; Kang, X. D.; Lu, G. Q.; Cheng, H. M. *Acta Materialia* **2008**, *56*, 6257.

[27]   Gross, A. F.; Vajo, J. J.; Van Atta, S. L.; Olson, G. L. *The Journal of Physical Chemistry C* **2008**, *112*, 5651.

[28]   Cahen, S.; Eymery, J. B.; Janot, R.; Tarascon, J. M. *Journal of Power Sources* **2009**, *189*, 902.

[29]   Liu, H.; Jiao, L.; Zhao, Y.; Cao, K.; Liu, Y.; Wang, Y.; Yuan, H. *Journal of Materials Chemistry A* **2014**, *2*, 9244.

[30]   Sun, W.; Li, S.; Mao, J.; Guo, Z.; Liu, H.; Dou, S.; Yu, X. *Dalton Transactions* **2011**, *40*, 5673.

[31]   Ngene, P.; Adelhelm, P.; Beale, A. M.; de Jong, K. P.; de Jongh, P. E. *The Journal of Physical Chemistry C* **2010**, *114*, 6163.

[32]   Gosalawit-Utke, R.; Meethom, S.; Pistidda, C.; Milanese, C.; Laipple, D.; Saisopa, T.; Marini, A.; Klassen, T.; Dornheim, M. *International Journal of Hydrogen Energy* **2014**, *39*, 5019.

[33]   Huang, J.; Yan, Y.; Ouyang, L.; Wang, H.; Liu, J.; Zhu, M. *Dalton Transactions* **2014,** *43*, 410.

[34]   Brun, N.; Janot, R.; Sanchez, C.; Deleuze, H.; Gervais, C.; Morcrette, M.; Backov, R. *Energy & Environmental Science* **2010**, *3*, 824.

[35]   Liu, X.; Peaslee, D.; Jost, C. Z.; Majzoub, E. H. *The Journal of Physical Chemistry C* **2010**, *114*, 14036.

[36]   Liu, X.; Peaslee, D.; Jost, C. Z.; Baumann, T. F.; Majzoub, E. H. *Chemistry*

of Materials **2011**, *23*, 1331.

[37] Shao, J.; Xiao, X.; Fan, X.; Huang, X.; Zhai, B.; Li, S.; Ge, H.; Wang, Q.; Chen, L. *Nano Energy* **2015**, *15*, 244.

[38] Ngene, P.; van den Berg, R.; Verkuijlen, M. H. W.; de Jong, K. P.; de Jongh, P. E. *Energy & Environmental Science* **2011**, *4*, 4108.

[39] Christian, M. L.; Aguey-Zinsou, K.-F. *ACS Nano* **2012**, *6*, 7739.

[40] Christian, M.; Aguey-Zinsou, K.-F. *Chemical Communications* **2013**, *49*, 6794.

[41] Yan, Y.; Au, Y. S.; Rentsch, D.; Remhof, A.; de Jongh, P. E.; Zuttel, A. *Journal of Materials Chemistry A* **2013**, *1*, 11177.

[42] Gu, J.; Gao, M.; Pan, H.; Liu, Y.; Li, B.; Yang, Y.; Liang, C.; Fu, H.; Guo, Z. *Energy & Environmental Science* **2013**, *6*, 847.

[43] Chen, P.; Xiong, Z. T.; Luo, J. Z.; Lin, J. Y.; Tan, K. L. *Nature* **2002**, *420*, 302.

[44] Chen, P.; Xiong, Z. T.; Luo, J. Z.; Lin, J. Y.; Tan, K. L. *Journal of Physical Chemistry B* **2003**, *107*, 10967.

[45] David, W. I. F.; Jones, M. O.; Gregory, D. H.; Jewell, C. M.; Johnson, S. R.; Walton, A.; Edwards, P. P. *Journal of the American Chemical Society* **2007**, *129*, 1594.

[46] Ichikawa, T.; Hanada, N.; Isobe, S.; Leng, H.; Fujii, H. *The Journal of Physical Chemistry B* **2004**, *108*, 7887.

[47] Leng, H. Y.; Ichikawa, T.; Hino, S.; Hanada, N.; Isobe, S.; Fujii, H. *The Journal of Physical Chemistry B* **2004**, *108*, 8763.

[48] Xiong, Z. T.; Wu, G. T.; Hu, H. J.; Chen, P. *Advanced Materials* **2004**, *16*, 1522.

[49] Ichikawa, T.; Tokoyoda, K.; Leng, H.; Fujii, H. *Journal of Alloys and*

Compounds **2005**, *400*, 245.

[50] Alapati, S. V.; Johnson, J. K.; Sholl, D. S. *The Journal of Physical Chemistry B* **2006**, *110*, 8769.

[51] Chen, P.; Xiong, Z. T.; Yang, L. F.; Wu, G. T.; Luo, W. F. *Journal of Physical Chemistry B* **2006**, *110*, 14221.

[52] Liu, Y.; Zhong, K.; Luo, K.; Gao, M.; Pan, H.; Wang, Q. *Journal of the American Chemical Society* **2009**, *131*, 1862.

[53] Xie, L.; Zheng, J.; Liu, Y.; Li, Y.; Li, X. *Chemistry of Materials* **2007**, *20*, 282.

[54] Demir-Cakan, R.; Tang, W. S.; Darwiche, A.; Janot, R. *Energy & Environmental Science* **2011**, *4*, 3625.

[55] Yang, J. B.; Lamsal, J.; Cai, Q.; James, W. J.; Yelon, W. B. *Applied Physics Letters* **2008**, *92*, 3.

[56] Shaw, W. J.; Linehan, J. C.; Szymczak, N. K.; Heldebrant, D. J.; Yonker, C.; Camaioni, D. M.; Baker, R. T.; Autrey, T. *Angewandte Chemie, International Edition* **2008**, *47*, 7493.

[57] Stowe, A. C.; Shaw, W. J.; Linehan, J. C.; Schmid, B.; Autrey, T. *Physical Chemistry Chemical Physics* **2007**, *9*, 1831.

[58] Shaw, W. J.; Bowden, M.; Karkamkar, A.; Howard, C. J.; Heldebrant, D. J.; Hess, N. J.; Linehan, J. C.; Autrey, T. *Energy & Environmental Science* **2010**, *3*, 796.

[59] Keaton, R. J.; Blacquiere, J. M.; Baker, R. T. *Journal of the American Chemical Society* **2007**, *129*, 1844.

[60] Heldebrant, D. J.; Karkamkar, A.; Hess, N. J.; Bowden, M.; Rassat, S.; Zheng, F.; Rappe, K.; Autrey, T. *Chemistry of Materials* **2008**, *20*, 5332.

[61] He, T.; Xiong, Z. T.; Wu, G. T.; Chu, H. L.; Wu, C. Z.; Zhang, T.; Chen, P.

Chemistry of Materials **2009**, *21*, 2315.

[62] Chua, Y. S.; Chen, P.; Wu, G.; Xiong, Z. *Chemical Communications* **2011,** *47*, 5116.

[63] Wang, P. *Dalton Transactions* **2012**, *41*, 4296.

[64] Spielmann, J.; Jansen, G.; Bandmann, H.; Harder, S. *Angewandte Chemie, International Edition* **2008**, *47*, 6290.

[65] Wu, H.; Zhou, W.; Yildirim, T. *Journal of the American Chemical Society* **2008**, *130*, 14834.

[66] Diyabalanage, H. V. K.; Nakagawa, T.; Shrestha, R. P.; Semelsberger, T. A.; Davis, B. L.; Scott, B. L.; Burrell, A. K.; David, W. I. F.; Ryan, K. R.; Jones, M. O.; Edwards, P. P. *Journal of the American Chemical Society* **2010**, *132*, 11836.

[67] Luedtke, A. T.; Autrey, T. *Inorganic Chemistry* **2010**, *49*, 3905.

[68] Zhang, Q.; Tang, C.; Fang, C.; Fang, F.; Sun, D.; Ouyang, L.; Zhu, M. *The Journal of Physical Chemistry C* **2010**, *114*, 1709.

[69] Xiong, Z. T.; Yong, C. K.; Wu, G. T.; Chen, P.; Shaw, W.; Karkamkar, A.; Autrey, T.; Jones, M. O.; Johnson, S. R.; Edwards, P. P.; David, W. I. F. *Nature Materials* **2008**, *7*, 138.

[70] Xiong, Z. T.; Chua, Y. S.; Wu, G. T.; Xu, W. L.; Chen, P.; Shaw, W.; Karkamkar, A.; Linehan, J.; Smurthwaite, T.; Autrey, T. *Chemical Communications* **2008**, 5595.

[71] Kang, X. D.; Fang, Z. Z.; Kong, L. Y.; Cheng, H. M.; Yao, X. D.; Lu, G. Q.; Wang, P. *Advanced Materials* **2008**, *20*, 2756.

[72] Chen, X.; Yu, X. *The Journal of Physical Chemistry C* **2012**, *116*, 11900.

[73] Guo, Y.; Jiang, Y.; Xia, G.; Yu, X. *Chemical Communications* **2012**, *48*, 4408.

[74] Guo, Y.; Wu, H.; Zhou, W.; Yu, X. *Journal of the American Chemical Society* **2011**, *133*, 4690.

[75] Guo, Y.; Xia, G.; Zhu, Y.; Gao, L.; Yu, X. *Chemical Communications* **2010**, *46*, 2599.

[76] Guo, Y.; Yu, X.; Sun, W.; Sun, D.; Yang, W. *Angewandte Chemie, International Edition* **2011**, *50*, 1087.

[77] Xia, G.; Gu, Q.; Guo, Y.; Yu, X. *Journal of Materials Chemistry* **2012**, *22*, 7300.

[78] Gutowska, A.; Li, L.; Shin, Y.; Wang, C. M.; Li, X. S.; Linehan, J. C.; Smith, R. S.; Kay, B. D.; Schmid, B.; Shaw, W.; Gutowski, M.; Autrey, T. *Angewandte Chemie, International Edition* **2005**, *44*, 3578.

[79] Feaver, A.; Sepehri, S.; Shamberger, P.; Stowe, A.; Autrey, T.; Cao, G. *The Journal of Physical Chemistry B* **2007**, *111*, 7469.

[80] Li, S. F.; Guo, Y. H.; Sun, W. W.; Sun, D. L.; Yu, X. B. *The Journal of Physical Chemistry C* **2010**, null.

[81] Li, L.; Yao, X.; Sun, C.; Du, A.; Cheng, L.; Zhu, Z.; Yu, C.; Zou, J.; Smith, S. C.; Wang, P.; Cheng, H.-M.; Frost, R. L.; Lu, G. Q. *Advanced Functional Materials* **2009**, *19*, 265.

[82] Nielsen, T. K.; Karkamkar, A.; Bowden, M.; Besenbacher, F.; Jensen, T. R.; Autrey, T. *Dalton Transactions* **2013**, *42*, 680.

[83] Sepehri, S.; García, B. B.; Cao, G. *European Journal of Inorganic Chemistry* **2009**, *2009*, 599.

[84] Wang, X.; Xie, L.; Huang, K.-W.; Lai, Z. *Chemical Communications* **2015**, *51*, 7610.

[85] Jeong, H. M.; Shin, W. H.; Park, J. H.; Choi, J. H.; Kang, J. K. *Nanoscale*

2014, *6*, 6526.

[86] Gao, L.; Li, C.-Y. V.; Yung, H.; Chan, K.-Y. *Chemical Communications* **2013**, *49*, 10629.

[87] Gadipelli, S.; Ford, J.; Zhou, W.; Wu, H.; Udovic, T. J.; Yildirim, T. *Chemistry – A European Journal* **2011**, *17*, 6043.

[88] Li, Z.; Zhu, G.; Lu, G.; Qiu, S.; Yao, X. *Journal of the American Chemical Society* **2010**, *132*, 1490.

[89] Yang, Z.; Liang, J.; Cheng, F.; Tao, Z.; Chen, J. *Microporous and Mesoporous Materials* **2012**, *161*, 40.

[90] Nathanson, A. S.; Ploszajski, A. R.; Billing, M.; Cook, J. P.; Jenkins, D. W. K.; Headen, T. F.; Kurban, Z.; Lovell, A.; Bennington, S. M. *Journal of Materials Chemistry A* **2015**, *3*, 3683.

[91] Peng, Y.; Ben, T.; Jia, Y.; Yang, D.; Zhao, H.; Qiu, S.; Yao, X. *The Journal of Physical Chemistry C* **2012**, *116*, 25694.

[92] Dehouche, Z.; Klassen, T.; Oelerich, W.; Goyette, J.; Bose, T. K.; Schulz, R. *Journal of Alloys and Compounds* **2002**, *347*, 319.

[93] Liang, G.; Huot, J.; Boily, S.; Van Neste, A.; Schulz, R. *Journal of Alloys and Compounds* **1999**, *292*, 247.

[94] Dehouche, Z.; Djaozandry, R.; Goyette, J.; Bose, T. K. *Journal of Alloys and Compounds* **1999**, *288*, 312.

[95] Cheng, F.; Tao, Z.; Liang, J.; Chen, J. *Chemical Communications* **2012,** *48*, 7374.

[96] Wagner, L. K.; Majzoub, E. H.; Allendorf, M. D.; Grossman, J. C. *Physical Chemistry Chemical Physics* **2012**, *14*, 6611.

[97] Wu, Z.; Allendorf, M. D.; Grossman, J. C. *Journal of the American Chemical*

Society **2009**, *131*, 13918.

[98] Pauw, B. R.; Kalisvaart, W. P.; Tao, S. X.; Koper, M. T. M.; Jansen, A. P. J.; Notten, P. H. L. *Acta Materialia* **2008**, *56*, 2948.

[99] Berube, V.; Chen, G.; Dresselhaus, M. S. *International Journal of Hydrogen Energy* **2008**, *33*, 4122.

[100] Wagemans, R. W. P.; van Lenthe, J. H.; de Jongh, P. E.; van Dillen, A. J.; de Jong, K. P. *Journal of the American Chemical Society* **2005**, *127*, 16675.

[101] Chen, D.; Wang, Y. M.; Chen, L.; Liu, S.; Ma, C. X.; Wang, L. B. *Acta Materialia* **2004**, *52*, 521.

[102] Peng, B.; Li, L.; Ji, W.; Cheng, F.; Chen, J. *Journal of Alloys and Compounds* **2009**, *484*, 308.

[103] Li, W.; Li, C.; Ma, H.; Chen, J. *Journal of the American Chemical Society* **2007**, *129*, 6710.

[104] Aguey-Zinsou, K.-F.; Ares-Fernández, J.-R. *Chemistry of Materials* **2007**, *20*, 376.

[105] Jongh, P. E. d.; Wagemans, R. W. P.; Eggenhuisen, T. M.; Dauvillier, B. S.; Radstake, P. B.; Meeldijk, J. D.; Geus, J. W.; Jong, K. P. d. *Chemistry of Materials* **2007**, *19*, 6052.

[106] Shu, Z.; Adam, F. G.; Sky, L. V. A.; Maribel, L.; Ping, L.; Channing, C. A.; John, J. V.; Craig, M. J. *Nanotechnology* **2009**, *20*, 204027.

[107] Nielsen, T. K.; Manickam, K.; Hirscher, M.; Besenbacher, F.; Jensen, T. R. *ACS Nano* **2009**, *3*, 3521.

[108] Zhao-Karger, Z.; Hu, J.; Roth, A.; Wang, D.; Kubel, C.; Lohstroh, W.; Fichtner, M. *Chemical Communications* **2010**, *46*, 8353.

[109] Konarova, M.; Tanksale, A.; Norberto Beltramini, J.; Qing Lu, G. *Nano*

Energy **2013**, *2*, 98.

[110] Jeon, K.-J.; Moon, H. R.; Ruminski, A. M.; Jiang, B.; Kisielowski, C.; Bardhan, R.; Urban, J. J. *Nature Materials* **2011**, *10*, 286.

3   CHAPTER 3 EXPERIMENTAL

3.1 General procedure

The general procedure of this work is summarized in Figure 3.1. Firstly, nanoconfined hydrogen storage materials were synthesized via solution infiltration and/or in-situ synthesis methods, and were further characterized by a series of physical techniques to identify the as-prepared materials. Subsequently, the hydrogen storage performance was investigated to verify the nanoconfinement-induced effects.
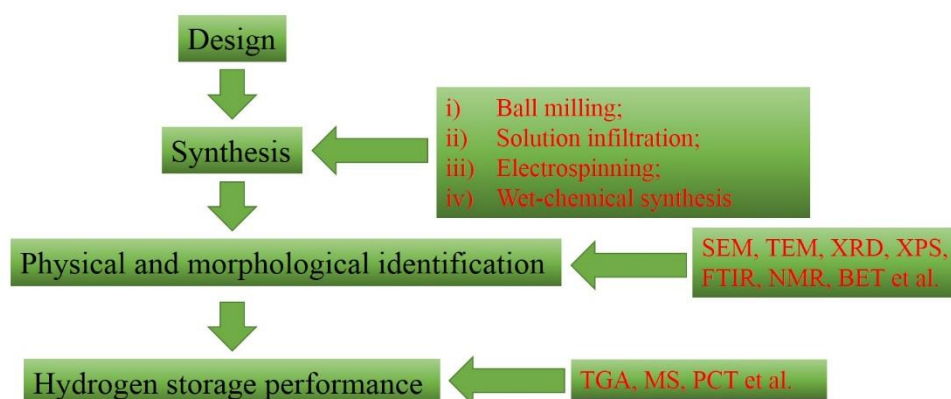
Figure 3.1 Outline of experimental procedures and techniques in this thesis.

3.2 Chemicals

All the chemicals were handled using an argon filled glove box (MBraun Unilab), in which the water and oxygen were kept below 1 ppm, to avoid oxidation and contamination with air. Detailed information on the materials adopted in this thesis is presented in Table 3.1.

Table 3.1 List of the materials used in the experiments of this thesis.

Chemical	Formula	Purity (%)	Supplier

Lithium borohydride	$LiBH_4$	98	Sigma-Aldrich
Lithium aluminium hydride	$LiAlH_4$	98	Sigma-Aldrich
Lithium azide solution	LiN_3	20 wt.%	Sigma-Aldrich
Zinc chloride	$ZnCl_2$	99.99	Sigma-Aldrich
Sodium borohydride	$NaBH_4$	98	Sigma-Aldrich
Tetrahydrofuran	C_4H_8O	99.999	Sigma-Aldrich
SBA-15	SiO_2	n/a	Nanjing XFNANO Materials Tech
Mesoporous carbon	C	n/a	Nanjing XFNANO Materials Tech
Poly(vinyl alcohol) $M_w = 88000$	$[CH_2CH(OH)]_n$	88	Alfa Aesar
Ammonia borane	BH_3NH_3	98	Sigma-Aldrich
Lithium nitride	Li_3N	99.4	Sigma-Aldrich
Potassium stannate trihydrate	$K_2SnO_3 \cdot 3H_2O$	99.9	Sigma-Aldrich
Urea	$CO(NH_2)_2$	99	Sigma-Aldrich
Glucose	$C_6H_{12}O_6$	99.5	Sigma-Aldrich
2,2,2-trifluoroethanol	CF_3CH_2OH	99	Sigma-Aldrich
Magnesium chloride	$MgCl_2$	98	Sigma-Aldrich

3.3 Synthetic method

The synthetic methods adopted in this thesis are briefly summarized as follows, and the experimental procedures for each topic will be discussed in detail in their respective chapters.

3.3.1   Ball milling

The ball-milling process in this thesis was carried out in a QM-3SP2 planetary ball mill machine purchased from Nanjing University Instrument Plant, as shown in Figure 3.2. Two or four milling jars with balls made of stainless steel (Figure 3.2(b)) can be simultaneously milled. As schematically illustrated in Figure 3.2(c), the grinding jars are arranged in such a way that each moves around its own axis and, in the opposite direction, around the common axis of the sun wheel when the turn-plate rotates.
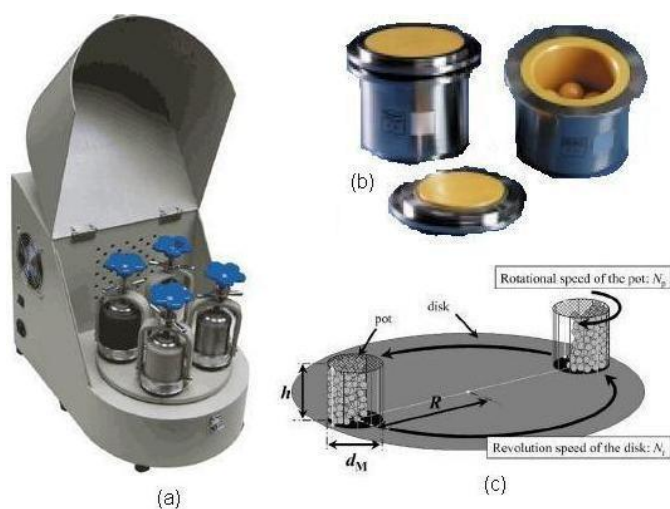
Figure 3.2 (a) QM-3SP2 planetary ball mill machine, (b) grinding jars and balls, and (c) schematic illustration of milling process.

3.3.2   Solution infiltration

Hydrogen storage materials were nanoconfined in various templates via solution infiltration through capillary action as illustrated in Figure 3.3. Firstly, the adopted

templates were thermally treated to remove moisture and/or oxygen. Subsequently, a solution containing the hydrogen storage materials was mixed with the templates via ultrasonication for complete infiltration. Finally, the solvent was removed at room temperature under dynamic vacuum.
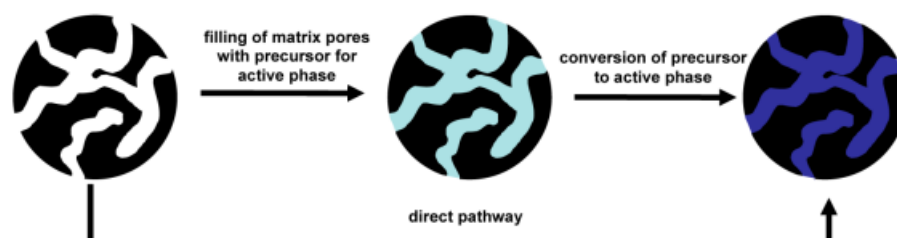
Figure 3.3 Schematic illustration of nanoconfinement via solution infiltration.

3.3.3   Electrospinning

Electrospinning is a simple and versatile technique to produce nanofibers using high electrostatic forces. Four major components, i.e., a metallic needle, a syringe to contain the precursors, a grounded conductive collector, and a direct current power supply, are required for electrospinning.
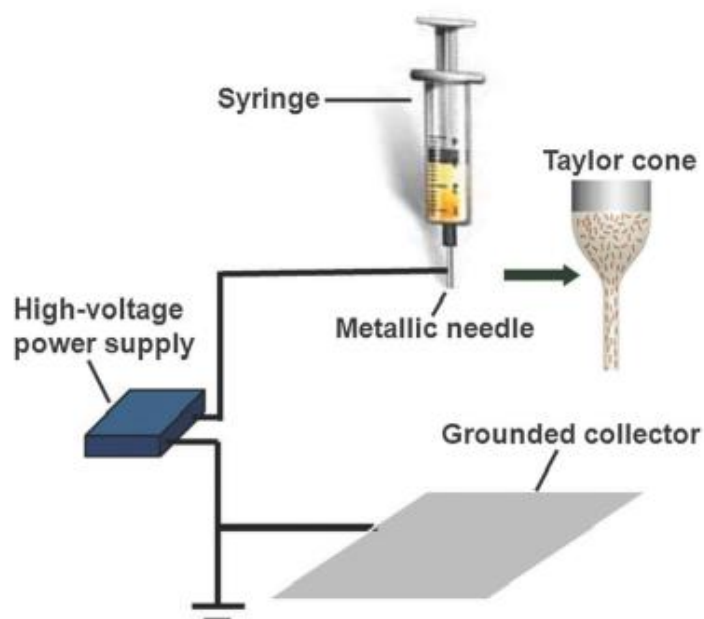
Figure 3.4 Schematic representation of the set-up for electrospinning. The inset is a sketch of the electrified Taylor cone.

3.4 Physical and Structural Characterization

3.4.1   Scanning Electron Microscopy

The scanning electron microscope (SEM) is a type of electron microscope and is one of the main tools to verify the morphology of the as-prepared nanoparticles. The SEM adopted in this work was a JOEL 7500F, which could achieve a resolution better than 1 nm under optimized conditions. For less conductive materials, a thin layer of platinum was sputtered on the surface of the samples.

3.4.2   Transmission Electron Microscopy

Transmission electron microscopy (TEM) is a microscopic method in which a beam of electrons is transmitted via an ultra-thin specimen, and then interacts with the sample when it passes through. Subsequently, an image of the sample is formed and magnified, and focused onto an imaging device. Due to the small de Broglie wavelength of electrons, a significantly high resolution of images could be obtained. The TEM adopted in this experiment was a JEOL 2011 (200 keV).

3.4.3   X-ray diffraction

X-ray diffraction (XRD) was the predominant tool for the qualitative analysis of the prepared samples during hydrogen storage measurements. In order to avoid oxidation during the XRD measurements, samples were loaded onto a glass slide 1 mm in thickness in an Ar-filled glovebox, which was further sealed with amorphous tape. The XRD diffractometer used in this work was a D8 Advance (Bruker AXS) with Cu Kα radiation.

3.4.4　Fourier Transform Infrared Spectroscopy

Fourier Transform Infrared Spectroscopy (FTIR) is a widely used technique to determine the types of chemical groups within a compound. The FTIR instrument adopted in this study was a Magna-IR 550 II, Nicolet, and the samples were measured within a multiple internal reflection (MIR) scan range of 500-4000 cm^{-1}. Samples for FTIR tests were obtained through grinding with KBr powder and pressing the mixture into a sample cup in the glove box.

3.4.5　X-ray Photoelectron Spectroscopy

X-ray photoelectron spectroscopy (XPS) is a surface-sensitive quantitative technique that measures the elemental composition in the parts per thousand range, along with the chemical states, empirical formula, and electronic states of the elements. The XPS equipment adopted in this work was a Perkin Elmer PHI 5000C ESCA system equipped with a dual X-ray source, in which an Mg Kα (1253.6 eV) anode and a hemispherical energy analyzer were used. The background pressure during data acquisition was maintained at $< 10^{-6}$ Pa, and measurements were performed at a pass energy of 93.90 eV. All binding energies were calibrated using contaminant carbon (C 1s = 284.6 eV).

3.5 Hydrogen storage measurements

3.5.1　Kinetics, thermodynamics, and cycling performance

The hydrogen storage properties of all the samples were tested on a Sieverts apparatus. The Sieverts apparatus adopted in this research was a Gas Reaction Controller (GRC) from the Advanced Materials Corporation, USA (Figure 3.5).

The GRC could be used to quantitatively analyze the gas-solid reaction. A controlled amount of gas is firstly introduced into the reaction chamber containing the sample with a accurate volume parameters. Therefore, the amount of gas absorbed and/ore desorbed by samples could be determined by monitoring the change of pressure and calculating the amount according to the gas equation.

Figure 3.5 GRC instrument from Advanced Materials Corporation of the USA.

3.5.2   Thermogravimetric analysis and mass spectra

Thermogravimetric analysis (TGA) was adopted to determine the changes of weight in relation to the change of temperature during hydrogenation and/or dehydrogenation, while mass spectra (MS) is an analytical technique used to determine the released gas during the TGA measurement. In this study, TGA (Netzsch STA 449 F3) connected to a mass spectrometer (Hiden HPR 20) was conducted in a glove box filled with Ar using various heating rates under dynamic argon with a purge rate of 80 ml min^{-1}. The detailed parameter for each experiment could be found in the experimental section of relative chapter.

4   CHAPTER 4 STABILIZATION OF NAZN(BH$_4$)$_3$ VIA NANOCONFINEMENT IN SBA-15 TOWARDS ENHANCED HYDROGEN RELEASE

4.1 Introduction

Complex metal borohydrides have been regarded as one of most promising systems for hydrogen storage in the light of their high hydrogen capacities.[1,2] During the past decades, intensive research has been performed on the synthesis and modification of these compounds so as to enhance their hydrogen storage properties.[3-5] The dehydrogenation temperatures of these candidates are still too high for practical low-temperature applications, however, because of their thermodynamic stability due to the strong B-H interactions, which is the main source for hydrogen release from borohydrides.[6-8] Recently, a credible correlation between the dehydrogenation temperature and the Pauling electronegativity, χ_P, (since the decomposition temperature of metal borohydrides decreases with increasing χ_P of the metal cations) was provided by means of first-principles calculations and experiments on the thermodynamic stability of metal borohydrides, $M(BH_4)_n$ (M = Li, Na, K, Cu, Mg, Zn, Sc, Zr, and Hf, n = 1-4), demonstrating a viable strategy for the development of new metal borohydrides with advantageous dehydrogenation properties via regulating the χ_P of the relevant metal cations.[9] It is also well known, however, that less stable metal borohydrides, due to the presence of relevant metal cations with high χ_P, release considerable amounts of diborane by-products in conjunction with the liberation of hydrogen, prohibiting their practical application as hydrogen storage materials in fuel cells.[10] Thus, a feasible approach is also desirable to achieve a compromise between the favorable release of hydrogen and the thermodynamic stability of metal borohydrides.

Recently, a series of dual-cation (M, Zn) compounds (M = Li, Na) formed by ball milling $ZnCl_2$ and MBH_4 (M = Li, Na),along with MCl (M = Li, Na) by-products, i.e., $LiZn_2(BH_4)_5$, $NaZn_2(BH_4)_5$, and $NaZn(BH_4)_3$, in which Zn^{2+} has a high χ_p of 1.65, were demonstrated experimentally and theoretically to undergo thermal decomposition of hydrogen below 100 ºC, which is much lower than for other pure metal borohydrides, e.g., $LiBH_4$, $NaBH_4$, $Mg(BH_4)_2$, and $Ca(BH_4)_2$, giving these dual-cation compounds remarkable potential to be practical for hydrogen storage applications.[11-15] We have recently realized the purification of $NaZn(BH_4)_3$, using a wet-chemical route with separation of the NaCl formed during synthesis, which significantly increases the practical hydrogen capacity of this system.[16] It has to be borne in mind, however, that as a result of the instability of Zn-based borohydrides, large amounts of boranes are released during pyrolysis, which is substantially harmful to proton exchange membrane fuel cells (PEMFC), reduces the effective hydrogen capacity, and decreases possibilities for reversibility. Therefore, suppression of boranes released during its decomposition is of vital importance for application of $NaZn(BH_4)_3$ as a hydrogen storage material.

On the other hand, after several years of exploration, entrapping hydrogen storage materials within the nanopores of solid mesoporous templates has been found to serve as an effective tool for enhancing the hydrogen storage properties of these materials, in such aspects as improved kinetics and thermodynamics for the hydrogen release reaction, as well as effective suppression of volatile gases.[17-30] For example, by confining ammonia borane (AB) in templates such as Li-doped mesoporous carbon (Li-CMK)[31] and metal organic frameworks (JUC-32-Y)[32], the dehydrogenation kinetics of ammonia borane at lower temperature was substantially increased, together with the total suppression of both borazine and ammonia. Moreover, the recyclable

dehydrogenation of ammonia borane was effectively achieved within graphene oxide-based hybrid nanostructures.[33] In regards to the pure borohydrides, numerous encouraging nanostructured or nanoporous materials have been adopted to modify the hydrogen storage properties of $LiBH_4$, such as carbon nanotubes, carbon fibers, mesoporous silica, nanoporous carbon, and metal-organic frameworks (MOFs), demonstrating that nanoconfinement is an effective way to improve the hydrogen desorption/absorption properties of borohydrides.[34-38] In particular, $LiBH_4$ that is nanoconfined via SBA-15 as a scaffold exhibits enhanced hydrogen desorption properties, with desorption starting at 150 ^{o}C, which is more than a 200 ^{o}C reduction compared with the bulk $LiBH_4$, confirming that SBA-15 is a suitable template for nanoconfinement of hydrogen storage materials.[36] Therefore, by taking advantage of the unique properties of hydrogen storage materials as nanoparticles, specifically based on their high surface-to-volume ratios, leading to shorter diffusion paths for hydrogen liberation from substrates, SBA-15 was applied as a scaffold to investigate the size effect on the desorption properties of $NaZn(BH_4)_3$ on the nanoscale.

4.2 Experimental section

4.2.1 Preparation of $NaZn(BH_4)_3$-THF solution

For the preparation of $NaZn(BH_4)_3$ in THF, anhydrous THF (~ 16 mL) was first transferred in an argon atmosphere into a 50 mL ball-milling vessel containing 11 mm diameter stainless steel spheres, with a ball-to-powder ratio of 30 : 1, followed by the addition of $NaBH_4$ (1.135 g) and $ZnCl_2$ (1.3631 g). To minimize heating in the vessel, the milling process was paused for 12 min after every 30 min milling, with 40 cycles at 300 rpm. After the ball-milling procedure, centrifugation for around 30 min in a sealed tube under Ar atmosphere was applied to separate the transparent $NaZn(BH_4)_3$-

THF solution from the precipitated by-products (e.g., NaCl), which were characterized by X-ray diffraction (XRD) as shown in Figure 4.1. Neat $NaZn(BH_4)_3$ was then prepared by vacuum-drying $NaZn(BH_4)_3$-THF solution (Figure 2) under vacuum at room temperature for 48 h.
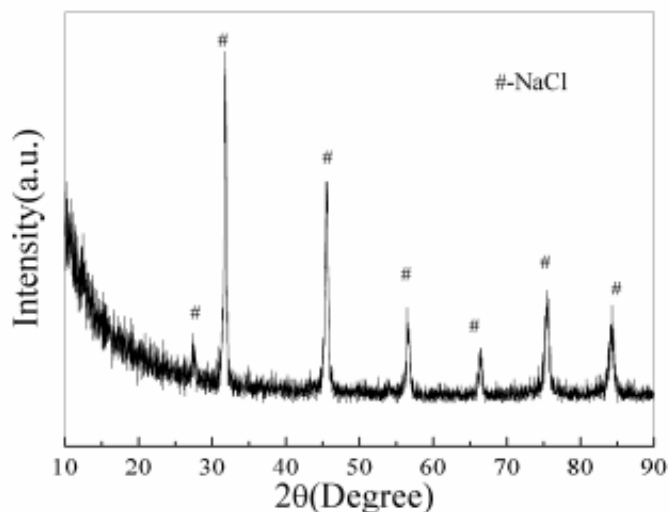
Figure 4. 1 XRD spectrum of the sediment after centrifugation during the synthesis

of $NaZn(BH_4)_3$.
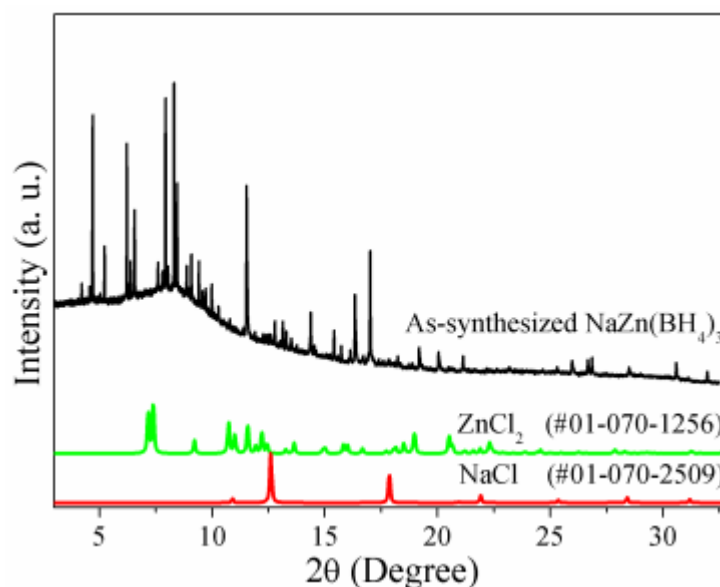
Figure 4. 2 High-resolution synchrotron X-ray diffraction ($\lambda = 0.6190$ Å) spectrum

of the as-synthesized $NaZn(BH_4)_3$.

4.2.2 Preparation of Control Sample

   A mixture of $NaZn(BH_4)_3$ with SBA-15 as a control sample was ball milled with a weight ratio of 1:3 via a planetary QM-1SP2 for 1 h. The ball-to-powder ratio was 30:1 with a milling speed of 250 rpm. Due to the relatively lower onset temperature of decomposition (approximately 100 $^{\circ}$C),[5,12,16] the milling procedure was carried out by alternating between 6 min of milling and 6 min of rest. In order to prevent contamination by air, all handling and manipulation of the materials were performed in the argon-filled glove box with a recirculation system to keep the H_2O and O_2 levels below 1 ppm.

4.2.3 Preparation of loaded $NaZn(BH_4)_3$/SBA-15 composite

   In this case, $NaZn(BH_4)_3$ was loaded into SBA-15 by the typical infusion method via capillary action. Typically, 25 drops of $NaZn(BH_4)_3$-THF solution were added to SBA-15 (~0.2 g) in the glove box, the mixture was then ultrasonicated for 2 h at around 25 $^{\circ}$C, and finally, the solvent was removed at room temperature under vacuum over 48 hours to yield the target compound. Meanwhile, the weight of the sample before and after every treatment was monitored by an electronic balance.

4.3 Results and discussion

4.3.1   Sample determination

   In order to confirm the successful infiltration of $NaZn(BH_4)_3$ into mesoporous SBA-15, XRD, FTIR, NMR, BET, SEM, and TEM measurements on pure SBA-15, and the loaded and ball-milled $NaZn(BH_4)_3$/SBA-15 composites were conducted. From the increased weight of SBA-15 after $NaZn(BH_4)_3$ incorporation, a weight loading rate of 24 wt. % is deduced for the loaded composite. In the XRD results, as shown in Figure

4.3, a broad peak was present in the range of 2 theta from 20° to 40° for all samples involving SBA-15, as a consequence of the components for amorphous silica that are present in SBA-15. With respect to the control sample of ball-milled $NaZn(BH_4)_3$/SBA-15 composite, peaks belonging to $NaZn(BH_4)_3$ are present, indicating that only a physical mixture was produced during the ball-milling process. In contrast to the ball-milled composite, peaks indexed to $NaZn(BH_4)_3$ are absent from the loaded $NaZn(BH_4)_3$/SBA-15 sample, which can be attributed to the nanoconfinement of $NaZn(BH_4)_3$ inside the pores of SBA-15, indicating the superior dispersion of $NaZn(BH_4)_3$ in the mesopores in comparison to the control sample. In the search for further evidence for the effective infiltration of $NaZn(BH_4)_3$ into the pores of SBA-15, N_2 adsorption/desorption analysis was employed to verify the specific surface area together with the cumulative pore volume of the mesoporous SBA-15. As we can see from Figure 4.4 and Table 4.1, both the BET surface area and the cumulative pore volume of SBA-15 after encapsulation of $NaZn(BH_4)_3$, 13.6 m^2 g^{-1} and 0.03 cm^3 g^{-1}, respectively, are substantially reduced, concurrent with a significant reduction of the intensity of the BJH pore size distribution, in comparison to SBA-15 without loading, providing further confirmation of successful encapsulation of $NaZn(BH_4)_3$ in the mesopores of SBA-15.
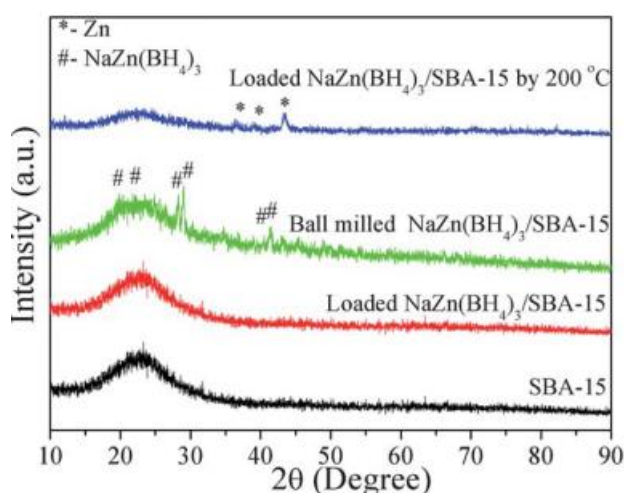
Figure 4. 3 X-ray diffraction patterns of pure SBA-15, ball-milled

NaZn(BH$_4$)$_3$/SBA-15 composite, and loaded NaZn(BH$_4$)$_3$/SBA-15 along with its

products after dehydrogenation to 200 °C.
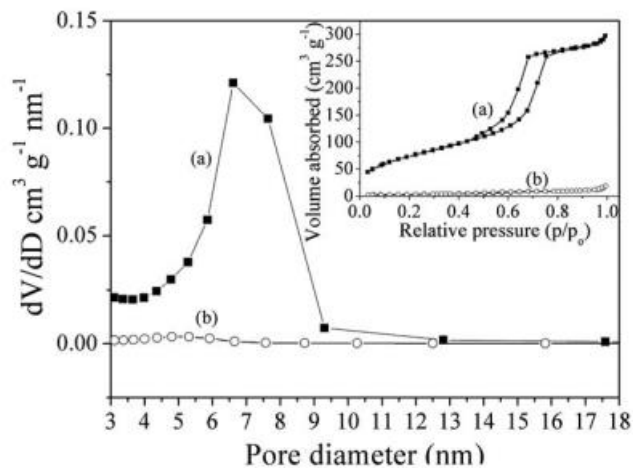
Figure 4. 4 Pore size distributions for (a) the mesoporous SBA-15 and (b) the loaded

NaZn(BH$_4$)$_3$/SBA-15 composite from the BET results. The inset shows the

corresponding nitrogen adsorption and desorption isotherms.

Table 4. 1 BET and Langmuir surface areas, and total pore volume of the

mesoporous SBA-15 with and without NaZn(BH$_4$)$_3$ loading.

Samples	Surface area ($m^2 g^{-1}$)		Total pore volume ($cm^3 g^{-1}$)
	BET	Langmuir	
Mesoporous SBA-15	274.6	442.1	0.4596
Loaded NaZn(BH$_4$)$_3$/SBA-15	13.6	22.1	0.0293

Owing to the amorphous state of nanoconfinement of NaZn(BH$_4$)$_3$ into SBA-15 on

the basis of the XRD results, both FTIR and NMR spectra were collected to further

characterize the NaZn(BH$_4$)$_3$ inside the pores of SBA-15. In addition to the peak at ~

1100 cm^{-1} assigned to the vibration of the Si-O-Si moiety as shown in the FTIR

spectrum (Figure 4.5), peaks of B-H bonds at 1120 cm^{-1}, attributed to bending modes,

and in the region of 2200-2400 cm^{-1}, also attributed to bending modes, which were quite analogous to those of the as-prepared $NaZn(BH_4)_3$, were observed after the infiltration of $NaZn(BH_4)_3$ into SBA-15, suggesting that $NaZn(BH_4)_3$ exists inside the pores of SBA-15 as fine crystallites. Moreover, for the as-prepared and nanoconfined $NaZn(BH_4)_3$, the absence of characteristic peaks of C-H bonds (Figure 4.6) in the range of 2800-3000 cm^{-1} indicates the complete removal of THF. It is interesting to see, however, that the intensity of B-H vibrations of nanoconfined $NaZn(BH_4)_3$ was significantly decreased compared with pure $NaZn(BH_4)_3$, while there was also increased intensity of the O-H vibrations compared with pure SBA-15, which presents only a slight peak due to O-H vibrations. This is indicative of weakened B-H bonds and a possible attractive interaction between O of SBA-15 and H of the BH_4 group after incorporation of nanoscale $NaZn(BH_4)_3$ into SBA-15. Furthermore, ^{11}B NMR spectra revealed that typical resonances of BH_4^{-1} groups centered at -42 ppm and -45.2 ppm for the synthesized $NaZn(BH_4)_3$ could be assigned to BH_4 groups related to Na^+ and Zn^{2+}, respectively, in agreement with the literature[16], while the resonances of BH_4^{-1} groups of $NaZn(BH_4)_3$ after infiltration into SBA-15 have a roughly 1.6 ppm shift to the downfield region, which was also observed for a $LiBH_4$ - $MgBH_4$ mixture after infiltration into carbon pores[40]. This result indicates the increased electron density of boron in $NaZn(BH_4)_3$ due to the different chemical environment induced upon nanoconfinement compared to pure $NaZn(BH_4)_3$. The downfield shift of BH_4 groups in the NMR spectra can be mainly attributed to (1) the attractive interaction between O of SBA-15 and H of the BH_4 moiety, as indicated by the FTIR spectra, which will weaken electron withdrawal by H from B in the BH_4 group and, vice versa, result in increased electron density of atomic B; and (2) the possible shielding effect of lone-pair electrons of O atoms from SBA-15 on the resonances of boron in the

NaZn(BH$_4$)$_3$ inside the pores of SBA-15, at least to a certain degree, indirectly demonstrating the successful infiltration of NaZn(BH$_4$)$_3$ into SBA-15. In addition, a low peak with a broad shoulder pertaining to amorphous boron in the region of 16 to -20 ppm appears in the NMR spectra of nanoconfined NaZn(BH$_4$)$_3$ in SBA-15, originating from possible decomposition during solid state NMR measurements, owing to its relatively much lower dehydrogenation temperature in contrast to pure NaZn(BH$_4$)$_3$ (as discussed below).
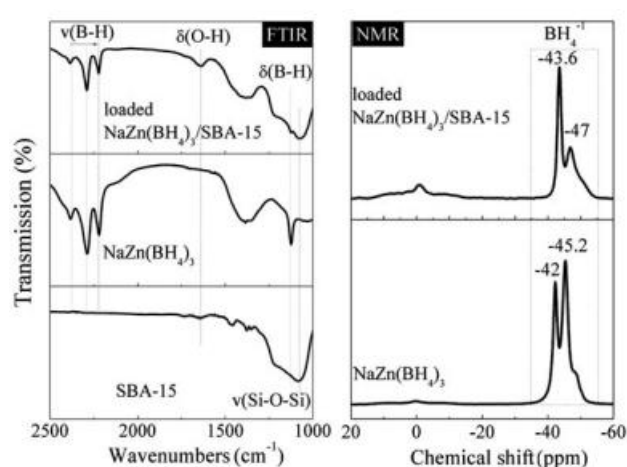
Figure 4. 5 FTIR (left) and ^{11}B MAS solid-state NMR (right) spectra of SBA-15, ball-milled NaZn(BH$_4$)$_3$/SBA-15 composite, and loaded NaZn(BH$_4$)$_3$/SBA-15.
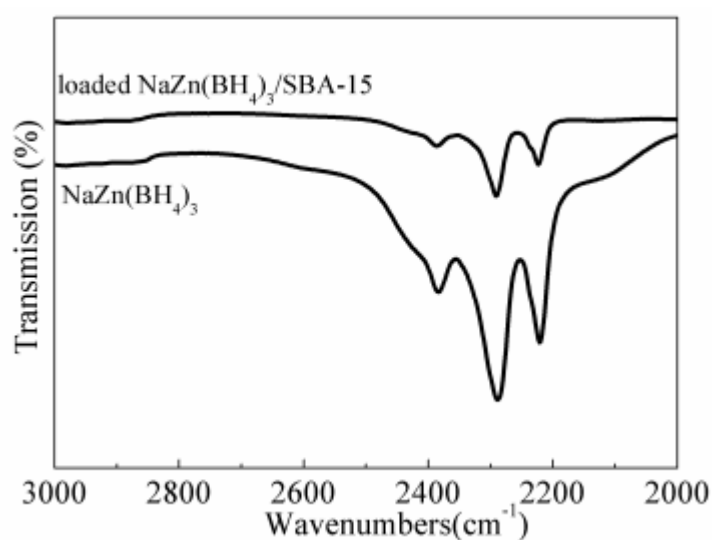
Figure 4. 6 FTIR spectra of the as-prepared $NaZn(BH_4)_3$ and loaded

$NaZn(BH_4)_3$/SBA-15 in the range of 2000-3000 cm^{-1}.

The surface morphology changes for the nanoconfined $NaZn(BH_4)_3$ before and after dehydrogenation were obtained through SEM and high resolution TEM (HRTEM) images. As shown in Figure 4.7(b), after vacuum drying, agglomeration due to the thus-crystallized $NaZn(BH_4)_3$ is obviously absent on the surfaces of SBA-15, while the Si map agrees well with the structure of the SBA-15 and the Zn map corresponds well with the Si map from the energy dispersive spectroscopy (EDS) elemental maps for the loaded compound (Figures 4(d-f)), suggesting good dispersion of $NaZn(BH_4)$ inside the pores of SBA-15. The TEM images in Figure 4.9 show the distribution of $NaZn(BH_4)_3$ in the channel pores of the samples before and after dehydrogenation. The characteristic hexagonal arrays of uniform channels with the typical honeycomb appearance of SBA-15 material (Figure 4.8), presenting a channel diameter of around 6.5 nm, were definitely observed, in accordance with the average pore diameter of approximately 6 nm derived from the BET results. Additionally, dark domains and spots inside the mesopores of SBA-15, resulting from the nanoconfined $NaZn(BH_4)_3$ and/or its decomposed products, denoted by arrows, are apparent, with EDS elemental maps of Si coinciding with those of Zn and Na, providing strong confirmation for the incorporation of $NaZn(BH_4)_3$ into SBA-15. Moreover, it should be pointed out that the pore structure of the loaded samples, after heat treatment to 200 ºC (Figures 4.9(c, d)), remains intact, which agrees well with the SEM images of the loaded samples (Figures 4.7 (b, c)) regardless of whether or not they had experienced heat treatment, demonstrating that SBA-15 can effectively maintain its nanoconfinement effects on the $NaZn(BH_4)_3$ inside its pores throughout the process for hydrogen desorption.

Based on the above-mentioned characterization, we can, therefore, conclude that NaZn(BH$_4$)$_3$ was indeed incorporated into SBA-15 in nanoscale form and/or blocked the pores of SBA-15 by dint of infusion through the capillary effect.
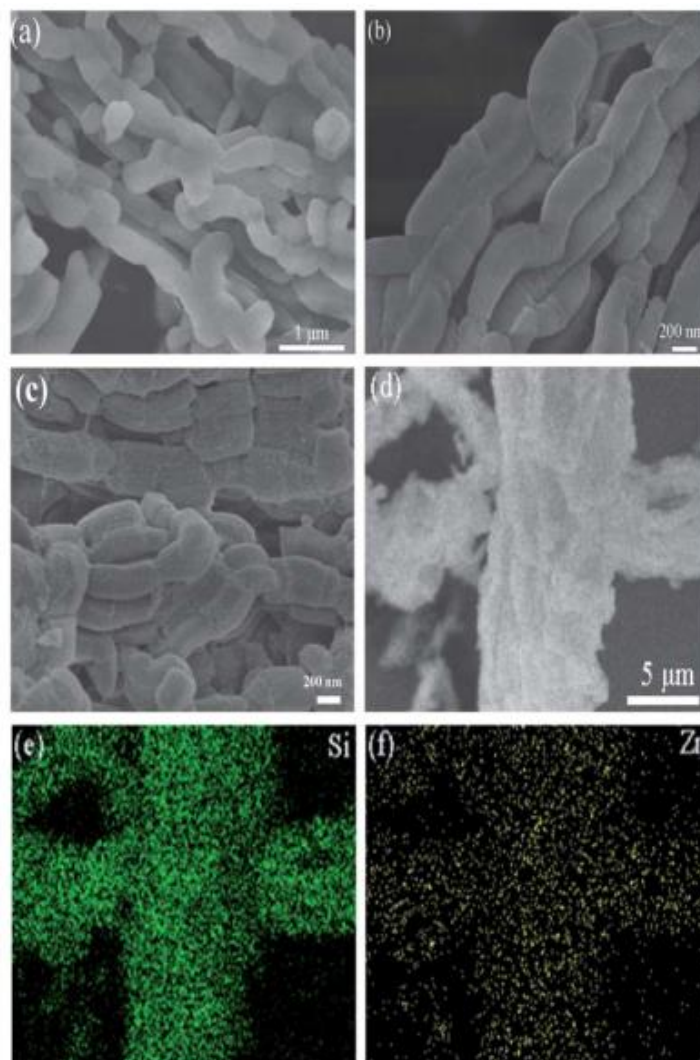
Figure 4. 7 SEM images of (a) pure SBA-15 for comparison, (b) loaded NaZn(BH$_4$)$_3$/SBA-15 after vacuum drying, (c) the products after dehydrogenation to 200 °C, and the corresponding EDS maps of Si (e) and Zn (f), corresponding to image (d), collected before dehydrogenation.
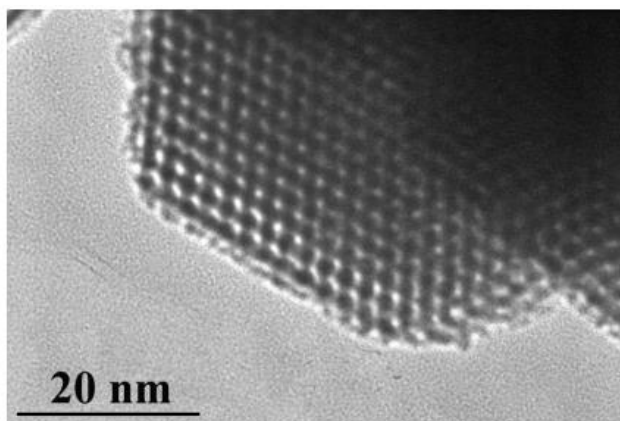
Figure 4. 8 TEM image of loaded NaZn(BH$_4$)$_3$/SBA-15 composite in the direction of

the pore axis.
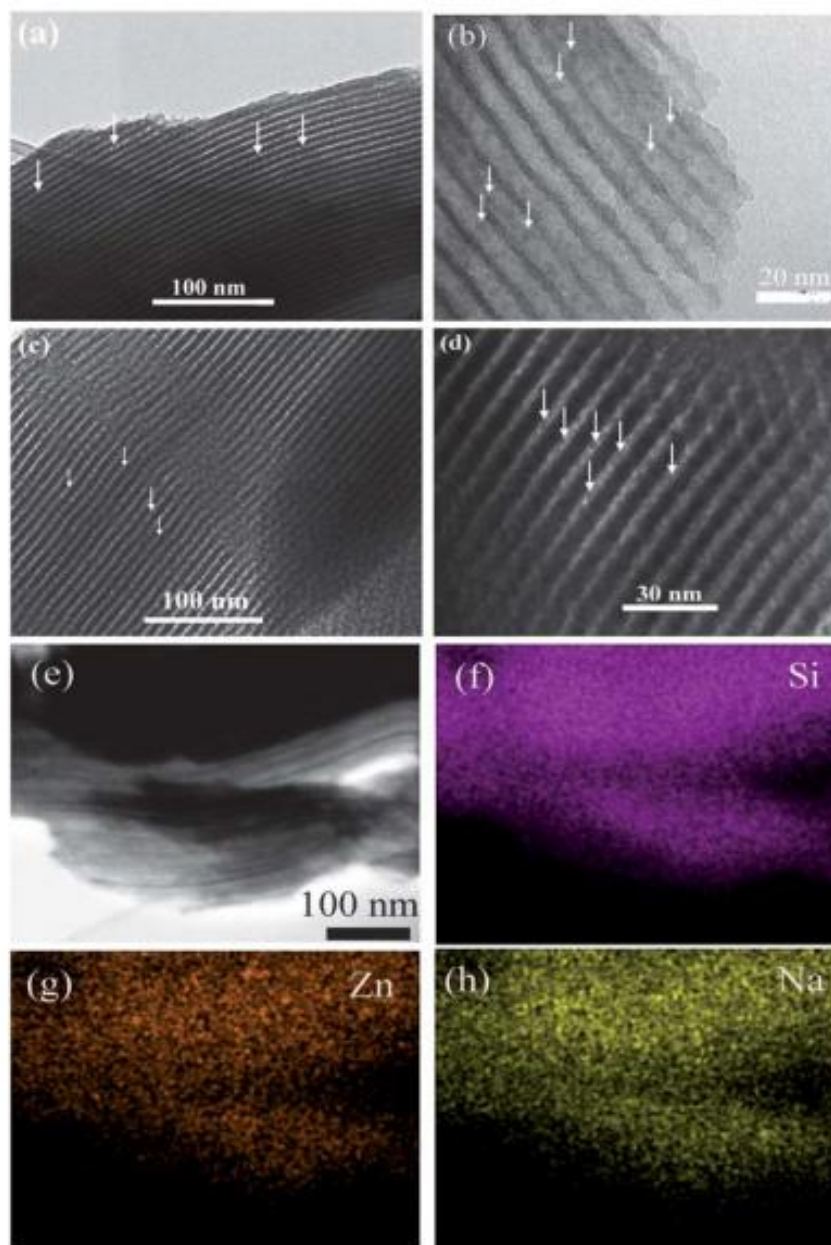
Figure 4. 9 HRTEM images at different magnifications of the loaded

NaZn(BH$_4$)$_3$/SBA-15 before (a, b) and after (c, d) dehydrogenation; TEM image

before dehydrogenation (e) and the corresponding EDS maps of Si (f), Zn (g), and

Na (h).

4.3.2   Hydrogen desorption properties

To explore the effects of SBA-15 as the scaffold on the hydrogen storage properties

of nanoconfined NaZn(BH$_4$)$_3$, a comparison of the thermal decomposition

performance of the as-prepared $NaZn(BH_4)_3$, the $NaZn(BH_4)_3$ loaded into SBA-15, and the ball-milled $NaZn(BH_4)_3$/SBA-15 composite as control sample was conducted by employing TGA and MS in tandem with volumetric measurements, as shown in Figures 4.10 and 4.11(a). The decomposition of the as-prepared $NaZn(BH_4)_3$ in the temperature range of 80-200 ^oC is similar to what was previously reported[16], with a weight loss of ~ 29 wt. %, accompanied by the release of a multitude of borane families, e.g., BH_3 and B_2H_6, which is further verified by the much lower amount of hydrogen release in comparison with its theoretical content, with only 1.35 mol of gas liberated during the thermolysis procedure, according to the volumetric results expressed with respect to the content of $NaZn(BH_4)_3$ in the sample under the same conditions, indicating a significantly reduced amount of effective hydrogen. In the case of the ball-milled mixture of $NaZn(BH_4)_3$ with SBA-15, as most $NaZn(BH_4)_3$ is present outside of the SBA-15, instead of being incorporated into the nanopores of SBA-15, it undergoes a decomposition process that is comparable with that of pure $NaZn(BH_4)_3$, exhibiting a 24.1 wt. % weight loss, which is much more than its theoretical hydrogen storage capacity (9.1 wt. %), but with only 1.4 mol of released gas from volumetric results. In contrast, from the MS spectra of $NaZn(BH_4)_3$ nanoconfined in SBA-15, only hydrogen was detected over the whole thermolysis process, coupled with a total suppression of BH_3 and/or B_2H_6. In addition, the onset decomposition temperature of $NaZn(BH_4)_3$ infiltrated into SBA-15 decreased to around 50 ^oC, along with one peak at 112 ^oC, which is slight lower than those of pure $NaZn(BH_4)_3$ and the control sample (~ 120 ^oC). Furthermore, the weight loss (6 wt. %) is in good agreement with the volumetric results, with around 3.98 mol of gas released upon heating, accounting for 99 % of theoretical hydrogen capacity, which further confirms the complete repression of release of boric by-products. The weight loss process for dehydrogenation ends

before 150 °C, in concurrence with the MS spectra, which is much lower than for pure NaZn(BH$_4$)$_3$, clearly demonstrating that the nanoconfinement of NaZn(BH$_4$)$_3$ facilitates the kinetics of hydrogen release.
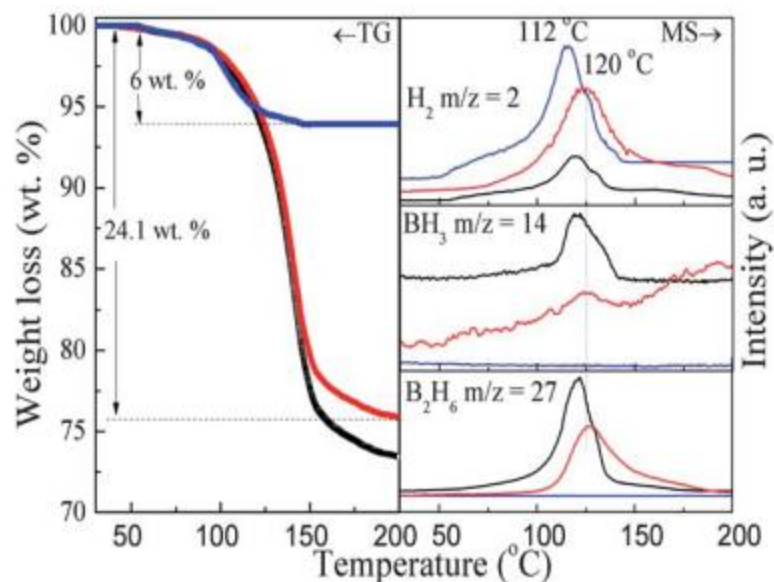
Figure 4. 10 TGA (left) and MS (right) results for pure NaZn(BH$_4$)$_3$ (black line), ball-milled NaZn(BH$_4$)$_3$/SBA-15 (red line), and loaded NaZn(BH$_4$)$_3$/SBA-15 (blue line), with a heating rate of 2 °C/min under dynamic argon atmosphere. The right axis of the TGA chart gives the amount of weight loss relative to the mass of NaZn(BH$_4$)$_3$ only.
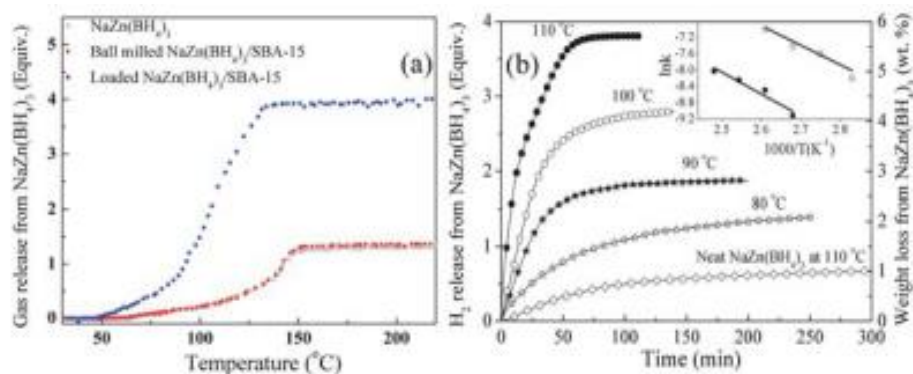
Figure 4. 11 (a) Volumetric gas release measurements for pure NaZn(BH$_4$)$_3$(black line), ball milled NaZn(BH$_4$)$_3$/SBA-15 (red line) and loaded NaZn(BH$_4$)$_3$/SBA-15

(blue line), with a heating rate of 2 °C/min under 1 atm argon, expressed with respect to the content of NaZn(BH$_4$)$_3$ only, and (b) isothermal volumetric results for gas release from loaded NaZn(BH$_4$)$_3$/SBA-15 composite at 80 °C, 90 °C, 100 °C, and 110 °C, and for neat NaZn(BH$_4$)$_3$ at 110 °C. The inset shows a comparison of the Arrhenius plots of the temperature-dependent rate data of the loaded NaZn(BH$_4$)$_3$/SBA-15 composite (●) and the pure NaZn(BH$_4$)$_3$ (○).
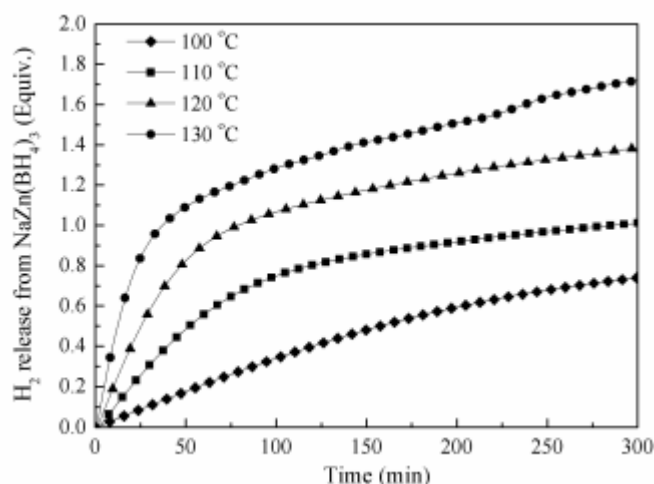
Figure 4. 12 Isothermal volumetric results for gas release from as-prepared NaZn(BH$_4$)$_3$ at 100 °C, 110 °C, 120 °C, and 130 °C.

Better information on the decomposition properties of nanoconfined and bulk NaZn(BH$_4$)$_3$ was gained via isothermal dehydrogenation at different temperatures through the method of volumetric gas release measurements, as shown in Figures 4.11(b) and 4.12, to investigate the dehydrogenation kinetics. As expected, the hydrogen desorption kinetics increases as the relative operating temperature increases. The results reveal that hydrogen release from the nanoconfined NaZn(BH$_4$)$_3$ proceeds slowly at the temperature of 80 °C, evolving about 2 wt. % hydrogen within 250 min. Upon heating, nanoconfined NaZn(BH$_4$)$_3$ could release around 3 wt. % hydrogen in 200 min at 90 °C and slightly more than 4 wt. % within 150 min at 100 °C. Specifically, 5.7 wt. % hydrogen, accounting for 95% of its theoretical hydrogen capacity, was

released from $NaZn(BH_4)_3$ after encapsulation in SBA-15 in only 90 min, while merely 0.5 mol gas was released from pure $NaZn(BH_4)_3$ at the same temperature, even with time extension to 300 min, which is much less than the hydrogen release capacity of the nanoconfined $NaZn(BH_4)_3$ even at 80 $^{\circ}$C. Clearly, a significant enhancement of the hydrogen release kinetics of $NaZn(BH_4)_3$ after encapsulation into SBA-15 is achieved due to the formation of nanocrystals, resulting in shorter diffusion paths for hydrogen spillover from the substrate, which lowers the kinetic dehydrogenation barrier. In order to quantitatively characterize the kinetic properties, Arrhenius plots of ln k were collected (where k is the reaction rate constant (s^{-1})) versus 1/T (where T is the absolute temperature for relative hydrogen release), as shown in the inset of Figure 4.11(b). The plots exhibit good linearity for the nanoconfined $NaZn(BH_4)_3$. By conducting a linear fit of the data points, the apparent activation energy E_a for hydrogen release from nanoconfined and bulk $NaZn(BH_4)_3$, by virtue of Arrhenius equation ($k = A \exp(-E_a/(RT))$), can be calculated to be only 38.9 kJ mol^{-1} and 44.2 kJ mol^{-1}, respectively. This directly confirms the enhancement of kinetics for $NaZn(BH_4)_3$ confined in mesopores of SBA-15. To the best of our knowledge, this is the first example of successful stabilization of a Zn-based metal borohydride via the nanoconfinement technique so as to achieve a pure hydrogen release, in tandem with enhanced hydrogen release kinetics, making $NaZn(BH_4)_3$ a promising hydrogen storage material for practical application.

4.3.3   Hydrogen desorption properties
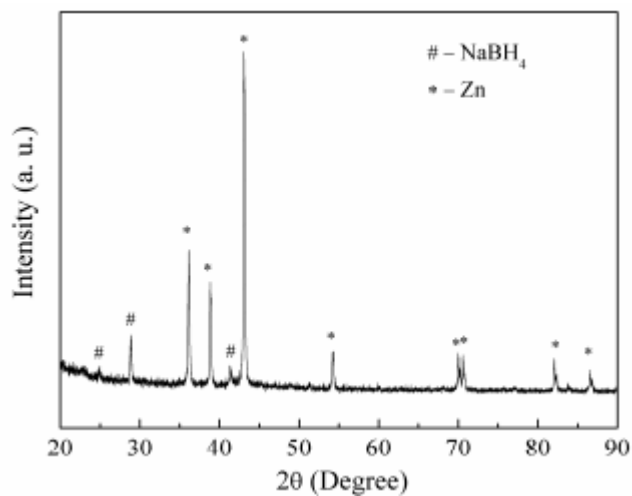
Figure 4. 13 XRD spectrum of the products of the decomposition of $NaZn(BH_4)_3$

after heating to 200 ^oC.
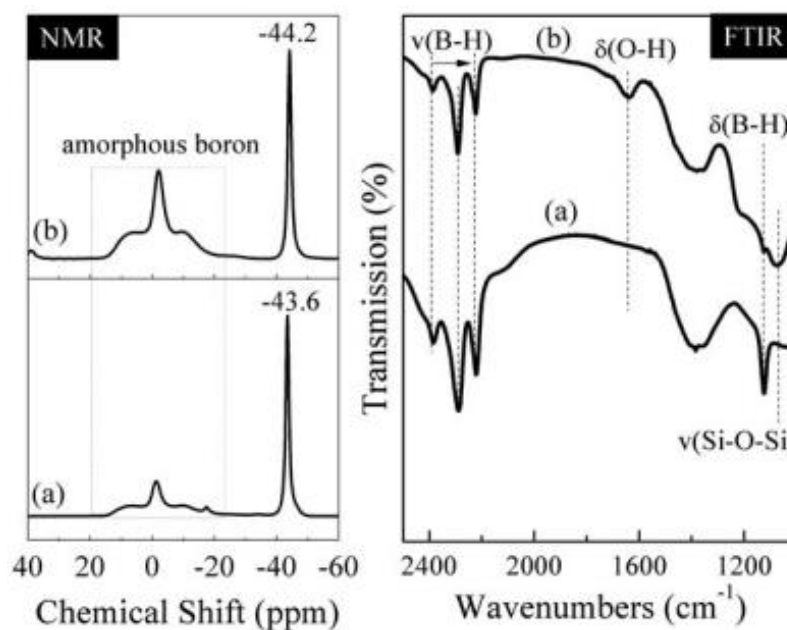
Figure 4. 14 ^{11}B MAS solid-state NMR (left) and FTIR (right) spectra of (a) pure

$NaZn(BH_4)_3$ and (b) loaded $NaZn(BH_4)_3$/SBA-15 composite after decomposition to

200 ^oC under 1 atm argon.

In the light of the above discussion, the confinement of $NaZn(BH_4)_3$ in SBA-15 on

the nanoscale, giving rise to shorter diffusion paths for hydrogen evolution, is the main

factor responsible for enhancing the hydrogen desorption properties, similar to what has been observed in other nanoconfined hydrogen storage materials[17-35]. Further investigation of the effects of SBA-15 as scaffold on the decomposition mechanism was conducted, in order to unravel the mechanism for improvement of the thermodynamics of hydrogen release. The XRD pattern (Figure 4.13) of $NaZn(BH_4)_3$ after decomposition to 200 °C demonstrates the formation of Zn and $NaBH_4$, without the appearance of any boron peaks due to its amorphous structure, which corresponds well with the results in a previous report[16]. Only peaks indexed to Zn are observed, however, for the dehydrogenated product of $NaZn(BH_4)_3$ loaded into SBA-15, with no presence of $NaBH_4$ (Figure 4.3). As apparent BH_4^{-1} groups corresponding to $NaBH_4$ centered at − 44.2 ppm were detected in the NMR spectra, in addition to the B-H bonds in both bending and stretching mode, as witnessed by the FTIR spectra (Figure 4.14), the disappearance of $NaBH_4$ from the XRD spectra may have resulted from its uniform dispersion in the mesoporous SBA-15 due to its amorphous and/or nanophase structure. This is directly confirmed by the TEM results (Figures 4.9(c, d)), which exhibit nanocrystals of products inside the mesopores of SBA-15 after hydrogen desorption. Simultaneously, the intensity of O-H interaction vibrations was decreased with decreasing intensity of B-H bond vibrations, suggesting that the presence of O-H interactions may promote hydrogen release from $NaZn(BH_4)_3$. With regard to the NMR spectra of the dehydrogenated products, the disappearance of peaks assigned to the BH_4 group linked to Zn^{2+} in $NaZn(BH_4)_3$ with and without infiltration into SBA-15 confirms the complete decomposition of the BH_4 group linked to Zn^{2+}, demonstrating the relatively unstable character of metal borohydrides with metal cations of a high Pauling electronegativity χ_p. Compared with the products of decomposition of pure $NaZn(BH_4)_3$, similar phenomena were observed in the NMR

spectra of the raw materials, with 0.6 ppm of downfield shift for the BH_4 group in the dehydrogenated $NaZn(BH_4)_3$ after infiltration into SBA-15. In addition, the ratio of the intensity of amorphous elemental B to that of the BH_4 group increased for dehydrogenated $NaZn(BH_4)_3$ infiltrated into SBA-15 towards that of pure $NaZn(BH_4)_3$, illustrating that $NaZn(BH_4)_3$ infiltrated into SBA-15, under the attractive interaction of O in SBA-15, finds it preferable to form boron by releasing hydrogen instead of BH_3 or B_2H_6, resulting in both suppression of gases that are detrimental for fuel cells and relatively higher hydrogen capacity. Based on the above facts, i.e., the formation of $NaBH_4$, amorphous B, and Zn along with the release of pure hydrogen upon decomposition, the decomposition process of the nanoconfined $NaZn(BH_4)_3$ can be expressed as follows:

$$NaZn(BH_4)_3 \text{ (on nanoscale)} \rightarrow NaBH_4 + Zn + B + 2H_2 \quad (4.1)$$
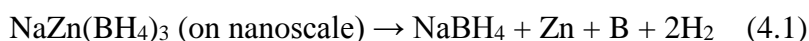
The above decomposition reaction delivers a theoretical hydrogen capacity of 6 wt. %, i.e., 4 equiv. H_2 per $NaZn(BH_4)_3$ formula unit, agreeing well with the observed experimental results (Figure 4.10 and Figure 4.11(a)). The hydrogenation of the decomposition products, however, was unsuccessful via solid-state reaction at 400 ^{o}C under 10 MPa H_2.

4.4 Results and discussion

Nanoconfinement of $NaZn(BH_4)_3$ in mesoporous SBA-15 was successfully realized by typical infusion via capillary action. Compared with pure $NaZn(BH_4)_3$, $NaZn(BH_4)_3$ infiltrated into SBA-15 displays significantly enhanced hydrogen release properties, including complete suppression of boranes and improved hydrogen release kinetics, offering pure hydrogen release in the temperature range of 50 to 150 ^{o}C. Our results indicate that nanoscale $NaZn(BH_4)_3$ obeys a completely different decomposition mechanism from its bulk counterpart, which enables unstable

borohydrides to release pure hydrogen rather than undesirable boranes, providing a viable strategy for improving the hydrogen desorption properties of relatively unstable metal borohydrides with high Pauling electronegativity for superior hydrogen release kinetics under lower temperature by designed nanostructures.

4.5 References

[1] Nan J. Yang and S. Hirano, *Advanced Materials*, 2009, **21**, 3023-3028.

[2] S.-I. Orimo, Y. Nakamori, J. R. Eliseo, A. Züttel and C. M. Jensen, *Chemical Reviews*, 2007, **107**, 4111-4132.

[3] A. Züttel, P. Wenger, S. Rentsch, P. Sudan, P. Mauron and C. Emmenegger, *Journal of Power Sources*, 2003, **118**, 1-7.

[4] X. B. Yu, D. M. Grant and G. S. Walker, *Chem Commun*, 2006, 3906-3908.

[5] R. Černý, Y. Filinchuk, H. Hagemann and K. Yvon, *Angewandte Chemie International Edition*, 2007, **46**, 5765-5767.

[6] T. J. Frankcombe, G.-J. Kroes and A. Züttel, *Chemical Physics Letters*, 2005, **405**, 73-78.

[7] Z. Łodziana and T. Vegge, *Physical Review Letters*, 2004, **93**, 145501.

[8] P. Mauron, F. Buchter, O. Friedrichs, A. Remhof, M. Bielmann, C. N. Zwicky and A. Züttel, *Journal of Physical Chemistry B*, 2007, **112**, 906-910.

[9] Y. Nakamori, K. Miwa, A. Ninomiya, H. Li, N. Ohba, S.-i. Towata, A. Züttel and S.-I. Orimo, *Physical Review B*, 2006, **74**, 045126.

[10] O. Friedrichs, A. Remhof, S. J. Hwang and A. Züttel, *Chemistry of Materials*, 2010, **22**, 3265-3268.

[11] D. Ravnsbaek, Y. Filinchuk, Y. Cerenius, H. J. Jakobsen, F. Besenbacher, J. Skibsted and T. R. Jensen, *Angewandte Chemie-International Edition*, 2009, **48**, 6659-6663.

[12]   R. Černý, K. Chul Kim, N. Penin, V. D'Anna, H. Hagemann and D. S. Sholl, *Journal of Physical Chemistry C*, 2010, **114**, 19127-19333.

[13]   M. Au, A. R. Jurgensen, W. A. Spencer, D. L. Anton, F. E. Pinkerton, S. J. Hwang, C. Kim and R. C. Bowman, *Journal of Physical Chemistry C*, 2008, **112**, 18661-18671.

[14]   A. Züttel, S. Rentsch, P. Fischer, P. Wenger, P. Sudan, P. Mauron and C. Emmenegger, *Journal of Alloys and Compounds*, 2003, **356-357**, 515-520.

[15]   A. Züttel, A. Borgschulte and S.-I. Orimo, *Scripta Materialia*, 2007, **56**, 823-828.

[16]   G. Xia, Q. Gu, Y. Guo and X. Yu, *Journal of Materials Chemistry*, 2012, **22**, 7300-7307.

[17]   H. Reardon, J. M. Hanlon, R. W. Hughes, A. Godula-Jopek, T. K. Mandal and D. H. Gregory, *Energy & Environmental Science*, 2012, **5**, 5951-5979.

[18]   T. K. Nielsen, F. Besenbacher and T. R. Jensen, *Nanoscale*, 2011, **3**, 2086-2098.

[19]   M. Fichtner, *Physical Chemistry Chemical Physics*, 2011, **13**, 21186-21195.

[20]   P. E. de Jongh and P. Adelhelm, *ChemSusChem*, 2010, **3**, 1332-1348.

[21]   P. Adelhelm and P. E. de Jongh, *Journal of Materials Chemistry*, 2011, **21**, 2417-2427.

[22]   H. Wu, W. Zhou, K. Wang, T. J. Udovic, J. J. Rush, T. Yildirim, L. A. Bendersky, A. F. Gross, S. L. Van Atta, J. J. Vajo, F. E. Pinkerton, and M. S. Meyer, *Nanotechnology*, 2009, **20**, 204002.

[23]   R. D. Stephens, A. F. Gross, S. L. Van Atta, J. J. Vajo, and F. E. Pinkerton, *Nanotechnology*, 2009, **20**, 204018.

[24]   T. K. Nielsen, M. Polanski, D. Zasada, P. Javadian, F. Besenbacher, J. Bystrzycki, J. Skibsted and T. R. Jensen, *ACS Nano*, 2011, **5**, 4056-4064.

[25]   P. Adelhelm, K. P. de Jong and P. E. de Jongh, *Chemical Communications*, 2009, 6261-6263.

[26]   P. Adelhelm, J. Gao, M. H. W. Verkuijlen, C. Rongeat, M. Herrich, P. J. M. van Bentum, O. Gutfleisch, A. P. M. Kentgens, K. P. de Jong and P. E. de Jongh, *Chemistry of Materials*, 2010, **22**, 2233-2238.

[27]   P. Ngene, R. van den Berg, M. H. W. Verkuijlen, K. P. de Jong and P. E. de Jongh, *Energy & Environmental Science*, 2011, **4**, 4108-4115.

[28]   T. K. Nielsen, U. Bösenberg, R. Gosalawit, M. Dornheim, Y. Cerenius, F. Besenbacher and T. R. Jensen, *ACS Nano*, 2010, **4**, 3903-3908.

[29]   T. K. Nielsen, K. Manickam, M. Hirscher, F. Besenbacher and T. R. Jensen, *ACS Nano*, 2009, **3**, 3521-3528.

[30]   X. Z. Xiao, L. X. Chen, X. L. Fan, X. H. Wang, C. P. Chen, Y. Q. Lei and Q. D. Wang, *Applied Physics Letters*, 2009, **94**, 041907-041903.

[31]   L. Li, X. Yao, C. Sun, A. Du, L. Cheng, Z. Zhu, C. Yu, J. Zou, S. C. Smith, P. Wang, H.-M. Cheng, R. L. Frost and G. Q. Lu, *Advanced Functional Materials*, 2009, **19**, 265-271.

[32]   Z. Li, G. Zhu, G. Lu, S. Qiu and X. Yao, *Journal of the American Chemical Society*, 2010, **132**, 1490-1491.

[33]   Z. Tang, H. Chen, X. Chen, L. Wu and X. Yu, *Journal of the American Chemical Society*, 2012, **134**, 5464-5467.

[34]   A. F. Gross, J. J. Vajo, S. L. Van Atta and G. L. Olson, *Journal of Physical Chemistry C*, 2008, **112**, 5651-5657.

[35]   X. Liu, D. Peaslee, C. Z. Jost and E. H. Majzoub, *Journal of Physical Chemistry C*, 2010, **114**, 14036-14041.

[36]   P. Ngene, P. Adelhelm, A. M. Beale, K. P. de Jong and P. E. de Jongh, *Journal of Physical Chemistry C*, 2010, **114**, 6163-6168.

[37]   W. Sun, S. Li, J. Mao, Z. Guo, H. Liu, S. Dou and X. Yu, *Dalton Transactions*, 2011, **40**, 5673-5676.

[38]   P. Ngene, M. van Zwienen and P. E. de Jongh, *Chemical Communications*, 2010, **46**, 8201-8203.

[39]   S. Sepehri, B. B. García and G. Cao, *European Journal of Inorganic Chemistry*, 2009, **2009**, 599-603.

[40]   S. Sabrina, D. K. Kenneth, H. Fredrik Sydow, H. H. Richard, B. Elisa Gil, Z.-K. Zhirong, F. Maximilian and C. H. Bjørn, *Nanotechnology*, 2012, **23**, 255704.

5   CHAPTER 5 EFFECTS OF NANOCONFINEMENT ON THE HYDROGEN SORPTION PERFORMANCE OF 2LIBH4-LIALH4 COMPOSITES

5.1 Introduction

In general, the partial dehydrogenation of LiBH$_4$ can yield 13.8 wt. % H$_2$, leading to the formation of a mixture of amorphous boron and lithium hydride, although possibly in more than one step. Unfortunately, the application of LiBH$_4$ as a solid-state hydrogen storage medium is encumbered by both thermodynamic and kinetic deficiencies due to the strong bonding of atoms; i.e., the standard reaction enthalpy (ΔH) of ~ 67 kJ mol^{-1} H$_2$ for LiBH$_4$ decomposition translates to a thermodynamic desorption temperature of 410 ^{o}C at 1 bar, with only half of the hydrogen content released below 600 ^{o}C, and, more importantly, the subsequent partial H$_2$ uptake only takes place under extreme conditions (600 ^{o}C, 150 bar H$_2$) [1-3].

In order to overcome the above-mentioned barriers, several effective approaches have recently been adopted to modify the thermodynamics and kinetics of both the dehydrogenation and the rehydrogenation of LiBH$_4$. One novel strategy is to develop reactive hydride composites or the so-called destabilization composites consisting of borohydrides and metallic hydrides [4-8]. By the reaction of metallic borohydrides with metallic hydrides, thermodynamic tuning is accessible to adjust equilibrium temperatures and pressures towards reversible H$_2$ release/uptake for hydrogen storage application, owing to the formation of thermodynamically stable metal boride [8]. Typically, the combination of MgH$_2$ with LiBH$_4$ reversibly releases 8-10 wt. % H$_2$ within two cycles, with a reaction enthalpy of 40.5 kJ mol^{-1} H$_2$, which is 25 kJ mol^{-1} H$_2$ lower than that of pure LiBH$_4$, according to Eq. (5.2) [8]. Moreover, the equilibrium temperature for the decomposition of LiBH$_4$ using Al from LiAlH$_4$ as a destabilization

agent, with the formation of AlB_2, is calculated to be 188 $^\circ$C under 1 bar H_2, which is 220 $^\circ$C lower than that of pure $LiBH_4$ [9]. Therefore, the formation of relatively stable MgB_2/AlB_2, instead of pure boron from the decomposition of pure $LiBH_4$, thermodynamically destabilizes the hydrogenation/dehydrogenation of $LiBH_4$ towards the optimized desorption temperature [5, 8-21].

$$2LiBH_4 + MgH_2 \leftrightarrow 2LiH + MgB_2 + 4H_2 \quad (5.2)$$

$$2LiBH_4 + LiAlH_4 \leftrightarrow 3LiH + AlB_2 + 9/2H_2 \quad (5.3)$$

The kinetic barriers, however, result in a practical operating temperature for H_2 liberation of $LiBH_4$ destabilized by Al that is over 300 $^\circ$C, and the kinetics of the H_2 ab-/desorption in Eq. (5.3) is still slow at temperatures below 500 $^\circ$C [12, 14, 15, 22]. Moreover, the sustainable reversibility of the destabilized $LiBH_4$ is greatly limited due to the following reasons. Firstly, the sintering effects and particle agglomeration as a result of the consecutive H_2 release and uptake cycles at elevated temperatures considerably increase the diffusion pathways for both the dissociation of metallic boride and the following recombination of active substrates with H_2 to reversibly synthesize $LiBH_4$ for H_2 storage performance, which therefore significantly lowers the kinetics for reversible H_2 ab-/de-sorption and further degrades the related H_2 capacity [18, 23, 24]. Secondly, due to the phase separation, the amount of each active substrate after the H_2 sorption cycle might no longer be stoichiometric, subsequently limiting the formation of metallic borides, which is thermodynamically effective for the improvement of the cyclic performance of $LiBH_4$ [18, 23]. Thirdly, the evolution of toxic diborane during dehydrogenation of $LiBH_4$ leads to the loss of B on each cycle and therefore decreases the capacity regenerated from the dehydrogenated products [25]. Fourthly, the formation of stable "sinks", e.g., closo-borane $[B_{10}H_{10}]^{2-}$ and $[B_{12}H_{12}]^{2-}$ salts, during cyclic H_2 uptake and release processes can also significantly decrease the

reversible capacity as a consequence of the loss of boron to these compounds on each cycle [26, 27]. For instance, the amount of hydrogen release was dramatically reduced from 8.6 wt. % at the 1st hydrogen desorption to 5.5 wt. % at the 2nd hydrogen desorption, and further dropped to 1.8 wt. % at the 10th hydrogen desorption for post-milled $2LiBH_4-MgH_2$ composites [28], which is mainly ascribed to the formation of $Li_2B_{12}H_{12}$ and the incomplete formation of MgB_2 from the interaction between Mg and $LiBH_4$ during the dehydrogenation of $2LiBH_4-MgH_2$ composites [29]. Furthermore, the decrease in the hydrogen capacity was observed to be around 50% for the Al destabilized $LiBH_4$ within only 3 cycles [18], resulting from the separation of Al and B, and therefore, the incomplete formation of AlB_2. Hence, sufficient improvement of the reaction kinetics at lower temperatures towards stably reversible H_2 release and uptake is still a primary challenge for the destabilized $LiBH_4$ systems.

The latest studies have shown that confining $LiBH_4$ in various mesoporous templates results in significantly improved kinetics and thermodynamics of the hydrogen storage properties in comparison with its bulk counterpart [30-41]. For example, the nanoconfinement of $LiBH_4$ in nanoporous carbon with an average pore size of 2 nm leads to a significant decrease in the onset dehydrogenation temperature from 460 °C to 220 °C with respect to bulk $LiBH_4$ [35]. Although there is an improvement in the cycling stability for $LiBH_4$ infiltrated into mesoporous carbon due to the increased interfacial contact between LiH and B resulting from the decrease in the particle size, the H_2 capacity loss is still up to 40% for the nanoconfined $LiBH_4$ after only three cycles [4]. Furthermore, based on the combination of the above-mentioned effects of thermodynamic destabilization and nanoconfinement, $LiBH_4$ and MgH_2 were separately infiltrated into carbon aerogel scaffolds. Although this route cannot achieve good dispersibility due to the separate infiltration process of $LiBH_4$ and MgH_2, a

considerable improvement of the hydrogen desorption kinetics and reversibility compared with bulk counterparts was realized [42], suggesting the high potential of the nanoconfinement technique to improve the cycling of destabilized $LiBH_4$, especially when the combined composites are dispersed uniformly.

In the present study, synergistic coupling between reactive hydride composite and nanoconfinement effects was successfully adopted to improve the hydrogen storage properties of Al-destabilized $LiBH_4$ for the first time, i.e., the well-dispersion of $LiAlH_4$ and $LiBH_4$ inside the nanopores of carbon scaffolds. Interestingly, by virtue of the nanoconfinement effect, the interaction between $LiBH_4$ and $LiAlH_4$ particles that are well distributed inside mesopores results in the favorable formation of AlB_2 under the structure-directing function of carbon scaffolds, which can effectively limit the aggregation of the active substrates and thus enhances their cycling performance remarkably.

5.2 Preparation

5.2.1 Materials

The starting materials, solid-state $LiBH_4$ (98%) and $LiAlH_4$ (98%), and anhydrous tetrahydrofuran (THF, 99.9%) were purchased from Sigma-Aldrich and used in their as-received forms without further purification. Mesoporous carbons (MCs) were supplied by Nanjing XFNANO Materials Tech Co., Ltd, China. A mixture of $LiBH_4$ and $LiAlH_4$ with a molar ratio of 2:1 with or without carbon scaffolds (for a control sample) was mechanically ball milled via a planetary QM-1SP2 for 4 h in an argon atmosphere. A 50 mL ball-milling vessel with 11 mm diameter stainless steel spheres and a ball-to-powder ratio of 30:1 was chosen for the ball-milling procedure, which was carried out by alternating 6 min of milling and 6 min of rest to avoid a temperature

increase for the sample in the vial. The post-milled composites were denoted as C-LB+LA and BM-LB+LA for the samples with and without the addition of carbon scaffolds. In order to prevent contamination with air, all handling and manipulation of the chemicals were performed in argon-filled glove boxes with a recirculation system to keep H_2O and O_2 levels below 1 ppm.

5.2.2 Preparation of nanoconfined complex hydrides in MCs

Selected MCs were firstly activated at 400 $^{\circ}$C in vacuum for several hours in order to remove moisture and gases from the porous matrix. Subsequently, a solution of $LiBH_4$ and $LiAlH_4$ with a molar ratio of 2:1 in THF, which was stirred in advance for 2 h to ensure the homogeneous mixing of raw materials, was added into the MCs. Then, the obtained mixture was sonicated using a SCQ-5201 ultrasonic bath cleaner (500 W, Shanghai Sheng-yan Ultrasound Machines Co., Ltd) for 3 h at around 10 $^{\circ}$C in order to achieve the efficient infiltration of the solution into the nanopores of the MCs via the capillary effect. Finally, the sample was vacuum-dried at 55 $^{\circ}$C for 3 days to remove the solvent completely. Several successive steps of infiltration/vacuum-drying were conducted in order to produce a space-confined nanocomposite with an uploading capacity of approximately 20 wt. %, which was denoted as NP-LB+LA, and, on the other hand, to guarantee high dispersion of the starting materials inside the nanopores of MCs. The scheme for the preparation of the nanoconfined $2LiBH_4$-$LiAlH_4$ composites is shown in Figure 5.1. A mixed solution of $LiBH_4$ and $LiAlH_4$ with a molar ratio of 2:1 in THF was also vacuum-dried under the same conditions as a control sample, which was denoted as VD-LB+LA.

Figure 5. 1 Schematic diagram of the preparation process for nanoconfined $2LiBH_4$-$LiAlH_4$ composites

5.3 Improved hydrogen storage performance of $2LiBH_4$-$LiAlH_4$ composites via nanoconfinement

5.3.1 Synthesis and characterization of as-synthesized nanoconfined $2LiBH_4$-$LiAlH_4$ composite
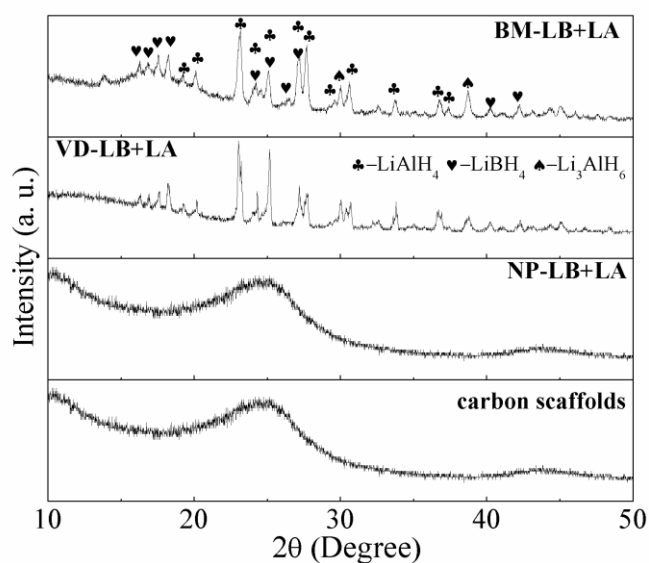
Figure 5. 2 Regular powder XRD results for the ball-milled $2LiBH_4$-$LiAlH_4$ composites (BM-LB+LA), the vacuum-dried $2LiBH_4$-$LiAlH_4$ composites (VD-LB+LA), the nanoconfined composites in carbon scaffolds (NP-LB+LA), and the neat carbon scaffolds.

From the powder X-ray diffraction (XRD) patterns of the as-prepared samples (Figure 5.2), the vacuum-dried $2LiBH_4$-$LiAlH_4$ composite in THF (denoted as VD-LB+LA), without addition of carbon scaffolds, presents comparable peaks, i.e., the characteristic diffraction peaks of $LiBH_4$ and $LiAlH_4$, to the ball-milled $2LiBH_4$-$LiAlH_4$ composite (denoted as BM-LB+LA), indicating the feasibility of this strategy for producing well-distributed binary composites by solvent mediated infiltration. For the control sample of post-milled $2LiBH_4$-$LiAlH_4$ composite with carbon scaffolds, the characteristic peaks assigned to $LiBH_4$ and $LiAlH_4$ dominate the spectra (Figure 5.3a), suggesting that the ball-milling process only induces a physical mixture. However, peaks indexed to $LiBH_4$ and $LiAlH_4$ are absent after infiltration into the MCs (for the sample denoted as NP-LB+LA), which is mainly attributed to the nanoconfinement of the starting materials (Figure 5.3a) and leads to a lack of long-range order for the highly dispersed nanoparticulate materials. Further evidence for the effective infiltration of the composite into the MCs is provided by N_2 adsorption/desorption analysis (Figure 5.4 and Table 5.1), which demonstrates that the total pore volume of the carbon scaffolds decreased from 0.393 cm^3 g^{-1} to 0.032 cm^3 g^{-1} after infiltration, together with a significant reduction of the intensity of the Barrett-Joyner-Hallenda (BJH) pore size distribution, forcefully demonstrating that the $LiBH_4$ and $LiAlH_4$ composite penetrates the pore network of carbon templates and occupies a large fraction of the void space of their mesopores or blocks the pores.
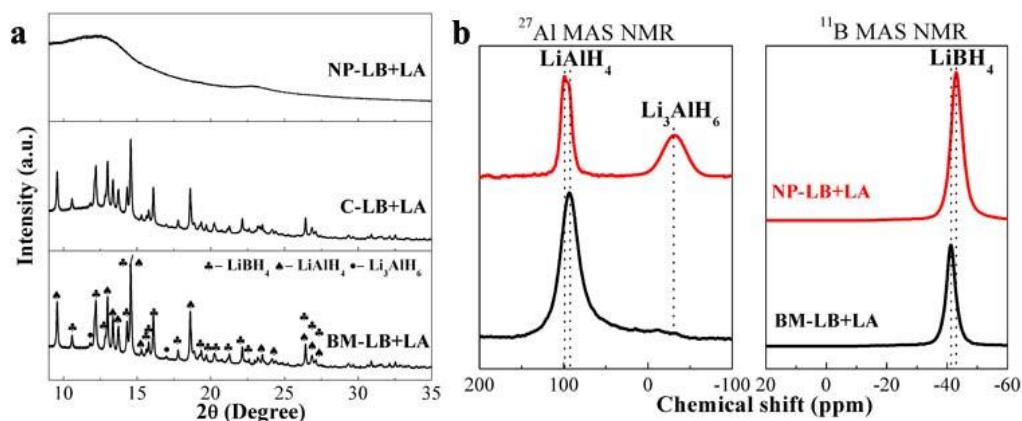
Figure 5. 3 (a) High-resolution XRD profiles and (b) solid-state NMR spectra for the post-milled 2LiBH$_4$-LiAlH$_4$ composites (BM-LB+LA), the post-milled 2LiBH$_4$-LiAlH$_4$ composites with carbon hosts (C-LB+LA), and the nanoconfined 2LiBH$_4$-LiAlH$_4$ composites (NP-LB+LA).
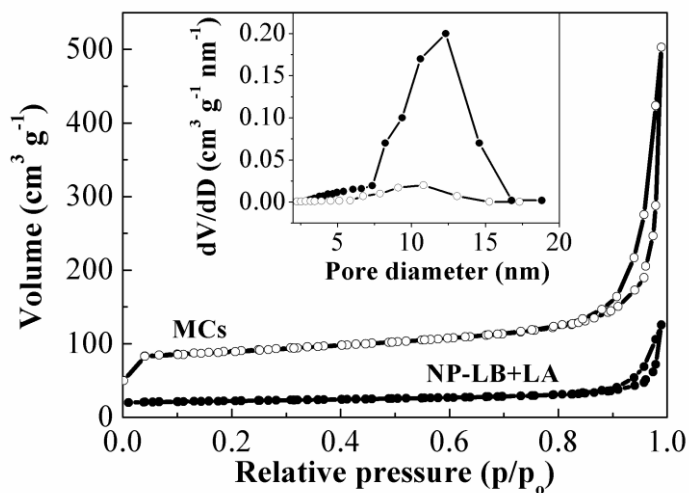
Figure 5. 4 The N$_2$ absorption-desorption isotherms of the mesoporous carbon scaffolds (MCs) and the nanoconfined 2LiBH$_4$-LiAlH$_4$ composites in carbon scaffolds (NP-LB+LA) from the BET results at -196 ^{o}C. The inset shows the corresponding pore size distributions.

Table 5. 1 BET and Langmuir surface areas and the total pore volume of the mesoporous carbon scaffolds with and without loading of $2LiBH_4$-$LiAlH_4$ composites.

Samples	Surface area (m^2 g^{-1})		Total pore volume (cm^3 g^{-1})
	BET	Langmuir	
MCs	235.1	378.5	0.393
NP-LB+LA	15.2	24.7	0.032

Due to the amorphous state of the $2LiBH_4$-$LiAlH_4$ composite when space-confined in the MCs, solid-state nuclear magnetic resonance (NMR), in tandem with the Fourier transform infrared (FTIR) technique, was employed to further characterize the compounds inside the pores of scaffolds. As illustrated in Figure 5.3b, the ^{27}Al MAS NMR spectra show a principal resonance of the AlH_4 group in $LiAlH_4$ at around 93 ppm for the ball-milled composites, in good accordance with the ^{27}Al chemical shift for the four-coordinated Al of $LiAlH_4$ [43]. The peak for the AlH_4 groups in the nanoconfined $LiAlH_4$, however, shows a slight increase in chemical shift compared with its ball-milled counterpart, which was previously detected for $NaAlH_4$ after nanoconfinement in mesoporous carbon, where it was attributed to a higher degree of disorder for Al in $NaAlH_4$ as a result of the close contact with the carbon matrix [44-46]. Moreover, the ^{11}B NMR spectra (Figure 5.3b) reveals the presence of the typical resonances of BH_4 groups centered at -41 ppm for the ball-milled $2LiBH_4$-$LiAlH_4$ composite, while the resonances of BH_4 groups in $LiBH_4$ infiltrated into carbon scaffolds have a roughly 2 ppm shift to the downfield region, which was also observed for a $LiBH_4$-$Mg(BH_4)_2$ mixture after infiltration into carbon mesopores [47]. This may have resulted from a weak interaction of the carbon walls with the boron in the $2LiBH_4$-$LiAlH_4$ composite within the pores of the mesoporous carbon, which is

similar with the observation of NaAlH$_4$ infiltrated into carbon templates as discussed above. These observations also suggest that the bonding characteristics of LiBH$_4$ and LiAlH$_4$ are not greatly changed after infiltration into carbon containers. Furthermore, in addition to the resonance from LiAlH$_4$, a resonance at approximately -30 ppm representing six-coordinated Al in Li$_3$AlH$_6$ was also present in the nanoconfined 2LiBH$_4$-LiAlH$_4$ composites, indicating the decomposition of LiAlH$_4$ during the preparation process, owing to its relatively lower dehydrogenation temperature (as discussed below). Moreover, the presence of characteristic peaks for the BH bonds of LiBH$_4$ and LiAlH, and for the AlH bonds of LiAlH$_4$ and/or Li$_3$AlH$_6$ was further confirmed by FTIR spectra for the space-confined 2LiBH$_4$-LiAlH$_4$ composite in the mesoporous carbon matrix, as shown in Figure 5.5. Additionally, it should be noted that, in the case of NP-LB+LA, the absence of typical peaks for C-H bonds in the range of 2800-3000 cm^{-1} validates the complete removal of solvent (THF), thus eliminating contamination due to the solvent during the decomposition of hydrogen storage materials.
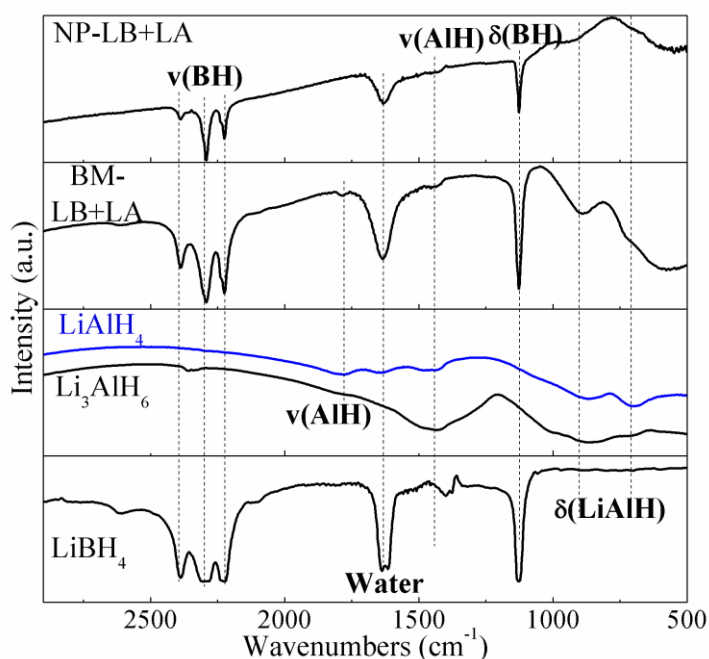
Figure 5. 5 FTIR spectra of the post-milled $2LiBH_4$-$LiAlH_4$ composite (BM-LB+LA) and the nanoconfined composite in carbon scaffolds (NP-LB+LA), with neat $LiAlH_4$, Li_3AlH_6, and $LiBH_4$ included for comparison.

No changes in the surface morphology for the nanoconfined composites before or after dehydrogenation were observed according to the SEM images (Figure 5.6). As shown in Figure 5.7(a), the transmission electron microscope (TEM) images for the pure mesoporous carbon reveal no long-range pore ordering. The short diffusion paths may promote the uniform distribution of active substrates, i.e., the mixed solution of $LiBH_4$ and $LiAlH_4$ inside the carbon supports after vacuum-drying, as evidenced by the TEM images for the nanoconfined $2LiBH_4$-$LiAlH_4$ composite before and after dehydrogenation, where no aggregation was observed (Figure 5.7(b, c)). In addition, the energy dispersive spectroscopy (EDS) elemental map of C coincides well with those of B, Li, and Al from the active substrates for the nanoconfined compounds before and after dehydrogenation (Figure 5.8, Figure 5.7(d)), which also substantiates the homogeneous incorporation of $2LiBH_4$-$LiAlH_4$ composite into the carbon matrix. The fact that the pore structure of the MCs remains unchanged and no agglomeration was observed for the nanoconfined samples after dehydrogenation to 450 ^{o}C clearly demonstrates the space-confining effects of the carbon containers on the $2LiBH_4$-$LiAlH_4$ composite inside their mesopores during the reversible hydrogen storage cycling measurements, resulting in no phase separation and no aggregation during the H_2 release and uptake.
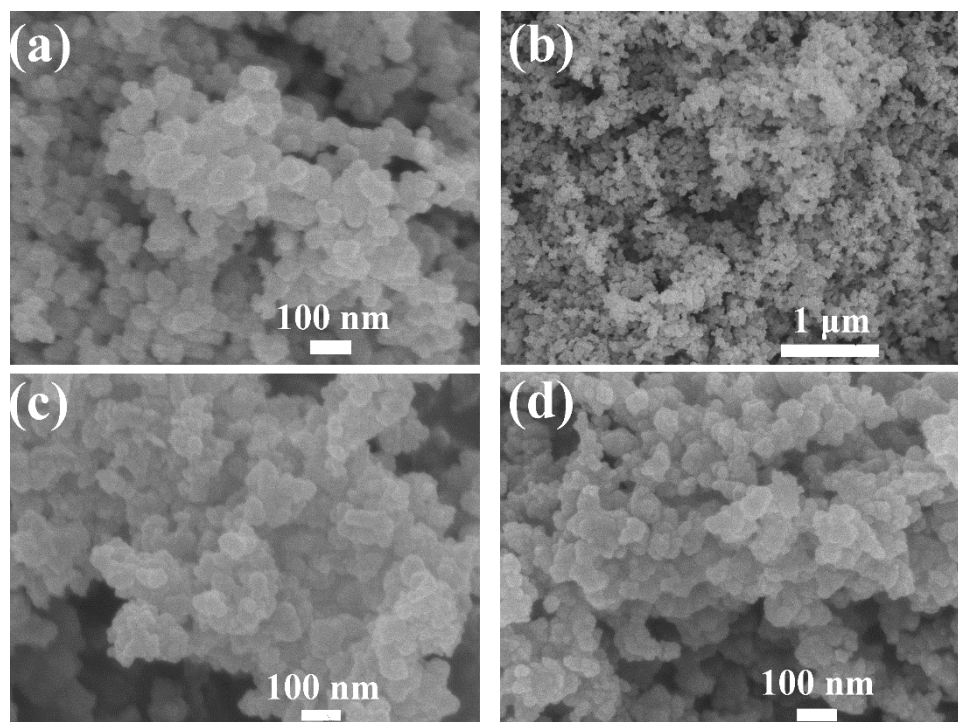
Figure 5. 6 SEM images of (a) pure carbon scaffolds and the nanoconfined 2LiBH$_4$-

LiAlH$_4$ composite before (b, c) and after (d) dehydrogenation.
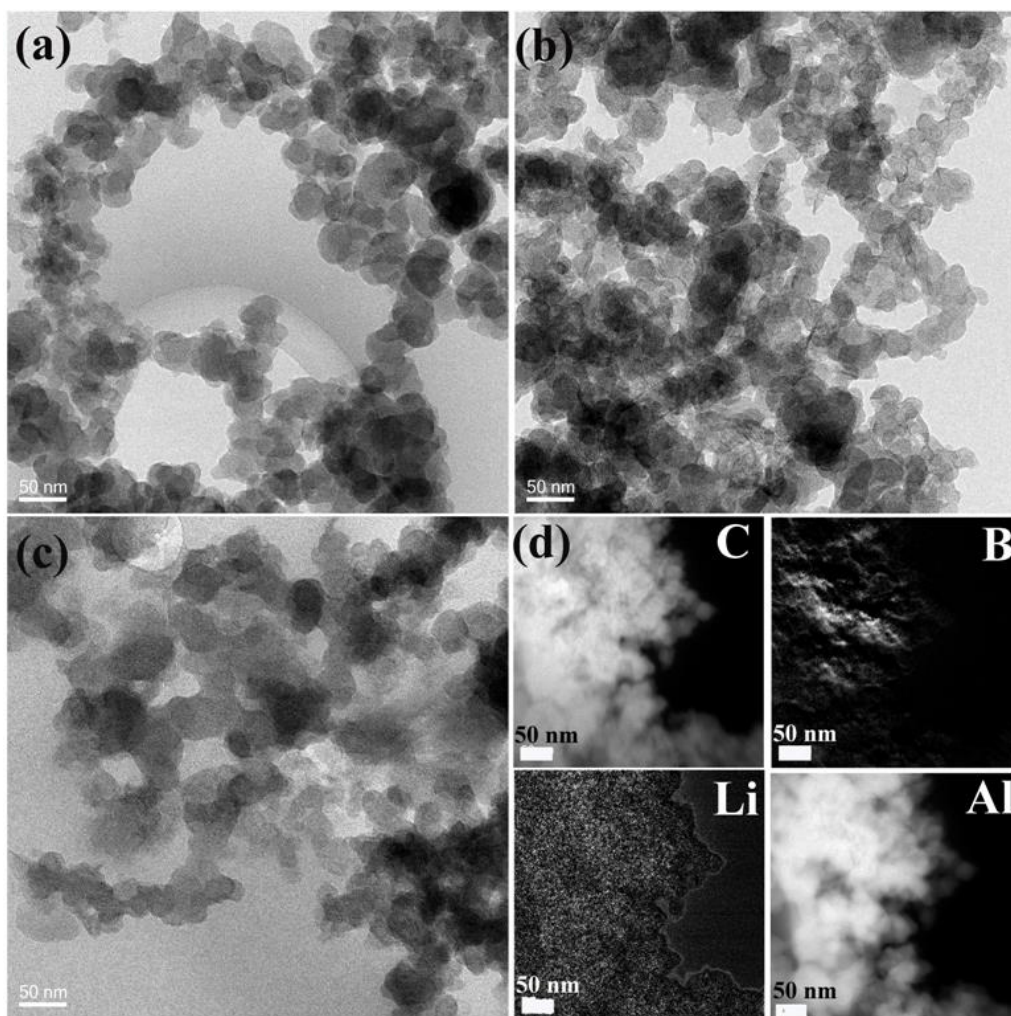
Figure 5. 7 High-resolution TEM images of (a) pure carbon scaffolds and the

nanoconfined $2LiBH_4$-$LiAlH_4$ composite before (b) and after (c) dehydrogenation.

(d) EDS maps of C, B, Li, and Al for the nanoconfined $2LiBH_4$-$LiAlH_4$ after

dehydrogenation to 450 $^{\circ}$C.
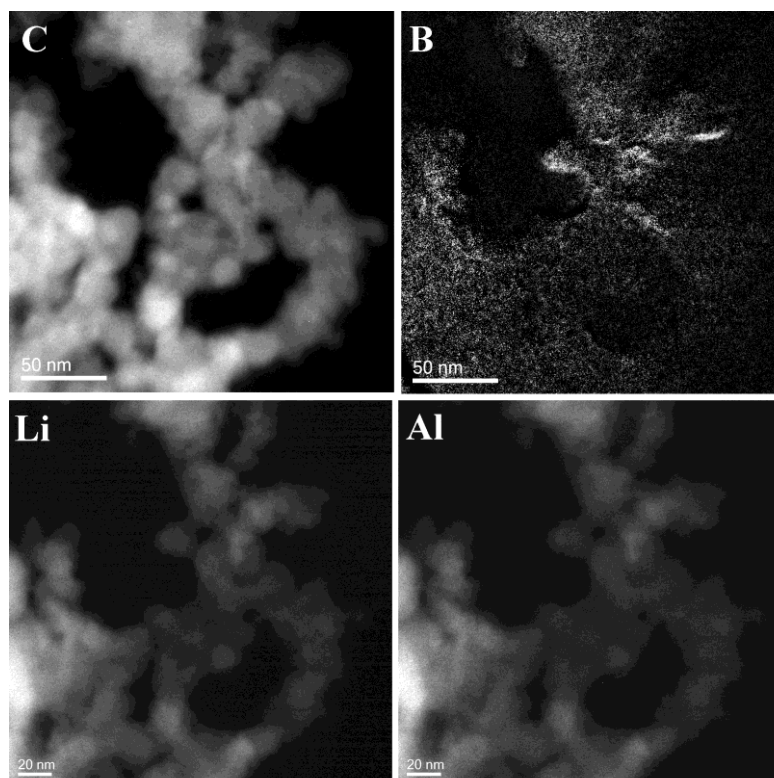
Figure 5. 8 EDS maps of C for the nanoconfined 2LiBH₄-LiAlH₄ composite from the TEM image and the corresponding EDS maps of B, Li, and Al before dehydrogenation.

5.3.2 H_2 desorption properties of nanoconfined 2LiBH₄-LiAlH₄ composite

Comparison of the hydrogen release behavior of BM-LD+LA, VD-LD+LA, and NP-LB+LA, in tandem with the post-milled 2LiBH₄-LiAlH₄/carbon composite with a weight ratio of 4:1, denoted as C-LB+LA, was conducted using volumetric temperature programmed desorption (TPD), together with mass spectrometry (MS) (Figure 5.9). For the BM-LB+LA, a two-step dehydrogenation is obviously present. The first step with onset dehydrogenation just above 120 $^{\circ}$C corresponds to the decomposition of LiAlH₄. The second step just above 375 $^{\circ}$C is attributed to the decomposition of LiBH₄ under the destabilizing influence of Al, one of the products formed from the decomposition of LiAlH₄. These results agree well with a previous

report in the literature [14]. In the case of the VD-LB+LA, H_2 liberation from the decomposition of $LiBH_4$ exhibits enhanced kinetics in comparison with the ball-milled composite. This difference may originate from both the intimate interaction of $LiAlH_4$ with $LiBH_4$ and the size-mediated effect, which relates to the fact that the direct precipitation from homogeneous liquid phase may result in homogeneous distribution of the starting materials, in analogy to the superior hydrogen release performance of MgH_2 from dibutylmagnesium in heptane compared to bulk MgH_2 [48]. As for the C-LB+LA, the dehydrogenation of Al-destabilized $LiBH_4$ starts at around 325 ^{o}C, which is approximately 50 ^{o}C lower than for the sample without addition of carbon scaffolds. This is due to the catalytic effect of the carbon matrix on the H_2 desorption properties of $LiBH_4$, in accordance with a previous report in the literature [35]. With respect to the NP-LB+LA, H_2 desorption starts at ~80 ^{o}C for $LiAlH_4$ and ~230 ^{o}C for $LiBH_4$, with a reduction of 40 ^{o}C and 145 ^{o}C, respectively, compared with its bulk counterpart. Additionally, the H_2 liberation process of the space-confined composite is complete before 400 ^{o}C, with a total weight loss of approximately 2.4 wt. % for the 1st step from $LiAlH_4$ and ~7.4 wt. % for the 2nd step from $LiBH_4$, which accounts for around 65% and 100% of the theoretical capacity of releasable hydrogen over the 1st and 2nd step decomposition, respectively. Apparently, due to the relatively low temperature for H_2 desorption from nanostructured $LiAlH_4$, H_2 tends to evolve during the vacuum-drying process for the removal of THF, as evidenced by the appearance of six-coordinated Al in Li_3AlH_6 in the ^{27}Al MAS NMR spectra (Figure 5.3b). In contrast, only ~9.3 wt. % H_2 is released, even with further heating to 500 ^{o}C, for the post-milled composite. Moreover, as evidenced by the mass spectroscopy (MS) spectra (Figure 5.9), the evolution of diborane was observed for the post-milled and vacuum-dried 2LiBH$_4$-LiAlH$_4$ composites, which may be due to the possible decomposition of $LiBH_4$, which

cannot react with the thus-formed Al, while there is no measureable release of diborane for the nanoconfined composite. This indicates that the uniform distribution and the nanoconfinement of $2LiBH_4$-$LiAlH_4$ composites can effectively prevent the loss of B due to the liberation of volatile B_2H_6 upon dehydrogenation, and thus enhance the hydrogen storage properties under cycling.
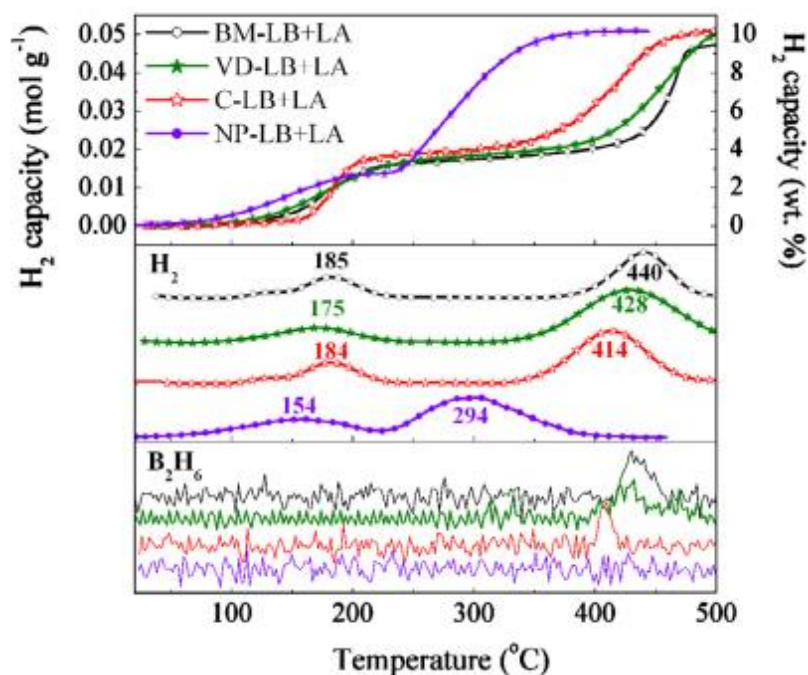
Figure 5. 9 TPD and MS results for the post-milled $2LiBH_4$-$LiAlH_4$ composite (BM-LB+LA), vacuum-dried $2LiBH_4$-$LiAlH_4$ composite (VD-LB+LA), post-milled $2LiBH_4$-$LiAlH_4$ composite with carbon host (C-LB+LA), and nanoconfined $2LiBH_4$-$LiAlH_4$ composite (NP-LB+LA).

Theoretical calculations reveal that the chemical reactivity of nanocrystals is positively correlated with a large surface area and short diffusion path of hydrogen [49-51]. Therefore, the H_2 desorption capacity of nanoconfined $2LiBH_4$-$LiAlH_4$ composite was further measured in comparison with its bulk counterpart (Figures 5.10 and 11). Apparently, the two-step decomposition stages can be distinguished in the isothermal curves of the nanoconfined $2LiBH_4$-$LiAlH_4$ composite (inset in Figure 5.10(a)),

corresponding to the rapid dehydrogenation of LiAlH$_4$ and the relatively slow decomposition of LiBH$_4$ destabilized by the thus-produced Al, respectively. For the post-milled sample, only 4 wt. % H$_2$, mainly attributable to the decomposition of LiAlH$_4$, according to the TPD results (Figure 5.9), was released within 300 min, even at 350 °C. In contrast, for the space-confined 2LiBH$_4$-LiAlH$_4$ composite, the value reaches ~8.2 wt. % at 250 °C, and further increases to ~9.3, 9.9, and 10.0 wt. % at temperatures of 275, 300, and 350 °C, respectively, over the same period of 300 min, exhibiting a significant improvement in the H$_2$ release kinetics in comparison with its bulk counterpart. To quantitatively estimate the enhancement of kinetics for dehydrogenation, the apparent activation energy from Arrhenius analysis based on the curves of H$_2$ desorption at different temperatures (Figure 5.10(b)) was determined. From the slope of the linear plot of ln k (k, rate constant) versus 1/T (T, absolute temperature), the activation energy (E$_a$) for H$_2$ evolution from LiBH$_4$ destabilized by Al was verified to be 90.0 kJ mol^{-1}, comparable to that of post-milled 2LiBH$_4$-Al (94 kJ mol^{-1}) [52]. A considerable reduction in E$_a$, i.e., 41.3 kJ mol^{-1}, was established for the nanoconfined 2LiBH$_4$-LiAlH$_4$ composite, however, compared to its bulk counterpart.
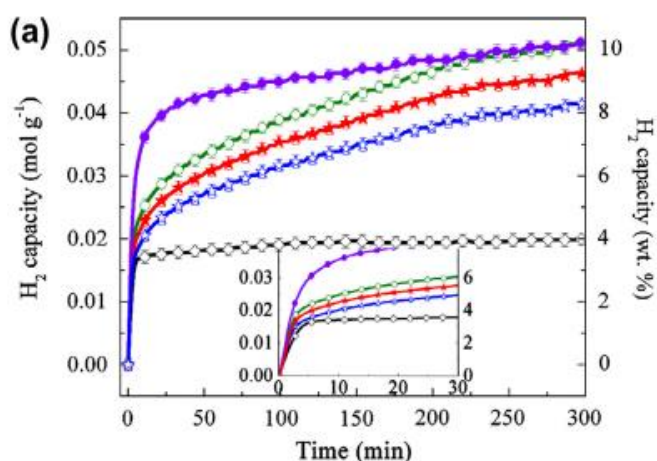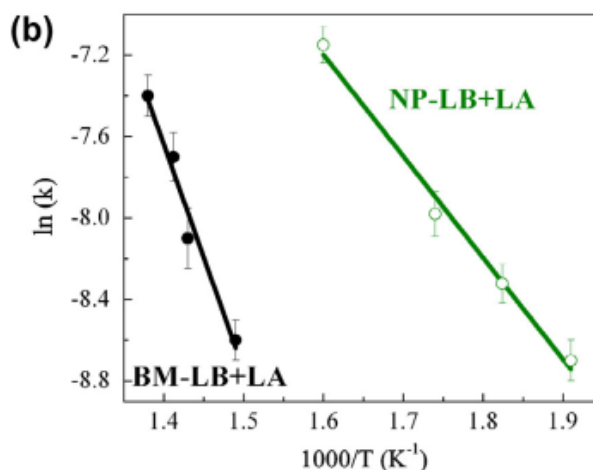
Figure 5. 10 (a) Isothermal H_2 release of the nanoconfined 2LiBH$_4$-LiAlH$_4$ composite at the temperature of 250 ^{o}C (☆), 275 ^{o}C (★), 300 ^{o}C (○), and 350 ^{o}C (●), including the post-milled 2LiBH$_4$-LiAlH$_4$ composite at 350 ^{o}C (◇) for comparison. The inset is an enlargement of (a) for dehydrogenation time from 0 to 30 min. (b) Arrhenius plots of the temperature-dependent rate data for the post-milled and nanoconfined 2LiBH$_4$-LiAlH$_4$ composites.
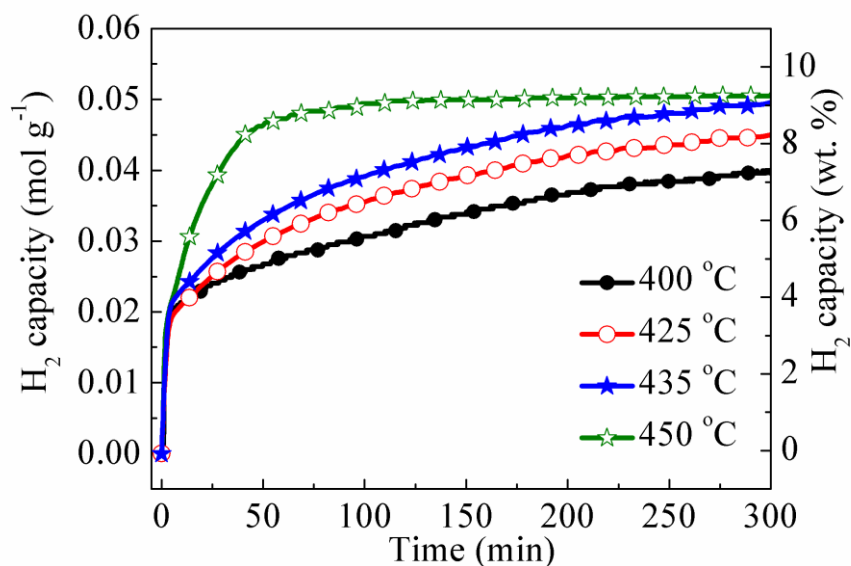
Figure 5. 11 Isothermal H_2 release of the post-milled 2LiBH$_4$-LiAlH$_4$ composite at various temperatures.

5.3.3 Reversible hydrogen storage performance of nanoconfined $2LiBH_4$-$LiAlH_4$ composite

Subsequently, the H_2 release and uptake cycling performance of the post-milled, vacuum-dried, and nanoconfined $2LiBH_4$-$LiAlH_4$ composites were investigated in order to evaluate the effects of nanoconfinement on the reversibility of the $2LiBH_4$-$LiAlH_4$ composites. As shown in Figure 5.12(a), the amount of H_2 released from the BM-LB+LA significantly decreased upon successive dehydrogenation/hydrogenation treatments, from 9.4 wt. % to only 1.2 wt. % for the 5th desorption cycle, which only accounts for 12.6% of the initial desorption capacity. In the case of the VD-LB+LA (Figure 5.12(b)), upon consecutive H_2 uptake/release cycles, although a considerable improvement of the dehydrogenation properties is observed compared with the post-milled composite, the capacity is still decreased from 10.0 wt. % for the 1st cycle to 2.4 wt. % for the 5th cycle. The significant degradation upon cycling for the ball-milled and vacuum-dried $2LiBH_4$-$LiAlH_4$ composites is ascribed to the liberation of diborane and the persistent aggregation of dehydrogenated products during heat treatment, in which the former may lead to the loss of B species and the formation of very stable $Li_2B_{12}H_{12}$, as shown in the FTIR spectra (Figure 5.13), which will reduce the reversible capacity of $LiBH_4$ at each cycle [27]; and the latter may cause slower kinetics for H_2 uptake due to the longer diffusion pathways for H_2.[37] By contrast, for the nanoconfined $2LiBH_4$-$LiAlH_4$ composite, except for a capacity decrease from 10.0 wt. % for the 1st cycle to 8.5 wt. % for the 2nd cycle, no further degradation is observed for the following cycles. The solid-state NMR spectra in Figure 5.14 confirm the presence of Li_3AlH_6 and $LiBH_4$ in the hydrogenated products after the 5th and 7th cycles of H_2 absorption. In addition, both the B-H bonds of $LiBH_4$, and the Al-H and/or LiAl-H bonds are also recovered after hydrogenation of the decomposed products, based on

the FTIR spectra (Figure 5.15), which also indicates the successful regeneration of Li_3AlH_6 and $LiBH_4$. It is noteworthy that in this study, the rehydrogenation of Li_3AlH_6 from the as-formed LiH and Al in the nanoconfined $2LiBH_4$-$LiAlH_4$ composite was realized under 10 MPa H_2 without the addition of any metal based catalyst [53,54], while rehydrogenation failed in the ball-milled and vacuum-dried systems (Figure 5.12(a, b)). Obviously, the thermodynamically irreversible hydrogenation of $LiAlH_4$ from Li_3AlH_6 in a practically accessible temperature and hydrogen pressure range [55] contributes to the H_2 capacity degradation of the 2nd dehydrogenation cycle. Based on the above analysis, the reversible reaction of the nanoconfined $2LiBH_4$-$LiAlH_4$ composite from the 2nd cycle can be ascribed to the reversible formation of Li_3AlH_6 and $LiBH_4$.
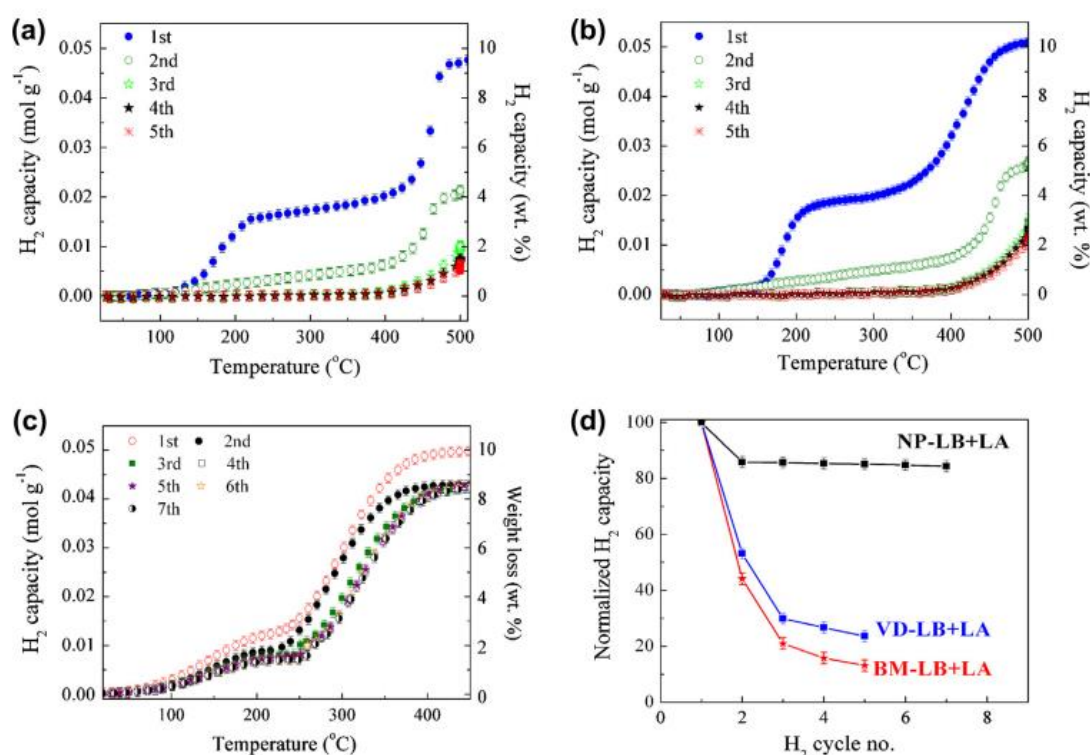
Figure 5. 12 Evolution of consecutive H_2 desorption curves: five cycles for the ball-milled (a) and vacuum-dried (b) composites; (c) seven cycles for the nanoconfined $2LiBH_4$-$LiAlH_4$ composite; and (d) normalized H_2 capacity as a function of cycle

number for the post-milled, vacuum-dried, and nanoconfined 2LiBH₄-LiAlH₄ composites, respectively.
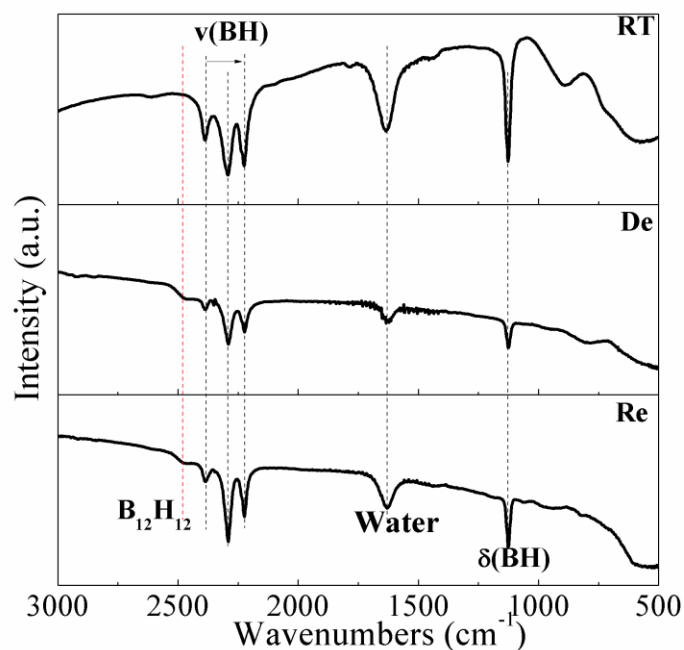
Figure 5. 13 FTIR spectra for the freshly prepared ball-milled 2LiBH₄-LiAlH₄ composite after ball milling (RT), dehydrogenation to 500 °C (De), and 1ˢᵗ rehydrogenation cycle (Re).
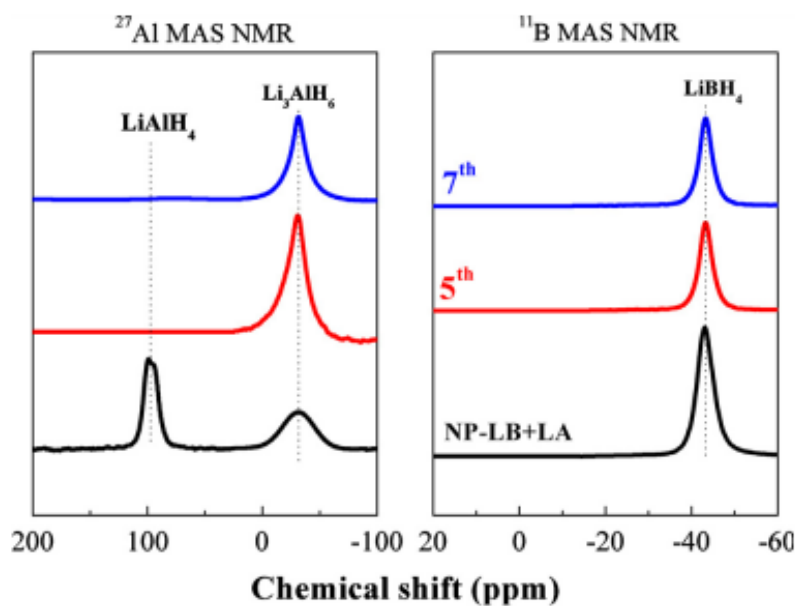
Figure 5. 14 Solid-state NMR spectra of the the freshly-prepared nanoconfined 2LiBH$_4$-LiAlH$_4$ composite (NP-LB+LA), and its rehydrogenated products after five and seven absorption cycles.
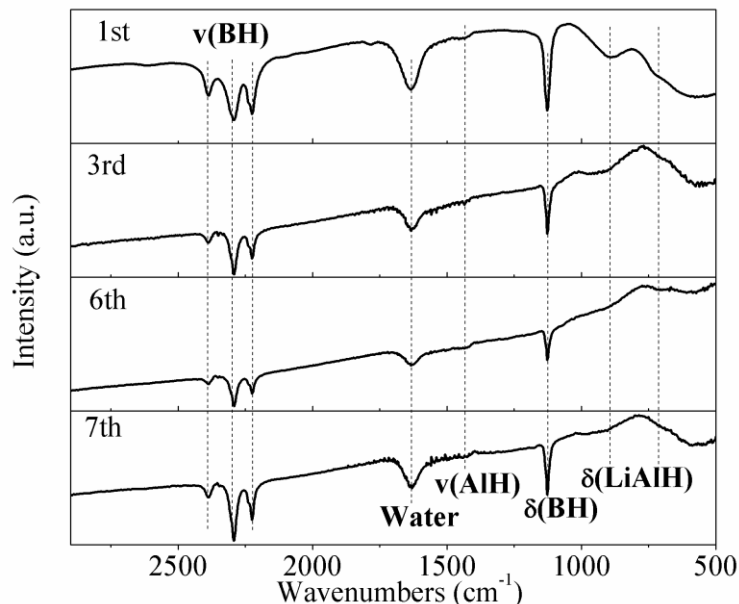
Figure 5. 15 FTIR spectra of the rehydrogenated products of the nanoconfined 2LiBH$_4$-LiAlH$_4$ composite after various H$_2$ absorption cycles.

According to the normalized hydrogen capacity as a function of the cycling number (Figure 5.12(d)), the capacity retention for the nanoconfined 2LiBH$_4$-LiAlH$_4$ composite is still in excess of 84% after 7 cycles of H$_2$ desorption/re-absorption, and notably, the weight retention from the 2nd to the 7th desorption is even over 98%, while weight retentions lower than 15% and 24% were observed for the ball-milled and vacuum-dried composites, even after only 5 cycles. These results clearly confirm that the reversible H$_2$ ab-/de-sorption performance in terms of the capacity retention and kinetics of the 2LiBH$_4$-LiAlH$_4$ composites is remarkably improved via co-infiltration into the mesoporous carbon hosts. It can be deduced that the synergetic effects between the nanoconfinement and the thermodynamic destabilization are what mainly contribute to the improved cyclic behavior of 2LiBH$_4$-LiAlH$_4$. Besides, it should be

pointed out that the extra LiH also plays a positive role in enhancing the reversibility of the nanoconfined LiBH$_4$, as evidenced by a previous report in the literature [41]; therefore, the de-/re-hydrogenation of the nanoconfined composite can be surprisingly improved by taking advantage of the LiH formed in situ, which is derived from the decomposition of LiAlH$_4$ in the 1st desorption cycle and effectively promotes enduring cycling performance. Nonetheless, during the cyclic H$_2$ hydriding/dehydriding process, the onset temperature for the main decomposition of LiBH$_4$ slightly shifts to higher temperature (Figure 5.12(c)) as a result of the phase agglomeration of reactants and/or products, although under the spatial limitation of the carbon scaffolds, which is also observed in the cyclic performance of most of the other nanoconfined complex hydrides [42,56,57].

5.3.4   Hydrogen storage mechanism of nanoconfined 2LiBH$_4$-LiAlH$_4$ composite

In further investigation of the effects of nanoconfinement on the significantly improved H$_2$ ab-/de-sorption behavior of the 2LiBH$_4$-LiAlH$_4$ composite, X-ray diffraction was employed to monitor the phase transition during dehydrogenation. As shown in Figure 5.16(a), after dehydrogenation to 260 $^{\circ}$C, the resultant products in the ball-milled 2LiBH$_4$-LiAlH$_4$ composite were mainly composed of LiBH$_4$, Al, and LiH, while the diffraction peaks of LiAlH$_4$ and Li$_3$AlH$_6$ disappeared, indicating the decomposition of LiAlH$_4$ to LiH and Al in the 1st step of dehydrogenation. On further elevating the operating temperature to 500 $^{\circ}$C, the LiBH$_4$ phase vanished, which was accompanied by the weakening of Al and the appearance of AlB$_2$ phase, suggesting that dehydrogenation had proceeded according to Eq. (5.4). The presence of Al in the dehydrogenated products suggests the incomplete formation of AlB$_2$ due to the poor kinetics for the desired destabilized reaction, which agrees well with previous observations [16, 17, 52]. The simultaneous presence of Al and AlB$_2$ was also verified by

the XPS spectra (Figure 5.17(b)), further demonstrating the fact of only partial transformation of Al into AlB_2 upon reaction with $LiBH_4$, resulting in the formation of residual amorphous B in the dehydrogenated products, which significantly degrades the hydrogen capacity under cycling due to the harsh conditions for the regeneration of $LiBH_4$ from amorphous B and LiH [3]. Additionally, the incomplete reaction between Al and B also gives rise to the decomposition of individual $LiBH_4$ particles, leading to the liberation of diborane (Figure 5.9) and the formation of stable $Li_2B_{12}H_{12}$ (Figure 5.13), which further increases the loss of B species and thus decreases the hydriding capacity during consecutive H_2 release and uptake cycles. It is worth noting that upon dehydrogenation to 500 °C, more AlB_2 is yielded in the vacuum-dried $2LiBH_4$-$LiAlH_4$ composite compared with the ball-milled sample, as inferred from the intensity of the relative characteristic peaks in the XRD spectra (Figure 5.18). This may be due to the uniform distribution of $LiBH_4$ and $LiAlH_4$ after vacuum-drying from the homogenous solution in comparison with the mechanical ball-milling process, which leads to the homogeneous dispersion of the thus-formed Al in the matrix of $LiBH_4$, and accordingly, accounts for the advantageous formation of AlB_2 and less liberation of B_2H_6 during dehydrogenation.

$$2\ LiBH_4 + LiAlH_4 \rightarrow 2\ LiBH_4 + LiH + Al + 3/2\ H_2 \quad (5.4)$$

$$2\ LiBH_4 + LiH + Al \rightarrow 3\ LiH + (x)\ Al + (1-x)\ AlB_2 + (2x)\ B + 3\ H_2\ (x < 1) \quad (5.5)$$

$$2\ LiBH_4 + 1/3\ Li_3AlH_6 + 2/3\ Al \Leftrightarrow 3\ LiH + AlB_2 + 3.5\ H_2 \quad (5.6)$$
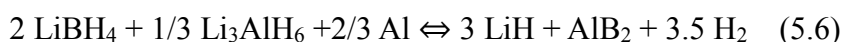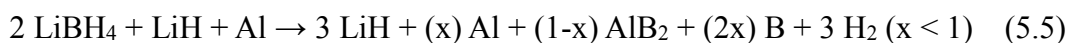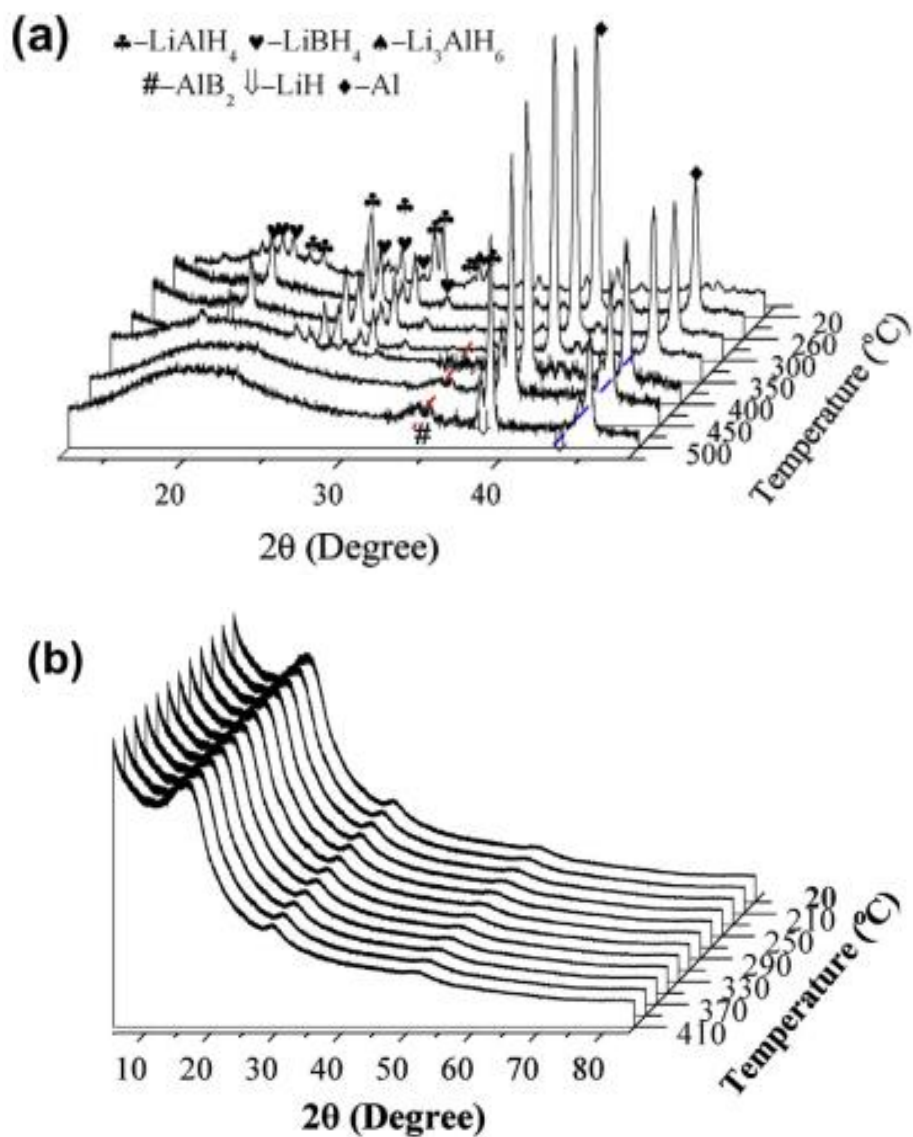
Figure 5. 16 (a) XRD spectra of the ball-milled 2LiBH$_4$-LiAlH$_4$ composite at various temperatures, and (b) high-resolution XRD spectra of the nanoconfined 2LiBH$_4$-LiAlH$_4$ composite upon heating to various temperatures.
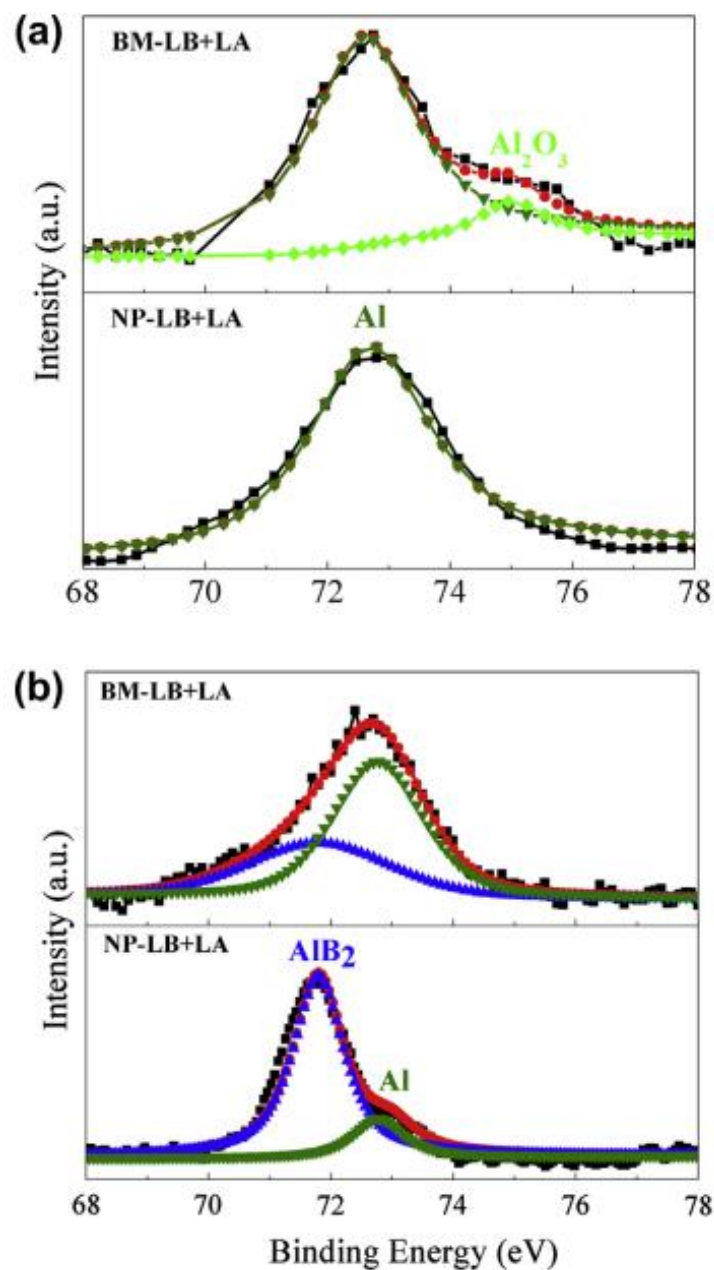
Figure 5. 17 Al 2p XPS spectra (error within 0.2 eV) of the dehydrogenated products of the ball-milled (BM-LB+LA) and nanoconfined $2LiBH_4$-$LiAlH_4$ (NP-LB+LA) composites after (a) the 1st and (b) the 2nd step decomposition, respectively.
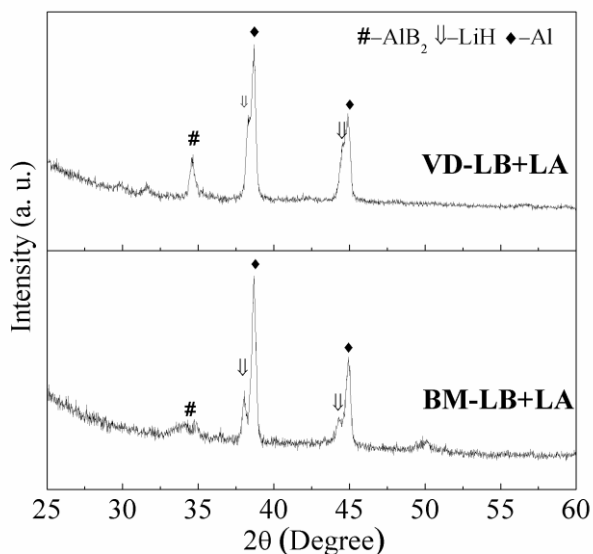
Figure 5. 18 XRD patterns of the dehydrogenated products of the post-milled (BM-LB+LA) and vacuum-dried (VD-LB+LA) $2LiBH_4$-$LiAlH_4$ composites after dehydrogenation to 500 °C.

Nevertheless, in contrast to the post-milled and vacuum-dried $2LiBH_4$-$LiAlH_4$ composites, diffraction peaks assigned to all the possible products are absent in the NP-LB+LA upon heating from room temperature to 400 °C, indirectly indicating the good distribution of the compounds in the mesopores, as observed in the TEM results (Figure 5.7(d)). The amorphous state of the nanoconfined composite directly demonstrates the lack of long-range order after infiltration, possibly due to small pore spaces available. Therefore, with the aim of unraveling the mechanism for the improvement of the hydrogen release properties due to the presence of carbon scaffolds, further efforts are required to investigate the effects of nanoconfinement on the decomposition pathways of $2LiBH_4$-$LiAlH_4$ composites. Upon heating to approximately 210 °C, as expected from Eq. (5.4), the characteristic peak of Al (Figure 5.17(a)) emerged from the XPS spectra, in tandem with the disappearance of $LiAlH_4$ and Li_3AlH_6 from the FTIR spectra (Figure 5.19). Meanwhile, the presence of the relevant B-H bonds of $LiBH_4$ remains unchanged. This result indicates that the 1st

dehydrogenation of NP-LB+LA also corresponds to the decomposition of LiAlH$_4$, as suggested in Eq. (5.4), which is analogous to the hydrogen release reaction of its bulk counterpart. In regards to the 2nd step decomposition, the H$_2$ evolution stems from the dehydrogenation of LiBH$_4$ that is destabilized by the as-formed Al from the 1st step dehydrogenation, which is directly verified by the complete disappearance of B-H bonds from the FTIR spectra (Figure 5.19) of the nanoconfined 2LiBH$_4$-LiAlH$_4$ composite after heating to 400 ^{o}C. By contrast, the presence of B-H bonds (Figure 5.13) belonging to LiBH$_4$ is still detected for the post-milled 2LiBH$_4$-LiAlH$_4$ composite, even after heating to 500 ^{o}C, further indicating the much slower kinetics for H$_2$ release compared with the nanoconfined composite. Additionally, the XPS data show the appearance of the characteristic peaks of Al and AlB$_2$ in the dehydrogenated products on heating to 400 ^{o}C, which is similar to the case of the bulk composite. However, the molar ratio of AlB$_2$ to Al in the dehydrogenated products of the nanoconfined 2LiBH$_4$-LiAlH$_4$ composite on heating to 400 ^{o}C, as inferred from the intensity of the corresponding resonances from the XPS spectra, is very much higher (>20 times) than for the bulk sample. This indicates that the formation of AlB$_2$ is favored in the nanoconfined sample due to the reduction of both reaction and diffusion pathways across the reactive interfaces of the as-formed AlB$_2$, which are required for B-containing species to react with the Al inside along with the hydrogen release. On the other hand, the homogeneous distribution of LiBH$_4$ and LiAlH$_4$ inside the mesopores of carbon supports that were vacuum-dried from the solution also facilitates the heterogeneous solid-state reaction towards the formation of AlB$_2$, as discussed above. The almost complete transformation of Al and B into AlB$_2$, which avoids the loss of boron to the formation of stable Li$_2$B$_{12}$H$_{12}$ during cycling, coincides with the fact that no measurable diborane was released during the dehydrogenation of the NP-LB+LA.

Furthermore, both the NMR spectra (Figure 5.14) and the FTIR spectra (Figures 5.13 and 5.15) confirm the absence of $Li_2B_{12}H_{12}$ in the rehydrogenated and dehydrogenated products, which confirms that the nanoconfinement can effectively prevent the possible loss of reversible H_2 capacity. Therefore, the reversible reaction for nanostructured Li_3AlH_6 and $LiBH_4$ proceeds according to Eq. (5.6), with a theoretical H_2 capacity of 8.8 wt. %, which corresponds well with the experimental results. Based on the above-mentioned analysis, the reasons for the significant improvement of the hydrogen storage properties of $2LiBH_4$-$LiAlH_4$ via nanoconfinement in MCs can be summarized as follows: (i) the thermodynamic destabilization of $LiBH_4$ by Al through the formation of AlB_2 instead of the stable $Li_2B_{12}H_{12}$ can effectively facilitate the reversibility of the hydrogen sorption, since the activation energy to break a metal-B bond is significantly lower than for a B-B bond [58]; (ii) the nanoconfinement leads to a low mean coordination number of surface atoms, and thus an excess of surface energy, which then results in a modification of the thermodynamics parameters, i.e., enthalpy and entropy, towards enhanced hydrogen storage properties [59,60]; (iii) the decrease in particle size can lead to nanoscale diffusion distances for pulling H_2 into and out of the nanoconfined active substrates, thereby leading to the significantly improved H-exchange kinetics [49]; and (iv) the in-situ formed LiH from the 1st desorption of $LiAlH_4$ can effectively resolve the possible loss of reactive alkali metal species due to the reaction with impurities during the cyclic heating treatment [41]. As a result, the cyclic stability of the $2LiBH_4$-$LiAlH_4$ composite after co-infiltration under the structure-directing effects of MCs, which further results in favorable thermodynamics and kinetics towards H_2 ab-/de-sorption, is, thereby, significantly improved.
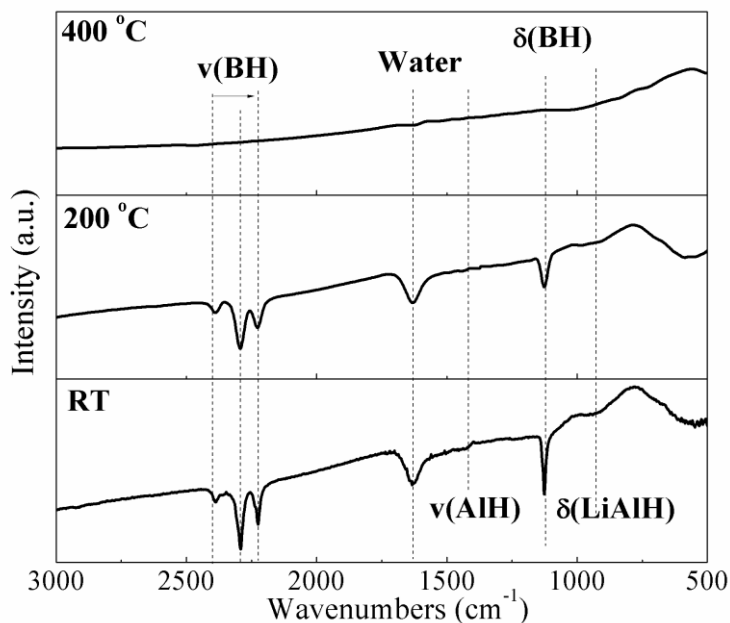
Figure 5. 19 FTIR spectra of the dehydrogenated products of the nanoconfined

2LiBH$_4$-LiAlH$_4$ composite after dehydrogenation to various temperatures.

5.4 Conclusion

In summary, the hydrogen storage properties of the nanoconfined 2LiBH$_4$-LiAlH$_4$

composite were systematically studied. After infiltration of uniformly distributed

2LiBH$_4$-LiAlH$_4$ composite into carbon scaffolds, the onset dehydrogenation

temperature of LiAlH$_4$ and Al-destabilized LiBH$_4$ was significantly decreased to 80

and 230 °C, respectively. The favorable synergetic coupling of both nanoconfinement

effects and thermodynamic destabilization effectively facilitates the H$_2$ release

performance, leading to a reduction of 41.3 kJ mol^{-1} in apparent activation energy for

the Al-destabilized LiBH$_4$ in the nanoconfined 2LiBH$_4$-LiAlH$_4$ composite compared

with the post-milled composite. More importantly, the promotion by nanoconfinement

of the favorable formation of AlB$_2$ is identified for the well-distributed 2LiBH$_4$-

LiAlH$_4$ composite as due to the short diffusion pathways, which further effectively

prevent the liberation of diborane and the subsequent formation of $Li_2B_{12}H_{12}$ during dehydrogenation. Based on the combined action of the above-mentioned effects, in tandem with the presence of the nanoscale LiH formed in situ, the nanoconfined composite shows a high degree of regeneration, without degradation from the 2nd to the 7th cycle. Obviously, these advances give the nanoconfined $2LiBH_4$-$LiAlH_4$ composite advantages as an alternative practical hydrogen storage material. Moreover, our results yield interesting clues towards the further improvement of the binary hydrogen storage system, i.e., $LiBH_4$ and $LiAlH_4$, including the adoption of functional porous materials as templates and/or the optimization of the pore sizes and structures of templates. More issues, however, especially with respect to increased uploading capacity, still need to be addressed before its commercialization as a hydrogen carrier.

5.5 References

[1] S. Orimo, Y. Nakamori, G. Kitahara, K. Miwa, S. Ohba, A. Züttel. *Journal of Alloys and Compounds* **2005**, *427*, 404-406.

[2] A. Züttel, P. Wenger, S. Rentsch, P. Sudan, P. Mauron, C. Emmenegger. *Journal of Power Sources* **2003**, *1*, 118.

[3] P. Mauro, F. Buchter, O. Friedrichs, A. Remhof, M. Bielmann, CN. Zwicky, A. Züttel. *The Journal of Physical Chemistry B* **2007**, *112*, 906.

[4] J. J. Vajo, SL. Olson. *Scripta Materialia* **2007**, *56*, 829.

[5] U. Bösenberg, S. Doppiu, L. Mosegaard, G. Barkhordarian, N. Eigen, A. Borgschulte, TR. Jensen, Y. Cerenius, O. Gutfleisch, T. Klassen, M. Dornheim, R. Bormann. *Acta Materialia* **2007**, *55*, 3951.

[6] XB. Yu, DM. Grant, GS. Walker. *Chem Commun* **2006**, 3906.

[7] XB. Yu, Z. Wu, QR. Chen, ZL. Li, BC. Weng, TS. Huang. *Applied Physics Letters* **2007**, *90*, 034106.

[8] JJ. Vajo, SL. Skeith, F. Mertens. *The Journal of Physical Chemistry B* **2005**, *109*, 3719.

[9] YW. Cho, J-H. Shim, B-J. Lee. *Calphad - Computer Coupling of Phase Diagrams and Thermochemistry* **2006**, *30*, 65.

[10] FE. Pinkerton, MS. Meyer, GP. Meisner, MP. Balogh, JJ. Vajo. *The Journal of Physical Chemistry C* **2007**, *111*, 12881.

[11] LL. Shaw, X. Wan, JZ. Hu, JH. Kwak, Z. Yang. *The Journal of Physical Chemistry C* **2010**, *114*, 8089.

[12] XD. Kang, P. Wang, LP. Ma, HM. Cheng. *Applied Physics A: Materials Science & Processing* **2007**, *89*, 963.

[13] J. Yang, A. Sudik, C. Wolverton. *The Journal of Physical Chemistry C* **2007**, *111*, 19134.

[14] SA. Jin, JH. Shim, YW. Cho, KW. Yi, O. Zabara, M. Fichtner. *Scripta Materialia* **2008**, *58*, 963.

[15] O. Friedrichs, JW. Kim, A. Remhof, F. Buchter, A. Borgschulte, D. Wallacher, YW. Cho, M. Fichtner, KH. Oh, A. Züttel. *Physical Chemistry Chemical Physics* **2009**, *11*, 1515.

[16] Choi YJ, Lu J, Sohn HY, Fang ZZ. *The Journal of Physical Chemistry C* **2011**, *115*, 6040.

[17] Meggouh M, Grant DM, Walker GS. *The Journal of Physical Chemistry C* **2011**, *115*, 22054.

[18] Remhof A, Friedrichs O, Buchter F, Mauron P, Kim JW, Oh KH, Buchsteiner A, Wallacher D, Züttel A. *Journal of Alloys and Compounds* **2009**, *484*, 654.

[19] Ravnsbaek DB, Jensen TR. *Journal of Applied Physics* **2012**, *111*, 112621.

[20] Li Y, Xiao X, Chen L, Han L, Shao J, Fan X, Li S, Wang Q. *The Journal of Physical Chemistry C* **2012**, *116*, 22226.

[21] Wu X, Wang X, Cao G, Li S, Ge H, Chen L, Yan M. *Journal of Alloys and Compounds* **2012**, *517*, 127.

[22] Yu XB, Xia GL, Guo ZP, Liu HK. *Journal of Materials Research* **2009**, *24*, 2720.

[23] Kim JW, Friedrichs O, Ahn J-P, Kim DH, Kim SC, Remhof A, Chung H-S, Lee J, Shim J-H, Cho YW, Züttel A, Oh KH. *Scripta Materialia* **2009**, *60*, 1089.

[24] Ampoumogli A, Steriotis T, Trikalitis P, Giasafaki D, Bardaji EG, Fichtner M, Charalambopoulou G. *Journal of Alloys and Compounds* **2011**, *509*, Supplement 2:S705.

[25] Kostka J, Lohstroh W, Fichtner M, Hahn H. *The Journal of Physical Chemistry C* **2007**, *111*, 14026.

[26] Hwang S-J, Bowman RC, Reiter JW, Rijssenbeek, Soloveichik GL, Zhao J-C, Kabbour H, Ahn CC. *The Journal of Physical Chemistry C* **2008**, *112*, 3164.

[27] Ozolins V, Majzoub EH, Wolverton C. *Journal of the American Chemical Society* **2008**, *131*, 230.

[28] Sridechprasat P, Suttisawat Y, Rangsunvigit P, Kitiyanan B, Kulprathipanja S. *International Journal of Hydrogen Energy* **2011**, *36*, 1200.

[29] Yan Y, Li H-W, Maekawa H, Miwa K, Towata S-i, Orimo S-i. *The Journal of Physical Chemistry C* **2011**, *115*, 19419.

[30] Ngene P, van Zwienen M, de Jongh PE. *Chemical Communications* **2010**, *46*, 8201.

[31] Fang ZZ, Wang P, Rufford TE, Kang XD, Lu GQ, Cheng HM. *Acta Materialia* **2008**, *56*, 6257.

[32]   Gross AF, Vajo JJ, Van Atta SL, Olson GL. *The Journal of Physical Chemistry C* **2008**, *112*, 5651.

[33]   Cahen S, Eymery JB, Janot R, Tarascon JM. *Journal of Power Sources* **2009**, *189*, 902.

[34]   Chen XY, Guo YH, Gao L, Yu XB. *Journal of Materials Research* **2010**, *25*, 2415.

[35]   Liu X, Peaslee D, Jost CZ, Majzoub EH. *The Journal of Physical Chemistry C* **2010**, *114*, 14036.

[36]   Ngene P, Adelhelm P, Beale AM, de Jong KP, de Jongh PE. *The Journal of Physical Chemistry C* **2010**, *114*, 6163.

[37]   Liu X, Peaslee D, Jost CZ, Baumann TF, Majzoub EH. *Chemistry of Materials* **2011**, *23*, 1331.

[38]   Ngene P, Verkuijlen MHW, Zheng Q, Kragten J, van Bentum PJM, Bitter JH, de Jongh PE. *Faraday Discussions* **2011**, *151*, 47.

[39]   Si X, Li F, Sun L, Xu F, Liu S, Zhang J, Zhu M, Ouyang L-Z, Sun D, Liu Y-L. *The Journal of Physical Chemistry C* **2011**, *115*, 9780.

[40]   Sun T, Liu J, Jia Y, Wang H, Sun D, Zhu M, Yao X. *International Journal of Hydrogen Energy* **2012**, *37*, 18920.

[41]   Gao J, Ngene P, Lindemann I, Gutfleisch O, de Jong KP, de Jongh PE. *Journal of Materials Chemistry* **2012**, *22*, 13209.

[42]   Nielsen TK, Bösenberg U, Gosalawit R, Dornheim M, Cerenius Y, Besenbacher F, Jensen TR. *ACS Nano* **2010**, *4*, 3903.

[43]   Wiench JW, Balema VP, Pecharsky VK, Pruski M. *Journal of Solid State Chemistry* **2004**, *177*, 648.

[44] Gao J, Adelhelm P, Verkuijlen MHW, Rongeat C, Herrich M, van Bentum PJM, Gutfleisch O, Kentgens APM, de Jong KP, de Jongh PE. *The Journal of Physical Chemistry C* **2010**, *114*, 4675.

[45] Verkuijlen MHW, Gao J, Adelhelm P, van Bentum PJM, de Jongh PE, Kentgens APM. *The Journal of Physical Chemistry C* **2010**, *114*, 4683.

[46] Nielsen TK, Polanski M, Zasada D, Javadian P, Besenbacher F, Bystrzycki J, Skibsted J, Jensen TR. *ACS Nano* **2011**, *5*, 4056.

[47] Sabrina S, Kenneth DK, Fredrik Sydow H, Richard HH, Elisa Gil B, Zhirong Z-K, Maximilian F, Bjørn CH. *Nanotechnology* **2012**, *23*, 255704.

[48] Nielsen TK, Manickam K, Hirscher M, Besenbacher F, Jensen TR. *ACS Nano* **2009**, *3*, 3521.

[49] Mueller T, Ceder G. *ACS Nano* **2010**, *4*, 5647.

[50] Koukaras EN, Zdetsis AD, Sigalas MM. *Journal of the American Chemical Society* **2012**, *134*, 15914.

[51] Lin C, Xu T, Yu J, Ge Q, Xiao Z. *The Journal of Physical Chemistry C* **2009**, *113*, 8513.

[52] Zhang Y, Tian Q, Zhang J, Liu S-S, Sun L-X. *The Journal of Physical Chemistry C* **2009**, *113*, 18424.

[53] Chen J, Kuriyama N, Xu Q, Takeshita HT, Sakai T. *Journal of Physical Chemistry B* **2001**, *105*, 11214.

[54] Rafi ud d, Xuanhui Q, Ping L, Zhang L, Ahmad M. *The Journal of Physical Chemistry C* **2011**, *115*, 13088.

[55] Jang J-W, Shim J-H, Cho YW, Lee B-J. *Journal of Alloys and Compounds* **2006**, *420*, 286.

[56]   Gosalawit-Utke R, Nielsen TK, Saldan I, Laipple D, Cerenius Y, Jensen TR, Klassen T, Dornheim M. *The Journal of Physical Chemistry C* **2011**, *115*, 10903.

[57]   Gosalawit−Utke R, Nielsen TK, Pranzas K, Saldan I, Pistidda C, Karimi F, Laipple D, Skibsted J, Jensen TR, Klassen T, Dornheim M. *The Journal of Physical Chemistry C* **2011**, *116*, 1526.

[58]   Pendolino F, Mauron P, Borgschulte A, Züttel A. *The Journal of Physical Chemistry C* **2009**, *113*, 17231.

[59]   Christian ML, Aguey-Zinsou K-F. *ACS Nano* **2012**, *6*, 7739.

[60]   Xia GL, Li L, Guo ZP, Gu QF, Guo YH, Yu XB, Liu HK, Liu ZW. *Journal of Materials Chemistry A* **2013**, *1*, 250.

6 CHAPTER 6 NANO-CONFINED MULTI-SYNTHESIS OF LI-MG-N-H NANOCOMPOSITE TOWARDS LOW-TEMPERATURE HYDROGEN STORAGE WITH STABLE REVERSIBILITY

6.1 Introduction

The metal-N-H system has been regarded as one of the most promising materials for hydrogen storage due to its high hydrogen content, favorable thermodynamics, and good reversibility.[1-4] $Mg(NH_2)_2$-2LiH composite in particular could reversibly store 5.6 wt.% of hydrogen according to the following Equation 6.1:

$$Mg(NH_2)_2 + 2LiH \leftrightarrow Li_2Mg(NH)_2 + 2H_2 \quad (6.1)$$
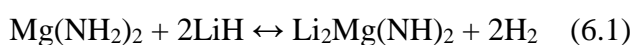
For this reaction, the thermodynamic calculation gives a favorable enthalpy change of ~ 39 kJ mol^{-1} for H_2 desorption, corresponding to an operating temperature as low as ~ 90 ^{o}C under the equilibrium pressure of 1 bar,[5] which can satisfy the operational requirements of proton exchange membrane (PEM) fuel cells. [6] Favorable kinetics for both dehydrogenation and hydrogenation, however, was practically achieved only at temperatures above 200 ^{o}C as the result of a rather high activation energy barrier (E_a: ~102 – 120 kJ mol^{-1}), [4] which is attributed to the sluggish interface reaction between the amide and hydride in the preliminary stage and the following mass transport through the thus-formed imide layer. [7] Moreover, the problematic release of ammonia during cycling is another major drawback, which not only significantly damages the active catalyst in the PEM fuel cells, but also induces loss of gravimetric capacity during cyclic H_2 sorption, which are serious obstacles to the practical application of the Li-Mg-N-H system. [8]

Modification of the hydrogen storage performance of Li-Mg-N-H system is often obtained by doping catalysts. It was reported that the kinetics of both dehydrogenation and hydrogenation could be improved by the introduction of metal borohydrides[6,9,10], K-based compounds[11-13], $Li_2Mg(NH)_2$[14], carbon nanofibers[15], or inorganic

transition metal compounds[16]. Another alternative approach to circumvent the above-mentioned problems in the Li-Mg-N-H system is to bring the particle size into the nanometer range, which can powerfully promote close proximity between $Mg(NH_2)_2$ and LiH, as well as decreasing the diffusion pathways for active substrates, leading to improved hydrogen storage performance. [17-20] For example, the nanosized $Mg(NH_2)_2$-2LiH composite produced by the hydrogenation during long ball milling of $Li_2Mg(NH)_2$ exhibits a dramatic 61% decrease in its activation energy compared with its hand-milled counterpart.[20] During the consecutive heat treatments for dehydrogenation and hydrogenation, however, the original particles, even though they have small sizes, are prone to aggregate, giving rise to a considerable reduction in the surface area and the extension of mass transport paths across the imides, which finally results in continuing deterioration of hydrogen storage properties,[21] e.g., the peak temperature for the ball-milled $Mg(NH_2)_2$-2LiH composite can even increase by ~20 °C through only one sorption cycle.[22] Hence, it is imperative but challenging to find an alternative approach that can not only fabricate suitable nanostructure in the Li-Mg-N-H system, but also preserve its stability during continuous H_2 cycling.

Recent progress on adopting nanoconfinement as an effective tool to load complex hydrides opens up fascinating possibilities for designing nanostructures of various hydrogen storage materials.[21,23-25] After the melt and/or solution impregnation into porous scaffolds by the molten and/or solution state of complex hydrides, the direct synthesis of nanostructured materials can be easily realized by the physical space-confinement functions of nanoscale pores. The porous matrix materials can physically prevent sintering and growth of the thus-formed nanoparticles during cycles of H_2 absorption and desorption, even at elevated temperatures, and effectively preserve the spatial dimensions of the nanosized

composite.[21,23] Additionally, the significant reduction of particle size leads to an increased surface area and intimate contact between reactive agents, which will tremendously enhance the reaction kinetics and decrease the diffusion pathways across the active substrates, resulting in improved H_2 sorption performance. The significantly enhanced kinetics and reversibility of various complex hydrides after nanoconfinement in porous templates have been widely confirmed in previous reports.[26-37]

As noted for the nanosize-induced effects on the hydrogen storage system and the aforementioned kinetics problems of Li-Mg-N-H composite, nanoconfinement seems to be capable of unleashing its potential as a practical hydrogen storage candidate. Unfortunately, due to the fact that all the components of Li-Mg-N-H composite have high chemical activity, low solubility, and/or high melting points, there is no report on the nanoconfinement of this system using the traditional technique mentioned above. In the present study, we report a novel synthetic methodology to successfully space-confine Li-Mg-N-H composite in thin-film hollow carbon spheres (THCSs), i.e., (1) the co-infusion of $MgCl_2$ and LiN_3 with uniform dispersion into the THCSs via a solution impregnation technique; (2) thermal treatment of the precursors, followed by a hydrogenation process, leading to the formation of $LiNH_2/LiH$ composite; (3) a solid metathesis reaction between $MgCl_2$ and the thus-formed $LiNH_2/LiH$, resulting in the final creation of a nanoconfined $Mg(NH_2)_2/LiH$ composite. To the best of our knowledge, this is the first realization of nanoconfinement of Li-Mg-N-H composite in a host template. The relatively thin films of the THCSs, on the one hand, could promote the co-infiltration of the precursors of $MgCl_2$ and LiN_3 solution, leading to homogeneous microstructure and distribution. On the other hand, the flexible double films could effectively encapsulate a large amount of complex hydrides, withstand

phase separation and growth, and meanwhile prevent the diffusion of active materials from the inside to the outside during cyclic heat treatment. Thus, taking advantage of the nanoconfinement effect of the THCSs, the nanostructured Li-Mg-N-H composite exhibits significantly improved dehydrogenation/rehydrogenation performance with a full cycle at 105 $^{\circ}$C for completely reversible hydrogen storage and tremendously lower than that of the pristine system (> 180 $^{\circ}$C), [7] and cyclic stability.

6.2 Experimental section

6.2.1 Synthesis of SnO$_2$ hollow spheres:

The hollow SnO$_2$ nanoparticles were prepared using a simple hydrothermal method in an ethanol-H$_2$O mixed solvent. In a typical synthesis, urea (0.36 g, 0.1 M) additive was firstly dissolved in 60 mL of ethanol/water mixed solvent with a volume ratio of 3:5. Thereafter, 0.288 g potassium stannate trihydrate (K$_2$SnO$_3$.3H$_2$O, Sigma-Aldrich, 99.9%) was slowly added, followed by gentle shaking by hand for around 3 min until a translucent solution was obtained, which was then transferred into a 100 mL Teflon-lined stainless steel autoclave and heated at 200 $^{\circ}$C for 20 h in an electric oven. The autoclave was then taken out of the oven and left to cool down to room temperature. The white precipitate was collected by centrifugation, washed thoroughly with water several times, and then dried at 60 $^{\circ}$C overnight.

6.2.2 Synthesis of thin-film hollow carbon spheres

The carbon spheres were obtained by coating glucose on the SnO$_2$ hollow spheres by a simple hydrothermal process. In a typical synthesis, 0.1 g of the as-prepared SnO$_2$ hollow spheres was easily dispersed by ultrasonication in 20 mL of 0.5 M aqueous glucose solution. The suspension was then transferred into a 40 mL Teflon-lined

autoclave and kept in an electric oven at 180 $^\circ$C for 4 h. The product was harvested by centrifugation and washed with deionized water and ethanol several times. After drying at 60 $^\circ$C for around 5 h, the brown powder was heated to 650 $^\circ$C for 5 h in flowing H_2/N_2 (v/v = 10:90) with a heating rate of 1 $^\circ$C min^{-1}. Following that, the product was dispersed in 2 M HCl to remove the residual Sn particles, and the double-shelled hollow carbon spheres (THCSs) were collected by centrifugation, followed by drying at 60 $^\circ$C overnight.

6.2.3 Synthesis of thin-film hollow carbon spheres

Selected THCSs were firstly activated at 500 $^\circ$C under vacuum for several hours in order to remove moisture and gases from the porous matrix. Subsequently, a solution of LiN_3 and $MgCl_2$ with a molar ratio of 2:1 in 2,2,2-trifluoroethanol (TFE, CF_3CH_2OH), which was stirred in advance for around 5 h to ensure the homogeneous mixing of raw materials, was added to the pre-activated THCSs. After 0.5 h of infiltration via the capillary effect, the sample was vacuum dried at 150 $^\circ$C for 10 h to remove the solvent. To produce a space-confined nanocomposite with a relatively high loading capacity and good dispersion of the starting materials inside the nanopores of the THCSs, several successive steps of infiltration/vacuum-drying were conducted followed by washing with pure TFE and drying. Afterwards, the nanoconfined precursors were dried at 150 $^\circ$C and then activated under 150 bar hydrogen pressure at 200 $^\circ$C for 12 h by a metathesis reaction, as illustrated in Figure 1, which results in the formation of Li-Mg-N-H composite. According to elemental analysis, the resulting composite contained 15.79 mass% Li, 9.23 mass% Mg, 10.59 mass% N and 35.41 mass% C, which gives the mass concentration of $Li_2Mg(NH)_2$ to be ~ 25.8 mass% in the as-prepared products based on the combination of molar ratio in the raw precursors and the reaction mechanism.

6.2.4   Hydrogen storage tests

The hydrogen storage properties of the nanoconfined Li-Mg-N-H composite were examined with the aid of a Sieverts' apparatus, identified as a gas reaction controller (GRC, Advanced Materials Corp., USA). The apparatus was carefully calibrated from the H_2 sorption of a $LaNi_5$ reference sample with an accuracy of ±1%, and, typically, a ~500 mg sample was loaded into a stainless-steel autoclave for hydrogenation and dehydrogenation measurements. The H_2 absorption kinetics measurements were performed at various temperatures with an initial pressure of 35 atm, and the desorption properties were detected at various temperatures under hydrogen pressure below 0.02 atm. The pressure-concentration isotherm (PCI) measurements were performed at the desired temperatures, and the equilibrium time for each point was 600 s. For comparison, the amount of hydrogen released from the nanoconfined composite is based on the composite of $Mg(NH_2)_2$-2LiH, while the THCSs, LiCl, and extra LiH are excluded.

6.3 Results and discussion
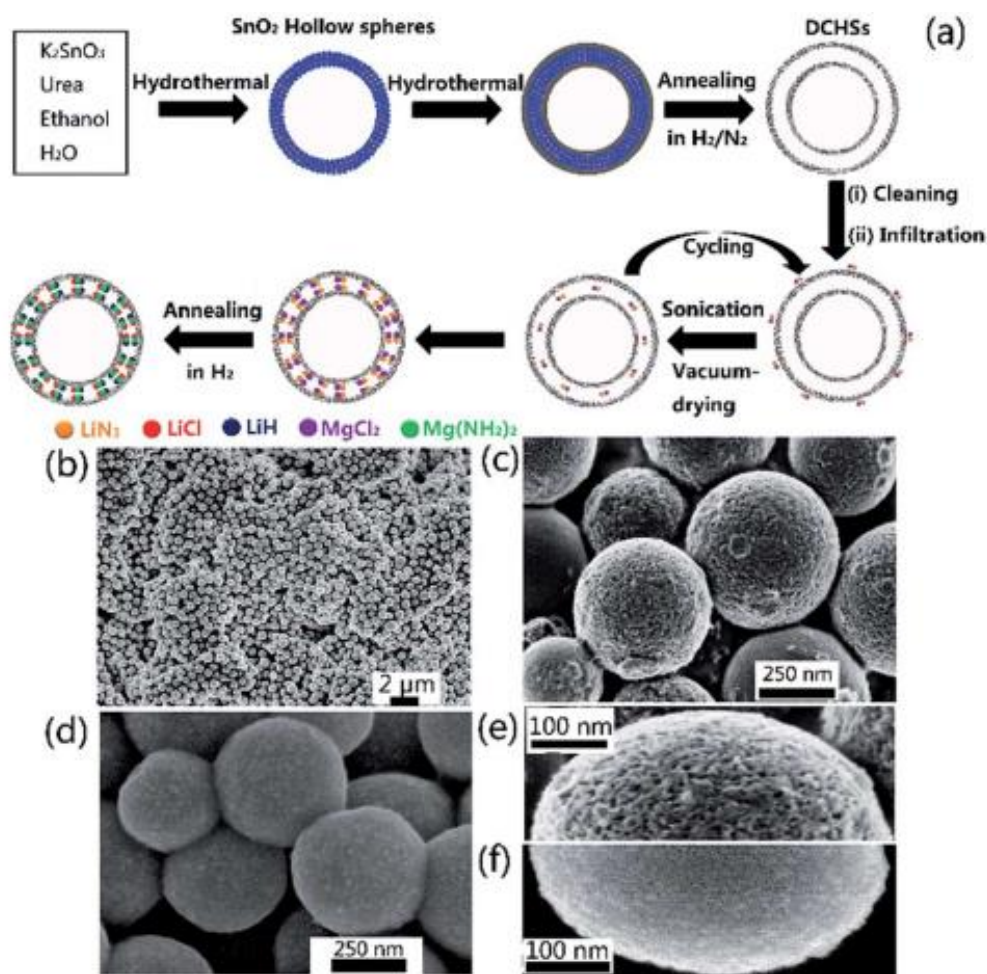
Figure 6. 1 (a) Schematic diagram of the approach to fabricate the nanoconfined Li-Mg-N-H composite into THCSs, and FESEM images of the as-synthesized SnO$_2$ hollow spheres (b), THCSs (c) and the nanoconfined Li-Mg-N-H composite inside THCSs (d). The (e) and (f) are the enlarged images of the freshly-prepared THCSs and its products after nanoconfinement of precursors, respectively.

The THCSs are manufactured using SnO$_2$ hollow spheres as the hard templates by a facile one-pot template-free approach, [38] as schematically illustrated in Figure 6.1. The morphology and microstructure of the products were characterized by field-emission scanning electron microscopy (FESEM) and transmission electron microscopy (TEM). As can be seen in Figures 6.1(b) and 6.2, the as-prepared SnO$_2$

hollow spheres are uniform with a diameter of around 250-500 nm. A glucose-derived polysaccharide on both the interior and exterior surfaces of the SnO_2 hollow spheres, as well as in the pores within the films, was then homogeneously coated by a method based on the hydrothermal technique. Subsequently, carbothermal treatment was carried out under H_2/N_2 atmosphere, accompanied by the reduction of SnO_2 into metallic Sn. Finally, THCSs were obtained by the dissolution of Sn nanoparticles in hydrochloric acid, followed by centrifugation, which perfectly duplicates the original shape and size of the SnO_2 nanostructures (Figure 6.1(c)). From the cracked spheres, the hollow interior can be verified directly, indicating the successful synthesis of rounded structures with inner cavities (Figure 6.2). Moreover, according to the transmission electron microscope (TEM) images (Figure 6.3(a)), the hollow interior of the as-prepared carbon nanospheres was further confirmed, and two thin films with a separation as little as ~50-100 nm between them could be clearly observed. Furthermore, the contrast within the inter-film cavity indicates the presence of carbon "links" connecting the internal and the external films, which were previously occupied by SnO_2 nanoparticles. The elimination of the SnO_2 nanoparticles leaves behind open and accessible mesopores on the surfaces (Figure 6.1 (e)) and between the thus-formed carbon sheets, leading to the formation of a highly mesoporous framework within these two thin films. The porous structure of the THCSs was quantitatively analyzed by N_2 adsorption-desorption isotherms, which gave a very high specific surface area of 748 $m^2\,g^{-1}$ and a large total pore volume of 1.685 $cm^3\,g^{-1}$ (Figure 6.4). Therefore, owing to these special features, two foundational advantages of adopting THCSs as porous supports can be demonstrated: (1) the mesopores between the double films provide a plethora of "rooms", with diameters ranging from 2 to 14 nm (Figures 6.1(d) and

6.4), for the effective infiltration of complex hydrides, and (2) the thin films with mesopores are feasible for the infiltration of active composites.
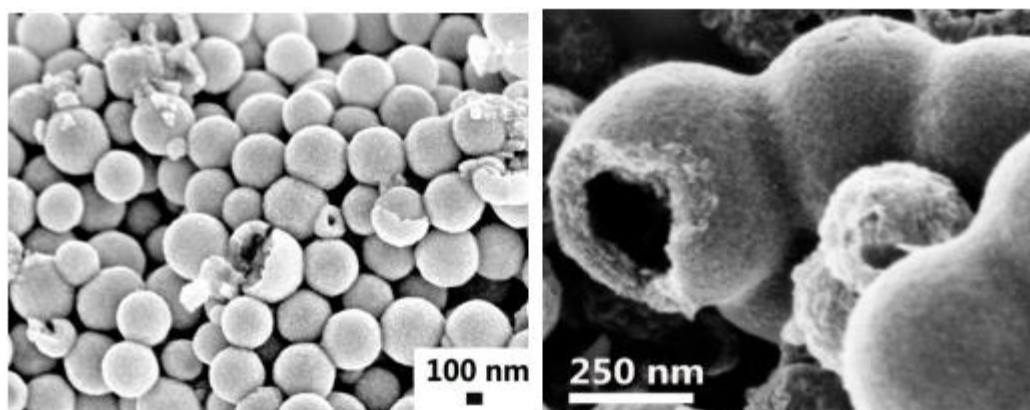
Figure 6. 2 FESEM images of the as-prepared SnO_2 hollow spheres (left) and THCSs (right). Some of the hollow spheres are cracked, exhibiting the exposed interior.
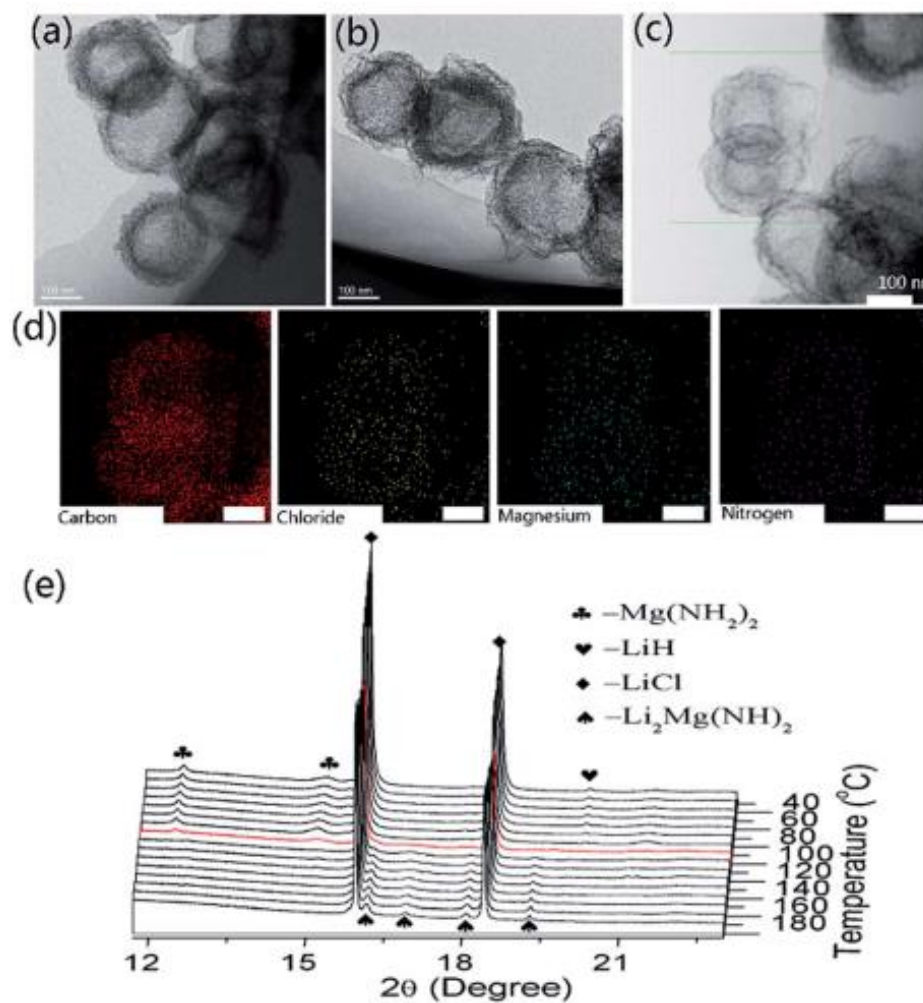
Figure 6. 3 TEM images of the as-prepared THCSs (a) and the nanoconfined precursors inside the THCSs (b). TEM image (c) and the corresponding elemental mapping (d) of THCSs with the nanoconfined precursors. (e) High-resolution XRD spectra of the nanoconfined Li-Mg-N-H composite upon heating to various temperatures.

The nanoconfinement of Li-Mg-N-H composite was realized by the co-infiltration of precursors, i.e., $MgCl_2$ and LiN_3, which are both easily soluble in trifluoroethanol, making them favorable for homogeneous distribution inside the scaffolds, into THCSs via the capillary effect and two typical *in-situ* reactions under physical restriction. During the removal of solvent upon heating to 200 °C, based on Equation 6.2, LiN_3 firstly decomposes into Li_3N with the release of nitrogen. Afterwards, on annealing under H_2 atmosphere, the hydrogenation of nanosized Li_3N leads to the formation of $LiNH_2$ and LiH according to Equation 6.3, which provides the source of NH_2 to synthesize $Mg(NH_2)_2$ and LiH as another constituent ingredient. Simultaneously, the freshly-formed $LiNH_2$ will react *in-situ* with $MgCl_2$ via a solid metathesis reaction 6.4, which, as a result, leads to the formation of $Mg(NH_2)_2$ and LiH with $LiCl$ as the by-product.[39] The feasibility of this procedure is indirectly proved by the presence of $Mg(NH_2)_2$, LiH, and $LiCl$ from the X-ray diffraction data after annealing the bulk precursors (Figure 6.5) without addition of THCSs.

$$3LiN_3 \rightarrow Li_3N + 4N_2 \quad (6.2)$$

$$Li_3N + 2H_2 \rightarrow LiNH_2 + 2LiH \quad (6.3)$$

$$MgCl_2 + 2LiNH_2 \rightarrow Mg(NH_2)_2 + 2LiCl \quad (6.4)$$
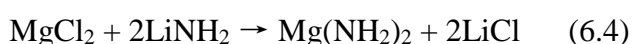
After the infiltration process, no surface morphology change could be clearly observed from the FESEM (Figure 6.1(d)) and TEM images (Figure 6.3(b)). With

careful observation (Figure 6.1(f)), compared with the freshly prepared THCSs, the mesopores on the exterior films disappeared after encapsulation, suggesting the successful nanoconfinement of precursors. No discernible agglomeration is present on the surfaces of the THCSs, while the C map in the energy dispersive spectroscopy (EDS) agrees well with the hollow structure of the carbon spheres, and the Cl, Mg, and N elemental maps correspond well with the C map from EDS (Figure 6.3(d)), indicating the good dispersion of precursors inside the THCSs due to the co-infiltration process. Moreover, the carbon signals are mainly distributed in the region of the two carbon films, which is similar to the distribution of Cl, Mg, and N, while their signals are obviously weaker in the center of the spheres, suggesting that the inner cavity still remains hollow and the good distribution of precursors is mainly achieved in the highly porous films. The effective infiltration of the precursors into the THCSs is further proved by N_2 adsorption/desorption analysis (Figure 6.4), which demonstrates a significant reduction of the surface area as well as the intensity of the Barrett-Joyner-Hallenda (BJH) pore size distribution and total pore volume (0.42 cm^3 g^{-1}). The Li-Mg-N-H composite thus undoubtedly penetrates the porous framework of the THCSs and occupies a large proportion of the void space in their mesopores, and/or blocks the pores.

The crystallographic phase of the products from the annealing of the nanoconfined precursors was determined by high-resolution X-ray powder diffraction (HRXRD) as shown in Figure 6.3(e). The diffraction peaks in the HRXRD pattern can be unambiguously indexed to LiCl, LiH, and $Mg(NH_2)_2$, while as H_2 desorption proceeds, the diffraction peaks of $Li_2Mg(NH)_2$ appear, obviously confirming the successful nanoconfinement of the Li-Mg-N-H composite by THCSs, which was further verified by the Fourier transform infrared (FTIR) results (Figure 6.6). It is worth noting that,

compared to the bulk counterpart, the carbon frameworks of THCSs can effectively restrict the *in-situ* crystallite growth of active substrates and preserve the close proximity between $Mg(NH_2)_2$ and LiH upon heating, which is favorable for the improvement of hydriding and dehydriding kinetics. Due to the physical space restriction of mesopores in the THCSs during the synthetic process, the average crystallite size of the thus-formed $Li_2Mg(NH)_2$, derived from the Debye-Scherrer equation, is only ~9 nm.
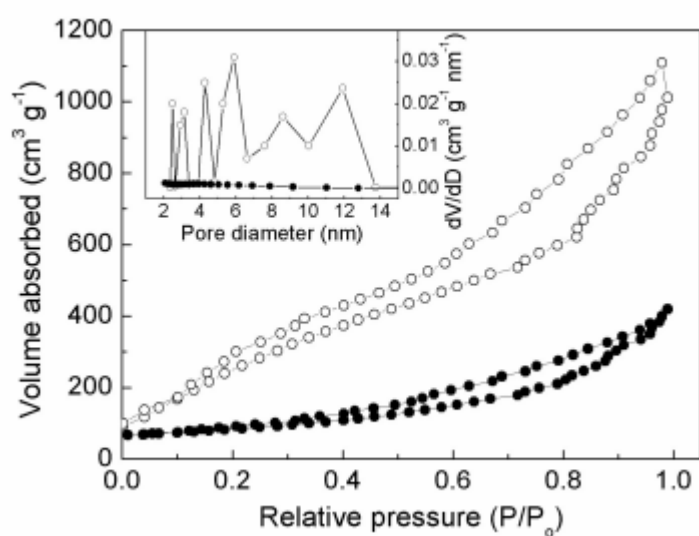
Figure 6. 4 Nitrogen isotherms and pore size distribution (inset) of the freshly-prepared THCSs (○) and the THCSs with the loading of Li-Mg-N-H composite (●).
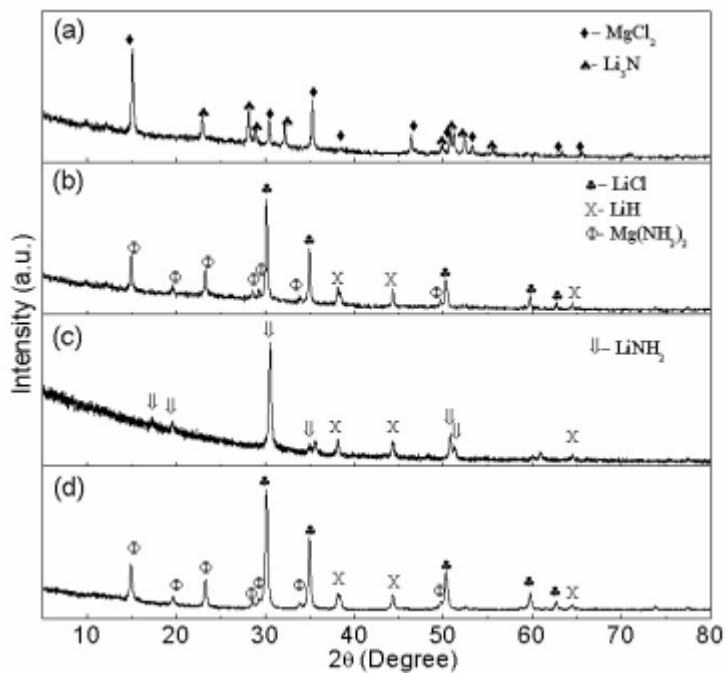
Figure 6. 5 XRD patterns of (a) the vacuum-dried products from the precursors of MgCl$_2$ and LiN$_3$ heat-treated at 200 ºC and (b) the products after annealing at 200 ºC under 150 bar of H$_2$, (c) Li$_3$N after annealing at 200 ºC under 150 bar of H$_2$, and (d) the mixed composite of MgCl$_2$ with the hydrogenated Li$_3$N after annealing at 200 ºC under 150 bar of H$_2$.
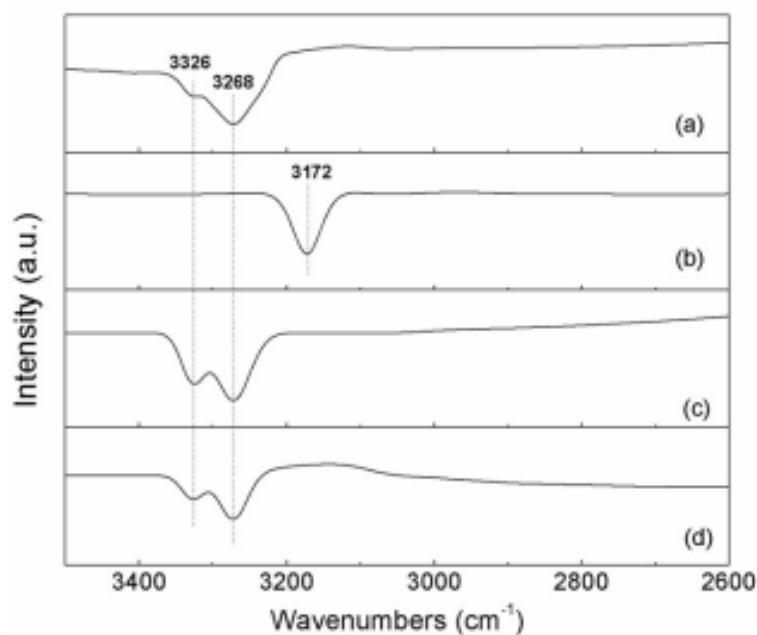
Figure 6. 6 FTIR spectra of the nanoconfined Li-Mg-N-H nanoparticles (a), and the products after the 1st dehydrogenation (b), 1st hydrogenation (c), and 20th hydrogenation (d).

To explore the effects of nanoconfinement by the THCSs on the hydrogen storage performance of the Li-Mg-N-H system, a comparison of the thermal decomposition behavior of the ball-milled Li-Mg-N-H composite without carbon, the nanoconfined Li-Mg-N-H composite, and the ball-milled Li-Mg-N-H composite with the addition of carbon spheres as a reference sample was conducted by employing mass spectroscopy (MS) and thermogravimetric analysis (TGA) (Figure 6.7(a)). For the ball-milled Li-Mg-N-H composite, a dehydrogenation peak was observed at ~198 $^{\circ}$C with an onset temperature of ~135 $^{\circ}$C, which agrees well with the previous reports.[12,42] A comparative experiment, where the carbon spheres were admixed with Li-Mg-N-H system *via* ball milling, was carried out for the H_2 desorption process. As illustrated in Figure 6.7(a), the ball-milled composite with the addition of carbon spheres exhibits a comparable process to that of the pure Li-Mg-N-H composite with a slightly lower temperature for dehydrogenation, indicating the presence of a weak catalytic effect of the carbon spheres, as with the function of carbon nanofibers towards catalyzing the dehydrogenation of Li-Mg-N-H composite.[15] Additionally, a simultaneous release of NH_3 was detected for the ball-milled Li-Mg-N-H system with or without addition of carbon spheres, due to the insufficient reaction between $Mg(NH_2)_2$ and LiH (Figure 6.8). On the contrary, the onset and peak temperatures of H_2 desorption from the nanoconfined Li-Mg-N-H composite downshifted to ~ 90 $^{\circ}$C and 123 $^{\circ}$C, respectively, which are 45 $^{\circ}$C and 75 $^{\circ}$C lower than for the ball-milled Li-Mg-N-H composite, respectively, and even lower than those obtained from various catalysts doped materials.[40-42] Interestingly,

as suggested by the MS spectra, there is no measureable release of NH_3 for the nanosized composite. The TGA results reveal that the weight loss of the nanoconfined nanoconfined Li-Mg-N-H sample is ~5.5 wt.%, coinciding well with its theoretical value (5.6 wt.%). In order to further clarify the reaction mechanism, *in-situ* high-resolution XRD (Figure 6.3(e)) was performed during the dehydrogenation of the nanoconfined Li-Mg-N-H composite. With increasing heating temperature, the peaks assigned to $Mg(NH_2)_2$ and LiH obviously weakened at ~100 °C, followed by the appearance of the characteristic peaks of $Li_2Mg(NH)_2$ at ~110 °C, which is in good agreement with the H_2 desorption temperature according to the TGA and MS results (Figure 6.7(a)). Therefore, HRXRD clearly demonstrates the important role of the space-confinement effects of THCSs in the tremendous enhancement of H_2 desorption from the Li-Mg-N-H system.
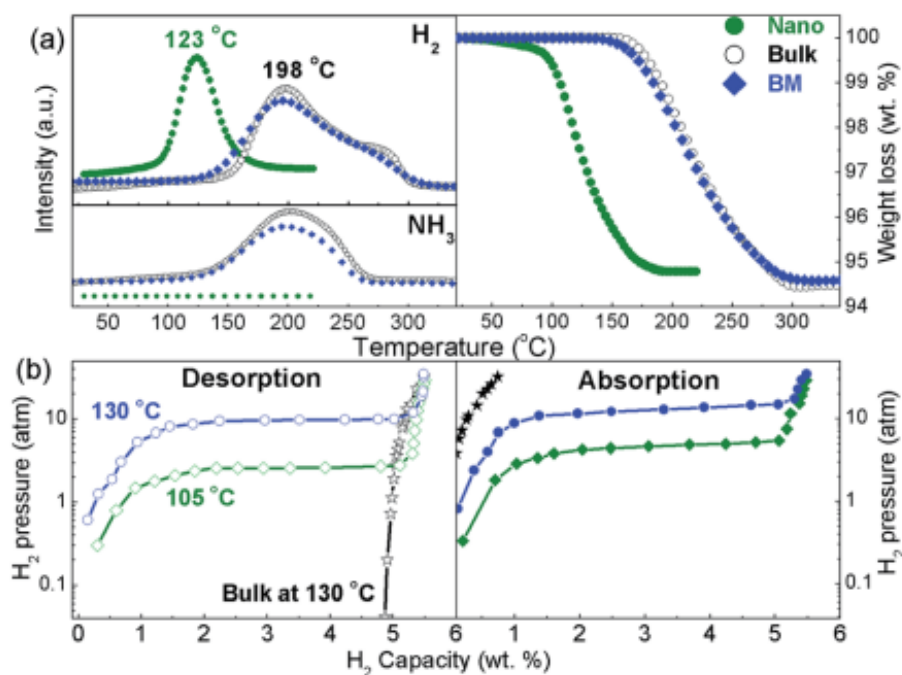
Figure 6. 7 (a) TGA-MS spectra of the nanoconfined Li-Mg-N-H composite (Nano), the ball-milled composite of $Mg(NH_2)_2$-2LiH (Bulk) and the control sample (BM). (b) The pressure-composition isotherms (PCI) of the nanoconfined Li-Mg-N-H

composites at the temperatures of 105 $^{\circ}$C and 130 $^{\circ}$C, respectively, as compared with the ball-milled Li-Mg-N-H composite at the temperature of 130 $^{\circ}$C.
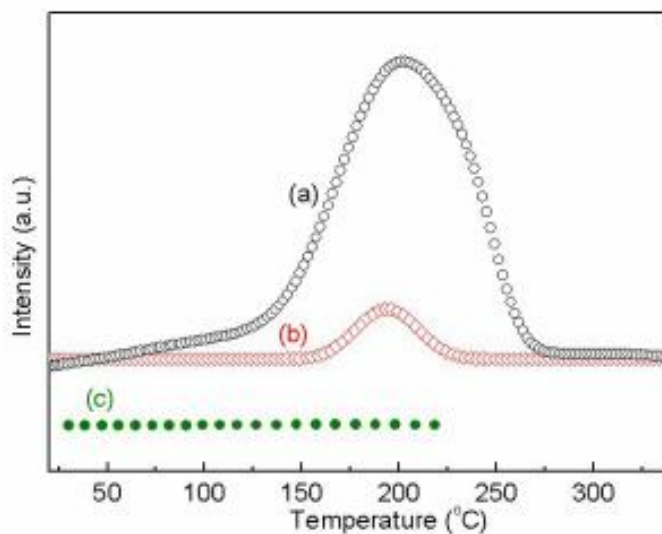
Figure 6. 8 NH_3 signals of mass spectra during the decomposition of (a) nanoconfined Li-Mg-N-H composite compared with ball-milled composite of (b) $Mg(NH_2)_2$-2LiH and (c) $Mg(NH_2)_2$-4LiH, respectively.

The influence of the nanoconfinement of THCSs on the reversibility of Li-Mg-N-H system was first investigated by pressure-composition isothermal (PCI) analysis in comparison with the ball-milled composite (Figure 6.7(b)). No plateaus can be observed for the ball-milled Li-Mg-N-H composite, while it is surprising to find that a full cycle of H_2 ab-/de-sorption for the nanoconfined Li-Mg-N-H compound, with a capacity of ~5.4 wt.%, approaching the theoretical value (5.6 wt.%), can be realized at a temperature as low as 105 $^{\circ}$C. Specifically, a plateau pressure of ~2.6 atm was obtained at 105 $^{\circ}$C from the desorption curve and rose to ~9.5 atm as the operating temperature was increased to 130 $^{\circ}$C. By contrast, only a capacity of less than 1 wt.% was obtained for the ball-milled composite, even at the relatively high temperature of 130 $^{\circ}$C, indicating the tremendous kinetic barriers to H_2 uptake and release from the bulk Li-Mg-N-H composites. Furthermore, based on

the differential scanning calorimetry (DSC) results (Figure 6.9), during dehydrogenation, the overall reaction heat for the H_2 desorption from the ball-milled Li-Mg-N-H composite is calculated to be ~43.5 kJ mol^{-1} H_2, which agrees well with the previous reports.[9] In the case of the space-confined Li-Mg-N-H nanoparticles, the integration of the endothermic peak gives an enthalpy of 39.9 kJ mol^{-1} H_2, which equals an approximately 8.2% reduction compared with the ball-milled composite. This confirms that the nanoconfinement of Li-Mg-N-H composite in the THCSs also modifies the thermodynamics of the reaction pathway for H_2 release.
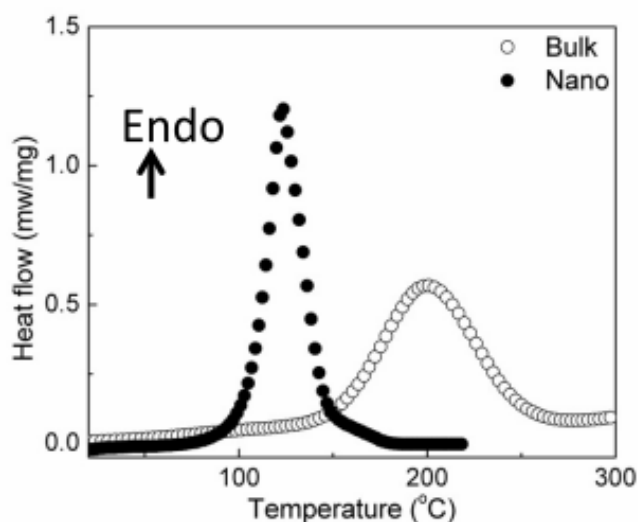
Figure 6. 9 DSC curve of the nanoconfined Li-Mg-N-H nanoparticles (Nano) compared with their ball-milled counterpart (Bulk), obtained with a heating rate of 2 °C min^{-1} under dynamic N_2.

The isothermal hydriding/dehydriding curves of the nanoconfined Li-Mg-N-H composite, in relation to its ball-milled counterpart, were further measured, using a Sieverts PCT-Pro at variable temperatures (Figure 6.10). Due to the enormous kinetic barrier, as mentioned in the introduction, only less than 0.5 wt.% H_2 can be de-/re-absorbed from the bulk Li-Mg-N-H within 60 min, even at 135 °C. In contrast, after nanoconfinement in THCSs, the Li-Mg-N-H nanoparticles could slowly release ~1.6

wt.% H_2 and absorb ~2 wt.% H_2 over the same period of 60 min, even at the relatively low temperature of 105 °C. At elevated temperatures, as expected, both the kinetics and the capacity increase for both absorption and desorption. In particular, H_2 release and uptake amounts to approximately 5 wt.% and 5.1 wt.%, respectively, at 135 °C in only 60 min, with the nanoparticles exhibiting a significant improvement in the hydriding/dehydriding kinetics in comparison with their bulk counterpart. In the quest for quantitative estimation of the enormous enhancement of kinetics for dehydrogenation and hydrogenation, the apparent activation energy (E_a) was determined according to the Arrhenius equation by fitting the isothermal sorption curves at various temperatures. Based on the slope of the linear plot of ln k (k, rate constant) vs. $1/T$ (T, absolute temperature), the activation energy of H_2 absorption and desorption from the nanoconfined Li-Mg-N-H composite (Figure 6.11) was verified to be 42.0 and 47.5 kJ mol^{-1} H_2, respectively, which is considerably lower than the value reported for its ball-milled and KH-catalysed counterpart, that is, 102 kJ mol^{-1} H_2[43] and 84.8 kJ mol^{-1} H_2[12], respectively.
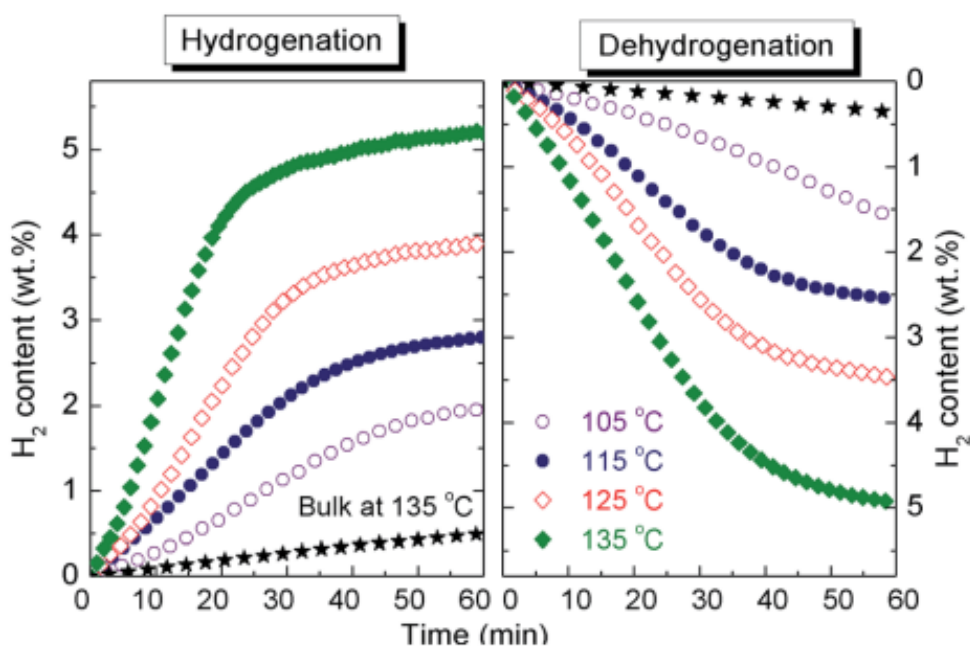
Figure 6. 10 Isothermal H₂ absorption and desorption curves of the nanoconfined Li-

Mg-N-H composite at various temperatures, compared with the bulk Li-Mg-N-H

composite at 135 °C.
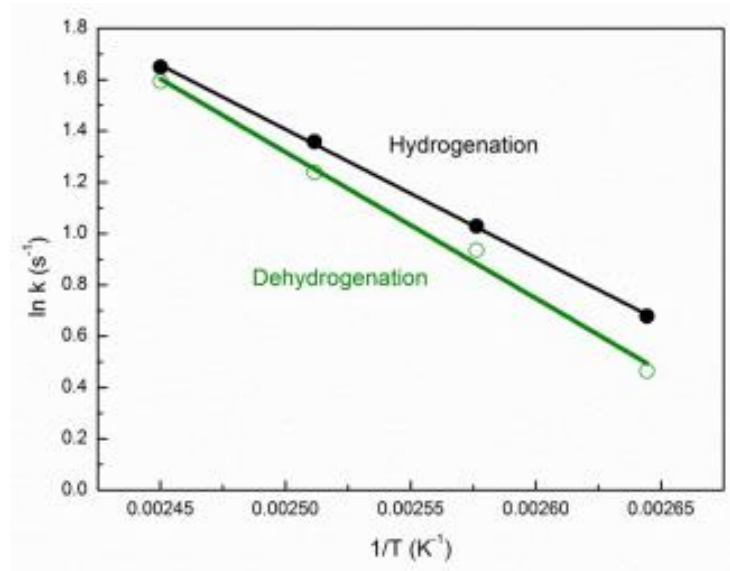
Figure 6. 11 Arrhenius plots for the isothermal hydrogenation and dehydrogenation

of the nanoconfined Li-Mg-N-H composite.
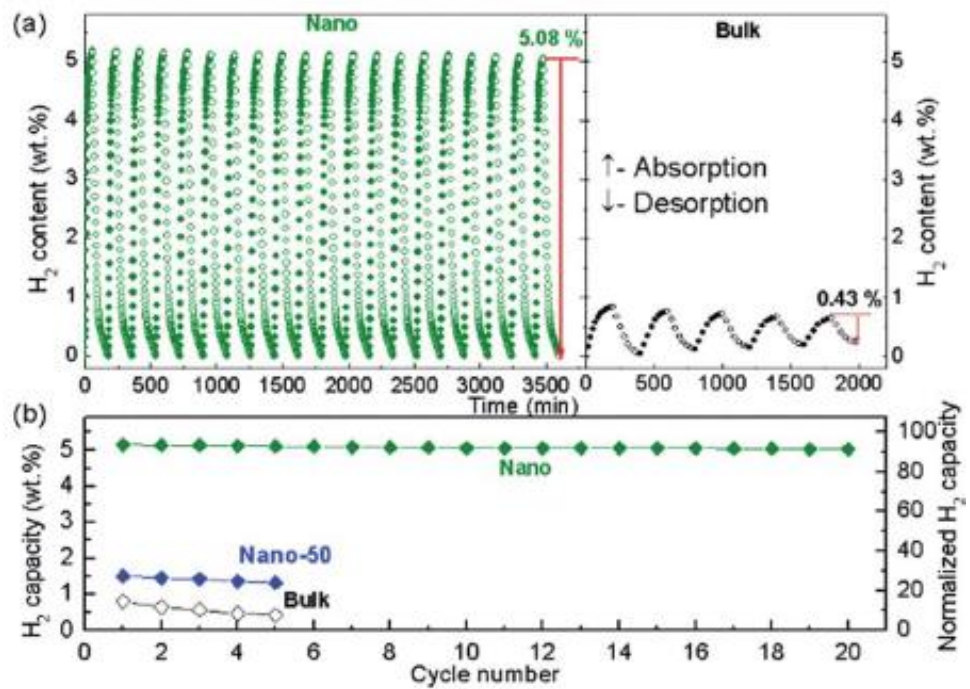
Figure 6. 12 (a) Reversible H$_2$ absorption and desorption of bulk (Bulk) and nanoconfined Li-Mg-N-H composite with a loading capacity of 25.8% (Nano) and 50% (Nano-50), respectively, at 135 °C; (b) Normalized H$_2$ capacity as a function of cycle number, where the hydrogen capacities are normalized to the theoretical value of Li$_2$Mg(NH)$_2$ (5.6 wt.%).

It is well-known that the sintering effects and particle agglomeration during the consecutive H$_2$ release and uptake cycles at elevated temperatures are inevitable, which could considerably increase the diffusion pathways for H$_2$ delivery and, thereby, lower the kinetics for dehydrogenation and hydrogenation, leading to the evolutionary degradation of H$_2$ cyclic capacity.[21] Therefore, a long-term kinetic measurement was carried out at 135 °C for the nanoconfined Li-Mg-N-H composite as compared to its bulk counterpart to investigate the space-confinement effects on the cycling performance (Figure 6.12). Obviously, in the case of the bulk Li-Mg-N-H composite, only ~0.85 wt.% hydrogen could be charged and ~0.8 wt.% could be subsequently discharged within 200 min at 135 °C. The value decreased to 0.45 wt.% for hydrogenation and 0.43 wt.% for dehydrogenation during the 5th cycle. By contrast, the Li-Mg-N-H nanoparticles embedded in THCSs exhibited well-preserved hydrogen cycling capacity and kinetics, even through 20 cycles of H$_2$ uptake and release within a relatively short heating time, i.e., 60 min for hydrogenation and 120 min for dehydrogenation. In particular, a reversible hydrogen capacity of 5.08 wt.% could be achieved, and the capacity retention was still in excess of 91% after 20 cycles of H$_2$ desorption/reabsorption, with a only slight degradation of 2.5%, while the weight retention was already lower than 8% after only 5 cycles for the bulk composite. These results obviously demonstrate that the reversible H$_2$-storage performance of the Li-Mg-N-H composite, in terms of the

both capacity retention and kinetics, is tremendously improved via infiltration into the mesopores of the THCS host.
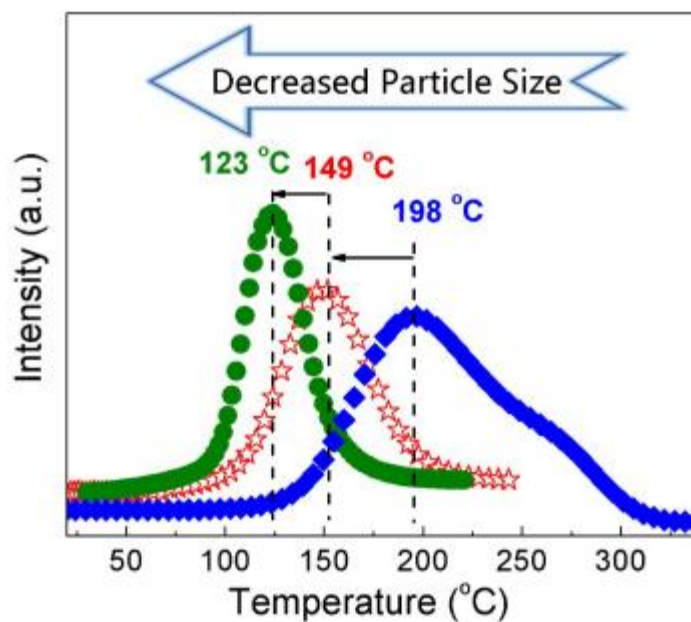
Figure 6. 13 Mass spectra of the nanoconfined $Li_2Mg(NH)_2$ with a loading capacity of 25.8 wt.% (●) and 32.1 wt.% (☆), respectively, as compared with bulk $Li_2Mg(NH)_2$ (♦).
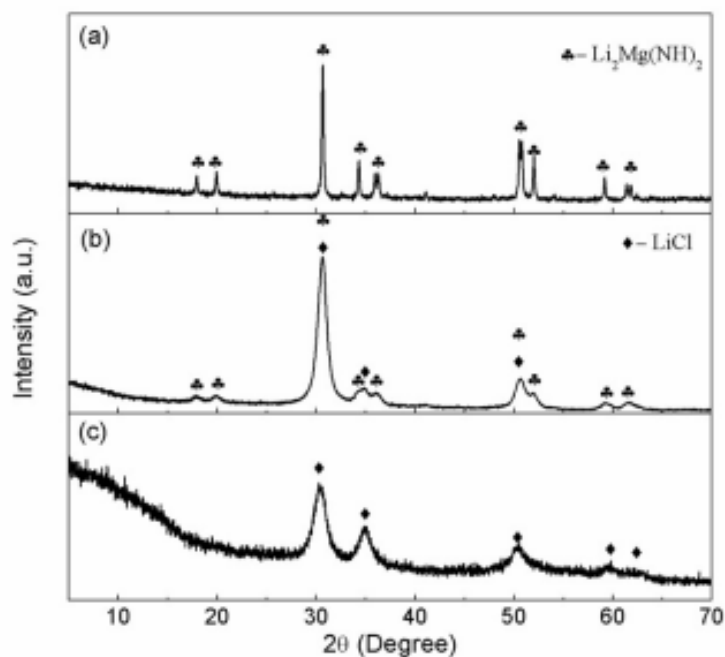
Figure 6. 14 Regular XRD spectra of the dehydrogenated products: (a) the ball-milled Li-Mg-N-H composite, and the nanoconfined Li-Mg-N-H composite with a loading capacity of 32.1% (b) and 25.8% (c), respectively.
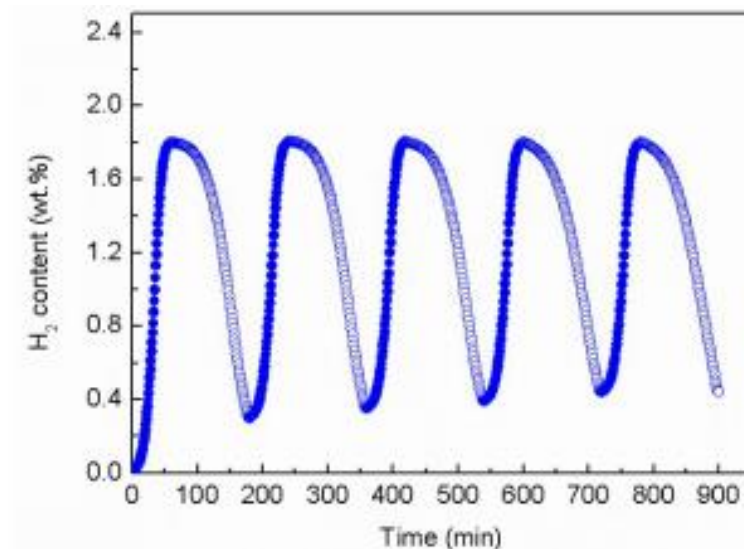
Figure 6. 15 Reversible H_2 absorption and desorption of nanoconfined Li-Mg-N-H composite with a loading capacity of 50% at 135 °C.

On the basis of the above observations, the de-/re-hydrogenation kinetics, reversibility and cycling stability are all significantly improved by confining Li-Mg-N-H composite into THCSs. Theoretical studies on hydrogen storage mechanism of Li-Mg-N-H composite revealed that the migration of small ions (e.g., Li^+, Mg^{2+}, and H^+) in both amides and hydrides and the subsequent mass transport play an important role for hydrogenation/dehydrogenation of the amide-hydride combination systems.[17,44] As a result, the decrease of particle size, which would decrease the diffusion pathways of ions and the mass transport lengths and increase the interface area between amides and hydrides, could significantly improve the H_2 sorption performance of Li-Mg-N-H system.[17-20] In the present work, with decreasing particle size down to nanometer scale, both the onset and the peak temperatures for dehydrogenation (Figure 6.13) of $Li_2Mg(NH)_2$ after hydrogenation

are significantly decreased. Moreover, it is no accident that upon increasing the loading capacity of $Li_2Mg(NH)_2$ from 25.8% to 32.1%, the onset and peak temperatures of dehydrogenation are increased, while they are still much lower than in the bulk counterpart. As verified by the XRD spectra (Figure 6.14), the diffraction peaks assigned to $Li_2Mg(NH)_2$ and the by-product, i.e., LiCl, are obviously sharpened with increased intensities, suggesting that the particle size and crystallite size are increased by increasing the loading capacity. As a result, with the further increased loading capacity to 50%, the cycling capacity and stability is also significantly degraded compared with the nanoconfined Li-Mg-N-H composite with a loading capacity of 25.8% (Figures 6.10 and 6.15). Therefore, this further confirms a bulk versus surface-dominated mechanism and the size-dependent enhancement of hydrogen storage performance. In addition, it is notable that the nanoconfinement of $Li_2Mg(NH)_2$ in THCSs, followed by thermal annealing can, on the one hand, realize the direct synthesis of nanosized $Li_2Mg(NH)_2$ (~9 nm particle size), inducing significant improvement of its hydrogen storage performance (Figures 6.7 and 6.10), and, on the other hand, the structural features down to the nanometer scale resulting from the space-confinement function of the porous THCSs can be well preserved during consecutive cycles, which therefore gives the composite stable reversibility without apparent degradation, even through up to 20 cycles of de-/re-hydrogenation (Figure 6.12).

6.4 Conclusions

In conclusion, a novel procedure is reported for the nanoconfinement of the Li-Mg-N-H system via infiltration of a mixed solution of $MgCl_2$ and LiN_3 into THCSs. The unique properties of the THCSs, i.e., the concentric thin films and the highly mesoporous framework between them, can effectively accommodate myriads of

nanosized particles and physically prevent their sintering and growth during consecutive sorption cycles. The Li-Mg-N-H that was space-confined within the nanoscale range showed a high reversible capacity of up to 5.5 wt. % at a temperature as low as 105 ^{o}C, and a stable cycling capacity close to its theoretical value is achieved for up to 20 cycles. However, it should be noted that, due to the extra weight of the porous templates as the intrinsic drawback of nanoconfinement and LiCl as the by-product, the actual reversible H$_2$ capacity is limited to be around 1.42 wt.% by taking into account the templates and LiCl. Therefore, further works, especially in the search of an effective solvent to remove the inactive LiCl and other scaffolds with large porous volumes and light weight to achieve a high loading percent of precursors, are still required to achieve a high hydrogen storage capacity in the whole system. Nevertheless, the novel strategy explored in this study provides new insights in improving the kinetics and cycling properties of Li-Mg-N-H system and will promote further optimization of this system via nanotechnology.

6.5 References

[1] S.-i. Orimo, Y. Nakamori, J. R. Eliseo, A. Züttel, C. M. Jensen, *Chemical Reviews,* **2007***, 107*, 4111.

[2] X. F. Liu, G. S. McGrady, H. W. Langmi, C. M. Jensen, *Journal of the American Chemical Society,* **2009**, *131*, 5032.

[3] G. Moussa, R. Moury, U. B. Demirci, T. Sener, P. Miele, *International Journal of Energy Research,* **2013**, *37,* 825.

[4] K. F. Aguey-Zinsou, J. R. Ares-Fernandez, *Energy & Environmental Science*, **2010**, *3*, 526.

[5] Z. T. Xiong, J. J. Hu, G. T. Wu, P. Chen, W. F. Luo, K. Gross, J. Wang, *Journal of Alloys and Compound*, **2005**, *398*, 235.

[6] H. Pan, S. Shi, Y. Liu, B. Li, Y. Yang, M. Gao, *Dalton Transactions*, **2013**, *42*, 3802.

[7] P. Chen, Z. T. Xiong, L. F. Yang, G. T. Wu, W. F. Luo, *Journal of Physical Chemistry B*, **2006**, *110*, 14221.

[8] D. E. Demirocak, S.S. Srinivasan, M. K. Ram, J. N. Kuhn, R. Muralidharan, X. Li, D. Y. Goswami, E. K. Stefanakos, *International Journal of Hydrogen Energy*, **2013**, *38*, 10039.

[9] B. Li, Y. Liu, J. Gu, M. Gao, H. Pan, *Chemistry-An Asian Journal*, **2013**, *8*, 374.

[10] J. Hu, Y. Liu, G. Wu, Z. Xiong, Y. S. Chua, P. Chen, *Chemistry of Materials*, **2008**, *20*, 4398.

[11] J. Wang, T. Liu, G. Wu, W. Li, Y. Liu, C. M. Araijo, R. H. Scheicher, A. Blomqvist, R. Ahuja, Z. Xiong, P. Yang, M. Gao, H. Pan, P. Chen, *Angewandte Chemie-International Edition*, **2009**, *48*, 5828.

[12] C. Li, Y. Liu, Y. Pang, Y. Gu, M. Gao, H. Pan, *Dalton Transactions,* **2014**, *43*, 2369.

[13] C. Liang, Y. Liu, M. Gao, H. Pan, *Journal of Material Chemisty A*, **2013**, *1*, 5031.

[14] A. Sudik, J. Yang, D. Halliday, C. Wolverton, *Journal of Physical Chemistry C*, **2007**, *117*, 6568.

[15] R. R. Shashi, H. Raghubanshi, M. A. Shaz, O. N. Srivastava, *International Journal of Hydrogen Energy*, **2012**, *37*, 3705.

[16] C. Price, J. Gray, R. Lascola Jr., D. L. Anton, *International Journal of Hydrogen Energy*, **2012**, *37*, 2742.

[17] C. Liang, Y. Liu, H. Fu, Y. Ding, M. Gao, H. Pan, *Journal of Alloys and Compound*, **2011**, *509*, 7844.

[18] J. Yang, S. Hirano, *Adv. Mater.*, **2009**, *21*, 3023.

[19] L. Xie, Y. Liu, G. Li, X. Li, *Journal of Physical Chemistry C*, **2009**, *113*, 14523.

[20] Y. Liu, K. Zhong, K. Luo, M. Gao, H. Pan, Q. Wang, *Journal of the American Chemical Society*, **2009**, *131*, 1862.

[21] P. E. de Jongh, M. Allendorf, J. J. Vajo, C. Zlotea, *MRS Bull.*, **2013**, *38*, 488.

[22] J. Wang, J. Hu, Y. Liu, Z. Xiong, G. Wu, H. Pan, P. Chen, *Journal of Materials Chemistry*, **2009**, *19*, 2141.

[23] T. K. Nielsen, F. Besenbacher, T. R. Jensen, *Nanoscale*, **2011**, *3*, 2086.

[24] X. Fan, X. Xiao, J. Shao, L. Zhang, S. Li, H. Ge, Q. Wang, L. X. Chen, *Nano Energy*, **2013**, *2*, 995.

[25] P. E. de Jongh, P. Adelhelm, *ChemSusChem*, **2010**, *3*, 1332.

[26] T. K. Nielsen, M. Polanski, D. Zasada, P. Javadian, F. Besenbacher, J. Bystrzycki, J. Skibsted, T. R. Jensen, *ACS Nano*, **2011**, *5*, 4056.

[27] J. Gao, P. Adelhelm, M. H. W. Verkuijlen, C. Rongeat, M. Herrich, P. J. M. van Bentum, O. Gutfleisch, A. P. M. Kentgens, K. P. de Jong, P. E. de Jongh, *Journal of Physical Chemistry C*, **2010**, *114*, 4675.

[28] Y. Yan, Y. A. Au, D. Rentsch, A. Remhof, P. E. de Jongh, A. Zuttel, *Journal of Materials Chemistry A*, **2013**, *1*, 11177.

[29] A. F. Gross, J. J. Vajo, S. L. Van Atta, G. L. Olson, *Journal of Physical Chemistry C*, **2008**, *112*, 5651.

[30] T. K. Nielsen, U. Bösenberg, R. Gosalawit, M. Dornheim, Y. Cerenius, F. Besenbacher, T. R. Jensen, *ACS Nano*, **2010**, *4*, 3903.

[31] M. L. Christian, K. F. Aguey-Zinsou, *ACS Nano*, **2012**, *6*, 7739.

[32] P. E. de Jongh, R. W. P. Wagemans, T. M. Eggenhuisen, B. S. Dauvillier, P. B. Radstake, J. D. Meeldijk, J. W. Geus, K. P. de Jong, *Chemistry of Materials*, **2007**, *19*, 6052.

[33] R. Demir-Cakan, W. S. Tang, A. Darwiche, R. Janot, *Energy & Environmental Science*, **2011**, *4*, 3625.

[34] P. Ngene, P. Adehelm, A. M. Beale, K. P. de Jong, P. E. de Jongh, *Journal of Physical Chemistry C*, **2010**, *114*, 6163.

[35] S. Zheng, F. Fang, G. Zhou, G. Chen, L. Ouyang, M. Zhu, D. L. Sun, *Chemistry of Materials*, **2008**, *20*, 3954.

[36] A. Gutowska, L. Li, Y. Shin, C. M. Wang, X. S. Li, J. C. Linehan, R. S. Smith, B. D. Kay, B. Schmid, W. Shaw, M. Gutowski, T. Autrey, *Angewandte Chemie-International Edition*, **2005**, *44*, 3578.

[37] H. Kim, A. Karkamkar, T. Autrey, P. Chupas, T. Proffen, *Journal of Physical Chemistry*, **2009**, *131*, 13749.

[38] C. F. Zhang, H. B. Wu, C. Z. Yuan, Z. P. Guo, X. W. Lou, *Angewandte Chemie-International Edition*, **2012**, *51*, 9592.

[39] H. Y. Leng, Z. Wu, W. Y. Duan, G. L. Xia, Z. L. Li, *International Journal of Hydrogen Energy*, **2012**, *37*, 903.

[40] C. Li, Y. Liu, Y. Yang, M. Gao, H. Pan, *Journal of Materials Chemistry A*, **2014**, *2*, 7345.

[41] C. Li, Y. Liu, R. Ma, X. Zhang, Y. Li, M. Gao, H. Pan, *ACS Applied materials & interfaces*, **2014**, *6*, 17024.

[42] H. Cao, H. Wang, T. He, G. Wu, Z. Xiong, J. Qiu, P. Chen, *RSC Advances,* **2014**, *4*, 32555.

[43] Z. T. Xiong, G. T. Wu, J. J. Hu, P. Chen, W. F. Luo, J. Wang, *Journal of Alloys and Compound*, **2006**, *417*, 190.

[44] H. Wu, *Journal of the American Chemical Society*, **2008***, 130*, 6515.

7   CHAPTER 7 CARBON-COATED LI$_3$N NANOFIBERS FOR ADVANCED HYDROGEN STORAGE

7.1 Introduction

Li-N-H-based compounds are an appealing class of hydrogen storage materials, with a total sorption of 11.5 wt.% hydrogen for lithium nitride (Li$_3$N) by the following two-step reactions: [1-5]

$$Li_3N + 2H_2 \Leftrightarrow Li_2NH + LiH + H_2 \qquad (7.1)$$

$$Li_2NH + LiH + H_2 \Leftrightarrow LiNH_2 + 2LiH \qquad (7.2)$$
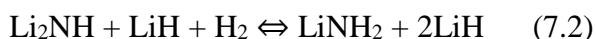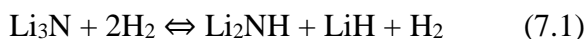
During heating treatment, the interaction among various intermediates not only promotes H$_2$ release but also prevents the formation of ammonia from the decomposition of pure LiNH$_2$. However, due to the much higher enthalpy change (ΔH) in the case of the first reaction (- 115 kJ mol^{-1}) compared with that of the second step (- 45 kJ mol^{-1}), a complete desorption to generate Li$_3$N required temperatures above 320 $^{\circ}$C even in dynamic vacuum[5]. Therefore, only the second reaction with a favorable enthalpy has been regarded as a viable pathway to reversibly storage H$_2$, which only provides a storage capacity of 6.5 wt. % based on pure Li$_2$NH.[6] In addition, as a consequence of the multiple solid-state intermediate phases, it is evident that the thermodynamics and kinetics for either dehydrogenation or hydrogenation of Li-N-H system extremely depend on the reactivity and the diffusivity of active materials across the reactive interfaces.[7] Therefore, the H$_2$ release normally requires a high temperature of ~280 $^{\circ}$C at a pressure close to 1 atm due to the sluggish kinetics even for the 2nd reaction.[8] Moreover, upon consecutive heating treatment, the particle growth of active substrates and phase separation between LiNH$_2$ and LiH are inevitable, resulting in the release of NH$_3$, which will further degrade the cycling H$_2$ storage capacity over time and introduce an impurity into the H$_2$ stream that is harmful to PEM fuel cells.[9] For example, the H$_2$ capacity

of bulk Li_3N decreased down to 0.5 wt. % after eleven cycles, which is less than 10% of its initial capacity.[10] Hence, it is of great importance to resolve these issues before before the practical application of Li-N-H based hydrogen storage materials.

Fortunately, recent theoretical calculations have shown that the nanostructuring of hydrogen storage materials is a viable way to significantly enhance the hydrogen storage performance by decreasing both diffusion path lengths for hydrogen and active substrates and the thickness of reactive interfaces during H_2 ab-/desorption.[11, 12] However, the direct synthesis of hydrogen storage materials within nanoscale, including the Li-N-H-based system, is greatly limited by the inherent difficulty in stabilizing the thus-synthesized particles and maintaining the nanoeffects upon consecutive heating treatment.[13] Nanoconfinement, which can efficiently prevent particle sintering and growth, therefore, has been widely adopted to infiltrate the hydrides into mesoporous scaffolds.[14, 15] The thus-formed nanosized materials resulting from the space-confinement functions of templates subsequently exhibited highly enhanced hydrogen storage properties,[14] e.g., lower dehydrogenation temperature,[16] change of reaction pathway,[17] and even promoted reversibility,[18] due to the modification of thermodynamics and/or kinetics. Unfortunately, several drawbacks are still present for the adoption of general nanoconfinement. Firstly, a porous template with high specific surface area and clean surface that is inert to the targeted hydrogen storage materials is a prerequisite for the infiltration. Clearly, it is troublesome to find or synthesize a proper template that fulfills all the requirements. Secondly, as a result of the mesoporous characteristics of scaffolds, the blocking of pores is inevitable during the infiltration process, which enormously impedes the full encapsulation and the well distribution of reactive substrates. Thirdly, the overall infiltration process is rather tedious due to the slow kinetics and the long ranges for

the diffusion of solution, therefore, successive steps of infiltration and drying are necessary to achieve a relatively high loading level and good distribution. Thus a simple one-pot method of synthesizing space-confined hydrogen storage materials without using any template would be highly appreciated in order to avoid the above-mentioned disadvantages.

Electrospinning is an inexpensive, simple and versatile technique for the fabrication of continuous nanofibers[19, 20] of various materials, e.g., polymers, ceramic metal oxides, metals, and so forth, under electrostatic force.[19] More importantly, by adopting different precursors with compatible properties, a variety of porous, hollow, amorphous or polycrystalline carbon nanowires[21] with the encapsulation and well distribution of metal-containing compounds can be directly prepared through electrospinning followed by a simple calcination process. Herein, we present a simple one-pot template-free synthesis of carbon-coated Li_3N porous nanofibers via electrospinning with low-cost. In particular, discrete carbon nanofibers comprising of well-distributed Li_3N can be prepared by the calcination of the as-electrospun PVA-coated LiN_3 nanofibers. Meanwhile, the micropores, mesopores and macropores can be further introduced by the decomposition of PVA and LiN_3 during the calcination. These features can effectively limit the growth of Li_3N particles and facilitate the H_2 diffusion through pores of carbon walls to react with the active species. To the best of our knowledge, it is the first report on the *in-situ* synthesis of carbon-coated complex hydrides with 3D porous nanostructures.

7.2 Experimental section

7.2.1 Synthesis of 3D porous carbon-coated Li_3N nanofibers

Poly(vinyl alcohol) (0.5 g, Alfa Aesar, M_v = 88000, CAS: 9002-89-5) was mixed with deionized water (5 mL) and stirred in water bath at 90 ^{o}C for 8 h to make PVA solution. After cooling down to room temperature, LiN_3 solution (0.4 mL, 20 wt. %) in water was then added and vigorously stirred for 6 h to make a homogeneous spinning dope. The resultant precursor solution was poured into a syringe with a 18-gauge blunt tip needle. The flow rate of solution was approximately 500 μL h^{-1} controlled by a syringe pump (Longer, TJP-3A, China), and a grounded stainless steel plate was horizontally placed 10 cm from the needle to collect the nanowires. A high voltage of 15 kV was applied by a high-voltage power supply. The as-collected electrospun fibers were firstly dewatered at a temperature of 75 ^{o}C under dynamic vacuum for 15 h and then calcined at 550 ^{o}C for 3 h under dynamic N_2 atmosphere to obtain the 3D porous carbon-coated Li_3N nanofibers (heating rate: 2 ^{o}C min^{-1}). The mass concentration of Li_3N in the as-prepared fibers, which was calculated to be 18.6%, was obtained by elemental analysis.

7.2.2 Hydrogen storage tests

The hydrogen storage properties of the thus-synthesized carbon-coated Li_3N nanofibers were carried out on a Sievert's apparatus, named as gas reaction controller (GRC, Advanced Materials Corp., USA). The H_2 absorption kinetics measurements were performed at various temperatures with an initial pressure of 35 atm, and the desorption properties were detected at various temperatures under a hydrogen pressure below 0.02 atm. The pressure-concentration isotherms (PCI) measurements were performed at the desired temperatures, and the equilibrium time for each point was

600 s. For comparison purpose, the carbon scaffold mass was excluded when determining the amount of hydrogen released from the relevant composites containing carbon scaffolds.

Mass spectrometry (MS; Hidden HPR 20) was conducted from room temperature, using a heating rate of 5 ^oC min^{-1} under dynamic nitrogen with a purge rate of 80 ml min^{-1}. Differential scanning calorimetry (DSC) measurements were performed by TAQ 2000 DSC under N_2 with a gas flow of 40 mL min^{-1} at a heating rate of 5 ^oC min^{-1}.

7.3 Results and discussion
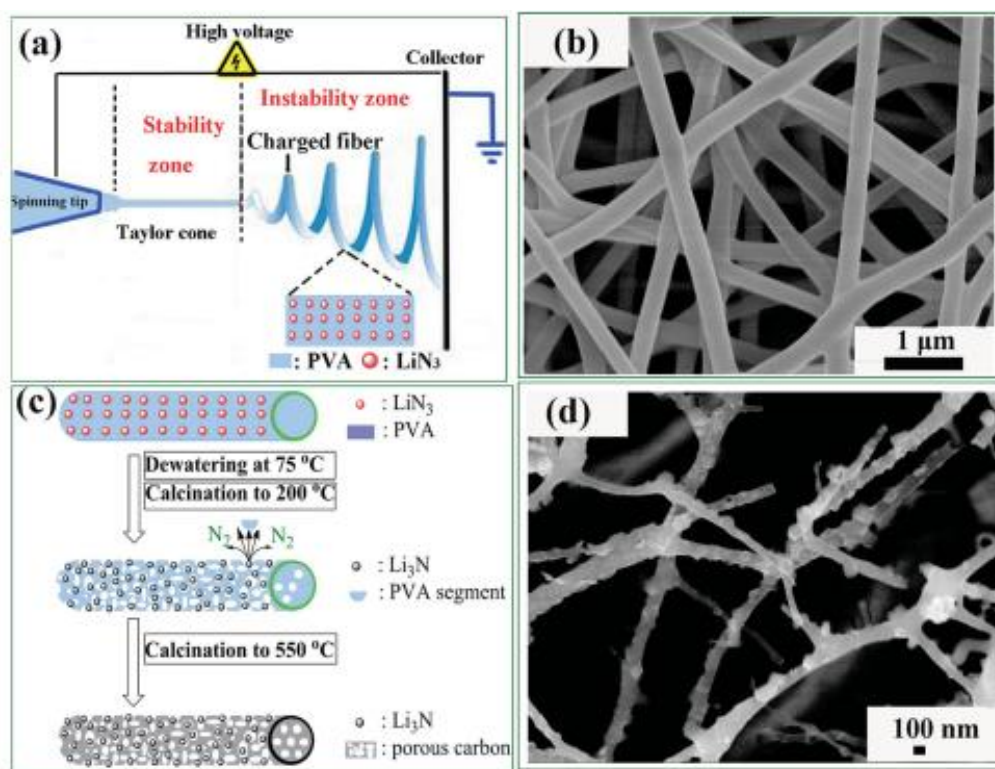
Figure 7. 1 (a) Schematic illustration of the electrospinning process of a LiN_3-PVA mixture using a single-needle nozzle; (b) SEM micrograph of the as-collected PVA-coated LiN_3 nanofibers; (c) Proposed synthetic scheme for the formation of Li_3N nanoparticles encapsulated in 3D porous carbon nanofibers during the calcination; (d) SEM image of the carbon-coated Li_3N nanofibers.
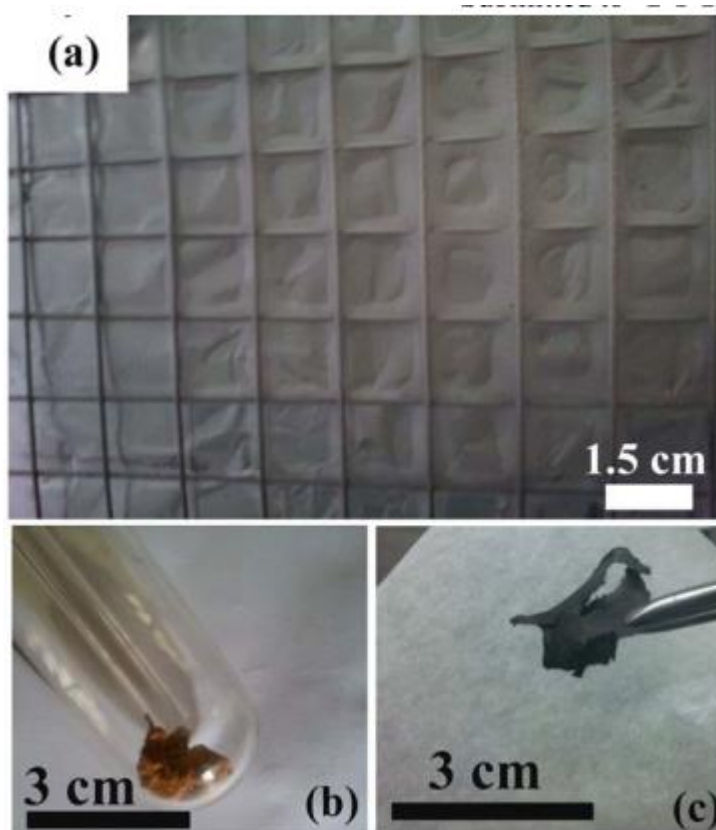
Figure 7. 2 The photos of the as-electrospun PVA-coated LiN₃ nanofibers (a) at room temperature, (b) after calcination to 200 ℃ (the color of fibers transformed to the characteristic color of Li₃N, confirming the formation of Li₃N), and (c) after calcination to 550 ℃ for carbonization.
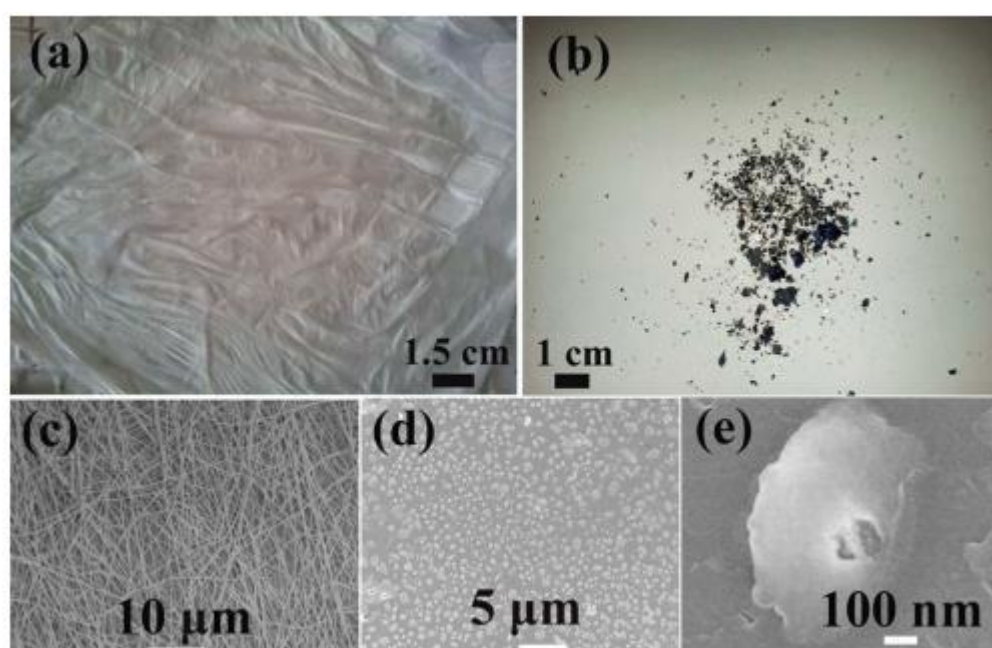
Figure 7. 3 The views of the as-electrospun PVA nanofibers (a) at room temperature, and (b) after calcination to 550 ℃. SEM images of the as-electrospun PVA nanofibers (c) at room temperature and (d, e) after calcination to 550 ℃.

An aqueous precursor solution containing LiN_3 and poly (vinyl alcohol) (PVA) was used for the electrospinning process. A sketch of the typical electrospinning setup is illustrated in Figure 7.1a. A high voltage is applied between the needle and the collector. Once the strength of the electric field is high enough to allow the electrostatic forces to overcome the surface tension of the polymer solution, a liquid jet formed via the outer solutions is stretched by electrostatic forces to generate PVA-coated LiN_3 fibers. The scanning electron microscopy (SEM) image in Figure 7.1b reveals the morphology of the as-electrospun fibers, demonstrating that the as-synthesized nanofibers are long and continuous with a relatively uniform diameter distribution of ~ 200 nm. As shown in Figure 7.1c, the as-collected electrospun fibers were firstly dewatered in dynamic vacuum at 75 ℃, and then stabilized under N_2 atmosphere at 200 ℃ in order to transform LiN_3 into Li_3N nanoparticles encapsulated in the PVA fibers. Due to an explosive release of N_2 during this reaction, small pieces of PVA were repulsed from the surface of the nanofibers. After carbonization under N_2 atmosphere at a temperature up to 550 ℃, the fibers were transformed into porous carbon fibers with Li_3N nanoparticles embedded in. Figure 7.1d shows the SEM image of the carbon-coated Li_3N nanofibers. It can be observed that the nanofibers are uniform with an average diameter of ~ 100 nm. The view of the as-electrospun fibers shown in Figure 7.2 clearly presents the color change from white to the ruby red, which is the characteristic color of Li_3N, after heating to 200 ℃, indicating the transformation of LiN_3 into Li_3N. On further calcination to 550 ℃, a carbonized film with the encapsulation of Li_3N was formed, whereas the pure PVA fibers through thermolysis

cannot maintain the firm film and no fibrous structure was observed in the SEM images (Figure 7.3). Elemental analysis reveals that the carbonization yield of the LiN$_3$ added PVA nanofibers is 16.6%, which is significantly higher than that of the pure PVA fibers (lower than 8%) as confirmed by the TG result (Figure 7.4). This suggests that the incorporation of LiN$_3$ into the precursor also plays an important role in improving the carbonization yield of PVA and thus stabilizing the structure of nanofibers.
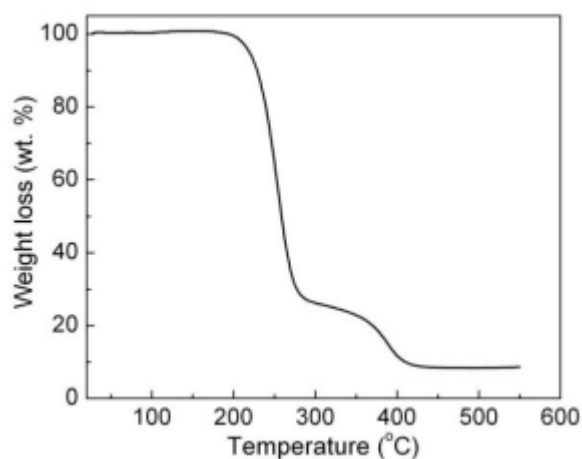
Figure 7. 4 TGA curves of the as-electrospun PVA nanofibers after calcination to 550 ºC.
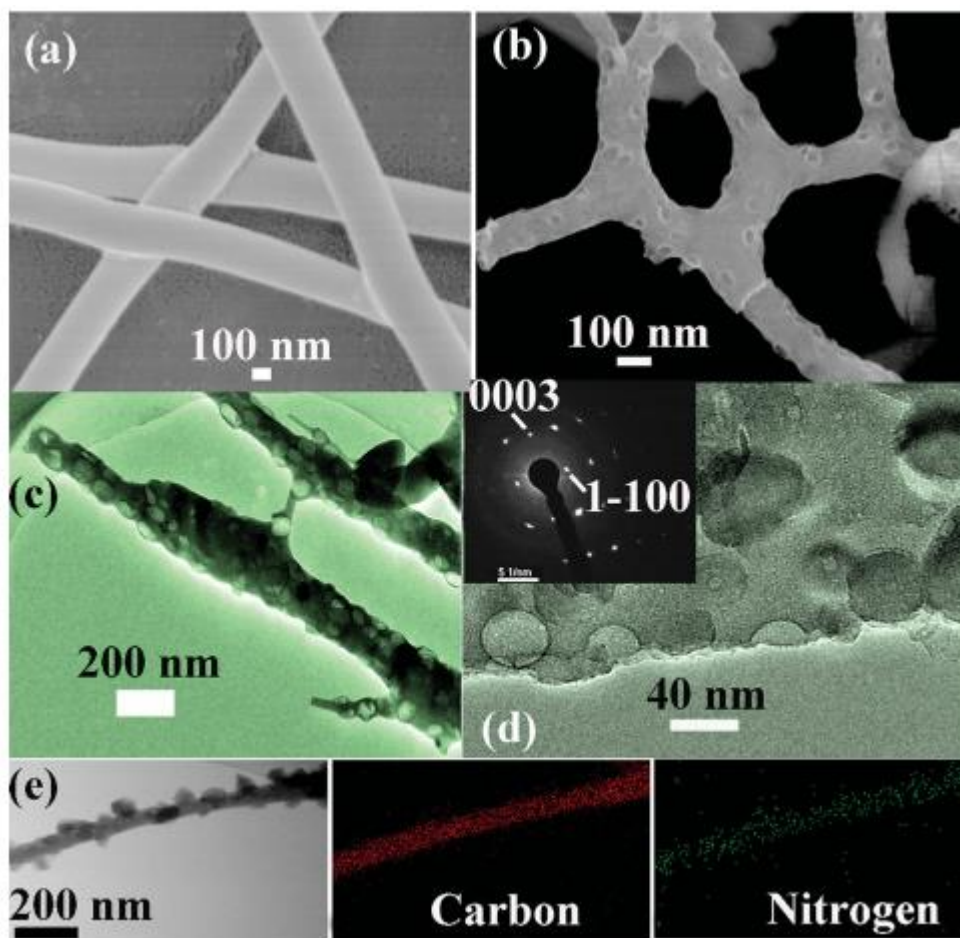
Figure 7. 5 (a) SEM image of the as-electrospun PVA-coated LiN$_3$ nanofibers; (b) SEM and (c, d) TEM images of the carbon-coated Li$_3$N nanofibers (the inset of d shows the corresponding SAED pattern of Li$_3$N nanoparticles); (e) TEM image and the corresponding elemental mapping of a single carbon-coated Li$_3$N nanofiber.
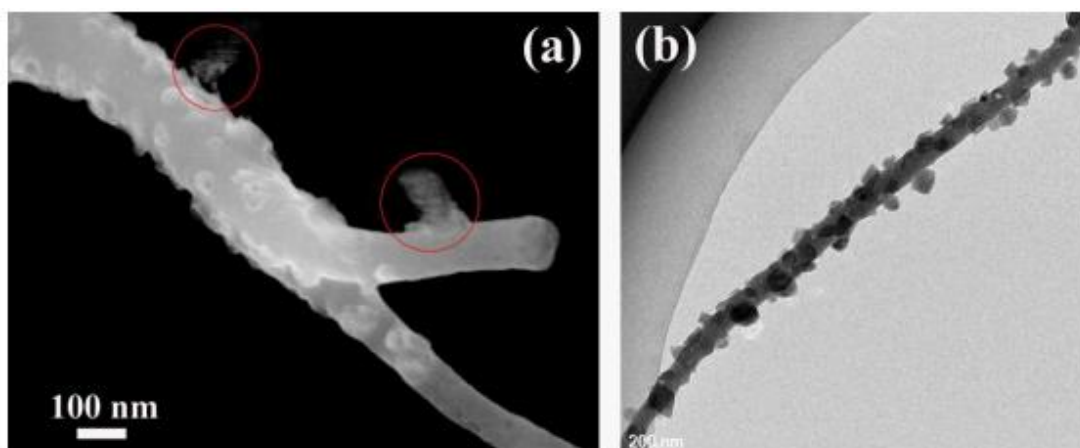
Figure 7. 6 (a) SEM and (b) TEM images of the as-prepared carbon-coated Li_3N nanofibers. Red circles in (a) indicate that a small piece of relic still existed after calcination due to the explosive release of N_2 from the LiN_3.
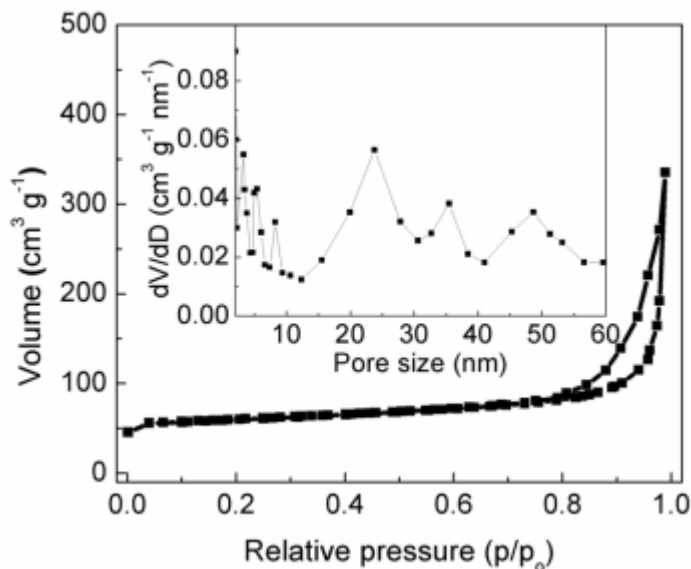
Figure 7. 7 N_2 sorption isotherm and pore size distribution (inset) of the as-electrospun carbon-coated Li_3N nanofibers.

Table 7. 1 Pore structure parameters for the as-electrospun carbon-coated Li_3N nanofibers.

Sample	S_{BET} ($m^2 g^{-1}$)	S_{ext} ($m^2 g^{-1}$)	S_{mic} ($m^2 g^{-1}$)	V_t ($m^3 g^{-1}$)
The as-electrospun carbon-coated Li_3N nanofibers	365	298	67	0.681

Note: S_{BET}, S_{ext}, S_{mic}, and V_t are the BET surface area, external surface area, micropore surface area and total pore volume, respectively.

Figure 7.5a shows a magnified SEM image of the as-electrospun PVA-coated LiN_3 fibers with smooth surface, whereas, after calcination, the *in-situ* formed carbon-coated Li_3N nanofibers (Figure 7.5b) reveal both mesopores and macropores on the surface with various diameters (10-55 nm), resulting from the loss of PVA as a result of N_2 strong releasing. Due to the high toughness of PVA, the fibrous nanostructure was maintained and some relics (Figure 7.6) can still be observed on the surface of the

carbonized nanofibers, clearly demonstrating the intense release of N_2 from the PVA-coated LiN_3 nanofibers. The hollow interior and geometrical structure of the as-obtained Li_3N nanofibers with the carbon coating are directly elucidated by transmission electron microscopy (TEM), as shown in Figures 7.5c and d. The N_2 adsorption-desorption plots (Figure 7.7) of the carbon-coated Li_3N nanofibers present a type IV isotherm with a steep increase of nitrogen absorption at a high relative pressure, indicating the main contribution of large size pores to the pore volume as indicated in the TEM image (Figure 7.5c). Despite of these large pores, some small pores with a diameter less than 10 nm were also detected, which is consistent with the observation in Figure 7.5d. Furthermore, an obvious adsorption uptake at low relative pressure indicates the presence of micropores in the carbon-coated Li_3N nanofibers, which may be attributed to the disordered packing of the turbostratic carbon sheets and clusters resulting from the carbonization process of micro-/nanosctructured polymer, which leads to the formation of free volume and microporosity in the carbon matrix in general[22]. Moreover, a specific surface area of 365 m^2 g^{-1} and pore volume of 0.681 cm^3 g^{-1} were obtained for the as-prepared carbon-coated Li_3N nanofibers according to the Brunauer-Emmett-Teller (BET) analysis (Table 7.1), and the t-plot method gives the surface area of micropores and external large-sized pores equal to 67 and 298 m^2 g^{-1}, respectively, which further demonstrates that the carbonized nanofibers are hierarchically full of micropores, mesopores and macropores induced by the disordered packing of the turbostratic carbon sheets and/or clusters and the volume expansion of PVA during the release of N_2 stemming from the well distribution of LiN_3 in the as-electrospun nanofibers. Therefore, it is verified that, based on its special thermolysis properties, metallic azides can be further explored as porogen on the synthesis of 3D porous substrates. The spot- and ringlike patterns in the selected-area

electron diffraction (SAED) pattern (inset of Figure 7.5d) can be indexed to the β-Li₃N

with a hexagonal unit cell parameter of a = 3.552 Å and c = 6.331 Å along the [0001]

axis, which corresponds well with the XRD results (Figure 7.8) and the previous

report[23]. The average size of Li₃N nanocrystals calculated through the Debye-

Scherrer's equation by analyzing the XRD diffraction peaks is ~ 3.7 nm. Such a small

size is attributed to the well-distribution and the confined aggregation of the Li₃N

nanoparticles in the carbon nanofibers. Additionally, the C map agrees well with the

structure of the nanofibers and the N map corresponds well with the C map from the

energy dispersive spectroscopy (EDS) elemental maps for the carbon-coated Li₃N

nanofibers (Figure 7.5e), directly authenticating a good dispersion of Li₃N

nanoparticles inside the carbonized nanofibers.
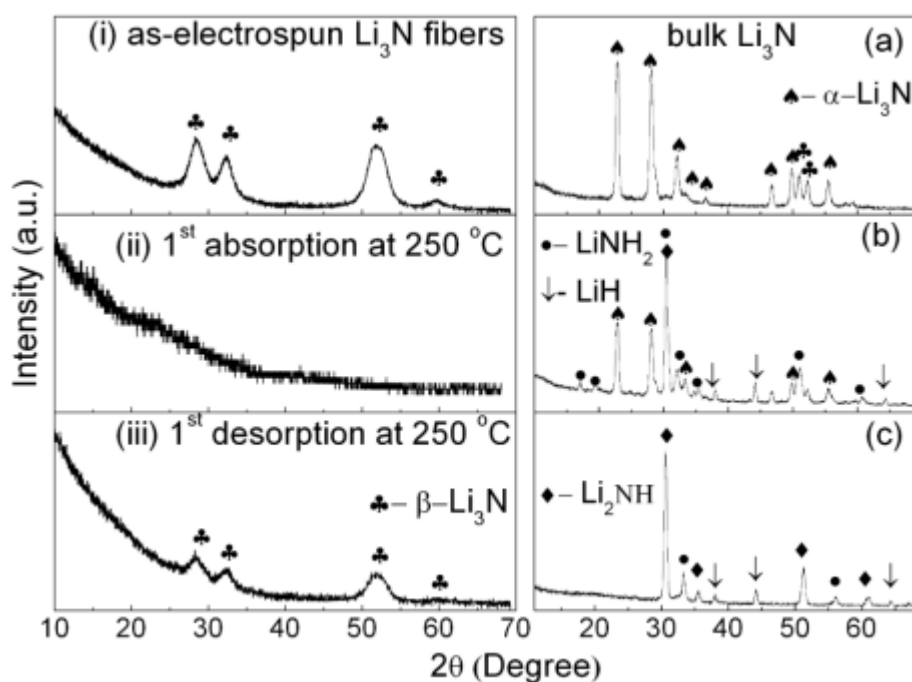
Figure 7. 8 X-ray diffraction results of the as-electropun Li₃N nanofibers (left) and

bulk Li₃N (right). (i) the as-electrospun carbon-coated Li₃N nanofibers at room

temperature; (ii) the Li₃N nanofibers after hydrogenation at 250 °C under 35 atm for

60 min; (iii) the hydrogenated Li₃N nanofibers after desorption at 250 °C for 180 min

(iii); (a) bulk Li₃N; (b) the bulk Li₃N powder after hydrogenation at 250 °C under 35 atm for 120 h. (c) The fully hydrogenated bulk Li₃N after dehydrogenation at 350 °C for 180 min.
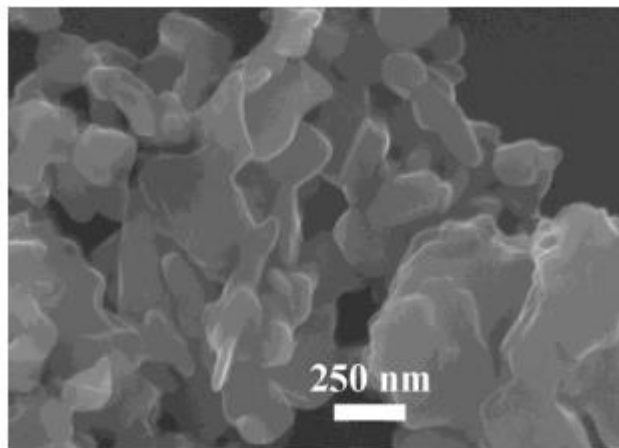
Figure 7. 9 SEM of the commercial Li₃N powders after ball milling.
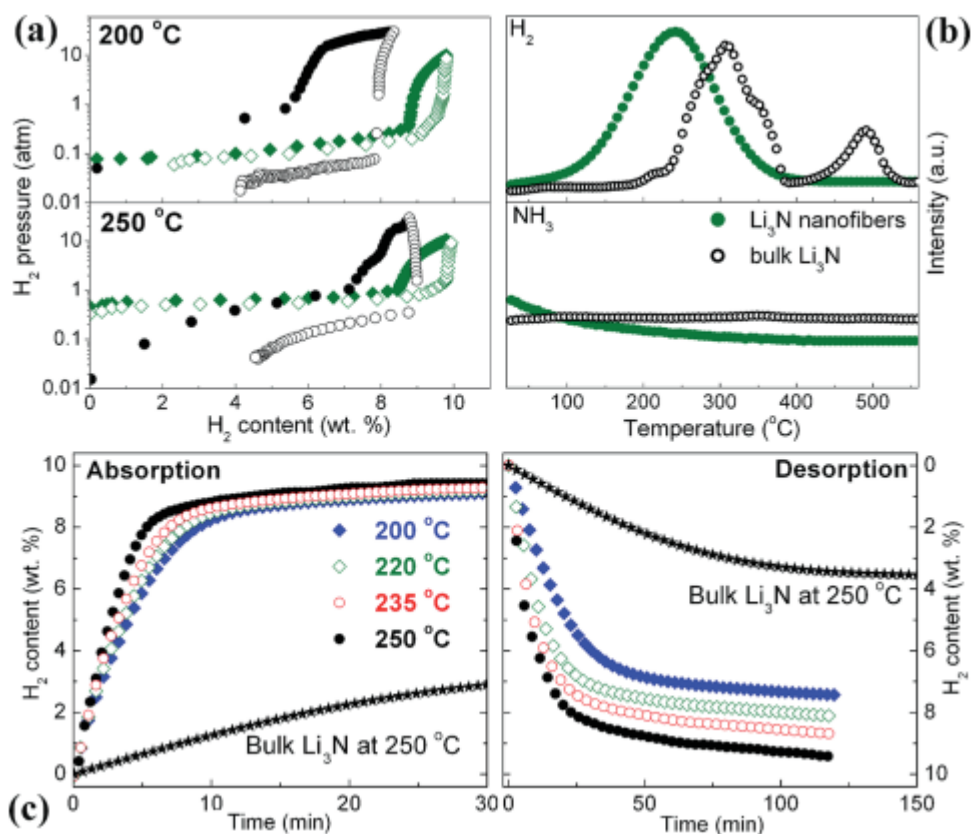
Figure 7. 10 (a) Pressure-composition isotherms (PCI) of the carbon-coated Li₃N nanofibers (◆: Absorption; ◇: Desorption) and bulk Li₃N (●: Absorption; ○:

Desorption) at the temperatures of 200 °C and 250 °C, respectively; (b) Mass spectra of the carbon-coated Li_3N nanofibers and bulk Li_3N after the complete hydrogenation upon heating to 560 °C; (c) Hydrogen absorption and desorption curves of the carbon-coated Li_3N nanofibers at different temperatures, including bulk Li_3N at 250 °C for comparison. Carbon was not considered as an active component for the hydrogen storage measurements.

The hydrogen storage properties of the as-prepared carbon-coated Li_3N nanofibers was firstly measured by Pressure-composition isothermal (PCI) analysis in relation to commercial Li_3N powder (Figure 7.9) as shown in Figure 7.10a. At 200 °C, ~ 8 wt. % hydrogen was absorbed by pure Li_3N with a plateau pressure at ~ 0.3 atm, of which only 47.5%, i.e., 3.8 wt. % H_2, could be released at a pressure below 0.08 atm, owing to the decomposition of $LiNH_2$ interacting with LiH[4]. It should be noted that the desorption isotherm shows considerable hysteresis from that of the absorption. By contrast, for the carbon-coated Li_3N nanofibers, both the hysteresis and slope between absorption and desorption isotherm are much smaller in comparison with the bulk counterparts. Moreover, the desorption plateau pressure is much higher than that of the bulk Li_3N, indicating the significant thermodynamic enhancement for the carbon-coated Li_3N nanofibers. Specifically, the absorption isotherm has a slope plateau of under 0.15 atm with a capacity of ~ 10 wt. %, which is close to the theoretical H_2 capacity for Li_3N, at a temperature as low as 200 °C. The desorption isotherm presents a H_2 capacity of ~ 7.65 wt. % and 9.9 wt. % at 200 °C and 250 °C, respectively, which account for 76.5% and 99% of the absorbed hydrogen, indicating that a full reversibility of Li_3N can be realized at a temperature as low as 250 °C (the lowest temperature reported to date for a complete reversibility of Li_3N). This was further confirmed by the XRD (Figure 7.8) and FTIR (Figure 7.11) results, in which the β-

Li$_3$N was regenerated for the hydrogenated Li$_3$N nanofibers after dehydrogenation at 250 °C for 180 min. However, only a mixture of Li$_2$NH/LiH (Figure 7.8) was formed for the bulk sample even heated at a higher temperature of 350 °C for 180 min. The mass spectra (MS) results in Figure 7.10b delineate that the hydrogenated bulk Li$_3$N undergoes a two-step decomposition, in which the 1st step with a peak temperature at 307 °C corresponds to the combination of LiH with LiNH$_2$ to form Li$_2$NH, and the 2nd step peaked at 491 °C corresponds to the formation of Li$_3$N through the reaction of Li$_2$NH with LiH.[4, 5] In comparison, the hydrogenated carbon-coated Li$_3$N nanofibers show a one-step decomposition with the onset and peak temperatures of H$_2$ desorption downshifted to ~ 100 and 250 °C, respectively, which are 100 °C and 57 °C lower than that for the 1st step reaction between LiNH$_2$ and LiH, coinciding well with the above PCT and XRD discussions. To clarify the effect of carbon on the thermodynamics of hydrogen sorption of Li$_3$N, the dehydrogenation performance of a ball-milled composite of carbon with Li$_3$N after hydrogenation was investigated. It shows comparable process with that of pure Li$_3$N (Figure 7.12), indicating the important role of size-confined effect in improving the thermodynamics of hydrogen sorption of Li$_3$N.
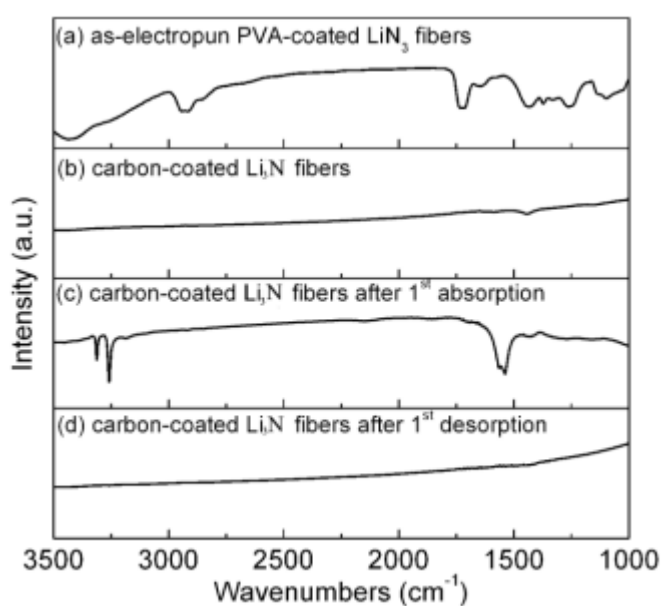
Figure 7. 11 FTIR spectra of (a) as-electrospun PVA-coated LiN$_3$ nanofibers, (b) the

carbon-coated Li$_3$N nanofibers; (c) the carbon-coated Li$_3$N nanofibers after 1st H$_2$

absorption at 250 ^{o}C under 35 atm for 60 min; (d) the carbon-coated Li$_3$N nanofibers

after 1st H$_2$ desorption at 250 ^{o}C for 120 min.
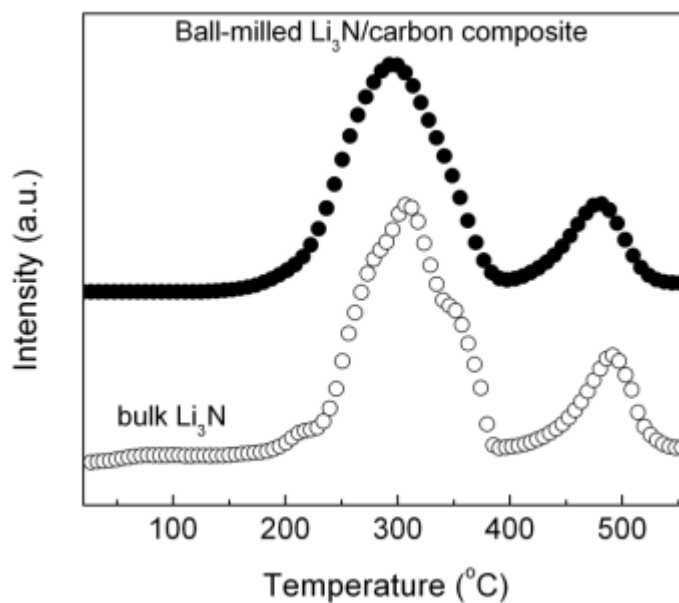
Figure 7. 12 Mass spectra of the bulk Li$_3$N powder compared with the ball-milled

composite of Li$_3$N and carbon powder after hydrogenation. The weight ratio between

Li$_3$N and carbon is 1:4, which is similar to the content of Li$_3$N in the electrospun

fibers after calcination.
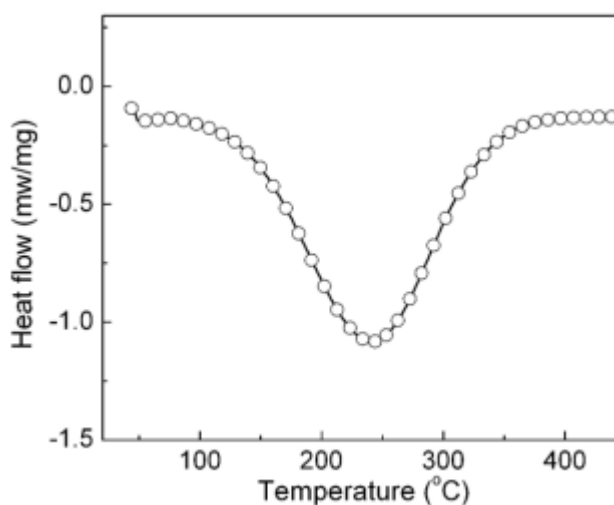
Figure 7. 13 DSC curves of the hydrogenated carbon-coated Li₃N nanofibers at a

heating rate of 5 °C min⁻¹ under dynamic N₂, which gave an enthalpy of ~65 kJ mol⁻¹

H₂, much lower than that from the LiNH₂ + 2LiH composite (~ 160 kJ mol⁻¹ H₂).

 The differential scanning calorimetry (DSC) results (Figure 7.13) from the thermal

decomposition of the hydrogenated Li₃N nanofibers reveal that the differential heat for

the dehydrogenation is calculated to be only ~ 65 kJ mol⁻¹ H₂, much lower than that

from the LiNH₂ + 2LiH composite (~ 160 kJ mol⁻¹ H₂)[4]. This result directly verifies

the remarkable enhancement of thermodynamics via encapsulation of Li₃N into porous

carbon nanofibers, leading to the regeneration of β-Li₃N at a low temperature of 250

°C. The formation of β-Li₃N instead of α-Li₃N, which is generally generated by the

complete dehydrogenation of the LiNH₂ + 2LiH composite in bulk form as indicated

in the XRD results (Figure 7.8) and the previous report[4, 5], was proposed to be a key

factor in modifying the thermodynamics of Li₃N towards the improved hydrogen

storage properties.[24]
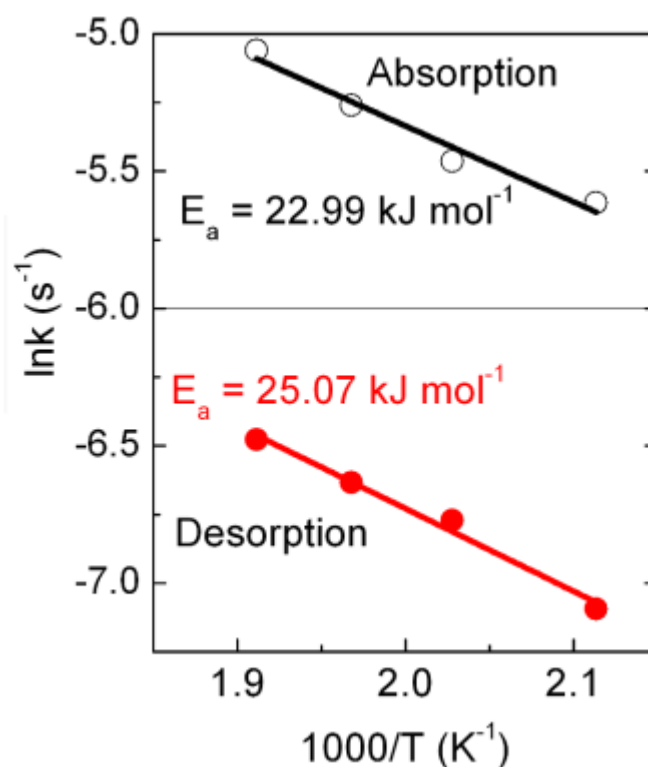
Figure 7. 14 Arrhenius plot for the isothermal H_2 absorption and desorption of the

carbon-coated Li_3N nanofibers.

The kinetics of hydrogen absorption/desorption in the samples of carbon-coated Li_3N nanofibers and pure Li_3N was further tested, using a Sieverts PCT-Pro at different temperatures (Figure 7.10c). The bulk Li_3N has a hydrogen uptake of ~ 3 wt. % after absorption for 30 min and a hydrogen release of ~ 3.6 wt. % after following desorption within 150 min at 250 °C. In comparison with the bulk Li_3N, not only do the operating temperatures decrease obviously, but also the absorption rate significantly increases. As presented in Figure 7.10d, the carbon-coated Li_3N nanofibers can absorb over 8 wt. % hydrogen at 200 °C within 10 min. During the desorption process, a hydrogen release as high as ~7.4 wt. % within 120 min was achieved at 200 °C and the value further increased to ~8, 8.5, and 9.2 wt. % at temperatures of 220 °C, 235 °C and 250 °C, respectively, over the same period of 120 min. To quantitatively estimate the enormously improved hydriding/dehydriding kinetics of the as-prepared carbon-coated Li_3N nanofibers, the apparent activation energy (E_a) during the absorption/desorption was determined by combining the Johnson-Mehl-Avrami equation with Arrhenius equation after fitting the experimental data at different temperatures. From the slope of the linear plot of ln k (k, rate constant) versus 1/T (T, absolute temperature), the activation energy (Figure 7.14) for H_2 absorption and desorption from the carbon-coated Li_3N nanofibers was verified to be 22.99 and 25.07 kJ mol^{-1}, respectively, significantly lower than that for the bulk counterpart (110 kJ mol^{-1} even under the catalysis effect of $TiCl_3$).[6]
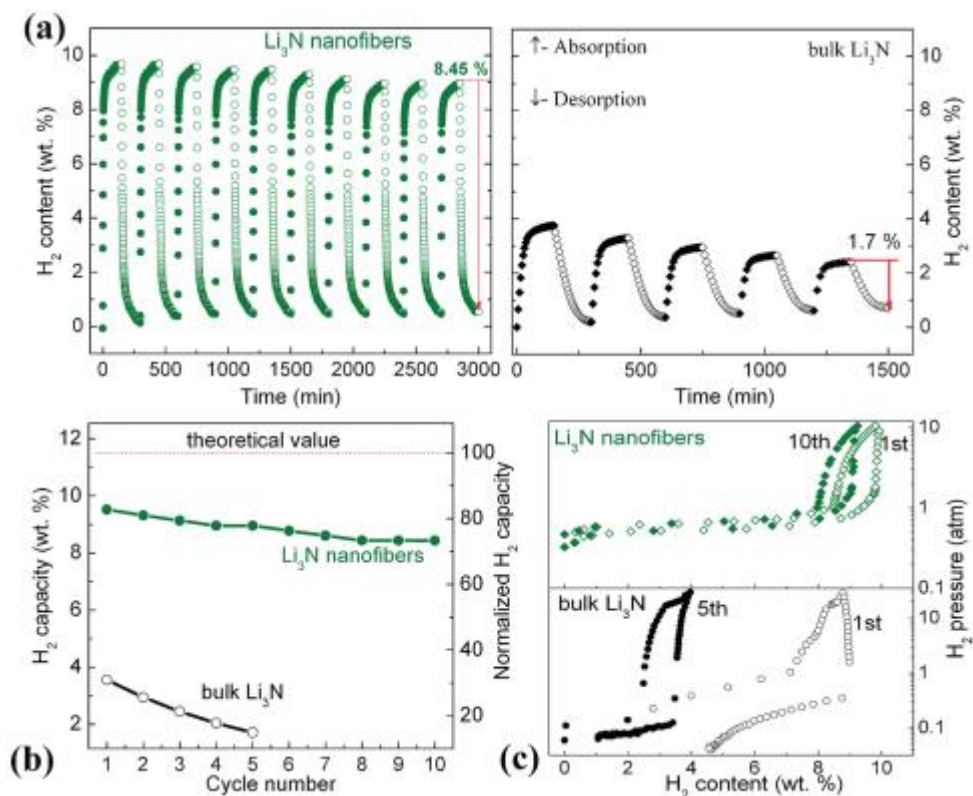
Figure 7. 15 (a) Reversible H_2 absorption (under 35 atm H_2) and desorption of the bulk Li_3N and carbon-coated Li_3N nanofibers at 250 °C; (b) Normalized H_2 capacity as a function of cycle number, where the hydrogen capacities are normalized to the theoretical value of Li_3N (11.48 wt. %); and (c) PCI curves for the bulk Li_3N and carbon-coated Li_3N nanofibers at 250 °C. Carbon was not considered as an active component for the hydrogen storage measurements.
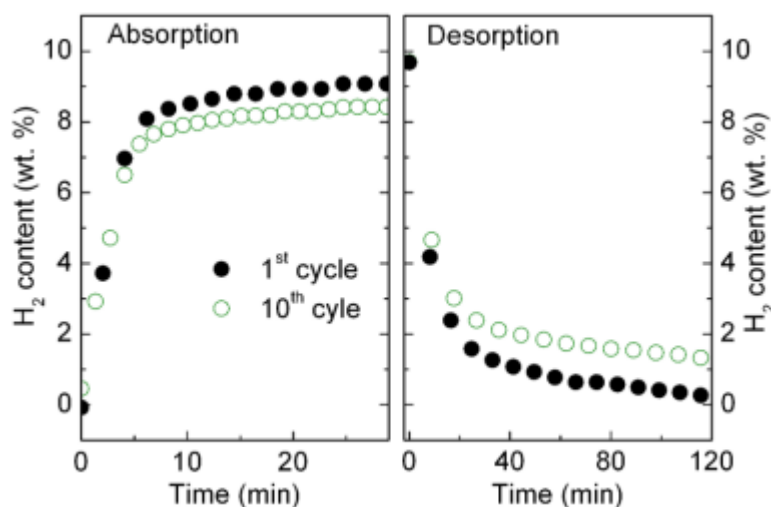
Figure 7. 16 Comparison of the kinetics for H_2 absorption/desorption of the carbon-coated Li_3N nanofibers between the 1st and 10th cycle at the temperature of 250 °C. The absorption was conducted under a H_2 pressure of 35 atm.
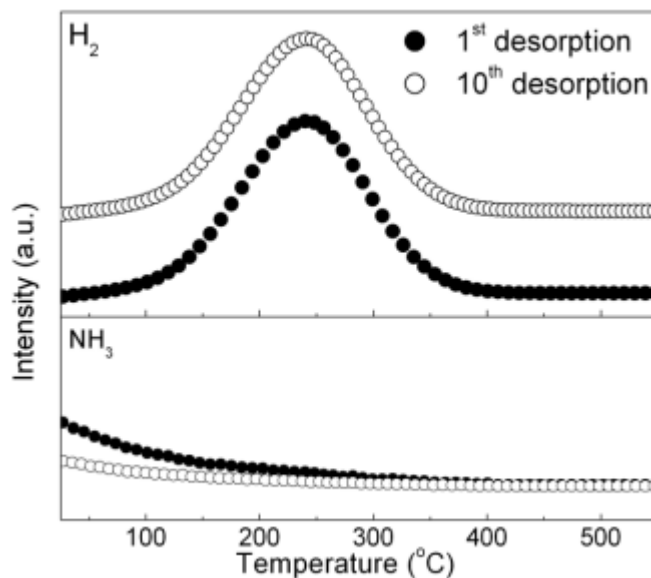
Figure 7. 17 Mass spectra of the carbon-coated Li_3N nanofibers during the 1st and 10th desorption cycles.
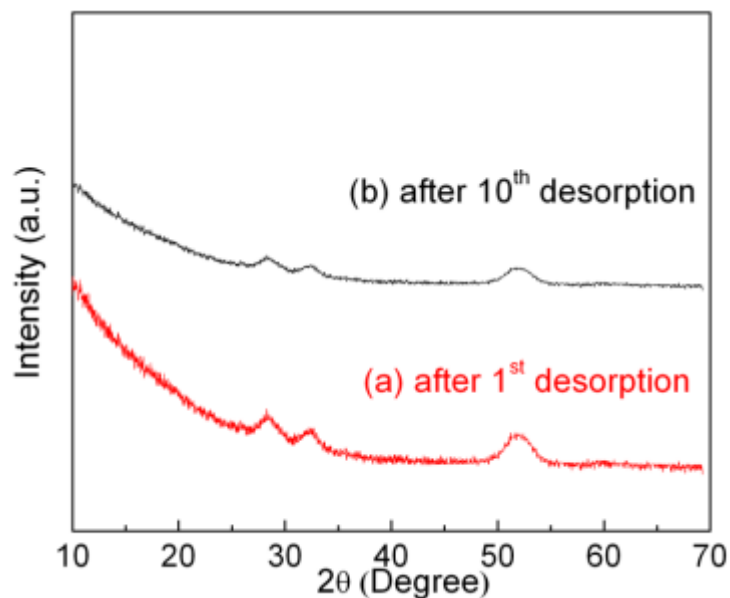
Figure 7. 18 X-ray diffraction patterns of the carbon-coated Li_3N nanofibers and the dehydrogenated product after the 10th desorption.

Subsequently, the H_2 absorption and desorption cycling performance of the carbon-coated Li_3N nanofibers was investigated and compared with that of the bulk Li_3N. As shown in Figure 7.15a, the amount of H_2 released from the bulk sample significantly decreased upon successive sorption treatments, from ~4 wt. % for the 1st desorption to 1.7 wt. % for the 5th desorption. By contrast, the hydrogen sorption capacity of the carbon-coated Li_3N nanofibers was well-preserved even through 10 cycles with constant absorption/desorption kinetics (Figure 7.15a and Figure 7.16). The normalized H_2 capacity as a function of the cycling number reveals that the capacity retention for the carbon-coated Li_3N nanofibers is over 73% even through 10 cycles while only 15% capacity for the bulk counterpart was remained after 5 cycles (Figure 7.15b). Moreover, in contrast to the bulk Li_3N that shows a significant degrade on the hydrogen capacity after 5th PCT cycle, both absorption and desorption capacity as well as the plateau pressure (Figure 7.15c) remain stable after 10 cycles for the carbon-coated Li_3N nanofibers, illustrating the great modification of thermodynamics on this sample. Additionally, ammonia is still undetectable during the 10th desorption process (Figure 7.17) and the characteristic peaks of β-Li_3N are also present in the carbon-coated Li_3N nanofibers after the 10th desorption (Figure 7.18). To the best of our knowledge, this is the first report on the stable reversibility of Li_3N with a capacity close to its theoretical value at a temperature as low as 250 °C.

In our *in-situ* preparation of carbon-coated Li_3N nanofibers, on one hand, the electrospinning technique can realize transformation of the precursor solution, i.e., the well-distributed LiN_3 with PVA, into nanofibers, and, therefore, nanoconfinement of LiN_3 nanoparticles inside PVA. On the other hand, the following calcination process can effectively maintain the nanofibrous structure and the formation of 3D porous carbon-coating restricts the growth of Li_3N nanoparticles. Based on synchrotron x-ray

diffraction data, the transformation during hydrogen release and uptake for the Li-N-H-based system mainly involves the migration of Li^+ and H^+ ions.[25] The comprehensive first-principles calculation results verified that the effective activation energy for both dehydrogenation and hydrogenation closely depends on the surface-to-volume ratio or the specific surface area, which relates to the concentration of Li^+ and H^+ on the surface and their following diffusion pathway.[12, 26] In the case of the carbon-coated Li_3N nanofibers, the dramatically improved H_2 storage performance can be attributed to the combination effect of the formation of β-Li_3N, the larger specific surface area of the Li_3N nanoparticles, and a short ion diffusion path due to the nanosize nature of the Li_3N particles (~ 3.7 nm) and their uniform distribution in the porous carbon nanofibers. Moreover, the 3D distribution of micropores, mesopores and macropores inside the nanofibers can also provide a favorable way for H_2 delivering, and the phase growth and separation for active materials can be effectively prevented during successive H_2 discharge and refuel due to the space-confinement of porous carbon-coating on the nanosized Li_3N. These endow the carbon-coated Li_3N porous nanofibers a stable reversibility without apparent degradation after even 10 de-/re-hydrogenation cycles at a temperature as low as 250 ^{o}C.

7.4 Conclusions

In summary, we have successfully developed a new, simple, and one-pot method to synthesize the carbon-coated Li_3N nanofibers by a single-nozzle electrospinning technique. The novelty of the methodology lies on the use of the PVA-LiN_3 mixture as the precursor, which can serve as the templating agent for the well distribution of Li_3N and the porogen for the fabrication of carbon coating with micropores, mesopores and macropores. The thus-fabricated carbon-coated Li_3N porous nanofibers exhibit significantly enhanced hydrogen storage properties, with a stable reversibility close to

the theoretical value over 10 de-/re-hydrogenation cycles at a temperature of 250 $^{\circ}$C. More importantly, the strategy of utilizing electrospinning technique for fabricating carbon-coated Li$_3$N nanofibers opens up a prospective route for advancing other hydrogen storage materials. Furthermore, the special nanofiberous structure with 3D porosity is also promising as supporting substrates for the encapsulation of other active substances such as catalyst, and electrode materials for energy storage.

7.5 References

[1] L. Schlapbach, A. Zuttel, *Nature* **2001**, *414*, 353;

[2] J. Yang, A. Sudik, C. Wolverton, D. J. Siegel, *Chemical Society Reviews* **2010**, *39*, 656.

[3] C. Weidenthaler, M. Felderhoff, *Energy & Environmental Science* **2011**, *4*, 2495.

[4] P. Chen, Z. T. Xiong, J. Z. Luo, J. Y. Lin, K. L. Tan, *Nature* **2002**, *420*, 302.

[5] P. Chen, Z. T. Xiong, J. Z. Luo, J. Y. Lin, K. L. Tan, *Journal of Physical Chemistry B* **2003**, *107*, 10967.

[6] T. Ichikawa, S. Isobe, N. Hanada, H. Fujii, *Journal of Alloys and Compound* **2004**, *365*, 271.

[7] S. Nayebossadri, K.-F. Aguey-Zinsou, *Physical Chemistry Chemical Physics* **2011**, *13*, 17683.

[8] C. Lu, J. Hu, J. H. Kwak, Z. Yang, R. Ren, T. Markmaitree, L. L. Shaw, *Journal of Power Sources* **2007**, *170*, 419.

[9] Y. H. Hu, E. Ruckenstein, *Industrial & Engineerinf Chemistry Research* **2005**, *44*, 1510.

[10] M. Menjo, Y. Hyodo, S. Moriyama, H.-W. Li, M. Matsuo, S. Semboshi, S.-i. Orimo, *Materials Transactions* **2011**, *52*, 623.

[11] T. Mueller, G. Ceder, *ACS Nano* **2010**, *4*, 5647.

[12] K. Hoang, A. Janotti, C. G. Van de Walle, *Angewandte Chemie-International Edition* **2011**, *50*, 10170.

[13] V. Stavila, R. K. Bhakta, T. M. Alam, E. H. Majzoub, M. D. Allendorf, *ACS Nano* **2012**, *6*, 9807.

[14] P. E. de Jongh, P. Adelhelm, *ChemSusChem* **2010**, *3*, 1332; M. Fichtner, *Physical Chemistry Chemical Physics* **2011**, *13*, 21186; T. K. Nielsen, F. Besenbacher, T. R. Jensen, *Nanoscale* **2011**, *3*, 2086.

[15] H. Reardon, J. M. Hanlon, R. W. Hughes, A. Godula-Jopek, T. K. Mandal, D. H. Gregory, *Energy & Environmental Science* **2012**, *5*, 5951.

[16] P. Ngene, P. Adelhelm, A. M. Beale, K. P. de Jong, P. E. de Jongh, *Journal of Physical Chemistry C* **2010**, *114*, 6163.

[17] Z. Tang, H. Chen, X. Chen, L. Wu, X. Yu, *Journal of the American Chemical Society* **2012**, *134*, 5464.

[18] P. Ngene, R. van den Berg, M. H. W. Verkuijlen, K. P. de Jong, P. E. de Jongh, *Energy & Environmental Science* **2011**, *4*, 4108.

[19] D. Li, Y. Xia, *Advanced Materials* **2004**, *16*, 1151.

[20] S. Cavaliere, S. Subianto, I. Savych, D. J. Jones, J. Roziere, *Energy & Environmental Science* **2011**, *4*, 4761.

[21] M. Inagaki, Y. Yang, F. Kang, *Advanced Materials* **2012**, *24*, 2547.

[22] F. Xu, Y. Lai, R. Fu, D. Wu, *Journal of Materials Chemisty A* **2013**, *1*, 5001;

[23] H. J. Beister, S. Haag, R. Kniep, K. Strössner, K. Syassen, *Angewandte Chemie-International Edition* **1988**, *27*, 1101.

[24] R. Demir-Cakan, W. S. Tang, A. Darwiche, R. Janot, *Energy & Environmental Science* **2011**, *4*, 3625.

[25] W. I. F. David, M. O. Jones, D. H. Gregory, C. M. Jewell, S. R. Johnson, A. Walton, P. P. Edwards, *Journal of the American Chemical Society* **2007**, *129*, 1594.

[26] K. Hoang, A. Janotti, C. G. Van de Walle, *Physical Review B* **2012**, *85*, 064115.

8   CHAPTER 8 WELL-DISPERSED LITHIUM AMIDOBORANE NANOPARTICLES THROUGH NANOREACTOR ENGINEERING FOR IMPROVED HYDROGEN RELEASE

8.1 Introduction

Many recent efforts have been directed towards the development of chemical hydrides as promising hydrogen storage media.[1-6] Among them, ammonia borane (AB) is an excellent candidate for hydrogen storage owing to the ultrahigh hydrogen capacity (19.6 wt.%), satisfactory air stability, and relatively low molecular mass (30.7 g mol^{-1}).[7, 8] The direct use of pristine AB as a hydrogen energy carrier, however, is hindered by the long induction period, slow decomposition rate in the first step at 100 ^{o}C and the concurrent release of volatile by-products (*e.g.*, borazine, diborane and aminodiborane).[9-12] Interestingly, by the replacement of one H from AB with metal ions, the thus-formed metal amidoboranes show the significantly enhanced dehydrogenation kinetics and suppressed volatile by-products, due to the iconicity change of N-H and B-H bond introduced by the related metal ions.[13-22] Especially, lithium amidoborane (LiAB) with high hydrogen capacity (13.7 wt.%) and accessible low temperature is standout from other materials to be an appropriate candidate.[23, 24] Nonetheless, similar with the dehydriding behavior of AB, the dehydriding rate of LiAB at low temperature is still low for practical application, especially for the second-step dehydrogenation that may be attributed to the sluggish diffusion of both positive and negative hydrogen across the reactive solid interfaces.[25]

Recent theoretical calculations and experiments have demonstrated that the nanoscaled structure offers hydrogen storage materials a shorter diffusion path length, the larger specific surface area and the decreased thickness of reactive interfaces during H$_2$ ab-/desorption process.[26-31] Moreover, the excess of surface energy occurring in small particles could facilitate the material's destabilization.[32] These

advantages are capable of enhancing the thermodynamics and kinetics of dehydrogenation.[33-38] In particular, by confining AB in various porous templates, *e.g.*, metal organic frameworks,[39-41] mesoporous carbon,[42] silica hollow nanospheres,[43] and mesoporous boron nitride,[44] the significantly improved dehydrogenation kinetics at lower temperature and the complete suppression of volatile by-products have been successfully realized. Inspired by this method, constructing the nanosized LiAB might be a feasible route to improve its kinetics and thermodynamics for hydrogen release. To fabricate nanosized complex hydrides, considerable efforts have been devoted to impregnating them into various porous matrixes, which can not only directly synthesize the nanostructured composites but also physically hinder the agglomeration during thermal treatment for hydrogen desorption.[27, 28] During the infiltration process into mesoporous templates, the pores with relatively small sizes, however, are easier to be blocked more or less, which results in terrible encapsulation and agglomeration of reactive substrates.[45] Additionally, it is still of a big challenge to keep the thus-formed nanoparticles separated *via* the method of nanoconfinement so the agglomeration and particle growth during thermal dehydrogenation is inevitable.[46] Right now, facile control over the spatial distribution of precursors inside the scaffolds is largely lacking with existing strategies.

It should be noted that the low solubility of LiAB with lack of melting nature even makes traditional infiltration method unrealizable up to now. In order to achieve the synthesis of nanoconfined LiAB nanoparticles with effective infiltration and well-distribution, we established a simple and highly effective method using the reaction between AB and Li_3N well-distributed in the porous CNFs to produce uniformly distributed LiAB nanoparticles with improved dehydrogenation properties. As schematically illustrated in Figure 8.1, we firstly fabricated PVA-coated LiN_3

nanofibers using PVA-LiN$_3$ mixture as the precursor by a simple electrospinning technique. By successive calcination of the thus-formed nanofibers, a plenty of micropores, mesopores and macropores were generated upon the explosive release of N$_2$ from LiN$_3$ accompanied by the carbonization of PVA. It *in-situ* produces the Li$_3$N nanoparticles with well-distribution space-confined inside the separated pores and sufficient space for the accommodation of AB to interact with Li$_3$N.[46] Firstly, the three-dimensionally distributed porous carbon matrixes possess a large plenty of macropores between individual CNFs, providing favorable diffusion pathway for the effective infiltration of the precursors into the "nanoreactor". Secondly, during the reaction, each Li$_3$N nanoparticle serving as an active site separated by porous carbon shell inside the CNFs initiates the formation of LiAB *via* the reaction with AB with a molar ratio of 1:3 under the steric hindrance of carbon coating, simultaneously realizing the controllable synthesis of LiAB with high loading, well dispersion and robust stability. In addition, owing to the mechanical support of carbonaceous frameworks, the morphology of porous CNFs was well maintained during the whole reaction process and thermolysis process, which is able to effectively stabilize the physical environment of LiAB.

8.2 Experimental section

8.2.1 Synthesis of 3D porous carbon-coated Li$_3$N nanofibers

Poly(vinylalcohol) (0.5 g, Alfa Aesar, Mv=88000, CAS:9002-89-5) was mixed with deionized water (5 ml) and stirred in oil bath at 40 ℃ over night. After PVA molecules were fully swelled in water, then turn the temperature to the 90 ℃ for 8 h to make a well-proportioned and stable PVA solution. LiN$_3$ solution(0.4 mL, 20 wt.%) in water was then added into the cooled PVA solution and vigorously stirred for 6 h to make a

homogeneous spinning dope. The well-prepared precursor solution was poured into a syringe with an 18-gauge blunt tip needle. Set the voltage as 15KV which was provided by a high–voltage power supply between the needle and the collector. Also the flow rate of solution was approximately 500 μL h^{-1} controlled by a syringe pump (Longer, TJP-3A, China), and a grounded stainless steel plate was horizontally placed 10 cm from the needle to collect the nanowires. The as-collected fibers by electrospinning were firstly dewatered in the 75 °C water bath under dynamic vacuum for 15 h. Then the successive calcinations to 550 °C for 3 h was taken under dynamic N$_2$ atmosphere with a pressure of ~ 1 bar to obtain the 3D nanoporous carbon-coated Li$_3$N fibers with a heat rate of 2 °C min^{-1}.

8.2.2   Synthesis of 3D porous LiAB@CNFs

The thus-formed Li$_3$N@CNFs was then immersed into the solution of AB in THF in the glove box for ~4 h. The mixture was then ultrasonicated for ~5 min at room temperature for several times, and, subsequently, the CNFs in the form of film was then taken out and washed with pure THF for several times to remove the residual AB. Finally, the CNFs was treated under vacuum for ~ 12 h to remove solvent and yield the carbon-coated LiAB nanofibers (LiAB@CNFs). The mass concentration of LiAB in the as-prepared fibers, which was calculated to be 52.1 wt.%, was obtained by elemental analysis.

8.2.3   Preparation of LiAB powders

Li$_3$N (99.4 wt.%) and AB (97 wt.%) were commercial products and used as received. Tetrahydrofuran (THF) was purified by distilling with sodium-potassium alloy under an inert Ar atmosphere. AB (200 mg) was dissolved in THF (20 mL) under magnetic stirring for 3 min. Li$_3$N powder (75.2 mg) was added into AB solution in the golvebox.

Then the mixture was allowed to react for 60 min at 30 ^{o}C under the Ar atmosphere. At the end of the reaction, the white LiAB powder was obtained by vacuum drying the solution overnight at room temperature. All the samples were handled in a glove-box filled with Ar (99.9999%), which was equipped with a circulative purification system to control the H_2O/O_2 levels below 0.1 ppm. The reaction involved for the production of LiAB can be expressed in eq. 8.1

$$3 NH_3BH_3 + Li_3N \rightarrow 3LiNH_2BH_3 + NH_3 \quad (8.1)$$

8.2.4   Synthesis of LiAB/CNFs composite by ball-milling

In this case, the as-synthesized LiAB was mixed with CNFs in a weight ratio of 1:1 by ball milling for 2 h to form a mixture for the further experimental trials. The ball milling was performed on a planetary ball mill (QM-1SP2, Nanjing) with a ball-to-powder weight ratio of 30: 1 and a rotating speed of 350 rpm. Due to the relatively lower onset temperature of decomposition (approximately 80 ^{o}C), the milling procedure was carried out by alternating between 6 min of milling and 6 min of rest. In order to prevent contamination by air, all handling and manipulation of the materials were performed in an argon-filled glove box.

8.2.5   Hydrogen storage tests

Dehydrogenation of the ball-milled LiAB/CNFs composite, LiAB@CNFs and the bulk LiAB composite were characterized by temperature-programmed desorption (TPD) performed on a Sieverts-type apparatus, connected to a reactor filled with sample (0.04g) under argon atmosphere (1 bar) at a heating rate of 5 ^{o}C min^{-1}. Simultaneous thermogravimetric analysis and mass spectrometry (TGA-MS, Netzsch STA 449C) were conducted at room temperature, using a heating rate of 5 ^{o}C min^{-1} under dynamic argon with a purge rate of 80 mL min^{-1}. Differential scanning

calorimetry (DSC) measurements were performed by TAQ 2000 DSC under argon with a gas flow of 40 mL Ar min^{-1} at a heating rate of 5 $^{\circ}$C min^{-1}.

8.3 Results and discussion
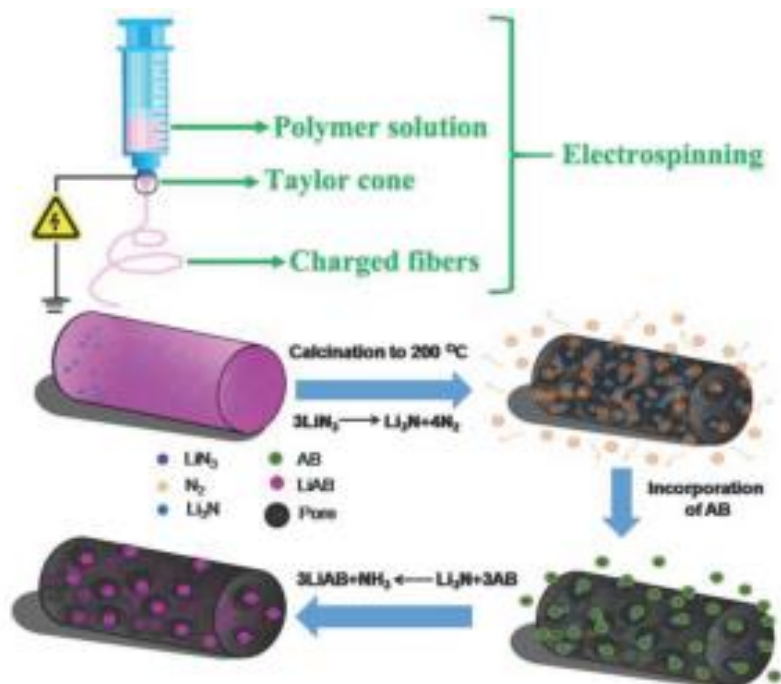
Figure 8. 1 Schematic illustration of the synthetic procedure of the LiAB@CNFs.

Figure 8.2a shows an overall SEM morphology of the as-electrospun nanofibers. It demonstrates that the as-synthesized PVA-coated LiN$_3$ fibers are continuous with quite smooth surface and a relatively uniform diameter distribution of ~200 nm. After calcination to 550 $^{\circ}$C, the uniform fibrous nanostructure is well preserved and the average diameter was decreased to ~150 nm resulting from the huge mass loss of PVA upon carbonization (Figure 8.2b). The relatively high-magnification SEM images clearly illustrate that the previous smooth surface turns to be rough and is filled with both mesopores and macropores with various diameters (5–50 nm) (Figure 8.2c) due to the strong release of N$_2$ from the decomposition of LiN$_3$. Moreover, the SEM image of an occasionally broken fiber (highlighted by the red circle in Figure 8.2c) verified the presence of mesopores inside the CNFs. This is attributed to the well-distribution

of LiN$_3$ in the as-electrospun PVA nanofibers. Numerous mesopores can be directly observed in the TEM image (Figures 8.2e), confirming the 3D porous architectures of the as-prepared carbon-coated Li$_3$N nanofibers (Li$_3$N@CNFs). The highly porous structure of the Li$_3$N@CNFs is further illustrated by the N$_2$ adsorption-desorption plots (Figure 8.3). From the plots, an obvious absorption was observed both at high relative pressure and low pressure, demonstrating the existence of large size pores and micropores, respectively. In addition, there is a broad distribution between 2 nm and 50 nm in the pore size distribution results, which agrees well with the SEM and TEM results. Hence, it confirms that the CNFs are hierarchically full of micropores, mesopores and macropores. The multiple and interconnected pores are favorable for the encapsulation of AB thoroughly, and, more importantly, they can simultaneously offer sufficient room around each Li$_3$N nanoparticles inside the nanoreactor for the subsequent reaction. After the infiltration of AB, the morphology of CNFs is well-maintained during the whole reaction process as evidenced by the SEM image in Figure 1d. Nonetheless, comparing to the as-prepared CNFs, no obvious pores are observed after the interaction with AB from TEM image (Figure 8.2f), indicating that most of the mesopores have been filled up. Moreover, both the BET surface area and the cumulative pore volume of the CNFs is substantially reduced resulting from the encapsulation of AB, concurrent with a significant reduction of the intensity of the Barrett-Joyner-Hallenda (BJH) pore size distribution. It undoubtedly demonstrates that AB penetrates the porous network of CNFs and occupies a large fraction of the pores and/or blocks the pores. Furthermore, it should be noted that the formation of LiAB is initiated by the interaction of AB with the pre-existing Li$_3$N nanoparticles, which therefore ensures the well-distribution of the thus-formed LiAB particles.
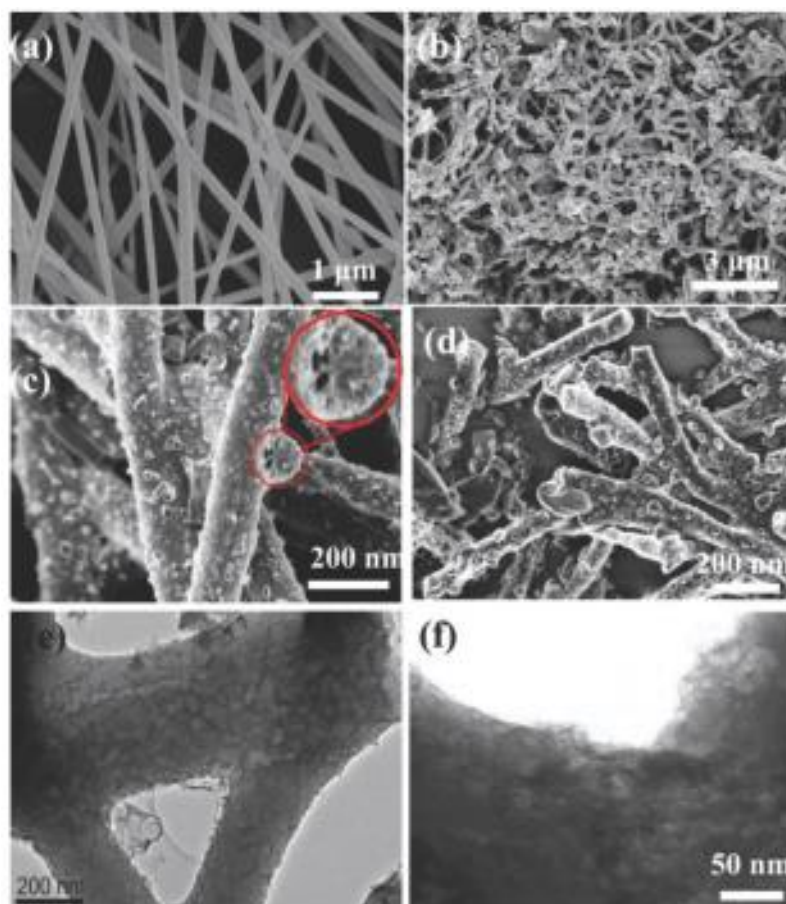
Figure 8. 2 SEM images of (a) the as-electrospun PVA-coated LiN$_3$ nanofibers, (b) the as-prepared Li$_3$N@CNFs and its large magnification image (c). (d) SEM images of the LiAB@CNFs. TEM images of Li$_3$N@CNFs (e) and LiAB@CNFs (f).
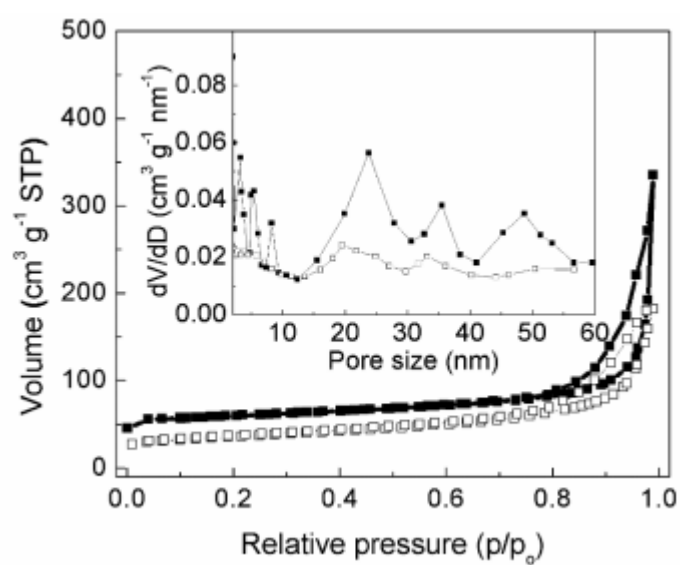
Figure 8. 3 N_2 sorption isotherm and pore size distribution (inset) of the as-prepared Li$_3$N@CNFs (a) and LiAB@CNFs (b).

In the XRD results as shown in Figure 8.4, characteristic peaks of LiAB, which is similar with LiAB produced from the reaction between LiH and AB *via* ball-milling,[23] are present for the as-formed composites from the interaction of Li$_3$N with AB in THF. It therefore verifies the feasibility to synthesize LiAB by this wet-chemical reaction.[47] After the interaction of the CNFs containing Li$_3$N with the solution of AB, the peaks belonging to LiAB appeared along with the disappearance of Li$_3$N (Figure 8.4a). It directly confirms the stabilization of LiAB inside during the reaction process. Some peaks belonging to NH$_3$BH$_3$ were also observed in the product. This may result from the insufficient washing of the CNFs. Moreover, it can be seen that the peaks attributed to LiAB inside the CNFs are broader than that of pure LiAB, suggesting the smaller crystallite dimension of LiAB owing to the nanoconfinement effects. The average particle size of LiAB, calculated from Debye-Scherrer's equation, is ~ 25.3 nm. The presence of the characteristic peaks of N-H and B-H bonds assigned to LiAB for the LiAB@CNFs was further confirmed by FTIR spectra (Figure 8.5). Besides, it is observed that, in the whole spectrum, the peaks assigned to PVA disappeared after carbonization only with the presence of LiAB, suggesting the chemical inertness of the CNFs that only serves as the nanoreactor.
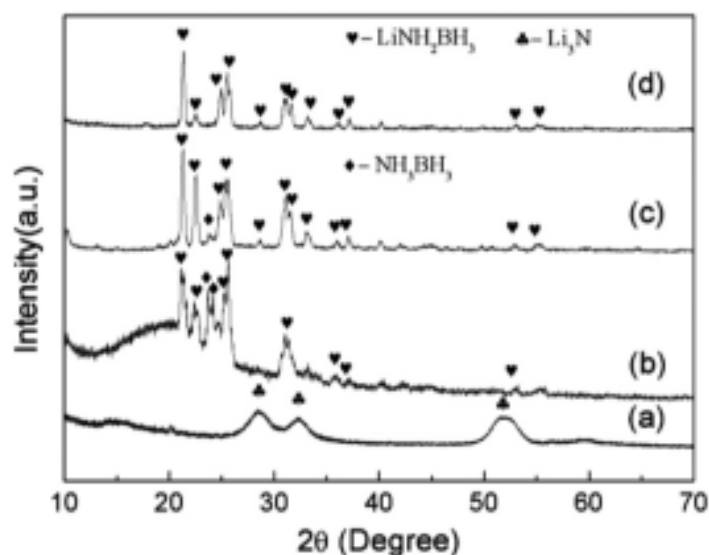
Figure 8. 4 XRD patterns of the as-prepared Li₃N@CNFs (a), LiAB@CNFs (b), including the products of Li₃N and AB *via* the wet-chemical method (c) and referenced LiAB (d) for comparison.
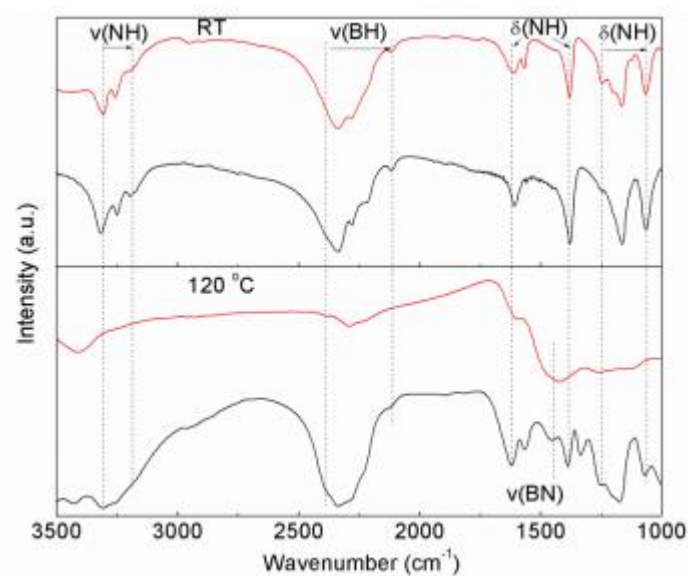
Figure 8. 5 FTIR spectra of the bulk LiAB (black line), LiAB@CNFs (red lines) and their decomposed products to 120 °C.

To explore the nanosize effects on the hydrogen storage properties, a comparison of the thermal decomposition performance of the as-prepared LiAB@CNFs, with the ball-milled LiAB and LiAB/CNFs composite as control sample, was conducted by

employing TG and MS in tandem with volumetric measurements. As shown in Figure 8.6, the decomposition process of bulk LiAB could be divided into two steps. The onset and peak temperature of the first step desorption were 70 $^{\circ}$C and 98 $^{\circ}$C, respectively, and the second step began at 120 $^{\circ}$C with a peak at 150 $^{\circ}$C, which agrees well with the TG results. In addition, the total weight loss was 10.2 wt.% with a gradual decomposition during the second stage, corresponding well with previous reports.[14, 23, 24, 48] In the case of the ball-milled LiAB/CNFs mixture, it underwent a decomposition process starting at 50 $^{\circ}$C and ceasing at 180 $^{\circ}$C with a broader decomposition temperature range compared with LiAB, giving a weight loss of ~10.2 wt.% similar to pure LiAB. Therefore, it could be concluded that the carbonaceous materials have no effects on facilitating the kinetics of hydrogen release. In contrast, the as-prepared LiAB@CNFs showed a one-step decomposition with the onset and peak temperature of H_2 desorption downshifted to~40 $^{\circ}$C and 80 $^{\circ}$C, respectively, which were 30 $^{\circ}$C and 20 $^{\circ}$C lower than that for the first step reaction of pure LiAB. The one-step desorption of LiAB@CNFs was also observed from the MS curve, suggesting that the decomposition route of LiAB may be changed owing to the nanoconfinement effects. It is similar with the observation of the nanoconfinement effects on the decomposition of AB.[39, 41, 43, 49, 50] Furthermore, TG results illustrated that most of H_2 was quickly released before 105 $^{\circ}$C, in concurrence with the MS spectra, which performed much higher desorption rate under the same weight loss (~10.5 wt.%) compared with bulk LiAB. Moreover, the weight loss is in good agreement with the volumetric results, confirming the high-purity of the released hydrogen from LiAB@CNFs (Figure 8.7). All the remarkable desorption performance verifies that the carbon-coated LiAB nanofibers through nanoreactors engineering improved the hydrogen desorption kinetics.
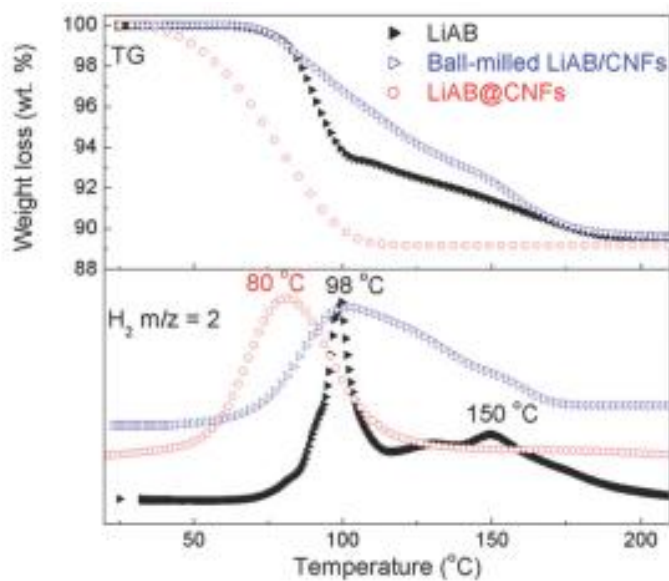
Figure 8. 6 TG and MS results for bulk LiAB, ball-milled LiAB/porous carbon, and

LiAB@CNFs, with a heating rate of 5 °C/min. H_2 storage capacity is normalized to

the LiAB in the composite.
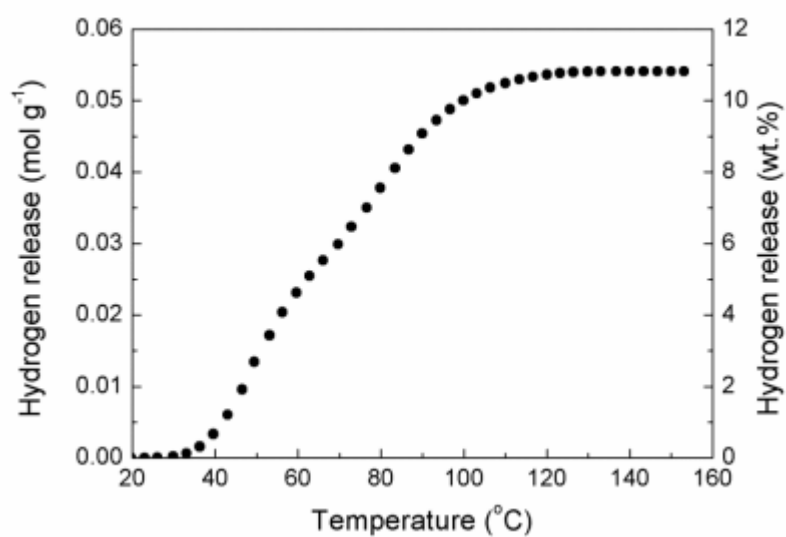
Figure 8. 7 Volumetric results for the decomposition of LiAB@CNFs.
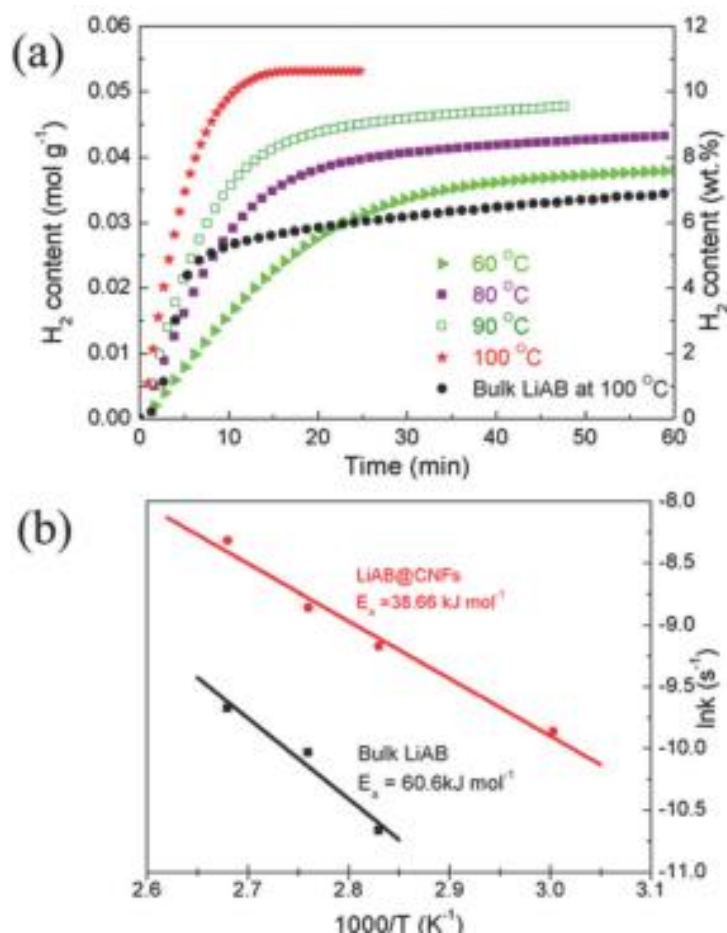
Figure 8. 8 (a) Hydrogen desorption curves of the LiAB@CNFs at different temperatures, including bulk LiAB at 100 °C for comparison. Carbon was not considered as an active component for the hydrogen storage measurements; (b) Arrhenius plot according to the isothermal H_2 desorption of the LiAB@CNFs and bulk LiAB.

Insights into the dehydrogenation kinetics of LiAB@CNFs and bulk LiAB were gained by applying the volumetric desorption measurements at different temperatures (Figure 8.8 and Figure 8.9). As shown in Figure 8.8, even at a high temperature of ~100 °C, the bulk LiAB exhibits a hydrogen release of ~7 wt.% within 60 min. By contrast, the LiAB nanoparticles are able to release~7.5 wt.% hydrogen at a temperature as low as 60 °C through the same operation time. Apparently, with increasing operation temperature, faster kinetics is yielded for the LiAB@CNFs.

Specifically, upon further elevating the temperature to 80 and 90 °C, hydrogen capacities of 8.7 and 9.5 wt.% could be observed, respectively. The value can further reach to ~10.6 wt.%, approaching its theoretical releasable capacity, at 100 °C in less than 15 min. For a quantitative evaluation of the enormously improved dehydriding kinetics of the as-prepared LiAB@CNFs, the apparent activation energy (E_a) was calculated from various isothermal dehydrogenation results *via* linear Arrhenius plots of ln$k$, (k, rate constant), as a function of $1/T$ (T, absolute temperature). Figure 8.8(b) displays the details for calculation of apparent activation energies. It gives the activation energies of approximately 38.7 kJ mol^{-1} and 60.6 kJ mol^{-1} for the LiAB nanoparticles and bulk counterpart, respectively. The activation energies of pure LiAB is a little different from the value reported previously (75 kJ mol^{-1}),[51] possibly attributed to the various fabrication method involved. The significant decrease of activation energy gives a direct evidence of the improvement of hydrogen release kinetics resulting from the nanoconfinement and the nanoporous structure.
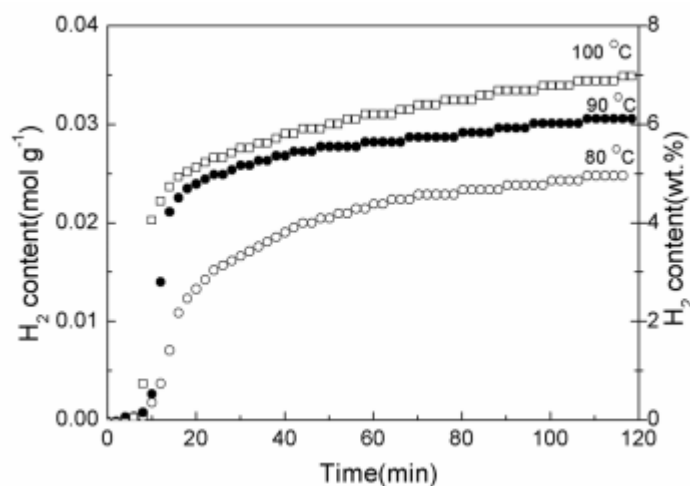
Figure 8. 9 Hydrogen desorption curves of the bulk LiAB at different temperatures.
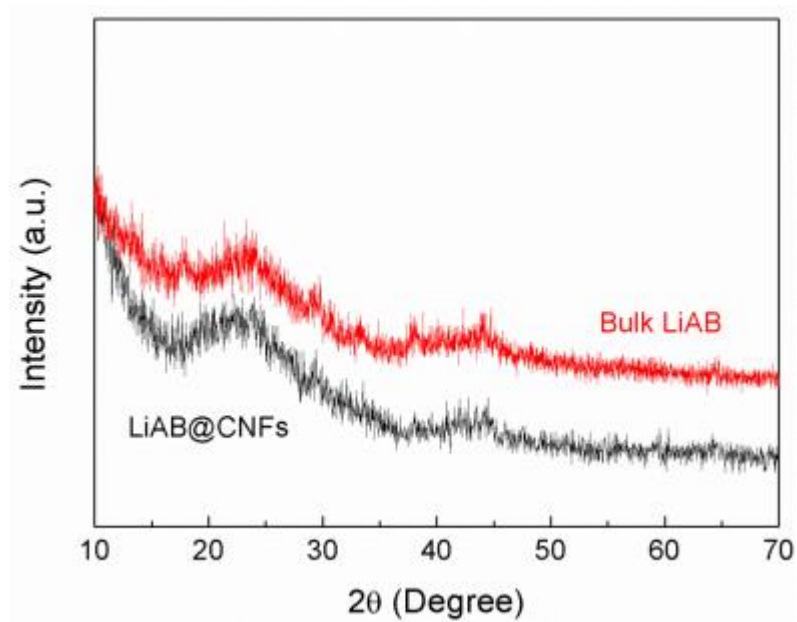
Figure 8. 10 XRD results of the bulk LiAB and LiAB@CNFs after heating to 200 ^{o}C.
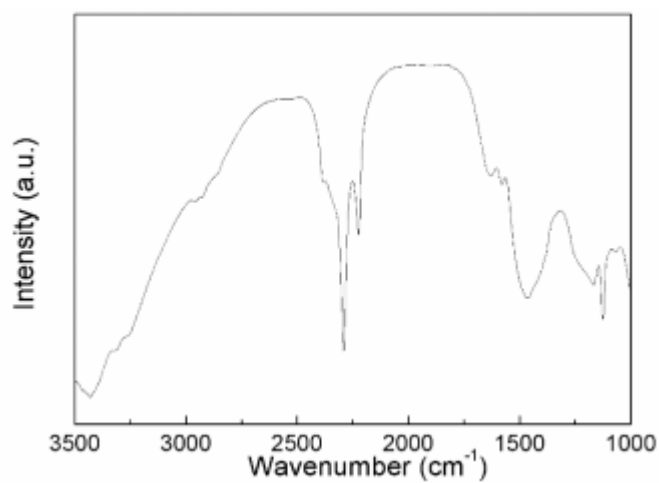
Figure 8. 11 FTIR spectra of the decomposed product of bulk LiAB to 250 ^{o}C.
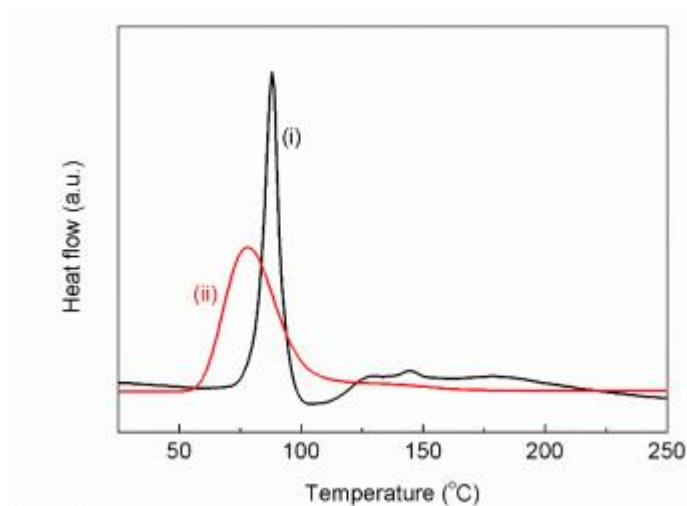
Figure 8. 12 DSC profiles for the dehydrogenation of (i) pristine LiAB and (ii) LiAB@CNFs. The heating rate is 5 $^{\circ}$C min^{-1}.

The XRD pattern of LiAB@CNFs after decomposition to 120 $^{\circ}$C (Figure 8.10) demonstrates the formation of an amorphous phase, which is similar with the bulk LiAB due to the polymerization occurring between N-H bonds and B-H bonds. Further information on the decomposition pathway was therefore provided by the FTIR spectra (Figure 8.5). It verifies the disappearance of N-H bonds and a dramatic decay of B-H bonds in both bending and stretching modes with the appearance of B-N bonds of LiAB@CNFs after dehydrogenation to 120 $^{\circ}$C. It indicates the complete dehydrogenation of LiAB nanoparticles owing to the interaction of B-H and N-H bonds. The weak peaks indexed to B-H bonds are attributed to the formation of a small amount of BH$_4$ group upon the thermolysis of LiAB, which is normally formed in the dehydrogenation of metal amidoboranes.[23, 52] Nonetheless, both N-H and B-H bonds are clearly observed for the bulk LiAB upon decomposition at 120 $^{\circ}$C and disappeared until heating to 250 $^{\circ}$C for a full dehydrogenation (Figure 8.11). It provides further evidence for the improved dehydrogenation kinetics of LiAB *via* stabilization inside the CNFs.

To understand the effects of nanoconfinement on the thermodynamics and reversibility of LiAB, DSC was employed to monitor the enthalpy change during dehydrogenation (Figure 8.12). It is noted that the hydrogen release process from LiAB@CNFs is still exothermic with an enthalpy change of -6.68 kJ mol^{-1} H$_2$, slightly less exothermic than that of pure LiAB (-7.83 kJ mol^{-1}). Although the reduced exothermicity could benefit the hydrogenation of the decomposition products of LiAB, no reversible phenomenon has been observed via solid-gas reaction under 10 MPa H$_2$ pressure at various temperatures due to the exothermic reaction between N-H and B-H for hydrogen desorption.

8.4 Conclusions

In summary, we established a simple and effective method, using mesopores *in-situ* formed during the formation of Li$_3$N as nanoreactors to support the reaction between AB and Li$_3$N, to synthesize the LiAB nanoparticles with well-dispersion and nanometer size. Porous Li$_3$N nanofibers not only were used as reactant to synthesize and stabilize LiAB, but also offered sufficient room and channels for the successive transportation and reaction. Taking advantage of the special architecture of the porous CNFs and the reaction mechanism between Li$_3$N and AB, the high loading capacity and well dispersion of LiAB were simultaneously realized. Due to the physical confinement effects, the growth of LiAB crystal is largely controlled. The nanosized LiAB particles present significantly enhanced hydrogen desorption properties with the rapid release of 10.6 wt.% hydrogen in 15 min at 100 $^{\circ}$C. The special methodology for stabilizing LiAB nanoparticles provides a viable strategy for synthesizing other nanostructured metal amidoborane towards improved hydrogen storage properties.

8.5 References

[1] L. Schlapbach, A. Zuttel, *Nature* **2001**, *414*, 353.

[2] U. Eberle, M. Felderhoff, F. Schuth, *Angewandte Chemie-International Edition* **2009**, *48*, 6608.

[3] M. Yadav, Q. Xu, *Energy & Environmental Science* **2012**, *5*, 9698.

[4] H.-L. Jiang , S. K. Singh , J.-M. Yan , X.-B. Zhang, Q. Xu, *ChemSusChem* **2010**, *3*, 541.

[5] Z.-H. LU, Q. Xu, Funct. *Materials Letters* **2012**, *05*, 1230001.

[6] S.-i. Orimo, Y. Nakamori, J. R. Eliseo, A. Züttel, C. M. Jensen, *Chemical Reviews* **2007**, *107*, 4111.

[7] Z. G. Huang, T. Autrey, *Energy & Environmental Science* **2012**, *5*, 9257.

[8] A. Staubitz, A. P. M. Robertson, I. Manners, *Chemical Reviews* **2010**, *110*, 4079.

[9] P. Wang, *Dalton Transactions* **2012**, *41*, 4296.

[10] H. K. Lingam, X. Chen, J.-C. Zhao, S. G. Shore, *Chemistry-A European Journal* **2012**, *18*, 3490.

[11] X. Chen, X. Bao, J.-C. Zhao, S. G. Shore, *Journal of the American Chemical Society* **2011**, *133*, 14172.

[12] R. Chiriac, F. Toche, U. B. Demirci, O. Krol, P. Miele, *International Journal of Hydrogen Energy* **2011**, *36*, 12955.

[13] Y. S. Chua, P. Chen, G. Wu, Z. Xiong, *Chemical Communication* **2011**, *47*, 5116.

[14] H. Wu, W. Zhou, T. Yildirim, *Journal of the American Chemical Society* **2008**, *130*, 14834.

[15] A. T. Luedtke, T. Autrey, Inorg. Chem. **2010**, *49*, 3905.

[16] G. L. Xia, Y. B. Tan, X. W. Chen, Z. P. Guo, H. K. Liu, X. B. Yu, *Journal of Materials Chemisty A* **2013**, *1*, 1810.

[17] X. Kang, J. Luo, Q. Zhang, P. Wang, *Dalton Transactions* **2011**, *40*, 3799.

[18] H. Wu, W. Zhou, F. E. Pinkerton, M. S. Meyer, Q. Yao, S. Gadipelli, T. J. Udovic, T. Yildirim, J. J. Rush, *Chemical Communication* **2011**, *47*, 4102.

[19] T. He, J. Wang, Z. Chen, A. Wu, G. Wu, J. Yin, H. Chu, Z. Xiong, T. Zhang, P. Chen, *Journal of Materials Chemisty* **2012**, *22*, 7478.

[20] Y. J. Choi, Y. Xu, W. J. Shaw, E. C. E. Rönnebro, *Journal of Physical Chemistry C* **2012**, *116*, 8349.

[21] R. V. Genova, K. J. Fijalkowski, A. Budzianowski, W. Grochala, *Journal of Alloys and Compound* **2010**, *499*, 144.

[22] H. V. K. Diyabalanage, T. Nakagawa, R. P. Shrestha, T. A. Semelsberger, B. L. Davis, B. L. Scott, A. K. Burrell, W. I. F. David, K. R. Ryan, M. O. Jones, P. P. Edwards, *Journal of the American Chemical Society* **2010**, *132*, 11836.

[23] Z. T. Xiong, C. K. Yong, G. T. Wu, P. Chen, W. Shaw, A. Karkamkar, T. Autrey, M. O. Jones, S. R. Johnson, P. P. Edwards, W. I. F. David, *Nat Mater* **2008**, *7*, 138-141.

[24] G. L. Xia, X. B. Yu, Y. H. Guo, Z. Wu, C. Z. Yang, H. K. Liu, S. X. Dou, *Chemistry-A European Journal* **2010**, *16*, 3763.

[25] Z. Tang, Y. B. Tan, X. W. Chen, X. B. Yu, *Chemical Communication* **2012**, 48, 9296.

[26] F. E. Pinkerton, *Journal of Alloys and Compound* **2011**, *509*, 8958.

[27] P. E. de Jongh, M. Allendorf, J. J. Vajo, C. Zlotea, *MRS Bulletin* **2013**, *38*, 488.

[28] T. K. Nielsen, F. Besenbacher, T. R. Jensen, *Nanoscale* **2011**, 3, 2086.

[29] P. E. de Jongh, P. Adelhelm, *ChemSusChem* **2010**, *3*, 1332.

[30] G. L. Xia, L. Li, Z. P. Guo, Q. F. Gu, Y. H. Guo, X. B. Yu, H. K. Liu, Z. W. Liu, *Journal of Materials Chemisty A* **2013**, *1*, 250.

[31] G. L. Xia, Q. Meng, Z. P. Guo, Q. F. Gu, H. K. Liu, Z. W. Liu, X. B. Yu, *Acta Materialia* **2013**, *61*, 6882.

[32] H. Wu, *ChemPhysChem* **2008**, *9*, 2157.

[33] J. Gao, P. Ngene, I. Lindemann, O. Gutfleisch, K. P. de Jong, P. E. de Jongh, *Journal of Materials Chemisty* **2012**, *22*, 13209.

[34] T. K. Nielsen, M. Polanski, D. Zasada, P. Javadian, F. Besenbacher, J. Bystrzycki, J. Skibsted, T. R. Jensen, *ACS Nano* **2011**, *5*, 4056.

[35] P. Ngene, R. van den Berg, M. H. W. Verkuijlen, K. P. de Jong, P. E. de Jongh, *Energy & Environmental Science* **2011**, *4*, 4108.

[36] T. K. Nielsen, U. Bösenberg, R. Gosalawit, M. Dornheim, Y. Cerenius, F. Besenbacher, T. R. Jensen, *ACS Nano* **2010**, *4*, 3903.

[37] T. K. Nielsen, K. Manickam, M. Hirscher, F. Besenbacher, T. R. Jensen, *ACS Nano* **2009**, *3*, 3521.

[38] P. E. d. Jongh, R. W. P. Wagemans, T. M. Eggenhuisen, B. S. Dauvillier, P. B. Radstake, J. D. Meeldijk, J. W. Geus, K. P. d. Jong, *Chemistry of Materials* **2007**, *19*, 6052.

[39] G. Srinivas, W. Travis, J. Ford, H. Wu, Z.-X. Guo, T. Yildirim, *Journal of Materials Chemisty A* **2013**, *1*, 4167.

[40] L. Gao, C.-Y. V. Li, H. Yung, K.-Y. Chan, *Chemical Communication* **2013**, *49*, 10629.

[41] Z. Li, G. Zhu, G. Lu, S. Qiu, X. Yao, *Journal of the American Chemical Society* **2010**, *132*, 1490.

[42] L. Li, X. Yao, C. Sun, A. Du, L. Cheng, Z. Zhu, C. Yu, J. Zou, S. C. Smith, P. Wang, H.-M. Cheng, R. L. Frost, G. Q. Lu, *Advanced Functional Materials* **2009**, *19*, 265.

[43] T. Zhang, X. Yang, S. Yang, D. Li, F. Cheng, Z. Tao, J. Chen, *Physical Chemistry Chemical Physics* **2011**, *13*, 18592.

[44] G. Moussa, U. B. Demirci, S. Malo, S. Bernard, P. Miele, *Journal of Materials Chemisty A* **2014**, *2*, 7717.

[45] M. L. Christian, K.-F. Aguey-Zinsou, *ACS Nano* **2012**, *6*, 7739.

[46] G. L. Xia, D. Li, X. W. Chen, Y. B. Tan, Z. Tang, Z. P. Guo, H. K. Liu, Z. W. Liu, X. B. Yu, *Advanced Materials* **2013**, *25*, 6238.

[47] Z. Xiong, Y. Chua, G. Wu, L. Wang, M. W. Wong, Z. M. Kam, T. Autrey, T. Kemmitt, P. Chen, *Dalton Transactions* **2010**, *39*, 720.

[48] Y. Wang, Z. X. Guo, *Journal of Materials Chemisty A* **2014**, *2*, 6801.

[49] Z. W. Tang, S. F. Li, Z. X. Yang, X. B. Yu, *Journal of Materials Chemisty* **2011**, *21*, 14616.

[50] S. Gadipelli, J. Ford, W. Zhou, H. Wu, T. J. Udovic, T. Yildirim, *Chemistry-A European Journal* **2011**, *17*, 6043.

[51] X. D. Kang, Z. Z. Fang, L. Y. Kong, H. M. Cheng, X. D. Yao, G. Q. Lu, P. Wang, *Advanced Materials* **2008**, *20*, 2756.

[52] K. Shimoda, Y. Zhang, T. Ichikawa, H. Miyaoka, Y. Kojima, *Journal of Materials Chemisty* **2011**, *21*, 2609.

CHAPTER 9 CONCLUSIONS AND OUTLOOK

This thesis is focused on adopting nanoconfinement to improve the kinetics, thermodynamics, and cycling performance of the complex hydrides, with the aim of designing a material which possesses high gravimetric and volumetric hydrogen densities and could achieve hydrogen storage under moderate conditions. The synthetic strategy, the characterization of the as-prepared samples, and the hydrogen storage performance for each of the materials investigated have been elucidated based on systematic experimental data.

Nanoconfinement of $NaZn(BH_4)_3$ in mesoporous SBA-15 was successfully realized by typical infusion via capillary action. Compared with pure $NaZn(BH_4)_3$, $NaZn(BH_4)_3$ infiltrated into SBA-15 displays significantly enhanced hydrogen release properties, including complete suppression of boranes and improved hydrogen release kinetics, offering pure hydrogen release in the temperature range of 50 to 150 ^{o}C. Our results indicate that nanoscale $NaZn(BH_4)_3$ obeys a completely different decomposition mechanism from its bulk counterpart, which enables unstable borohydrides to release pure hydrogen rather than undesirable boranes, providing a viable strategy for improving the hydrogen desorption properties of relatively unstable metal borohydrides with high Pauling electronegativity to achieve superior hydrogen release kinetics at lower temperature by designed nanostructures.

Subsequently, a uniformly distributed composite of $2LiBH_4$-$LiAlH_4$ was successfully nanoconfined in mesoporous carbon scaffolds according to the solvent mediated infiltration technique. The onset dehydrogenation temperature of $LiAlH_4$ and $LiBH_4$ in the infiltrated $2LiBH_4$-$LiAlH_4$ composite is decreased to ~ 80 ^{o}C and 230 ^{o}C, respectively, which are 40 ^{o}C and 145 ^{o}C lower than for its post-milled counterpart. Isothermal measurements reveal that ~10 wt.% H_2 could be released from the

nanoconfined $2LiBH_4$-$LiAlH_4$ composite at 300 ^{o}C within 300 min, while less than 4 wt.% H_2 was released from the post-milled mixture, even at 350 ^{o}C. Moreover, by taking advantage of both nanoconfinement and thermodynamic destabilization, the release of toxic diborane from $LiBH_4$ was successfully suppressed. The dehydrogenation mechanism reveals that, under the structure-directing effects of carbon supports, the decomposition of the well-distributed $2LiBH_4$-$LiAlH_4$ composite favors the formation of AlB_2 instead of the thermodynamically stable $Li_2B_{12}H_{12}$, which has been verified to play a crucial role in enhancing the hydrogenation of the $2LiBH_4$-$LiAlH_4$ composite. On combination with the extra LiH supplied by the in-situ decomposition of nanoconfined $LiAlH_4$, the thus-tailored thermodynamics and kinetics of the $2LiBH_4$-$LiAlH_4$ composite endow it with significantly advanced reversible hydrogen storage properties, with a stable reversibility without apparent degradation after 7 de-/re-hydrogenation cycles.

A new, simple, and one-pot method to synthesize carbon-coated Li_3N nanofibers by a single-nozzle electrospinning technique was developed by using poly(vinyl alcohol) and LiN_3 as the precursor, which can serve as the templating agent for good distribution of the Li_3N and the porogen for the fabrication of a carbon coating with micropores, mesopores, and macropores. The thus-fabricated carbon-coated Li_3N porous nanofibers exhibit significantly enhanced hydrogen storage properties, with a stable reversibility close to the theoretical value over 10 de-/re-hydrogenation cycles at a temperature of 250 ^{o}C. More importantly, the strategy of utilizing the electrospinning technique for fabricating carbon-coated Li_3N nanofibers opens up a prospective route for advancing other hydrogen storage materials. Furthermore, the special nanofibrous structure with 3D porosity is also promising as a supporting

substrate for the encapsulation of other active substances such as catalysts and electrode materials for energy storage.

Following that, well-distributed $LiNH_2BH_3$ nanoparticles were successfully fabricated *via* carbon nanofibers with homogenous pores uniformly containing Li_3N as the nanoreactor and reactant, which were simply prepared by a single-nozzle electrospinning technique for subsequent interaction with BH_3NH_3. The hierarchical porous structure consists of various macropores, mesopores, and micropores produced *in-situ* during the formation of Li_3N, with the pores simultaneously serving as the reaction initiator, which not only controllably realize a good distribution of $LiNH_2BH_3$ nanoparticles, but also provide favorable channels for hydrogen release. By virtue of the hierarchical porous architecture and the nanoscale size effects, the LiAB nanoparticles start to release hydrogen at only 40 ^oC, which is 30 ^oC lower than that of pure $LiNH_2BH_3$, and they dehydrogenate completely within only 15 min at 100 ^oC (10.6 wt.%). $LiNH_2BH_3$ provides a new perspective on the controllable fabrication of nanosized hydrogen storage materials.

In this thesis, a series of complex hydrides were nanoconfined based on different methodologies, i.e., solution infiltration, electrospinning, and nanoreactor engineering. These synthetic methods and optimized conditions could be extended to other potential hydrogen storage materials and/or energy storage materials. The nanoconfinement-induced improvement of the hydrogen storage properties of complex hydrides further verifies the important role of nanostructuring and space-confinement effects towards enhancing their performance.

In summary, based on the results in this thesis, it could be concluded that nanoconfinement is an effective and efficient tool to improve the hydrogen storage performance of complex hydrides based on the following advantages. First, the

diffusion distance of hydrogen and the thickness of reactive interfaces during hydrogenation and dehydrogenation could be significantly decreased owing to the decrease of particle size down to nanometer scale, leading to tremendously improved hydriding and dehydriding kinetics and the decrease of temperature for hydrogen strorage. Second, the significant reduction of particle size results in a low mean coordination number of surface atoms, and therefore an excess of surface energy, which could effectively modify the thermodynamics parameters of complex hydrides, i.e., enthalpy and entropy, towards superior hydrogen storage performance. Third, the porous scaffolds adopted in nanoconfinement could physically prevent the particle growth, aggregation, and phase segregation upon cyclic hydrogenation and dehydrogenation, which could enhance the cycling stability of complex hydrides. Unfortunately, the disadvantages of adopting nanoconfinement to enhance the performance of complex hydrides is also obvious. Clearly, due to the introduction of the templates for nanoconfinement, which are often inactive for hydrogen storage, the gravimetric and volumetric hydrogen densities of the system are significantly reduced, which makes them impossible for practical application. Moreover, the synthetic process is often tedious and the nanostructured hydrogen storage materials are unstable, which makes them difficult to scale up.

Therefore, further investigations could focus on developing a cost-effective and efficient strategy to obtain reasonable hydrogen storage performance with high volumetric and gravimetric hydrogen storage capacity under moderate conditions. To achieve this goal, a template with high surface area, large pore volume and ordered porous structure, which could facilitate the effective nanoconfinement of hydrogen storage materials, is required. More importantly, nanoparticles of complex hydrides is highly unstable and tend to aggregate and grow upon thermal treatment for hydrogen

storage. Therefore, in order to preserve the superior hydrogen storage performance induced by the nanosize effects, an effective method to achieve full encapsulation of complex hydrides with high loading is highly desirable.